



Universiteit
Leiden
The Netherlands

Mononuclear spin-transition materials based on the bapbpy scaffold

Zheng, S.

Citation

Zheng, S. (2014, June 25). *Mononuclear spin-transition materials based on the bapbpy scaffold*. Retrieved from <https://hdl.handle.net/1887/26519>

Version: Not Applicable (or Unknown)

License: [Leiden University Non-exclusive license](#)

Downloaded from: <https://hdl.handle.net/1887/26519>

Note: To cite this publication please use the final published version (if applicable).

Cover Page



Universiteit Leiden



The handle <http://hdl.handle.net/1887/26519> holds various files of this Leiden University dissertation.

Author: Zheng, Sipeng

Title: Mononuclear spin-transition materials based on the bapbpy scaffold

Issue Date: 2014-06-25

Mononuclear spin-transition materials based on the bapbpy scaffold

PROEFSCHRIFT

ter verkrijging van
de graad van Doctor aan de Universiteit Leiden,
op gezag van Rector Magnificus Prof. mr. C.J.J.M Stolker,
volgens besluit van het College voor Promoties
te verdedigen op woensdag 25 juni 2014
klokke 11:15 uur

door

Sipeng Zheng
geboren te Beijing, China
in 1982

Samenstelling Promotiecommissie

Promotor Prof. Dr. E. Bouwman

Co-promotor Dr. S. Bonnet

Overige leden Prof. Dr. J. Brouwer

Prof. Dr. J.A. Real (Universitat de València)

Prof. Dr. J. Reedijk

Prof. Dr. J.M. van Ruitenbeek

Printed by: Off Page

*To my parents
and Yuanyuan*

Table of Contents

List of abbreviations.....	5
Chapter 1 Introduction.....	7
Chapter 2 Increasing the transition temperature of bapbpy-based mononuclear spin-crossover compounds: interplay between molecular and crystal engineering.....	29
Chapter 3 Effect of metal dilution on the thermal spin transition of $[\text{Fe}_x\text{Zn}_{1-x}(\text{bapbpy})(\text{NCS})_2]$	57
Chapter 4 Influence of selenocyanate ligands on the transition temperature and cooperativity of bapbpy-based Fe(II) spin-crossover compounds.....	81
Chapter 5 Synthesis and magnetic properties of bapphen-based mononuclear iron(II) spin-crossover complexes.....	109
Chapter 6 High-temperature cooperative spin crossover of an iron(II) amine-bridged bis-bipyridine complex.....	131
Chapter 7 Synthesis, magnetic properties, and STM imaging of an iron(II) bapphen complex functionalized with a long alkyl chain.....	145
Chapter 8 Conclusions and outlook.....	169
AI Supplementary information on Chapter 3.....	179
AII Supplementary information on Chapter 4.....	183
AIII Supplementary information on Chapter 5.....	187
AIV Supplementary information on Chapter 6.....	191
AV Supplementary information on Chapter 7.....	197
Samenvatting.....	203
List of Publications.....	209
Curriculum Vitae.....	210

List of abbreviations

bapbpy	<i>N,N'</i> -di(pyrid-2-yl)-2,2'-bipyridine-6,6'-diamine
bapphen	<i>N,N'</i> -bis(pyrid-2-yl)-1,10-phenanthroline-2,9-diamine
bbpya	<i>N,N'</i> -bis(2,2'-bipyrid-6-yl)amine
BINAP	2,2'-bis(diphenylphosphanyl)-1,1'-binaphthyl
bpy	2,2'-bipyridine
d, dd, m, s, t	Doublet, doublet of doublet, multiplet, singlet, triplet (in NMR spectra)
DCM	Dichloromethane
DMF	<i>N,N</i> -Dimethylformamide
DMSO	Dimethyl sulfoxide
DSC	Differential Scanning Calorimetry
EA	Elemental analysis
eq	equivalent
ESI-MS	electron spray ionization mass spectrometry
HR-MS	high resolution mass spectrometry
HS, LS	High spin, low spin
ICP-OES	Inductively coupled plasma optical emission spectrometry
IR	Infrared
LFS	Ligand field splitting
LIESST	Light-induced excited spin state trapping
NMR	nuclear magnetic resonance
phen	1,10-phenanthroline
ppm	parts per million
PXRD	Powder X-ray diffraction
r.t.	room temperature
SCO	Spin Crossover
SQUID	Superconducting quantum interference device
STM	Scanning tunneling microscopy
TMS	Tetramethylsilane
<i>V</i> / <i>Z</i>	Volume per formula unit

1

Introduction

In computing and digital communication, a bit (short for *binary digit*) is the basic unit of information. The scientific and technological developments in the last sixty years have allowed for reducing the bit size from 250 μm to 22 nm following the so-called “top-down” approach.^{1, 2} However, this approach is reaching its limits both in terms of size (*e.g.*, lithography is limited by diffraction),³ and in terms of investments/price, as it becomes more and more expensive to manufacture such small systems. The bottom-up approach appears as an attractive alternative, as it is based on the idea that the smallest unit capable of performing information storage and data treatment is one molecule.⁴ The first advantage of molecular electronics is quantitative: molecules are ~ 1 nm in size, which represents a serious improvement in terms of information density and processing speed. But there is another qualitative advantage: individual molecules are not simply smaller than a collection of molecules, they also behave differently, *i.e.*, according to quantum physics. This might completely change the way information is stored and treated in future computers. In order to store information a molecule needs to behave as a switch, *i.e.*, to exist at least in two different states. One type of candidates for molecular switch comprises spin-crossover (SCO) complexes.⁵ In this Chapter, a general introduction to the subject of SCO is given, as well as a brief overview of state-of-art developments in this field, and some of the challenges researchers in the field of SCO are facing.

1.1 General background of spin crossover and ligand field theory

When Cambi and Szegő first described (1931) the thermal spin crossover (SCO) of disubstituted dithiocarbamate iron(III) compounds,⁶ little was known about this phenomenon. After several decades of continuous developments, the field of spin crossover research has greatly expanded, and the SCO phenomenon is recognized as one of the most fascinating phenomena in inorganic chemistry.⁷

In an octahedral or distorted octahedral geometry, first-row transition metals with d^4 - d^7 electronic configurations can adopt either a high-spin (HS) or a low-spin (LS) electronic configuration, depending on the crystal field splitting introduced by the ligands (Figure 1.1). When the HS and LS states are close in energy the metal ion can switch between these two states by external perturbations such as temperature variations,⁸ light irradiation,⁹⁻¹¹ or by the application of pressure,¹²⁻¹⁴ of a magnetic field,¹⁵ or of an electric field.¹⁶ In thermal SCO the LS state is populated at low temperatures, whereas the HS state becomes the most stable state at higher temperatures.

To date, iron(II) is certainly the metal ion for which the largest number of SCO compounds has been reported.⁷ Iron(II) has d^6 electronic configuration, the SCO converts the 1A_1 LS state into the 5T_2 HS state (Figure 1.1). Apart from Fe(II), examples for Co(III),¹⁷ Co(II),^{18, 19} Fe(III),^{20, 21} Ni(II),²² and a few cases of Cr(II) and Mn(III)²³ are reported in the literature. However, in the cases of Co(III) and Fe(III) the stronger ligand field splitting and weaker interelectronic repulsion energy makes them less favourable for the occurrence of SCO than for Fe(II).⁷ For the Fe(II) ion indeed the ligand field splitting is relatively weak, hence spin pairing is not so strongly favoured and it is possible to obtain stable HS or LS complexes with a broad range of ligand sets.⁷ The first iron(II) complexes reported to show thermal SCO behaviour included $[\text{Fe}(\text{phen})_2(\text{NCS})_2]$ (phen = 1,10-phenanthroline), $[\text{Fe}(\text{phen})_2(\text{NCSe})_2]$, and $[\text{Fe}(\text{bpy})_2(\text{NCS})_2]$ (bpy = 2,2'-bipyridine).²⁴⁻²⁶ In this thesis, the focus lies on iron(II) d^6 SCO complexes.

Thermal SCO is rationalized using the ligand field theory. In an octahedral geometry, the d orbitals of iron(II) split into the t_{2g} subset of three orbitals, namely d_{xy} , d_{yz} , and d_{xz} , and the e_g subset of two orbitals, d_{z^2} and $d_{x^2-y^2}$.²⁷ The t_{2g} orbitals are nonbonding and therefore lower in energy than the anti-bonding e_g orbitals (Figure 1.1).²⁷ The energy difference between the two sets of orbitals is referred to as the ligand field splitting and

is symbolized by the ligand field strength, $10 Dq$. The ligand field strength depends both on the ligand set as well as on the metal ion and its oxidation state.²⁸ When the ligand set only induces smaller splitting of the d orbitals of the metal ion, the energy difference $10 Dq$ will be smaller than the interelectronic repulsion energy (P), and the electrons will fill the five d orbitals according to Hund's rule, *i.e.*, to obtain the maximum spin multiplicity, resulting in a paramagnetic, HS ${}^5T_{2g}(t_{2g}^4 e_g^2)$ state (Figure 1.1). When the ligand set induces stronger splitting of the d orbitals of Fe(II) ion, $10 Dq$ is large compared to the interelectronic repulsion P , and the six d electrons will pair up in the low-energy t_{2g} orbitals, resulting in a diamagnetic, LS ${}^1A_{1g}(t_{2g}^6)$ state.²⁹ When $10 Dq$ and P are of comparable energy transitions between the two spin states may occur depending on the order of magnitude of the thermal energy kT .³⁰

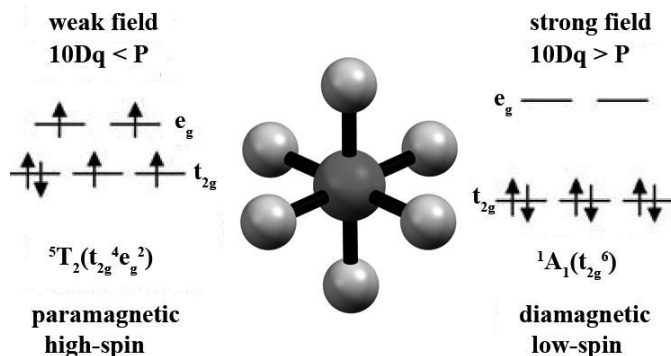


Figure 1.1. Representation of the HS and LS states for an octahedral Fe(II) complex. Adapted from reference 29.

The ligand field strength not only depends on the properties of the donor atoms, but also on the metal-ligand distance r . For neutral ligands, it can be expressed as $10 Dq \propto \frac{\mu}{r^6}$ where μ is the dipole moment of the ligand.²⁹ $10 Dq(r)$ can be estimated using the experimentally determined equilibrium distance r_0 of the corresponding ground state, which is now expressed as $10 Dq(r) = 10 Dq(r_0) \left(\frac{r}{r_0}\right)^6$. For both the LS and HS ground state, the electronic energies of the excited states can be calculated as a function of r , giving the two potential wells shown in Figure 1.2a.²⁹ The HS potential well is shifted to higher values of r since two out of the six d electrons are in the anti-bonding e_g orbitals. The difference between the zero-point energies of the HS and LS states is

expressed as $\Delta E_{\text{HL}}^{\circ} = \Delta E_{\text{HS}}^{\circ} - \Delta E_{\text{LS}}^{\circ}$. It has to be positive for the occurrence of a spin-crossover, and can be of the same order of magnitude as the thermal energy kT when a suitable ligand set is coordinated to the Fe(II) ion. In such a case, the complex will be in the LS state at low temperatures, whereas at higher temperatures, an entropy-driven, almost quantitative population of the HS state may be observed. There are two major contributions to the entropy difference between the HS and LS states. The electronic contribution due to the spin degeneracy of the HS state, and a vibrational contribution due to the larger Fe–N distances and the resulting lower vibrational frequencies hence much higher density of vibrational states in the HS state.²⁹

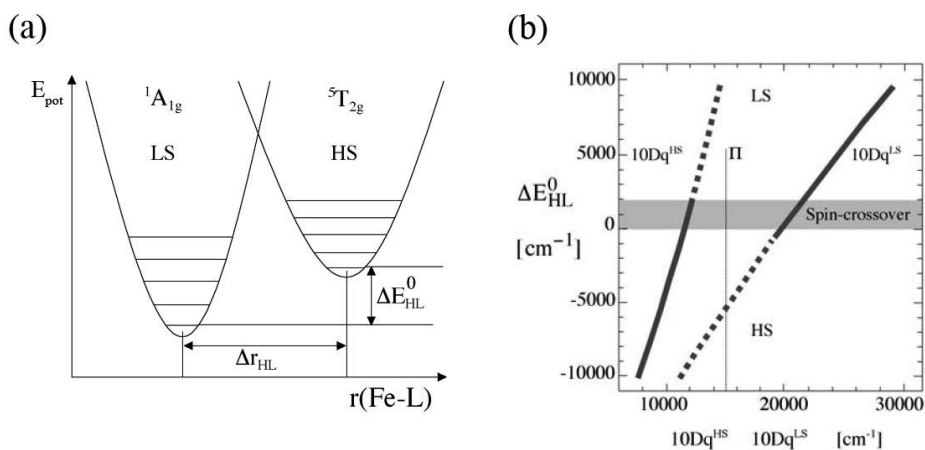


Figure 1.2. (a) Schematic representation of the potential wells of the LS and HS states of an Fe(II) complex, plotted as energy vs. the metal-ligand distance r . (b) Representation of the regions where each of the states (HS, LS) is stable as a function of ligand field strength $10 Dq$. The shaded area is the region where SCO can occur. Taken from reference 29.

Moreover, based on the metal-ligand distance dependence of $10 Dq$, also by knowing the typical values for r_{HS} (2.15 ~ 2.2 Å) and r_{LS} (1.95 ~ 2.0 Å) from X-ray crystal structure determinations, and applying the condition $\Delta E_{\text{HL}}^{\circ} \propto kT$, it is possible to estimate $10 Dq$ for which pure HS, LS or SCO species can be expected (Figure 1.2b).³¹ for $10 Dq^{\text{HS}} < 10000 \text{ cm}^{-1}$, the HS state is the thermodynamically most stable state at all temperatures. For $10 Dq^{\text{LS}} > 23000 \text{ cm}^{-1}$, the LS state remains the thermodynamically most stable state up to very high temperatures. For the narrow range of $10 Dq^{\text{HS}} \approx 11000\text{-}12500 \text{ cm}^{-1}$, and the corresponding range for $10 Dq^{\text{LS}} \approx 19000\text{-}22000 \text{ cm}^{-1}$ SCO can be expected. Such narrow range explains why the SCO phenomenon is very sensitive to minute changes of the ligand structure, and why minor

changes in the coordination environment or crystal lattice molecules may hinder the spin transition (see details in Section 1.2).³¹

A thermodynamic description of the spin transition can also be given. In a homogeneous host lattice, the $\text{Fe(II)}_{\text{LS}} \xrightleftharpoons{\Delta G} \text{Fe(II)}_{\text{HS}}$ equilibrium is considered to induce no change for the rest of the system. The relative stability of the two spin states, is determined by the difference in the Gibbs free energy $\Delta G = \Delta H - T\Delta S$ where $\Delta G = G_{\text{HS}} - G_{\text{LS}}$. At low temperature ($T < T_{1/2}$), the Gibbs free energy diagram (Figure 1.3a) is similar to that of the potential energy diagram shown in Figure 1.2a. The LS state is most stable since it corresponds to the lowest Gibbs free energy G . Because $\Delta G > 0$, the transition from an LS state to an HS state will not occur at low temperature. At elevated temperatures ($T > T_{1/2}$), the HS state has the lowest Gibbs free energy G , and the transition of LS \rightarrow HS will occur as $\Delta G < 0$ (Figure 1.3c). At the equilibrium ($T = T_{1/2}$), $G_{\text{HS}} = G_{\text{LS}}$ and hence $\Delta G = 0$ (Figure 1.3b), which results in $T_{1/2} = \frac{\Delta H}{\Delta S}$ where $T_{1/2}$ is defined as the transition temperature at which the two spin states are present in the ratio 1:1 ($\gamma_{\text{HS}} = \gamma_{\text{LS}} = 0.5$).

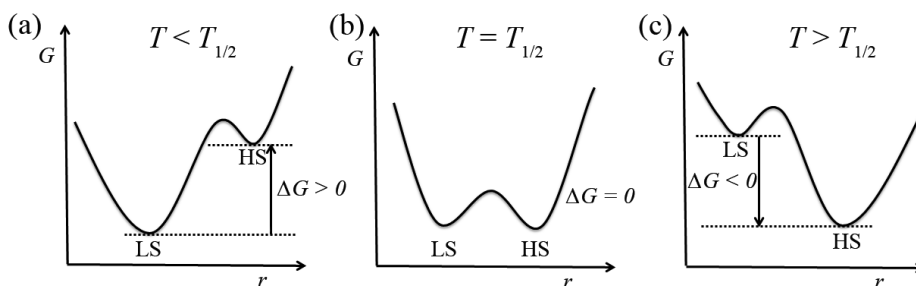


Figure 1.3. Schematic representation of the Gibbs free energy diagram of the LS and HS states of an Fe(II) complex when (a) $T < T_{1/2}$, (b) $T = T_{1/2}$, and (c) $T > T_{1/2}$, plotted as Gibbs free energy G vs. the metal-ligand distance r .

1.2 Solvent effects, polymorphism and SCO

As mentioned previously, the spin state of a system may be altered drastically by chemical and physical influences. In this section the chemical influence on SCO, namely, polymorphism and solvate effect are discussed.

The effect of polymorphism on the SCO behaviour has been known since the first studies on the classical system $[\text{Fe(L)}_2(\text{X})_2]$ [$\text{L} = \text{phen}$ ($\text{X} = \text{S}$ or Se) or bpy ($\text{X} = \text{S}$)].²⁶

³² Different polymorphs may arise from different sample preparation methods used, which may influence the abruptness of the transition, the residual fraction of HS molecules at low temperatures,³³ or even the mere occurrence of SCO.³⁴⁻³⁶ A classical example is $[\text{Fe}(\text{bt})_2(\text{NCS})_2]$ (bt = 2,2'-bi-2-thiazoline). Single crystals of form A exhibiting hysteretic SCO are obtained from slow evaporation of a warm ethanol solution of the compound. Crystals of form B are obtained by evaporation of an ethanol solution of the compound at room temperature and do not show SCO behaviour, remaining HS at all temperatures.³⁷ The different crystal packing in the two forms affect the FeN_6 coordination geometry, thereby playing a critical role in the spin-crossover properties of the material.

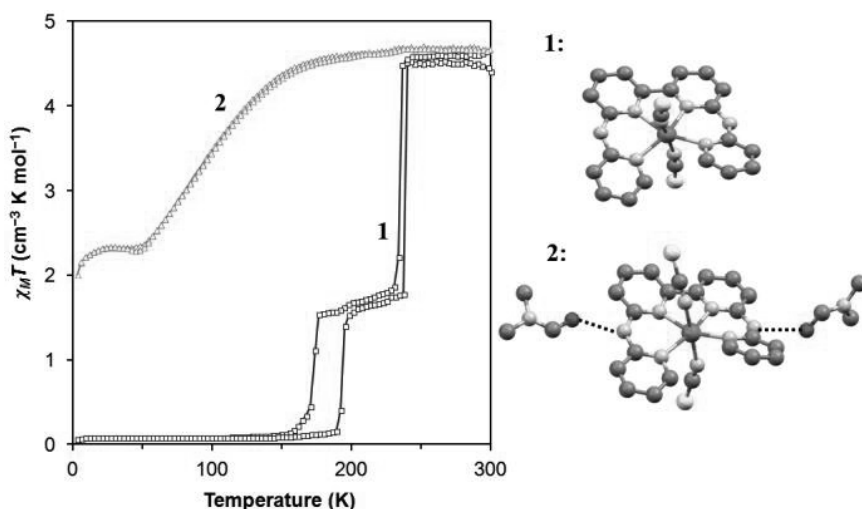


Figure 1.4. Comparison of $\chi_M T$ vs. T plots for crystals of $[\text{Fe}(\text{bapbpy})(\text{NCS})_2]$ (**1**) and $[\text{Fe}(\text{bapbpy})(\text{NCS})_2] \cdot 2\text{DMF}$ (**2**). The crystal structures for both complexes are also shown, hydrogen atoms are omitted for clarity. Adapted from reference 38.

Similarly, the presence of solvate molecules can exert a dramatic influence on crystal packing, hence on SCO.³⁹⁻⁴² As recently demonstrated by our group, $[\text{Fe}(\text{bapbpy})(\text{NCS})_2]$ (**1**, bapbpy = *N,N'*-di(pyridid-2-yl)-2,2'-bipyridine-6,6'-diamine) is a two-step SCO compound with two hysteresis cycles. It crystallizes in the monoclinic space group $C2/c$ with $Z = 4$ at 190 K.⁴³ The related DMF solvated complex $[\text{Fe}(\text{bapbpy})(\text{NCS})_2] \cdot 2\text{DMF}$ (**2**) shows SCO properties but no hysteresis cycle (Figure 1.4). It crystallizes in triclinic space group $P-1$ with $Z = 2$ at 150 K.³⁸ The strong

N–H⋯S hydrogen bonding network in compound **1** is critical for its cooperative behaviour, whereas in compound **2** this hydrogen bonding network is replaced by isolated {DMF⋯[Fe(bapbpy)(NCS)₂]⋯DMF} units which is correlated with a non-cooperative SCO.³⁸ Overall, the occurrence of SCO, as well as the transition temperatures and hysteresis cycles, are difficult to predict, as there is a significant influence of packing effects on the molecular crystal field strength and on the ability of an apparently suitable ligand set to generate spin-crossover Fe(II) compounds.

1.3 Theoretical models for cooperativity

One of the most important aspects in spin transition is the degree of cooperativity associated with the transition, *i.e.*, the extent to which the spin state of neighbouring molecules is influenced by the spin transition of a given molecule.⁸ With low cooperativity the spin transition will be a gradual process spanning over 100 to 150 K, but as cooperativity increases the transition becomes more abrupt and may occur within a very narrow range of temperature (1 to 5 K) and/or be associated with thermal hysteresis.⁸

Cooperativity originates from the change in volume when a given SCO molecule changes its spin state. It has thus an elastic origin and leads to long-range interactions throughout the crystal lattice. These interactions may be regarded as an internal pressure, and it exerts its effects on all the molecules in the crystal with the same strength, creating “communication” between the SCO metal centres.^{44, 45} Cooperativity has been a subject of experimental studies based on SCO compounds diluted in a host lattice (metal dilution effect, also see Chapter 3).^{31, 46} For a theoretical approach, the basic macroscopic behaviour of a SCO solid may be analyzed in the frame of the mean-field theory of phase transition⁴⁷ first used by Slichter and Drickamer.⁴⁸ A simple phenomenological definition of cooperativity is given by Eq. 1.1:

$$\ln\left(\frac{1-\gamma_{HS}}{\gamma_{HS}}\right) = \frac{\Delta_{SCO}H + \Gamma(1-2\gamma_{HS})}{RT} - \frac{\Delta_{SCO}S}{R} \quad \text{Eq. 1.1}$$

where γ_{HS} is the fraction of HS species, which can be obtained from magnetic measurements. $\Delta_{SCO}H$ and $\Delta_{SCO}S$ are the excess enthalpy (unit: kJ mol⁻¹) and entropy per mole (unit: J K⁻¹ mol⁻¹) of transiting iron centres. These thermodynamic parameters may be obtained from calorimetric measurements. The $\Delta_{SCO}H / \Delta_{SCO}S$ ratio corresponds to the transition temperature $T_{1/2}$, which is defined as the temperature

when $\gamma_{\text{HS}} = \gamma_{\text{LS}} = 0.5$. The cooperativity parameter Γ (unit: kJ mol^{-1}) represents the tendency of a SCO centre to be surrounded by other centres of the same spin state. Consequently, the term Γ reflects how efficiently the structural changes associated with the SCO are transmitted throughout the whole crystal. By using Eq. 1.1 it is possible to simulate SCO behaviours ranging from spin equilibrium ($\Gamma = 0$, e.g., in solution) to a first order transition with hysteresis ($\Gamma/RT_{1/2} > 2$), and the width of the resulting hysteresis cycle in the SCO curve increases with $\Gamma/RT_{1/2}$ (for more details and an example, see Chapter 6).

Another phenomenological model of cooperativity proposed by Sorai^{49, 50} has been widely used to analyze the SCO behaviour when accurate calorimetric data are available.⁵¹ This model is based on heterophase fluctuations and gives a measure of cooperativity through the number n of like-spin SCO centres per interacting domain. The larger the domains are, the more cooperative the transition is. According to this model, the excess heat capacity ΔC_p of a SCO compound can be written as in Eq. 1.2.

$$\Delta C_p = \frac{n(\Delta_{\text{SCO}}H)^2}{RT^2} \frac{\exp\left[\frac{n\Delta_{\text{SCO}}H}{R}\left(\frac{1}{T} - \frac{1}{T_{1/2}}\right)\right]}{\left\{1 + \exp\left[\frac{n\Delta_{\text{SCO}}H}{R}\left(\frac{1}{T} - \frac{1}{T_{1/2}}\right)\right]\right\}^2} \quad \text{Eq. 1.2}$$

The experimental ΔC_p data are thus fitted to this equation by using $\Delta_{\text{SCO}}H$ as derived from DSC experiments but leaving $T_{1/2}$ free, then the n values can be calculated. For $n = 1$ the model is equivalent to a pure solution behaviour (van't Hoff equation) with no cooperative effects, that is, compounds that show a gradual SCO usually give n values close to 1.^{52, 53} For the highly cooperative SCO compound $[\text{Fe}(\text{phen})_2(\text{NCS})_2]$, an n value as large as 95 has been derived from this equation.⁴⁹ For the two-step hysteretic SCO compound $[\text{Fe}(\text{bapbpy})(\text{NCS})_2]$, two separate values of n (11.6/22.5) can be obtained,⁵⁴ and this compound can be considered as a cooperative SCO compound (see Chapter 2).

It is important to realize that in mononuclear SCO compounds the cooperativity depends on intermolecular interactions, which have often been characterized by single-crystal X-ray diffraction techniques. The two theoretical models mentioned above are used to quantify the cooperativity of a SCO system based on calorimetric and/or magnetic data. Therefore, in order to fully understand the cooperativity of a SCO system, both the dynamic and energetic properties of the phase transition as well as

structural information obtained experimentally by single-crystal X-ray diffraction, must be combined.

1.4 Possible applications of SCO and LIESST effect

During spin transition, the metal-ligand distance changes abruptly and therefore $10 Dq$ changes abruptly, too.²⁹ This is accompanied with a change in various physical properties of the SCO compound.⁸ For example, most of the compounds showing a spin transition present different colours in the HS and LS states. Crystals of the well-known SCO compound $[\text{Fe}(\text{ptz})_6](\text{BF}_4)_2$ (ptz = 1-propyltetrazole), are colourless at room temperature, and turn deep red below 135 K.⁵⁵ Therefore, based on the changes in these physical properties SCO compounds might offer promising prospects for applications such as nano-sized chemical sensors,⁵⁶ nano-sized gas sensors,⁵⁷ and temperature sensors.⁵⁸

However the most interesting application in SCO research was suggested by Kahn *et al.*, who realised that spin-transition compounds with thermal hysteresis exhibit magnetic bistability, which could be harnessed in display or memory devices.¹ For example, inside the thermal hysteresis loop two equally stable states are present, constituting a binary system (*i.e.*, LS \rightarrow HS, bit 0 \rightarrow 1, or HS \rightarrow LS, bit 1 \rightarrow 0).

Compared with current information storage technologies, spin-crossover materials have already offered interesting capabilities such as low addressing power, short addressing time since the transition is intraelectronic in nature, and very small bit size.¹ However, up to now, there is no major interest in SCO materials from the electronic industry, mainly because several requirements have to be met before these materials would become economically competitive with the current technologies. First, the temperature range in which the SCO takes place has to be increased to room temperature or above, and the hysteresis loop must have a width of at least 40 K.¹ Although there are several coordination polymers that meet these two requirements,⁵⁹⁻⁶¹ almost none of the available mononuclear SCO compounds show these properties. Furthermore, for practical applications the SCO materials will have to be successfully immobilized onto a surface where they should keep their SCO properties.⁶² This field of research is still poorly investigated but is currently very active.

Current developments towards applications also make use of the so-called Light-Induced Excited Spin-State Trapping (LIESST) effect.^{9, 31} In the LIESST effect (Figure

1.5a), when green light for example falls upon the LS state at low temperature the spin allowed excitation $^1A_1 \rightarrow ^1T_1$ occurs with 1T_1 lifetimes typically of nanoseconds. A fast relaxation cascading over two successive intersystem crossing steps, $^1T_1 \rightarrow ^3T_1 \rightarrow ^5T_2$, populates the metastable 5T_2 state. Radiative relaxation $^5T_2 \rightarrow ^1A_1$ is forbidden, and decay by thermal tunnelling to the ground state 1A_1 is slow at low temperatures.⁸ Hence by continuous irradiation a quantitative population of the HS metastable state can be accessed. When the laser is switched off, the compound remains in its metastable HS state until it is warmed above the LIESST temperature T_{LIESST} where the thermal energy becomes sufficient to overcome the activation barrier (ΔE_{act} , see Figure 1.5a) for the thermal relaxation of the material to the LS state. However, the temperatures where the LIESST effect takes place are considered to be far too low for practical application, as most T_{LIESST} temperatures are lower than 100 K.^{63, 64} On the other hand, reverse LIESST can be achieved by application of typically red light (*ca.* 820 nm) where the 5T_2 state is excited to the 5E state; with two subsequent intersystem crossing processes, $^5E \rightarrow ^3T_1 \rightarrow ^1A_1$, this may lead back to the LS ground state.⁸

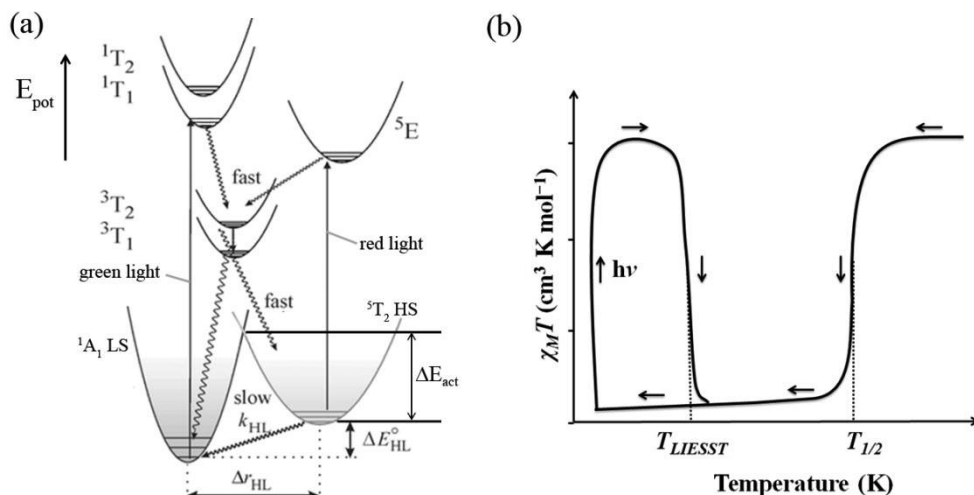


Figure 1.5. (a) Potential energy wells for the ground and excited states of Fe(II) SCO complexes, and mechanisms of LIESST and reverse-LIESST (wavy arrows). Taken from reference 8. (b) Schematic representation of relaxation processes when slow thermal spin-crossover and LIESST are followed by slow warming above T_{LIESST} , in the case of an abrupt SCO system and with $T_{LIESST} \ll T_{1/2}$.

Irradiation in the hysteresis cycle of an SCO compound is much more promising for applications as both the LS \rightarrow HS and HS \rightarrow LS spin switching can be obtained at room

temperature or above. This is another reason why developing SCO compounds with hysteresis near room temperature is important. For example, the group of Bousseksou reported a complete LS \rightarrow HS as well as HS \rightarrow LS photoconversion following a short one-shot laser irradiation of [Fe(pyrazine){Pt(CN)₄}] single crystals close to room temperature.⁶⁵ These results suggest that applications of light-induced bistability in optical information technology can be envisaged.

Overall, even though data storage or optical devices are still not ready for industrial use, prototype devices have been made based on SCO compounds.⁶² Improvements in transition temperatures, hysteresis width, and stability are needed before real devices that can store information can be proposed for large-scale use.

1.5 Effect of particle size reduction on SCO

As mentioned earlier, one potential advantage of SCO compounds over the current information storage technologies is the potentially very small bit size.¹ The state-of-the-art in spin-crossover research focuses on size reduction of SCO materials. Before single molecule information storage can be controlled, research has to focus on understanding the SCO properties of nanomaterials. Nanomaterials possess nano-scale, size-dependent physical and chemical properties that can be controlled.⁶¹ Most importantly, nanomaterials are expected to be used for information storage devices,⁶² as well as advanced materials for applications such as displaying elements, sensors, drugs, pigments *etc.*⁶¹

Spin-crossover nanomaterials include nanoparticles, thin films, amphiphilic structures, and surface patterns.^{61, 66} However, the spin-state switching performance of these nanostructures is often attenuated as their sizes decrease.⁶¹ An example of this behaviour is given by SCO nanoparticles of the well known three-dimensional (3D) coordination polymers [Fe(pyrazine){Pt(CN)₄}] (Figure 1.6a).⁶⁷ The study of the magnetic properties of nanoparticles of this material revealed that they display spin-crossover behaviour; however upon reduction in size the transition becomes smoother, the SCO transition shifts to lower temperature, and the hysteresis loop becomes narrower to vanish for the smallest particles (Figure 1.6b).⁶⁷ The macroscopic behaviour of bulk SCO material is strongly influenced by electron-lattice coupling effects. For example, the change of the volume and the shape of the molecules accompanying SCO leads to considerable elastic interactions within the crystal lattice, giving rise to cooperative phenomena (see Section 1.3).⁶¹ Therefore, size-reduction

effects in SCO materials may be expected when the number of interacting metal centres is reduced. In particular a decrease of the cooperativity may be expected. However, a counter example has been described which consists in nanoparticles of the SCO coordination polymer $[\text{Fe}(\text{pyrazine})\{\text{Ni}(\text{CN})_4\}]$, for which a cooperative thermal SCO with a hysteresis loop was observed for ultra-small nanoparticles (~ 4 nm).⁶⁸

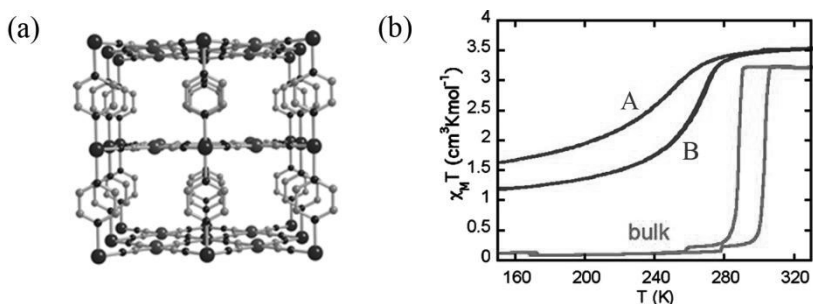


Figure 1.6. (a) Crystal structure of the $[\text{Fe}(\text{pyrazine})\{\text{Pt}(\text{CN})_4\}]$ complex. Taken from reference 69 (b) Magnetic properties of nanoparticles of $[\text{Fe}(\text{pyrazine})\{\text{Pt}(\text{CN})_4\}]$ of $8 \times 8 \times 3$ (A) and $15 \times 15 \times 5$ (B) nm^3 in size compared with that of the bulk material. Taken from reference 67.

Furthermore, the size-property relationship is also closely related to the dimensionality of the materials.⁶¹ The majority of the reports on SCO nanoparticles are based on either 1D iron(II) triazole coordination polymers,^{62, 70, 71} or 3D systems like the Hofmann clathrate networks.⁶⁷⁻⁶⁹ In both cases the metal centres situated at the boundaries of a crystalline domain will feel a different coordination environment compared to the metal centres in the bulk. Thus, the effect of size reduction might be amplified, and as a consequence these compounds may lose their SCO properties. It has been suggested that in ultra-small nanoparticles (~ 4 nm) of the SCO coordination polymer $[\text{Fe}(\text{pyrazine})\{\text{Ni}(\text{CN})_4\}]$, only *ca.* 1/3 of the Fe(II) centres undergo a cooperative thermal SCO with a hysteresis cycle, which may be related to the high fraction (*ca.* 2/3) of iron centres localized at the surface of the nanoparticles that do not have the appropriate coordination environment.⁶⁸ This in turn suggests that mononuclear SCO compounds may show less size reduction effects since the coordination environment of the switching metal centres remain identical throughout the crystalline domain.

Finally, the modification of the SCO properties of nanomaterials may not only occur because of the decreased number of interacting SCO centres and the associated decrease of cooperativity, but it may be also influenced by a number of other

parameters and material properties, such as the number of defects at the surface, different synthetic methods compared to bulk materials, or different physical environments around the nanomaterials (matrix effect).⁶¹ All these factors have to be considered in order to interpret the experimental observations obtained with SCO nanomaterials.

More recently, the miniaturization of SCO has been pushed further towards the observation of spin-state switching of single molecules,^{72, 73} which is particularly relevant for novel applications in molecular electronics and data storage.⁷⁴ That is, a single molecule behaves as a switch, which represents a serious improvement in terms of information density and processing speed. It is worth noticing that so far all reported cases of spin-switching single molecules are based on mononuclear Fe(II) SCO compounds deposited on a surface, as described in Section 1.6.

1.6 SCO on surfaces

As mentioned in Section 1.4, SCO compounds are one of the most prominent candidates for applications in nanomemory devices compared with other systems such as single-molecular magnets (SMMs) and single-chain magnets (SCMs). SMMs and SCMs require very low temperatures for changes in magnetization to be observable,⁷⁵ whereas SCO could in theory occur at room temperature or above.

For practical applications, SCO-based devices prepared following the bottom-up approach will require molecules or nanoparticulate arrays arranged in two dimensions, that is, on surfaces. The reason for this is to ensure the addressability of the single molecule or nanoparticle, which is a prerequisite for writing and reading information. In addition, the information should persist in time.⁷⁶ Thus, several requirements have to be met for achieving SCO on surfaces, such as the chemical stability of the system (that is, the switching should not induce any instability to the molecule, nor to the surface, so that SCO molecules can be individually and reproducibly switched between an HS and an LS state), and a precise control of the assembly or arrangements of SCO molecules on the surface should be obtained. At this point, there is a key feature that has to be emphasized: SCO behaviour of a molecule will depend on the interactions between the molecule and the surface. For nanosystems containing several molecules SCO will depend on the interactions between the SCO molecules as well. Anyhow, the electronic and magnetic properties of the SCO molecules on a surface are expected to

be markedly different from those of the bulk material, which poses challenges in this field as understanding those interactions becomes very important.

Recent developments in this field include the assembly of 2D/1D SCO complexes on different substrates. One approach is to evaporate SCO molecules under ultra-high vacuum conditions to obtain clean, easily identifiable objects on the surface. However, for this approach SCO complexes should have the following properties: (a) their molecular weight should be low, (b) they should be neutral molecules, and (c) they should not contain any solvent molecules in the crystal lattice. Another requirement is that the material should show a well-defined SCO behaviour in the bulk.⁷⁷ Up to this moment, there are only a few examples that match these requirements.⁷⁷⁻⁷⁹ One example is the classical SCO compound $[\text{Fe}(\text{phen})_2(\text{NCS})_2]$, for which the growth of high-quality thin films on different substrates has been demonstrated by evaporation under ultra-high vacuum. The SCO properties maintain even down to a thickness of 10 nm of such a thin film.⁷⁸ Further investigation by STM imaging on the same complex deposited on Cu(100) under ultra-high vacuum shows that the switching between an HS and an LS state can be detected in a single molecule, in the form of a change in the molecule's conductance.⁷³ However, it is also shown that the individual molecule has to be decoupled from the metallic substrate by a thin CuN insulating layer for the switch between the two spin states to be controllable by the tunnelling current.⁷³ This is rather similar to what has been found in bulk SCO materials: the SCO behaviour is very sensitive to the environment.

Similarly, the iron(II) SCO compounds $[\text{Fe}(\text{H}_2\text{B}(\text{pz})_2)_2(\text{bpy})]$ and $[\text{Fe}(\text{H}_2\text{B}(\text{pz})_2)_2(\text{phen})]$ ($\text{H}_2\text{B}(\text{pz})_2 = \text{bis}(\text{hydrido})\text{bis}(1H\text{-pyrazol-1-yl})\text{borate}$), also show clean evaporation under ultra-high vacuum yielding either microcrystallites or homogeneous thin films on a variety of substrates.^{77, 80-82} Further investigation on $[\text{Fe}(\text{H}_2\text{B}(\text{pz})_2)_2(\text{phen})]$ using STM imaging showed a double layer deposition on Au(111), where the electron-induced SCO is observed in the second molecular layer while the spin state of the molecules of the first layer that in contact with the gold surface could not be switched (Figure 1.7).⁷²

In contrast, for the iron(II) SCO compound $[\text{Fe}(\text{L})(\text{NCS})_2]$ ($\text{L} = \{6\text{-}[1,1\text{-di}(\text{pyridine-2-yl})\text{ethyl}]\text{-pyridin-2-yl}\}\text{-}N,N\text{-dimethylmethanamine}$) deposited on highly oriented pyrolytic graphite (HOPG) under ultra-high vacuum, X-ray absorption spectroscopy measurements show that the molecules undergo a thermally-induced, fully reversible,

gradual spin transition, which may suggest that by using HOPG the SCO behaviour can be preserved even for molecules that are in direct contact with a solid surface.⁷⁹

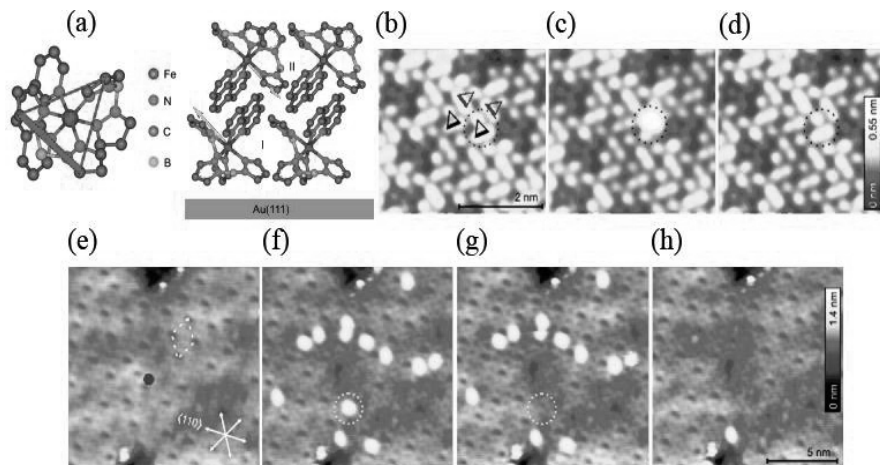


Figure 1.7. (a) Crystal structure of $[\text{Fe}(\text{H}_2\text{B}(\text{pz})_2)_2(\text{phen})]$ shown along a pseudo-trigonal molecular axis. A triangle is used to represent the orientation of the molecule. Proposed adsorption geometry on Au(111) is also shown. (b)-(h) Constant-current STM topographs of a double-layer of $[\text{Fe}(\text{H}_2\text{B}(\text{pz})_2)_2(\text{phen})]$ on Au(111) at submolecular resolution. Dotted circles in (b)-(d) indicate a molecule which is switched from LS (b) to HS (c) and back to LS (d). (e)-(h) Overview of a larger area before and after applying a pulse at the position indicated by the dot in (e). (f)-(g) The HS molecule switching to LS took place. (h) After applying pulses to all HS molecules in (g), most molecules have returned to the LS state. Taken from reference 72.

Another approach is to prepare ultrathin layers of SCO molecules by dip coating a solution of the complex on solid substrates.⁸³⁻⁸⁵ For example, STM images show molecules of $[\text{Fe}(\text{L})_2](\text{BF}_4)_2$ [$\text{L} = 2,6\text{-bis}(1H\text{-pyrazol-}1\text{-yl})\text{-}4\text{-(thiocyanatomethyl)pyridine}$] deposited from a 10^{-8} M acetonitrile solution forming lines at the step-edge of the HOPG surface. Though single-molecule resolution was not available, the differences in the current-imaging tunnelling spectroscopy (CITS) image between dark and bright spots have been attributed to the HS and LS states respectively (Figure 1.8).⁸³ The advantages of this dip-coating approach are that a wide range of SCO molecules can be deposited, and that the STM images can be recorded under ambient conditions (room temperature, aerobic, ambient pressure, and deposition from solution), in contrast to the often extreme conditions (liquid nitrogen or liquid helium

temperature, ultrahigh vacuum deposition, single crystalline metal substrate) required for other methods of preparation.

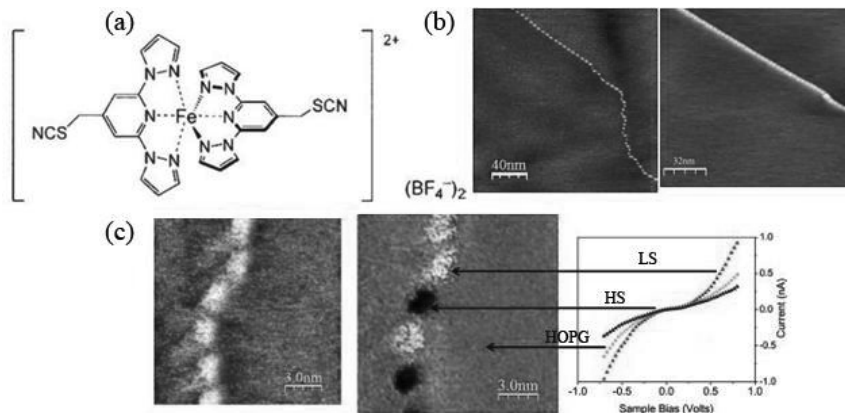


Figure 1.8. (a) Structural formula of $[\text{Fe}(\text{L})_2](\text{BF}_4)_2$. (b) Large area scans over a chain of small clusters of $[\text{Fe}(\text{L})_2](\text{BF}_4)_2$ deposited on an HOPG surface. (c) Topography and simultaneously recorded current-imaging tunnelling spectroscopy (CITS) images of the line of single molecules in smaller area scan. The CITS image shows significant contrasts that are assigned to the three types of different positions. Taken from reference 83.

Overall, the significant difference in molecular conductivity between the spin states of iron(II) complexes on surfaces holds considerable promise for new concepts in nano-sized data storage applications. The current challenge is to control the self organization and addressability of SCO molecules on surfaces, which will be discussed in more detail in Chapter 7.

1.7 Aim and scope of this thesis

For mononuclear SCO compounds, despite many efforts to shift transition temperatures to near room temperature or above while still keeping hysteresis cycles, encouraging results remain scarce. The main reason has been explained in the previous sections: the width of the hysteresis cycle in the SCO curve increases with $T/RT_{1/2}$ (see Section 1.3), that is, with increased transition temperature $T_{1/2}$ the SCO compounds have to be very cooperative (large T) to maintain a hysteresis cycle. The work described in this thesis initially aimed at making new mononuclear iron(II) compounds having a transition

temperature around room temperature while remaining cooperative by modifying the ligand bapbpy (Figure 1.9).

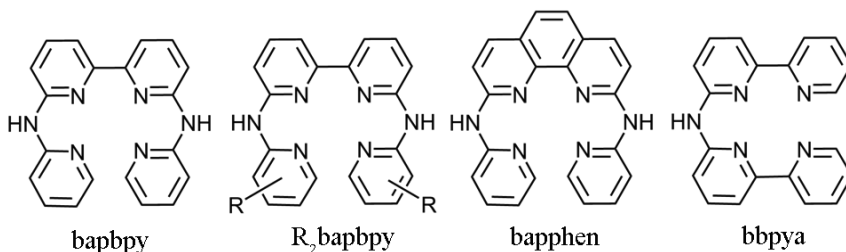


Figure 1.9. Overview of the tetradentate polypyridyl ligands described in this thesis.

In Chapter 2 the synthesis and spin-crossover properties of different isomers of the spin-crossover compounds $[\text{Fe}(\text{R}_2\text{bapbpy})(\text{NCS})_2]$ are presented. Both the cooperativity and transition temperature critically depend on the position of the substituents R on the terminal pyridine rings of the ligand; a qualitative model based on hydrogen-bonding networks is provided to explain the cooperativity of these compounds.

In Chapter 3 the cooperativity in $[\text{Fe}(\text{bapbpy})(\text{NCS})_2]$ is described, which was studied by diluting the complex with increasing amounts of its Zn(II) analogue. Although $[\text{Fe}(\text{bapbpy})(\text{NCS})_2]$ and $[\text{Zn}(\text{bapbpy})(\text{NCS})_2]$ do not have the same crystal structure, Zn-diluted samples $[\text{Fe}_x\text{Zn}_{1-x}(\text{bapbpy})(\text{NCS})_2]$ adopt the phase of the iron compound for $x > 0.53$. In this crystallographic phase the SCO remains two-step down to $x = 0.76$, to become one-step and lose its hysteresis cycle at lower iron content. The iron-containing molecules keep their SCO properties even at high dilution ($x = 0.24$), *i.e.*, in the phase of the zinc compound.

In Chapter 4 the synthesis and magnetic properties of the new SCO compounds $[\text{Fe}(\text{R}_2\text{bapbpy})(\text{NCSe})_2]$ are presented, *i.e.*, with the same bapbpy derivatives as in Chapter 2, but with different axial ligands. A trend in the transition temperature of the SCO upon substitution of NCS^- by NCSe^- is described. The importance of hydrogen-bonding networks for the cooperativity of $[\text{Fe}(\text{R}_2\text{bapbpy})(\text{NCSe})_2]$ SCO compounds is also described, and compared to that of the thiocyanate analogues.

In Chapter 5 the synthesis of a new rigid ligand bapphen [bapphen = *N,N'*-bis(pyridin-2-yl)-1,10-phenanthroline-2,9-diamine] is described. The syntheses and magnetic

properties of its iron(II) complexes [Fe(bapphen)(NCX)₂] (X = S, or Se) are presented, and the effect of sample preparation on SCO is highlighted.

In Chapter 6 the synthesis of a new rigid ligand bbpya [bbpya = *N,N*-bis(2,2'-bipyrid-6-yl)amine] is described. Its high-temperature, cooperative SCO complex [Fe(bbpya)(NCS)₂] is described and characterized.

In Chapter 7 the syntheses of a new tetradentate bapphen derivative bearing a long alkyl chain (C12) and two N–H bridges, and of its iron(II) complex, are presented. The self assembly of both the ligand and the complex on HOPG surfaces has been investigated by scanning tunnelling microscopy (STM). Two possible models for the self assembly of the ligand and the complex on HOPG are provided.

Parts of this thesis have been published^{54, 86} or are in preparation for publication (Chapters 4, 5, 6 and 7).

1.8 References:

1. O. Kahn and C. J. Martinez, *Science*, 1998, 279, 44-48.
2. Intel, Intel 22 nm 3D Tri-Gate Transistor Technology, available from: <http://newsroom.intel.com/docs/DOC-2032>, 2013.
3. R. F. Service, *Science*, 1996, 274, 1834-1836.
4. J. M. Seminario, *Nat. Mater.*, 2005, 4, 111-113.
5. O. Kahn, J. Kröber and C. Jay, *Adv. Mater.*, 1992, 4, 718-728.
6. L. Cambi and L. Szegö, *Ber. Dtsch. Chem. Ges.*, 1931, 64, 2591-2598.
7. P. Gütllich and H. A. Goodwin, *Top. Curr. Chem.*, 2004, 233, 1-47.
8. P. Gütllich, Y. Garcia and H. A. Goodwin, *Chem. Soc. Rev.*, 2000, 29, 419-427.
9. S. Decurtins, P. Gütllich, K. M. Hasselbach, A. Hauser and H. Spiering, *Inorg. Chem.*, 1985, 24, 2174-2178.
10. A. Hauser, *Coord. Chem. Rev.*, 1991, 111, 275-290.
11. A. Hauser, *Chem. Phys. Lett.*, 1986, 124, 543-548.
12. C. Roux, D. M. Adams, J. P. Itie, A. Polian, D. N. Hendrickson and M. Verdaguier, *Inorg. Chem.*, 1996, 35, 2846-2852.
13. J. K. McCusker, M. Zvagulis, H. G. Drickamer and D. N. Hendrickson, *Inorg. Chem.*, 1989, 28, 1380-1384.
14. Y. Garcia, V. Ksenofontov, G. Levchenko, G. Schmitt and P. Gutlich, *J. Phys. Chem. B*, 2000, 104, 5045-5048.
15. A. Bousseksou, N. Negre, M. Goiran, L. Salmon, J. P. Tuchagues, M. L. Boillot, K. Boukheddaden and F. Varret, *Eur. Phys. J. B*, 2000, 13, 451-456.
16. V. Meded, A. Bagrets, K. Fink, R. Chandrasekar, M. Ruben, F. Evers, A. Bernard-Mantel, J. S. Seldenthuis, A. Beukman and H. S. J. van der Zant, *Phys. Rev. B*, 2011, 83, 245415.
17. J. Zarembowitch, *New J. Chem.*, 1992, 16, 255-267.
18. A. B. Gaspar, M. C. Munoz, V. Niel and J. A. Real, *Inorg. Chem.*, 2001, 40, 9-10.
19. H. A. Goodwin, *Top. Curr. Chem.*, 2004, 234, 23-47.

-
20. P. J. van Koningsbruggen, Y. Maeda and H. Oshio, *Top. Curr. Chem.*, 2004, 233, 259-324.
 21. S. Hayami, Z. Z. Gu, H. Yoshiki, A. Fujishima and O. Sato, *J. Am. Chem. Soc.*, 2001, 123, 11644-11650.
 22. H. Werner, B. Ulrich, U. Schubert, P. Hofmann and B. Zimmergasser, *J. Organomet. Chem.*, 1985, 297, 27-42.
 23. Y. Garcia and P. Gutlich, *Top. Curr. Chem.*, 2004, 234, 49-62.
 24. W. A. Baker and H. M. Bobonich, *Inorg. Chem.*, 1964, 3, 1184-1188.
 25. E. Konig and K. Madeja, *Chem. Commun.*, 1966, 61-62.
 26. E. Konig and K. Madeja, *Inorg. Chem.*, 1967, 6, 48-55.
 27. D. F. Shriver and P. W. Atkins, *Inorganic Chemistry*, Oxford University Press, Oxford, 3rd edn., 1999.
 28. C. K. Jorgensen, *Absorption spectra and chemical bonding in complexes*, Pergamon Press, Oxford, 1962.
 29. A. Hauser, *Top. Curr. Chem.*, 2004, 233, 49-58.
 30. O. Kahn, *Curr. Opin. Solid State Mat. Sci.*, 1996, 1, 547-554.
 31. P. Gütlich, A. Hauser and H. Spiering, *Angew. Chem. Int. Ed.*, 1994, 33, 2024-2054.
 32. E. Konig, K. Madeja and K. J. Watson, *J. Am. Chem. Soc.*, 1968, 90, 1146-1153.
 33. B. Gallois, J. A. Real, C. Hauw and J. Zarembowitch, *Inorg. Chem.*, 1990, 29, 1152-1158.
 34. G. S. Matouzenko, A. Bousseksou, S. Lecocq, P. J. van Koningsbruggen, M. Perrin, O. Kahn and A. Collet, *Inorg. Chem.*, 1997, 36, 5869-5879.
 35. N. Moliner, M. C. Munoz, S. Letard, J. F. Letard, X. Solans, R. Burriel, M. Castro, O. Kahn and J. A. Real, *Inorg. Chim. Acta*, 1999, 291, 279-288.
 36. A. B. Gaspar, M. C. Munoz, N. Moliner, V. Ksenofontov, G. Levchenko, P. Gütlich and J. A. Real, *Monatsh. Chem.*, 2003, 134, 285-294.
 37. A. Ozarowski, B. R. McGarvey, A. B. Sarkar and J. E. Drake, *Inorg. Chem.*, 1988, 27, 628-635.
 38. S. Bonnet, G. Molnar, J. Sanchez Costa, M. A. Siegler, A. L. Spek, A. Bousseksou, W.-T. Fu, P. Gamez and J. Reedijk, *Chem. Mater.*, 2009, 21, 1123-1136.
 39. M. Sorai, J. Ensling, K. M. Hasselbach and P. Gütlich, *Chem. Phys.*, 1977, 20, 197-208.
 40. G. Ritter, E. Konig, W. Irlner and H. A. Goodwin, *Inorg. Chem.*, 1978, 17, 224-228.
 41. M. Hostettler, K. W. Tornroos, D. Chernyshov, B. Vangdal and H. B. Burgi, *Angew. Chem., Int. Ed.*, 2004, 43, 4589-4594.
 42. J. A. Real, M. C. Munoz, E. Andres, T. Granier and B. Gallois, *Inorg. Chem.*, 1994, 33, 3587-3594.
 43. S. Bonnet, M. A. Siegler, J. Sanchez Costa, G. Molnar, A. Bousseksou, A. L. Spek, P. Gamez and J. Reedijk, *Chem. Commun.*, 2008, 5619-5621.
 44. H. Spiering, T. Kohlhaas, H. Romstedt, A. Hauser, C. Bruns-Yilmaz, J. Kusz and P. Gütlich, *Coord. Chem. Rev.*, 1999, 192, 629-647.
 45. J. A. Real, A. B. Gaspar and M. C. Munoz, *Dalton Trans.*, 2005, 2062-2079.
 46. J. Jung, G. Schmitt, L. Wiehl, A. Hauser, K. Knorr, H. Spiering and P. Gutlich, *Z. Phys. B*, 1996, 100, 523-534.
 47. J. M. Honig, *J. Chem. Educ.*, 1999, 76, 848-853.
 48. C. P. Slichter and H. G. Drickamer, *J. Chem. Phys.*, 1972, 56, 2142.
 49. M. Sorai and S. Seki, *J. Phys. Chem. Solids*, 1974, 35, 555-570.
 50. M. Sorai, *Top. Curr. Chem.*, 2004, 235, 153-170.
 51. M. Sorai, M. Nakano and Y. Miyazaki, *Chem. Rev.*, 2006, 106, 976-1031.
 52. T. Nakamoto, Z. C. Tan and M. Sorai, *Inorg. Chem.*, 2001, 40, 3805-3809.

53. O. Roubeau, M. deVos, A. F. Stassen, R. Burriel, J. G. Haasnoot and J. Reedijk, *J. Phys. Chem. Solids*, 2003, 64, 1003-1013.
54. Z. Arcis-Castillo, S. Zheng, M. A. Siegler, O. Roubeau, S. Bedoui and S. Bonnet, *Chem. Eur. J.*, 2011, 17, 14826-14836.
55. A. Hauser, *J. Chem. Phys.*, 1991, 94, 2741-2748.
56. M. Ohba, K. Yoneda, G. Agusti, M. C. Munoz, A. B. Gaspar, J. A. Real, M. Yamasaki, H. Ando, Y. Nakao, S. Sakaki and S. Kitagawa, *Angew. Chem. Int. Ed.*, 2009, 48, 4767-4771.
57. P. D. Southon, L. Liu, E. A. Fellows, D. J. Price, G. J. Halder, K. W. Chapman, B. Moubaraki, K. S. Murray, J. F. Letard and C. J. Kepert, *J. Am. Chem. Soc.*, 2009, 131, 10998-11009.
58. L. Salmon, G. Molnar, D. Zitouni, C. Quintero, C. Bergaud, J. C. Micheau and A. Bousseksou, *J. Mater. Chem.*, 2010, 20, 5499-5503.
59. J. Kröber, E. Codjovi, O. Kahn, F. Groliere and C. Jay, *J. Am. Chem. Soc.*, 1993, 115, 9810-9811.
60. S. Bonhommeau, G. Molnar, A. Galet, A. Zwick, J. A. Real, J. J. McGarvey and A. Bousseksou, *Angew. Chem. Int. Ed.*, 2005, 44, 4069-4073.
61. A. Bousseksou, G. Molnar, L. Salmon and W. Nicolazzi, *Chem. Soc. Rev.*, 2011, 40, 3313-3335.
62. J. F. Létard, P. Guionneau and L. Goux-Capes, *Top. Curr. Chem.*, 2004, 235, 221-249.
63. J. F. Létard, L. Capes, G. Chastanet, N. Moliner, S. Létard, J. A. Real and O. Kahn, *Chem. Phys. Lett.*, 1999, 313, 115-120.
64. J. F. Letard, *J. Mater. Chem.*, 2006, 16, 2550-2559.
65. S. Cobo, D. Ostrovskii, S. Bonhommeau, L. Vendier, G. Molnar, L. Salmon, K. Tanaka and A. Bousseksou, *J. Am. Chem. Soc.*, 2008, 130, 9019-9024.
66. M. A. Halcrow, *Spin-Crossover Materials: Properties and Applications*, John Wiley & Sons, Chichester, 2013.
67. F. Volatron, L. Catala, E. Riviere, A. Gloter, O. Stephan and T. Mallah, *Inorg. Chem.*, 2008, 47, 6584-6586.
68. J. Larionova, L. Salmon, Y. Guarl, A. Tokarev, K. Molvinger, G. Molnar and A. Bousseksou, *Angew. Chem. Int. Ed.*, 2008, 47, 8236-8240.
69. I. Boldog, A. B. Gaspar, V. Martinez, P. Pardo-Ibanez, V. Ksenofontov, A. Bhattacharjee, P. Gutlich and J. A. Real, *Angew. Chem., Int. Ed.*, 2008, 47, 6433-6437.
70. T. Forestier, S. Mornet, N. Daro, T. Nishihara, S. Mouri, K. Tanaka, O. Fouche, E. Freysz and J. F. Letard, *Chem. Commun.*, 2008, 4327-4329.
71. E. Coronado, J. R. Galan-Mascaros, M. Monrabal-Capilla, J. Garcia-Martinez and P. Pardo-Ibanez, *Adv. Mater.*, 2007, 19, 1359-1361.
72. T. G. Gopakumar, F. Matino, H. Naggert, A. Bannwarth, F. Tuczek and R. Berndt, *Angew. Chem. Int. Ed.*, 2012, 51, 6262-6266.
73. T. Miyamachi, M. Gruber, V. Davesne, M. Bowen, S. Boukari, L. Joly, F. Scheurer, G. Rogez, T. K. Yamada, P. Ohresser, E. Beaurepaire and W. Wulfhekel, *Nat. Commun.*, 2012, 3, 938-943.
74. P. Gamez, J. S. Costa, M. Quesada and G. Aromi, *Dalton Trans.*, 2009, 7845-7853.
75. D. Gatteschi, A. Cornia, M. Mannini and R. Sessoli, *Inorg. Chem.*, 2009, 48, 3408-3419.
76. A. Grohmann, M. Haryono, K. Student, P. Muller and M. Stocker, *Eur. J. Inorg. Chem.*, 2013, 662-669.
77. T. Palamarciuc, J. C. Oberg, F. El Hallak, C. F. Hirjibehedin, M. Serri, S. Heutz, J. F. Letard and P. Rosa, *J. Mater. Chem.*, 2012, 22, 9690-9695.

-
78. S. Shi, G. Schmerber, J. Arabski, J. B. Beaufrand, D. J. Kim, S. Boukari, M. Bowen, N. T. Kemp, N. Viart, G. Rogez, E. Beaurepaire, H. Aubriet, J. Petersen, C. Becker and D. Ruch, *Appl. Phys. Lett.*, 2009, 95.
 79. M. Bernien, D. Wiedemann, C. F. Hermanns, A. Kruger, D. Rolf, W. Kroener, P. Muller, A. Grohmann and W. Kuch, *J. Phys. Chem. Lett.*, 2012, 3, 3431-3434.
 80. A. Pronschinske, R. C. Bruce, G. Lewis, Y. F. Chen, A. Calzolari, M. Buongiorno-Nardelli, D. A. Shultz, W. You and D. B. Dougherty, *Chem. Commun.*, 2013, 49, 10446-10452.
 81. A. Pronschinske, Y. F. Chen, G. F. Lewis, D. A. Shultz, A. Calzolari, M. B. Nardelli and D. B. Dougherty, *Nano Lett.*, 2013, 13, 1429-1434.
 82. B. Warner, J. C. Oberg, T. G. Gill, F. El Hallak, C. F. Hirjibehedin, M. Serri, S. Heutz, M.-A. Arrio, P. Sainctavit, M. Mannini, G. Poneti, R. Sessoli and P. Rosa, *J. Phys. Chem. Lett.*, 2013, 4, 1546-1552.
 83. M. S. Alam, M. Stocker, K. Gieb, P. Muller, M. Haryono, K. Student and A. Grohmann, *Angew. Chem. Int. Ed.*, 2010, 49, 1159-1163.
 84. H. Jacob, K. Kathirvel, F. Petersen, T. Strunskus, A. Bannwarth, S. Meyer and F. Tuczek, *Langmuir*, 2013, 29, 8534-8543.
 85. A. M. Ako, M. S. Alam, M. Rahman, J. P. Hill, N. M. Sanchez-Ballester, K. Ariga, G. Buth, C. E. Anson and A. K. Powell, *Chem. Eur. J.*, 2012, 18, 16419-16425.
 86. S. Zheng, M. A. Sieger, J. S. Costa, W. T. Fu and S. Bonnet, *Eur. J. Inorg. Chem.*, 2013, 1033-1042.

2

Increasing the transition temperature of bapbpy-based mononuclear spin-crossover compounds: interplay between molecular and crystal engineering

Abstract

In this chapter, it is shown that different isomers of the same mononuclear iron(II) complex give materials with different spin crossover properties, and that minor modifications of the bapbpy ligand allows for obtaining spin crossover (SCO) near room temperature. A qualitative model is provided to understand the link between the structure of bapbpy-based ligands and the SCO properties of their iron(II) compounds. Thus, seven new *trans*-[Fe(R₂bapbpy)(NCS)₂] compounds are reported, where the R₂bapbpy ligand bears picoline (**9-12**), quin-2-oline (**13**), isoquin-3-oline (**14**) or isoquin-1-oline (**15**) substituents. From this series, three compounds (**12**, **14** and **15**) have SCO properties; for **15** the SCO occurs at 288 K. The crystal structures of compounds **11**, **12** and **15** show similar intermolecular interactions to those found in the parent compound [Fe(bapbpy)(NCS)₂] (**1**), in which each iron complex interacts with its neighbours *via* N–H⋯S hydrogen bonding and π–π stacking. For compounds **12** and **15** hindering groups located near the N–H bridges weaken the N⋯S intermolecular interactions, resulting in non-cooperative SCO. For compound **14**, the substitution is further away from the N–H bridges and the SCO remains cooperative as in **1** with a hysteresis cycle. Optical microscopy pictures show the strikingly different spatio-temporal evolution of the phase transition in the non-cooperative SCO compound **12**, compared to that found in **1**. Heat capacity measurements were made for compounds **1**, **12**,

This Chapter has been published as a full paper:

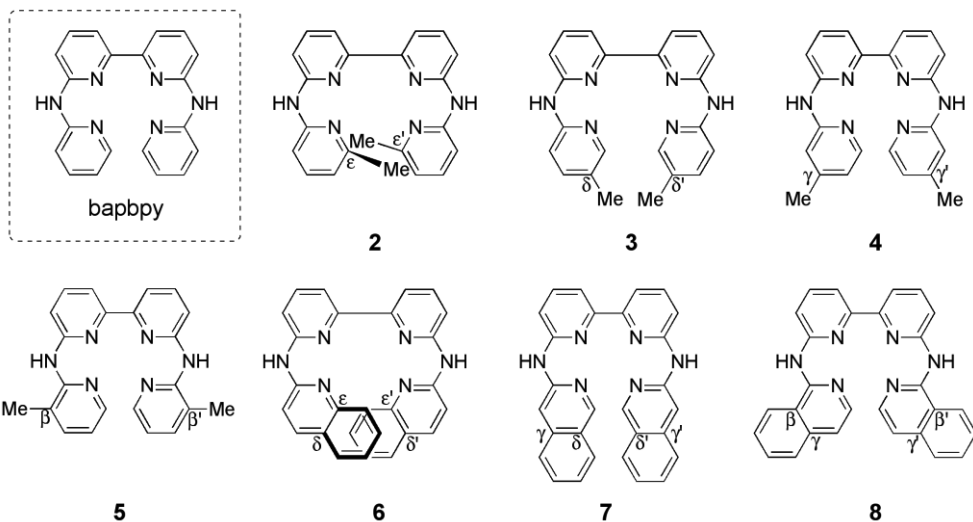
Z. Arcis-Castillo, S. Zheng, M. A. Siegler, O. Roubeau, S. Bedoui and S. Bonnet, *Chem. Eur. J.*, 2011, 17, 14826-14836.

14 and **15** and fitted to the Sorai domain model. The number n of like-spin SCO centres per interacting domain, which is related to the cooperativity of the spin transition, was found to be high for compounds **1** and **14** and low for compounds **12** and **15**. Finally, it is found that although the compounds **11-12** and **14-15** are pairs of isomers their SCO properties are surprisingly different.

2.1. Introduction

Iron-based spin crossover (hereafter, SCO) compounds are recognized as highly promising switchable molecular materials,¹⁻⁴ with potential applications in information storage,^{5, 6} image display,⁷ gas^{8, 9} or temperature sensors.¹⁰ The structure-function relationship for iron(II)-based SCO compounds has been under discussion for several decades, as it would be remarkable to design *de novo* an SCO material with pre-defined magnetic properties. In particular, many applications would ideally require materials for which SCO transitions occur near room temperature.¹¹ The occurrence of cooperative SCO with hysteresis loops is also thought to be critical for information storage applications, as it allows both low spin and high spin (hereafter, LS and HS) states to be populated at one defined temperature.^{12, 13} The occurrence of the spin transition is an inherent property of the ligand field strength created by the ligand set around the metal centre;¹⁴ thus, transition temperatures should ideally be tunable by molecular-engineering approaches. Cooperativity is the result of a combination of short- and long-range interactions between individual molecules in the solid state. There are several quantitative models for cooperativity based on the mean-field approach,¹⁵ elastic¹⁶⁻¹⁹ or electrostatic²⁰ interactions. However, such models only allow for rationalization of the magnetic behaviour of SCO compounds after the compounds have been synthesized and their properties measured.¹² Thus, a qualitative approach based on molecular engineering is still required in the search of new SCO materials.

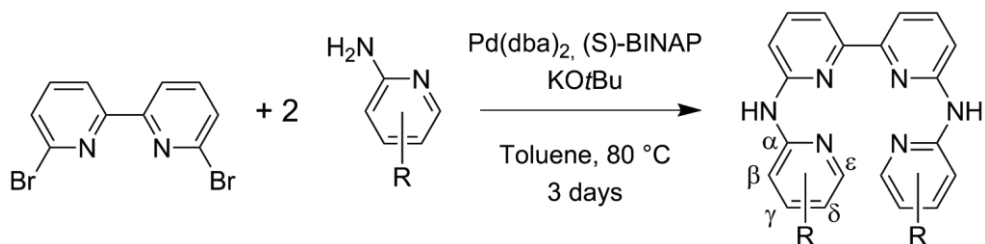
The mononuclear SCO compound [Fe(babppy)(NCS)₂] (compound **1**; babppy = *N,N'*-di(pyrid-2-yl)-2,2'-bipyridine-6,6'-diamine, see Scheme 2.1)²¹ was shown to be highly cooperative. Its two-step spin crossover features a rather unusual ordered intermediate [HS-LS-LS] phase that is stable over a surprisingly large temperature range.^{12, 22, 23} Unfortunately, both transition temperatures for this material are too low for any practical applications. Thus, we considered modifying the babppy ligand to increase the stability of the LS phase. Seven new *trans*-[Fe(R₂babppy)(NCS)₂] complexes were then synthesized (Table 2.1), and their SCO properties investigated.



Scheme 2.1. Representations of the ligand bapbpy and its disubstituted derivatives **2-8**.

2.2. Results

The ϵ, ϵ' (**2**), δ, δ' (**3**), γ, γ' (**4**), and β, β' (**5**) isomers of 6,6'-bis[*N*-(methyl-2-pyridyl)amino]-2,2'-bipyridine (Me_2bapbpy) were synthesized by a palladium-catalyzed Buchwald-Hartwig coupling reaction that involves the corresponding methyl-substituted α -aminopyridine and 2,2'-dibromo-6,6'-bipyridine,²⁴ using $\text{KO}t\text{Bu}$ as a base (Scheme 2.2). Under the same reaction conditions, the use of quinolin-2-amine, isoquinolin-3-amine and isoquinolin-1-amine led to ligands **6**, **7** and **8**, respectively.



Scheme 2.2. Synthesis route for bapbpy derivatives **2** to **8**. 2 mol% $\text{Pd}(\text{dba})_2$ and 4 mol% (S)-BINAP was used.

Coordination of ligands **2-8** to iron(II) thiocyanate was achieved in methanol at room temperature overnight, which leads to compounds **9** to **15**, respectively (see formulae in Table 2.1). As neither the free ligands nor their iron complexes are soluble in methanol, Fe(NCS)₂ was introduced in excess amount, and the complexes were filtered and washed with methanol after the reaction to remove the excess amount of metal precursor. The materials were analyzed by IR spectroscopy, magnetic susceptibility measurements, mass spectrometry, ¹H NMR in DMSO-*d*⁶, and for some of them (**10**, **11**, **12**, and **15**) by X-ray crystallography and elemental analysis. The IR spectra of the seven solids show the characteristic stretching vibrations of the coordinated thiocyanate ligands (see Table 2.1). By electron-spray mass spectrometry, all compounds showed the molecular peak that corresponds to the monocation [Fe(R₂bapbpy)(NCS)]⁺ (calculated at *m/z* = 482.08 for **9-12**, and 554.09 for **13-15**, see Experimental Part).

Table 2.1. Formulae and infrared thiocyanate stretching vibrations for compounds **9-15**.

Compound	Formula	NCS ⁻ vibration
9	<i>trans</i> -[Fe(2)(NCS) ₂]	2056
10	<i>trans</i> -[Fe(3)(NCS) ₂]	2061 (s), 2093 (m)
11	<i>trans</i> -[Fe(4)(NCS) ₂]	2075
12	<i>trans</i> -[Fe(5)(NCS) ₂]	2063
13	<i>trans</i> -[Fe(6)(NCS) ₂]	2036
14	<i>trans</i> -[Fe(7)(NCS) ₂]	2062
15	<i>trans</i> -[Fe(8)(NCS) ₂]	2071 (s), 2110 (m)

The temperature dependence of the $\chi_M T$ product, in which χ_M stands for the molar magnetic susceptibility and T the temperature, was measured for compounds **9-15** in the range 5-300 K, both in the cooling and in the heating modes. The magnetic measurements show that complexes **9**, **10**, **11** and **13** are in the high-spin (HS) state throughout the whole temperature range, with room-temperature $\chi_M T$ values that range from 2.7 to 3.4 cm³ K mol⁻¹, and a decrease of $\chi_M T$ below 50 K is a typical feature of a zero-field splitting. The data for compound **11** are shown in Figure 2.1 as an example. Unlike for compounds **9-11** and **13**, the crude powder of compound **12** shows a reversible colour change, that is, a rusty colour near room temperature but a dark red

colour at liquid nitrogen temperature, which suggests a reversible spin crossover. As shown in Figure 2.1, the room-temperature $\chi_M T$ value of about $3.5 \text{ cm}^3 \text{ K mol}^{-1}$ remains relatively constant in the temperature range of 275-300 K and indicates an HS Fe(II) species in an octahedral coordination environment.²⁵ In the range 125-275 K the $\chi_M T$ value diminishes gradually to reach $0.05 \text{ cm}^3 \text{ K mol}^{-1}$; it remains close to zero in the range 5-125 K. The transition temperature for compound **12**, determined as the maximum of $d(\chi_M T)/dT$, was found to be 170(2) K.

For isoquinolin-3-amino compound **14**, a similar colour change between room-temperature and liquid-nitrogen temperature is observed, however, the evolution of $\chi_M T$ as a function of T shows different features (Figure 2.1). From $3.51 \text{ cm}^3 \text{ K mol}^{-1}$ at 300 K the value of $\chi_M T$ remains roughly constant until 135 K, at which point it quickly drops to $0.85 \text{ cm}^3 \text{ K mol}^{-1}$ at 75 K. The transition temperature $T_{1/2\downarrow} = 113(2) \text{ K}$ was derived at the maximum of $d(\chi_M T)/dT$ vs. T in the cooling mode. The residual HS fraction remains roughly constant between 75 and 5 K, at which point the value of $\chi_M T$ is $0.63 \text{ cm}^3 \text{ K mol}^{-1}$. In the heating mode the transition temperature $T_{1/2\uparrow}$ is higher than $T_{1/2\downarrow}$ [$T_{1/2\uparrow} = 125(2) \text{ K}$], that is, the SCO behaviour of compound **14** is cooperative and shows a hysteresis loop characterized by a ΔT_{hyst} of approximately 11(3) K.

For isoquinolin-1-amino compound **15**, the colour of the crude powder near room temperature is significantly darker than that of compound **11**, **12** or **14**, but heating the powder under argon allowed for reversibly obtaining the lighter orange colour typical for HS iron(II) compounds based on the babppy manifold. Magnetic susceptibility measurements above room temperature confirmed the spin crossover of compound **15**, as the value of $\chi_M T$ gradually decreased from $3.34 \text{ cm}^3 \text{ K mol}^{-1}$ at 396 K (the upper limit of our SQUID magnetometer) down to $0.29 \text{ cm}^3 \text{ K mol}^{-1}$ at 80 K. The spin crossover was found to occur over a large T range of more than 150 K without any hysteresis loop, which suggests non-cooperative behaviour. The transition temperature for the spin transition, defined as the maximum of $d(\chi_M T)/dT$ vs. T , was estimated to be 288(5) K, which is the highest reported transition temperature for all of the babppy-based iron compounds synthesized so far, and very close to room temperature.

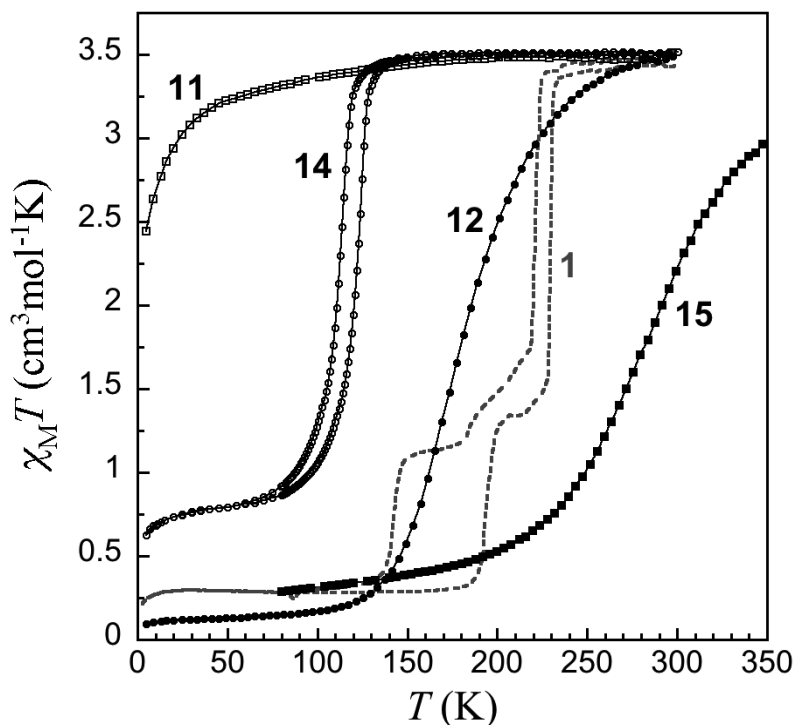


Figure 2.1. Plot of $\chi_M T$ vs. T for compounds **11**, **12**, **14** and **15**. There is no apparent hysteresis loop in the spin crossover for compounds **12** and **15**. The dashed line represents magnetic data for powder samples of compound **1**.²²

Single crystals suitable for X-ray structure determination were obtained for complexes **10**, **11**, **12** and **15** by liquid-liquid diffusion method: for compounds **11**, **12** and **15**, methanol was diffused into a solution of the complex in DMF, whereas for compound **10** the ligand **3** was first dissolved in DMF, followed by layering of 1.1 eq of $\text{Fe}(\text{NCS})_2$ and methanol. In all cases, single crystals appeared after three days. The structures of compounds **10** and **11** (HS only) was determined at 110 K. The structures of the SCO compounds **12** and **15** were determined both at 110 (LS) and near 295 K (HS for **12**, HS+LS for **15**) since no significant loss of crystallinity occurred when the crystals underwent the spin transition. The crystal lattice does not contain any solvent molecules in each structure, and the crystal structures are shown in Figure 2.2. A selected set of geometrical parameters is provided in Table 2.2. In all cases, the substituted ligands R_2bapby coordinate iron(II) in the basal plane of the coordination

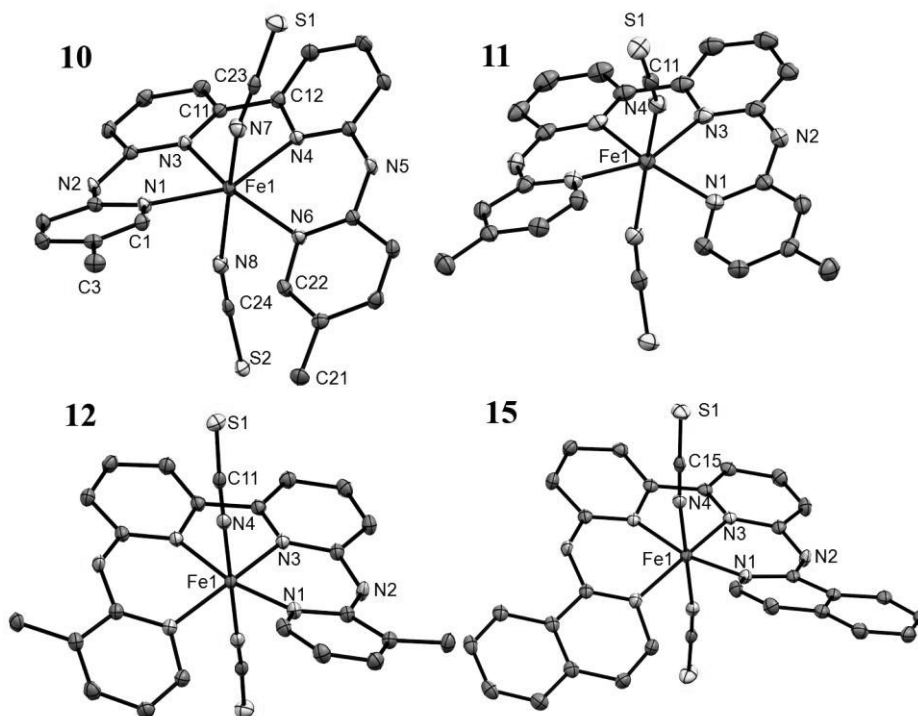


Figure 2.2. Displacement ellipsoid plots (50% probability level) at 110(2) K for compounds **10** and **11** in the HS state, and for compounds **12** and **15** in the LS state. Selected labelling is only shown for crystallographically independent atoms. Hydrogen atoms were omitted for clarity.

sphere, thus leaving the two thiocyanate anions in *trans* positions.

Compound **10** crystallizes in the triclinic space group $P\bar{1}$. The average Fe–N bond length is found at 2.16 Å, which is typical of an HS Fe(II) complex in an FeN_6 octahedral environment. The basal coordination angles vary from 77.05(6)° to 115.78(6)° (Table 2.2), and the torsion angles of [N1–N3–N4–N6 = 23.66(7)°] and [C1–N1–N6–C22 = 48.27(1)°], indicating a strong distortion of the octahedral geometry. The compounds **11**, **12** and **15** crystallize in the centrosymmetric $C2/c$ space group, and the iron centres are found at twofold rotation axes running through Fe1 and the middle of the central C–C bond of the ligand. As a result, only one half of the molecule is crystallographically independent (*i.e.*, $Z' = 0.5$). Like in complex **1** the octahedrons are significantly distorted so that the two facing hydrogen atoms located in an ϵ position on each substituted pyridine ring cannot be in contact. For complexes **12**

Table 2.2. Selected bond distances (Å) and angles (°) for the HS phase of **10**, **11** and for the two phases of **12** and **15**.

Compound	10		11		12		15	
T (K)	110(2)		110(2)		295(2)		110(2)	
Phase	HS		HS		HS		LS	
Fe1–N1	2.155(1)	Fe1–N1	2.1436(15)	2.1490(14)	2.0291(12)	2.0704(19)	1.9997(15)	
Fe1–N3	2.161(1)	Fe1–N3	2.1540(16)	2.1273(13)	1.9556(13)	2.0503(16)	1.9434(14)	
Fe1–N4	2.156(1)	Fe1–N4	2.1724(16)	2.1542(16)	1.9536(13)	2.083(2)	1.9518(15)	
Fe1–N6	2.170(1)	N1–Fe1–N1	113.75(8)	110.90(8)	97.43(7)	106.72(10)	97.04(9)	
Fe1–N7	2.144(2)	N1–Fe1–N4	86.21(6)	86.98(6)	87.28(5)	84.28(7)	84.97(6)	
Fe1–N8	2.176(2)	N3–Fe1–N1	85.83(6)	86.28(5)	90.68(5)	87.79(7)	91.11(6)	
N1–Fe–N6	115.78(6)	N3–Fe1–N3	76.96(9)	78.40(7)	82.51(7)	80.15(9)	82.76(9)	
N3–Fe1–N1	85.24(6)	N3–Fe1–N4	87.72(6)	83.19(6)	84.15(5)	84.12(7)	84.22(6)	
N4–Fe1–N3	77.05(6)	N4–Fe1–N4	162.48(9)	179.25(9)	178.24(7)	179.12(12)	178.73(9)	
N6–Fe1–N4	85.23(6)	Cg2···Cg1 [†]	3.934(9)	3.802(9)	3.797(8)	3.867(13)	3.7974(8)	
N7–Fe1–N8	166.17(6)	Cg5···Cg1 [†]	n. a.	n. a.	n. a.	3.798(6)	3.7473(11)	
N1–N3–N4–N6	23.66(7)	N2···S1	3.4592(17)	4.1605(16)	3.9657(13)	3.932(4)	3.8532(16)	
N2···S2 [†]	3.410(2)							
N5 [†] ···S2 [†]	3.403(2)							
Cg3···Cg4 [†]	3.921(10)							

n. a. = not applicable. Symmetry operator [†] = -x,-y,-z

and **15** the average Fe–N bond distance at 110 K is around 1.97-1.98 Å, which is characteristic of an LS Fe(II) complex in an FeN₆ octahedral environment. For compound **11** at 110 K and for compound **12** at 295 K, the average Fe–N bond distance is approximately 2.14-2.16 Å, whereas it is shorter (≈ 2.07 Å) for complex **15** at 300 K. The latter value is intermediate between those expected for a pure HS and a pure LS Fe(II) centres. This observation is in good agreement with the magnetic susceptibility measurements, which indicate that the SCO is only half-way done at 295 K. Finally, the X-ray diffraction measurements confirm the spin crossovers for compounds **12** and **15**. A bond-length analysis for the HS state shows that the Fe1–N3 and Fe1–N4 bond lengths [2.1350(15) and 2.1481(18) Å, respectively], which involve the bipyridine

chelate and the thiocyanate ions, respectively, are generally longer for compound **11** than for compound **12** (see Table 2.2) or **1**.²¹ In the LS state, longer Fe–N bonds would account for a weaker ligand field splitting; however in the HS state such conclusion cannot be drawn, because two electrons are located in antibonding orbitals. The absence of spin crossover for compound **11** remains intriguing (see Discussion).

The crystal packing of compounds **10**, **11**, **12** and **15**, like for **1**,²¹ are characterized by two sets of “supramolecular” interactions found along one-dimensional crystallographic direction (that is, the *c* axis). The first set includes N–H⋯S hydrogen bonds. For compounds **11**, **12** and **15**, the N–H bridges of each tetrapyrridyl ligand are donors to the thiocyanate ions of two neighbouring complexes (see Figure 2.3). The N⋯S intermolecular distances are shorter for compound **11** [3.459(2) Å], and are comparable to those found in the HS phase of compound **1** [3.424(2) Å]. By contrast, these distances are significantly longer for the near-room temperature structures of compound **12** [4.160(2) Å] and **15** [3.932(4) Å], indicating weaker N–H⋯S intermolecular interactions. Remarkably, compound **10** shows a different N–H⋯S network, where the S atom (Figure 2.3) on one thiocyanate ligand is accepting two N–H⋯S hydrogen bonds of the NH bridges from two neighbouring molecules. The corresponding N⋯S intermolecular distances are the shortest within this family of compounds [3.403(2) Å and 3.410(2) Å at 110 K].

The second set of intermolecular interactions includes π – π stacking between the terminal pyridine rings of two adjacent molecules, as shown in Figure 2.3. The centroid-centroid distances are 3.921(10), 3.934(9) and 3.8018(9) Å for compounds **10**, **11** and **12** respectively. Such distances are similar to that found in compound **1** [3.881(1) Å]. For compound **15**, each ring of the bipyridine fragment is involved in π – π stacking with the two fused aromatic rings of the isoquinoline groups of the neighbouring molecule, with centroid-centroid distances of 3.798(6) and 3.867(13) Å. Overall, π – π stacking interactions are similar within this family of compounds (that is, **1**, **10**, **11**, **12** and **15**). There seems to be no obvious correlation between the cooperativity of the SCO and the π – π stacking interactions in the solid state.

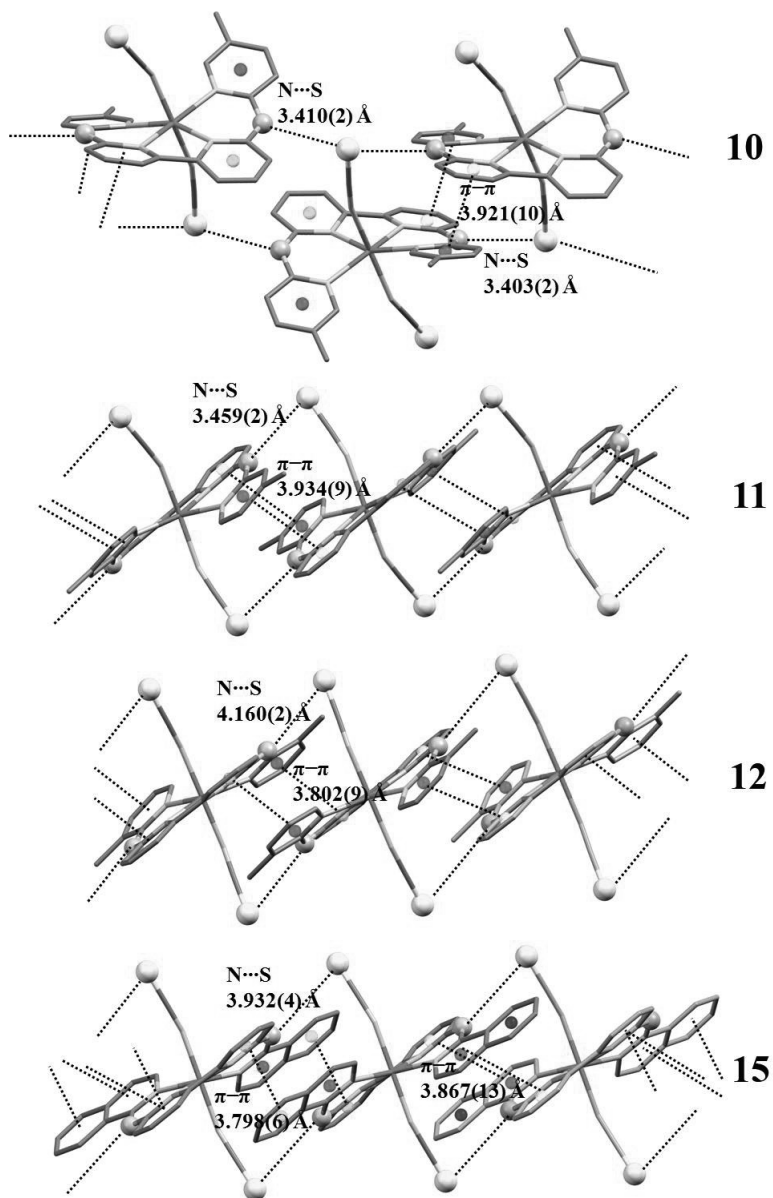


Figure 2.3. Crystal packing along the crystallographic c axis for compounds **10**, **11**, **12** and **15**. Distances are given for the HS (**10**, **11** and **12**) and LS + HS (**15**) phases.

In addition, two sets of data aimed at investigating the temperature dependence of the unit cell dimensions for **12** were collected between 150 and 250 K at ± 5 K intervals

for both cooling and heating regimes (data not shown), and from 290 to 110 K at -10 K intervals (see Figure 2.4). The first set shows no sign of hysteresis loop in the cell parameters between the cooling and heating regimes. The second set (see Figure 2.4) shows a continuous decrease of V/Z (that is, volume per formula unit) over a large temperature range as T decreases. The drop in V/Z is more pronounced between 140 and 240 K. Overall, temperature dependence of the unit cell dimensions for **12** is consistent with the results of the magnetic susceptibility measurements.

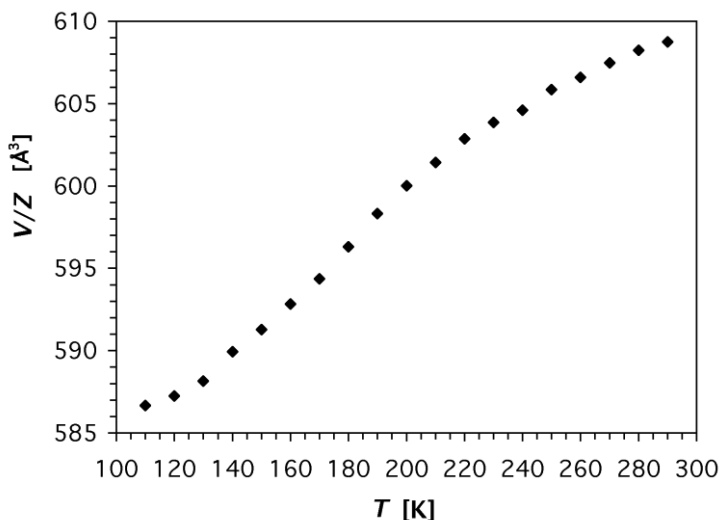


Figure 2.4. Plot of the volume per formula unit V/Z (\AA^3) versus T (K) for compound **12**. Values of V/Z are measured for the cooling transition HS \rightarrow LS at -10 K intervals.

The SCO transition of Fe(II) compounds in the solid state usually leaves clear signatures in calorimetric measurements, especially in the case of abrupt or cooperative SCO, for which sharp heat capacity peaks are detected. Molar heat capacities were determined at constant pressure, C_p , of compounds **12**, **14** and **15** from differential scanning calorimetry (DSC) experiments. For comparison molar heat capacity for a powder sample of compound **1** is also given, for which DSC traces and excess enthalpy and entropy due to the SCO ($\Delta_{SCO}H$ and $\Delta_{SCO}S$) were previously reported.^{21, 22} The results are given in Figure 2.5. The excess heat capacity, ΔC_p , due to the spin-crossover phenomenon in these compounds (shown in Figure 2.6) is obtained by estimating normal heat capacity curves with the high and low temperature data, which are

represented as dashed lines in Figure 2.5, and subtracting it from the total heat capacity. In this estimation no heat capacity step at the transition temperature was considered. The deduced calorimetric values associated with the SCO $\Delta_{SCO}H$ (integration of ΔC_p over T) and $\Delta_{SCO}S$ (integration of ΔC_p over $\ln T$) are gathered in Table 2.3.

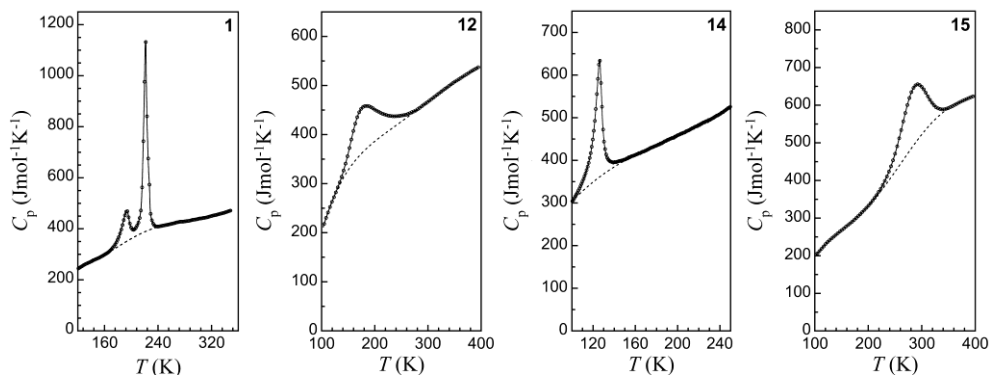


Figure 2.5. Molar heat capacities of compounds **1**, **12**, **14** and **15** upon warming. Dashed lines are estimated normal heat capacities used for ΔC_p determination. Data for **1** is taken from reference 21.

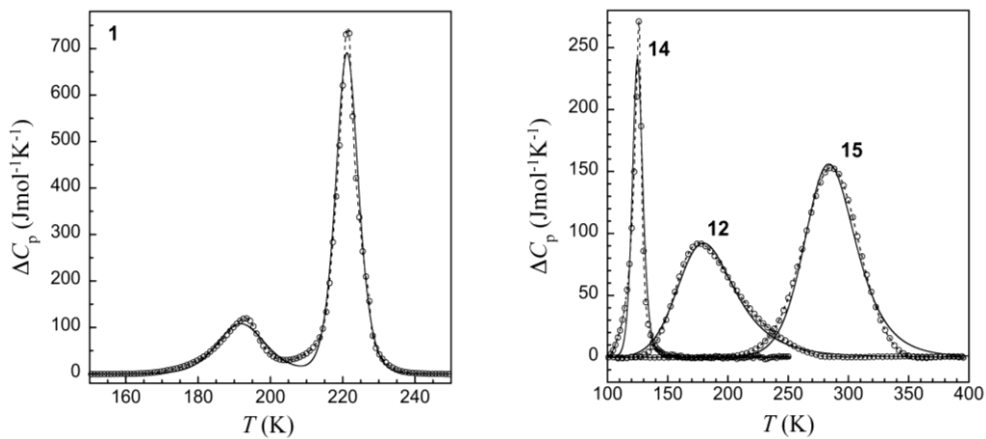


Figure 2.6. Excess heat capacity associated to the SCO transitions for compounds **1**,²¹ **12**, **14** and **15** upon warming. The full lines are the best fit to the domain model of Sorai, as described in the text.

Table 2.3. Excess enthalpy and entropy due to the SCO, and parameters describing the SCO ($T_{1/2}$) and its cooperativity (n) in compounds **1**, **12**, **14** and **15** as derived from the domain model (see text).

Compound	1 ^a	12	14	15
$\Delta_{SCO}H$ (kJ mol ⁻¹)	5.85 / 8.65	6.01	2.73	8.91
$\Delta_{SCO}S$ (J mol ⁻¹ K ⁻¹)	30.7/ 39.2	32.3	22.0	31.5
n	11.6 / 22.5	2.8	16.8	5.3
$T_{1/2}$ (K)	192 / 221	185	125	287

^a In the case of compound **1**, the two numbers given refer to the two steps observed in the SCO, while the enthalpies and entropies are given per mole of transiting Fe(II) centre for better comparison with single-step SCO compounds.

Compounds **12** and **15** present very broad heat capacity anomalies at temperatures comparable to the transition temperatures determined by the magnetic susceptibility measurements, that is, centred on 185 and 287 K, respectively. For both compounds no significant difference is found in molar heat capacities when the samples are either warmed or cooled. On the other hand, compound **14** exhibits one sharp heat capacity peak centred on 125 K, in excellent agreement with the magnetic measurements. Although large values of $\Delta_{SCO}H$ and especially $\Delta_{SCO}S$ (typically when largely surpassing the purely electronic entropy change $\Delta S = R \ln[(2S_{HS} + 1)/(2S_{LS} + 1)] = 13.45 \text{ J mol}^{-1} \text{ K}^{-1}$) are often taken as an indication of cooperativity, these values depend on the actual temperature at which the SCO takes place. It is thus rather difficult to make comparisons between compounds for which SCO transitions occur over different temperature ranges. To quantify and to compare the cooperative character of the SCO compounds presented in this work, we considered the phenomenological domain model proposed by Sorai, which has been widely used when accurate calorimetric data are available.²⁶ This model is based on heterophase fluctuations and gives a measure of cooperativity through the number n of like-spin SCO centres per interacting domain. The larger the domains are, the more cooperative the transition is. Compounds that show a gradual SCO usually give n values close to 1,^{27, 28} whereas values as large as 95 have been derived for the prototype cooperative SCO complex [Fe(phen)₂(NCS)₂] (phen = 1,10-phenanthroline).²⁹ According to this model, the excess heat capacity ΔC_p can be written as in Equation 2.1.

$$\Delta C_p = \frac{n(\Delta_{SCO}H)^2}{RT^2} \frac{\exp\left[\frac{n\Delta_{SCO}H}{R}\left(\frac{1}{T} - \frac{1}{T_{1/2}}\right)\right]}{\left\{1 + \exp\left[\frac{n\Delta_{SCO}H}{R}\left(\frac{1}{T} - \frac{1}{T_{1/2}}\right)\right]\right\}^2} \quad \text{Eq 2.1}$$

The experimental ΔC_p data (see Figure 2.6) were very satisfactorily fit to Equation 2.1 using $\Delta_{SCO}H$ as derived from DSC experiments but leaving $T_{1/2}$ free. In the case of compound **1**, two separate values of n and $\Delta_{SCO}H$ were used for each step. The resulting values for n are given in Table 2.3, and clearly correlate with the differences in abruptness of the SCO curves in magnetic susceptibility measurements or sharpness of heat capacity peaks in DSC. Both compounds **1** (especially the high temperature step) and **14** can be considered as cooperative SCO compounds with values of n of 22.5 and 16.8, respectively, whereas compounds **12** and **15** have low n values (2.8 and 5.3, respectively) and can be considered as poorly cooperative.

In line with this domain model, it is interesting to note that the colour changes occur in a very different manner for compounds **1** or **12**, correlating with the cooperativity of the spin-crossover process. Figure 2.7a displays bright-field images at five different temperatures in the cooling mode of a single crystal of compound **1**. At 233 K the crystal is totally in the HS state (red) and at 228 K it is totally in the intermediate phase (hereafter, IP, dark red). At 231 K one can clearly observe the epitaxial relation between the mother (HS) and daughter (IP) phases characterized by an obvious front, which indicates the first-order character of this transition.³⁰ By decreasing the temperature to 229 K this new phase propagates along the c axis of the crystal – similar to what was reported by Bedoui *et al.*²³ Figure 2.7b presents bright field images of a single crystal of **12** in the cooling mode. At 293 K the crystal is totally in the HS state, and at 120 K it is totally in the LS state. By lowering the temperature from 293 K to 120 K the crystal colour changes slowly from red to dark red, but here in a continuous and homogenous manner without any observable epitaxial relation between the mother and daughter phases. In line with the very continuous evolution of V/Z and $\chi_M T$ as a function of T , the spatiotemporal evolution of the SCO does not involve any observable phase separation and – within the limits of the experimental resolution – the sample seems to behave as a homogenous mixture of the HS and LS phases at intermediate

temperatures. The reproducibility of the observed phenomena has been confirmed using several other crystals.

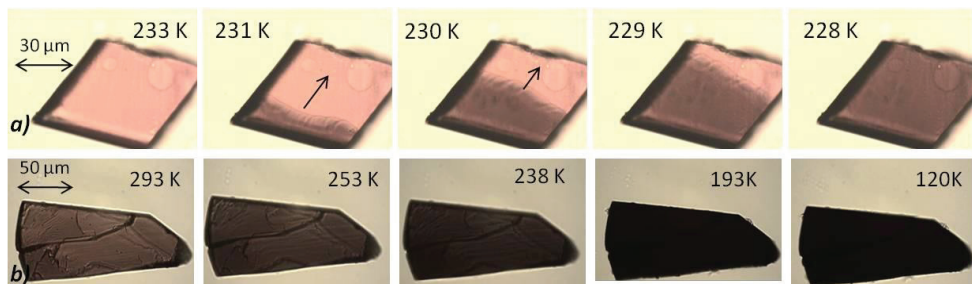


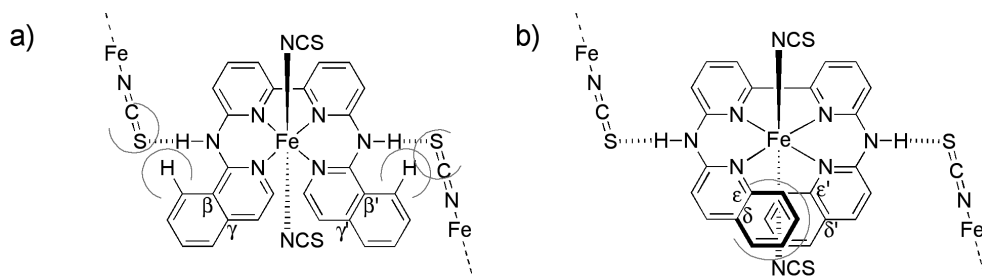
Figure 2.7. Bright-field optical microscopy images of single crystals of (a) **1** and (b) **12** recorded upon cooling in transmission mode.

2.3. Discussion

Ideally, the transition temperature of a spin-crossover material depends mostly on the ligand field created around iron(II) by the ligand set, whereas the cooperativity of the spin crossover depends on how molecules interact with each other in the solid state. To a certain extent, the new materials described in this study help to provide a qualitative model for the structure-property relationship of bapbpy-based SCO materials. The absence of uncoordinated counter anions and uncoordinated solvent molecules in the crystal lattice is beneficial in that respect.

Intermolecular N–H \cdots S hydrogen bonds seem to be critical for the cooperativity of iron(II)-based bapbpy derivatives. In a previous study,²² we have shown that the solvated compound [Fe(bapbpy)(NCS)₂] \cdot 2DMF is a non-cooperative SCO system, and that the uncoordinated DMF molecules are hydrogen-bonded to the N–H bridges of the ligand. In this work, the crystal structures of compounds **12** and **15** clearly show that the existence of hindering groups in the β positions results in longer N \cdots S distances. This structural feature is associated with a low cooperativity of the spin crossover in both cases, as shown by magnetic, thermal, single crystal X-ray diffraction and optical microscopy data. As the β substituents point in the same direction as that of the N–H bonds, they seem to contribute to weakening of the intermolecular N–H \cdots S interactions between two adjacent molecules (see Scheme 2.3a), which may explain the lower cooperativity of these two materials. In contrast, the SCO behaviour of compound **14** is

found to be cooperative as has been observed for compound **1**, with discontinuous spin transitions associated with hysteresis cycles. We associate such cooperativity to the absence of any substituent in the β position. Although the solubility of compound **14** in DMF was too low to grow single crystals, one may predict short N \cdots S intermolecular distances (that is, < 3.6 Å).



Scheme 2.3. Intermolecular vs. intramolecular steric hindrance for substituted bapbpy iron(II) SCO compounds. a) with substituents in β positions, steric bulk results in long N–H \cdots S hydrogen bonds, and thus low cooperativity for the SCO; b) with substituents in ϵ positions, intramolecular steric hindrance results in larger distortions in the equatorial plane, lowering splitting of the ligand field, thus stabilizing the HS state.

The transition temperatures ($T_{1/2}$) of an SCO compound may be tuned by changing the electronic and steric properties of the ligand. In the case where the transition temperature is too low or the compound is always HS, one possibility would be to increase the ligand field strength. In contrast, when the ligand field strength is lowered, an HS state will be favoured. For compounds **9**, **10** and **13**, each terminal pyridyl group bears a hindering substituent in the ϵ and/or δ position. Due to the embracing nature of this family of ligands, one might expect that intramolecular steric hindrance between these two facing substituents would lower the ligand field splitting of the complex by increasing the distortions of the organic backbone (see Scheme 2.3b).²¹ Thus, iron bis(thiocyanate) compounds based on ligands **2**, **3** and **6** are expected to remain in the HS state, which is indeed observed experimentally.

Consistently, we might expect compounds **11**, **12**, **14** and **15** to have SCO properties because they do not have substituents in the ϵ or δ position. The fact that compound **12** shows SCO properties whereas compound **11** does not, is hence a surprise. Based on the Hammett constants³¹ a methyl substituent is considered to be slightly more

electron-donating in the *para* position ($\sigma_p = -0.17$) than in the *meta* position ($\sigma_m = -0.07$), which, from a molecular engineering point of view, should favour an LS state for **11**. There must hence be subtle crystal packing effects that counter-balance this trend and lower the crystal field parameter of the molecule once packed in the crystal lattice. Similar exceptions have been described in the literature, for example by Gómez-García *et al.*,^{32, 33} who explained the absence of SCO for $[\text{Fe}(\text{abpt})_2(\text{tcnome})_2]$ ($\text{abpt} = 4\text{-amino-3,5-bis(pyridin-2-yl)-1,2,4-triazole}$; $\text{tcnome}^- = 1,1,3,3\text{-tetracyano-2-methoxypropenide anion}$) by a change in the π - π stacking mode compared to similar $[\text{Fe}(\text{abpt})_2(\text{X})_2]$ compounds with different apical X anions. Analysis of the crystal structures of the HS phases of **11** and **12** shows that the π - π stacking modes are similar in compounds **11**, **12**, and **15**, but that there are noticeable differences in the orientations of the two NCS^- anions for both compounds (see Figure 2.8a), which might play a role in terms of the crystal field strength of both compounds and hence their ability to undergo SCO.^{22, 34} The angles between the mean molecular plane of N3-N1-N1-N3 and the thiocyanate ligand N4-C11-S1 are 66.6 and 77.4° , respectively, for the HS phases of compounds **11** and **12**. The deviation from perpendicularity between the NCS^- anions and the mean molecular plane formed by the four basal N atoms is more pronounced for compound **11** due to short contacts between the NCS^- ions and the methyl groups in the γ, γ' positions of adjacent molecules (see Figure 2.8b, the intermolecular distance $\text{C11}\cdots\text{C12}$ is 3.29 Å). The bulkiness of these methyl groups promotes a more oblique orientation of the NCS^- anions. By contrast, the crystal packing of **12** shows no such contacts (Figure 2.8b, the intermolecular distances $\text{C11}\cdots\text{C12}$ and $\text{C3}\cdots\text{C11}$ are 3.65 and 3.98 Å, respectively). Our current hypothesis is that such intermolecular steric effects may lower the ligand field splitting, and thus the HS state is favoured for compound **11**. However, more theoretical insights into the influence of thiocyanate coordination on the crystal field parameter would be required to draw any final conclusions.

As already discussed for compound **1**,²¹⁻²³ the presence of a hysteresis cycle in the magnetic susceptibility curve (Figure 2.1) and the intense and sharp peaks observed in DSC (Figure 2.5) indicative of a first-order character for the transition of compound **14**. For first-order transitions, the first derivative of the Gibbs free energy is discontinuous, which implies that the enthalpy, the entropy and the volume must be discontinuous at the transition point.³⁰ Meanwhile, the large values of n derived for these compounds when modelling excess heat capacity data with Sorai's domain model clearly indicate a

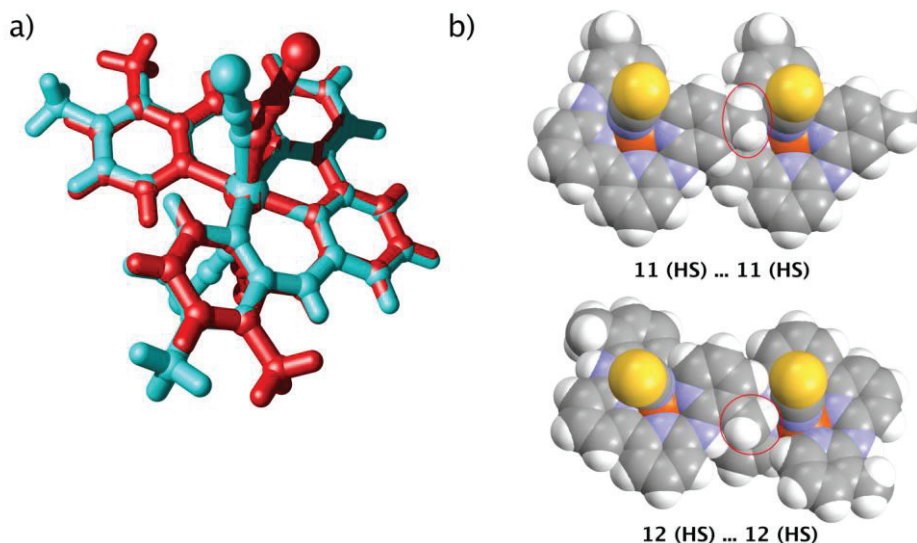


Figure 2.8. a) The different orientation of the thiocyanate ligands relative to the FeN_4 coordination plane, shown with a MOLDEN-generated superposition of the geometries of compounds **11** (blue) and **12** (red) in the HS state (according to crystal structures). b) CPK view of two adjacent molecules of **11** (top) and **12** (bottom) in the crystal structure, viewed perpendicularly to the average plane N1–C1–C2–C3–C4–C5.

cooperative abrupt SCO. For compounds **12** and **15**, the continuous evolution of V/Z and $\chi_M T$ with temperature agree well with the broad humps in C_p vs. T data and the derived low values of n , all of which point to gradual continuous SCO. The absence of discontinuity in V/Z at the transition for compound **12** and of hysteresis for both compounds **12** and **15** are clearly contradictory with a first-order transition. For purely second-order transitions however, the first derivative of the Gibbs free energy is continuous, which implies that the enthalpy, entropy and volume are continuous at the transition point, but their second derivative is discontinuous, and hence ΔC_p is non-zero. The large overall $\Delta_{\text{SCO}}H$ and $\Delta_{\text{SCO}}S$ that are still derived experimentally for these less-cooperative compounds (see Table 2.3), leaving us with the conclusion that the order for such transitions is neither purely first nor purely second-order.

2.4. Conclusion

A striking feature of the data presented herein is that different isomers of the same mononuclear iron(II) complex give materials with very different SCO properties. Studying these different materials provides valuable insights into the structure-function relationship for bapbpy-based spin crossover iron(II) compounds. First, all bapbpy-based compounds studied in this work are robust materials, for which crystals withstand cooling and heating cycles without substantial modification of their crystallinity or magnetic properties. All crystal lattices are solvent free provided that they are crystallized from DMF/MeOH mixtures.²² In addition, X-ray crystallography shows that they are all mononuclear with similar crystal packing, which features hydrogen-bond networks through intermolecular N–H···S interactions. For SCO compounds the strength of these N–H···S hydrogen bonds correlates well with the cooperativity of the spin transition. Compound **11** however represents a counter-example, as its crystal structure exhibit strong N–H···S networks but the compound shows no SCO transition.

The information gathered in this work is highly valuable for material design. However, the mere occurrence of SCO, as well as the transition temperatures, are more erratic and therefore difficult to control. For example the difference in transition temperatures between compounds **14** and **15** is very large ($\Delta T_{1/2} \approx 169$ K), which is surprising considering that they are built from two isomers of the same molecule. Compounds **11** and **12** provide other examples for which there is a significant influence of packing effects on the molecular crystal field strength and on the ability of an apparently suitable ligand to generate spin-crossover Fe(II) compounds. Last but not least, the near room-temperature transition found for compound **15** is promising,¹¹ provided it can be combined with a higher cooperativity.

2.5. Experimental

2.5.1. General information

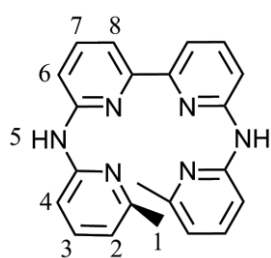
All reactions were performed under argon atmosphere using standard schlenk flask and vacuum line techniques. Toluene was dried over sodium and degassed, diethylether was dried over sodium and benzophenone, DMF was dried over CaH₂. 6,6'-dibromo-2,2'-bipyridine was synthesized in two steps according to the literature.²⁴ All others reagents from commercial sources were used without further purification. 0.1 M methanolic solution

of $[\text{Fe}(\text{NCS})_2]$ used for the synthesis of the iron complexes was prepared as follows: $\text{FeSO}_4 \cdot 7\text{H}_2\text{O}$ (277 mg, 1.00 mmol) and KSCN (194 mg, 2.00 mmol) were mixed in methanol (6 mL) and stirred for 30 min. Ascorbic acid (5 mg) was added to prevent oxidation. The solution was filtered over filter paper (to remove K_2SO_4) into a volumetric flask. The flask was filled up to 10 mL with methanol, resulting in a clear, colourless iron(II) solution, which must be used immediately. Filtration of the crude iron(II) compounds was done on Whatman membrane filters (regenerated cellulose) with 1 μm pores. ^1H NMR and ^{13}C NMR spectra were recorded at room temperature using a Bruker WM 300 MHz spectrometer. Chemical shifts are indicated in ppm relative to TMS. Infrared spectra were taken on a Perkin Elmer FT-IR Spectrometer Paragon 1000. Mass spectrometry was performed on a Finnigan Mat 900 spectrometer equipped with an electrospray interface. Elemental analysis was carried out on a Perkin-Elmer series II CHNS/O analyzer 2400.

2.5.2. Synthesis of R_2bapbpy ligands

General procedure: 6,6'-dibromo-2,2'-bipyridine (538 mg, 1.71 mmol), $\text{Pd}(\text{dba})_2$ (21 mg, 0.036 mmol), (S)-BINAP (43 mg, 0.069 mmol) and $\text{KO}t\text{Bu}$ (770 mg, 6.86 mmol, 4 eq.) were added in a dry schlenk flask and put under argon. Dry, degassed toluene (10 mL) and the required α -aminopyridine (3 mmol) were added, and the mixture was heated to 80 $^\circ\text{C}$ and stirred under argon during 3 days. The suspension was cooled to room temperature and water (50 mL) was added. The mixture was stirred vigorously for 1 h. The solid was filtered and washed with water, diethyl ether and hexane. If necessary, the crude solid was purified by column chromatography on alumina (eluent $\text{CH}_2\text{Cl}_2/\text{MeOH}$ mixtures) or reprecipitated from $\text{CH}_2\text{Cl}_2/\text{hexane}$, and finally dried under vacuum at 60 $^\circ\text{C}$.

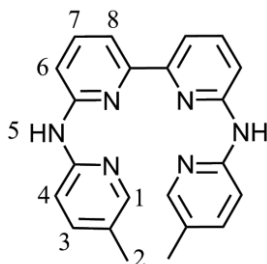
2: 2-amino-6-methylpyridine (324 mg, 3 mmol) was used. A crude white powder was obtained (141 mg, 26%). ^1H NMR (300 MHz, $\text{DMSO}-d_6$): δ =



9.69 (s, 2H, H5), 7.89 (m, 2H, H4), 7.81 (d, J = 7.1 Hz, 4H, H3 + H7), 7.70 – 7.54 (m, 4H, H6 + H8), 6.78 (d, J = 7.3 Hz, 2H, H2), 2.42 (s, 6H, H1). ^{13}C NMR (300 MHz, $\text{DMSO}-d_6$): 23.85(CH₃), 108.43(CH), 112.10(CH), 112.17(CH), 115.17(CH), 138.00(CH), 138.32(CH), 153.50(C), 153.61(C), 154.02(C), 155.89(C). ES-MS (DMF): m/z (calc): 369.14 (369.17, $[M + \text{H}]^+$).

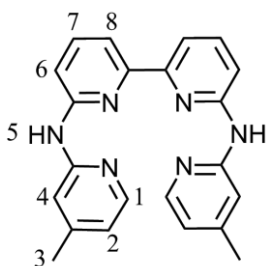
Elemental analysis calcd (%) for $\text{C}_{22}\text{H}_{20}\text{N}_6$: C 71.72, H 5.47, N 22.81; found: C 71.74, H 5.84, N 23.30. IR ν (cm^{-1}): 1593, 1558, 1564, 1516, 1456, 1436, 1361, 1322, 1263, 1238, 1148, 1090, 992, 872, 781, 733, 604, 546, 410, 317.

3: 2-amino-5-methylpyridine (324 mg, 3 mmol) was used. The resulting solid was purified



by column chromatography (250 mL neutral alumina, DCM:MeOH, 95:5, $R_f = 0.4$) to give a yellow powder (111 mg, 20%). ^1H NMR (300 MHz, $\text{DMSO-}d^6$): δ 9.65 (s, 2H, H5), 8.09 (s, 2H, H1), 7.90 (d, $J = 8.5$ Hz, 2H, H4), 7.87 – 7.67 (m, 4H, H4 + H6), 7.67 – 7.47 (m, 4H, H3 + H5), 2.23 (s, 6H, H2). ^{13}C NMR (300 MHz, $\text{DMSO-}d^6$): 17.21(CH₃), 111.41(CH), 111.82(CH), 112.09(CH), 124.64(C), 138.21(CH), 138.31(CH), 147.1(CH), 152.23(C), 153.55(C), 154.04(C). ES-MS (DMF): m/z (calc): 369.34 (369.17, $[M + \text{H}]^+$). Elemental analysis calcd (%) for $\text{C}_{22}\text{H}_{20}\text{N}_6$: C 71.72, H 5.47, N 22.81; found: C 69.21, H 5.70, N 23.03. IR ν (cm^{-1}): 1652, 1576, 1558, 1520, 1506, 1428, 1386, 1300, 1146, 986, 802, 738, 632, 601, 560, 460, 411, 334, 328.

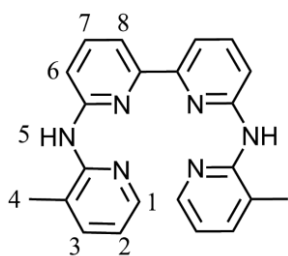
4: 2-amino-4-methylpyridine (324 mg, 3 mmol) was used to obtain a yellow powder (111



mg, 20%). ^1H NMR (300 MHz, $\text{DMSO-}d^6$): δ = 9.64 (s, 2H, H5), 8.10 (d, $J = 5.0$ Hz, 2H, H1), 7.81 (m, $J = 3.9$ Hz, 6H, H5 + H6 + H8), 7.65 (dd, $J = 6.5, 2.4$ Hz, 2H, H7), 6.74 (d, $J = 4.7$ Hz, 2H, H2), 2.31 (s, 6H, H3). ^{13}C NMR (300 MHz, $\text{DMSO-}d^6$): 21.35(CH₃), 112.29(CH), 112.41(CH), 112.56(CH), 117.63(CH), 132.04(C), 138.66(CH), 147.52(CH), 148.27(C), 154.28(C), 154.73(C). ES-MS (DMF): m/z (calc): 369.14 (369.17, $[M +$

$\text{H}]^+$). Elemental analysis calcd (%) for $\text{C}_{22}\text{H}_{20}\text{N}_6 \cdot \text{H}_2\text{O}$: C 68.38, H 5.74, N 21.75; found: C 68.85, H 5.59, N 21.11. IR ν (cm^{-1}): 1612, 1576, 1563, 1558, 1532, 1429, 1294, 1271, 1150, 986, 778, 730, 668, 641, 523, 448, 316, 334.

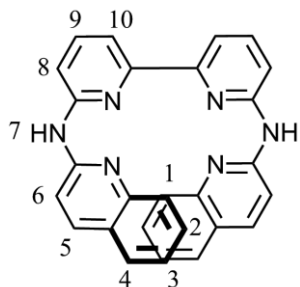
5: 2-amino-3-picoline (324 mg, 3 mmol) was used to obtain a yellow powder (201 mg,



36%). ^1H NMR (300 MHz, $\text{DMSO-}d^6$): δ = 8.32 (s, 2H, H5), 8.13 (d, $J = 4.7$ Hz, 2H, H3), 7.94 (d, $J = 8.1$ Hz, H6), 7.87 (d, $J = 7.4$ Hz, H8), 7.79 (t, $J = 7.8$ Hz, H7), 7.57 (d, $J = 7.3$ Hz, H1), 6.92 (dd, $J = 7.2, 5.0$ Hz, 2H, H2), 2.33 (s, 6H, H4). ^{13}C NMR (300 MHz, $\text{DMSO-}d^6$): 21.35(CH₃), 112.29(CH), 112.41(CH), 112.56(CH), 117.63(CH), 132.04(C), 138.66(CH), 147.52(CH), 148.27(C), 154.28(C), 154.73(C).

ES-MS (DMF): m/z (calc): 369.50 (369.17, $[M + \text{H}]^+$). Elemental analysis calcd (%) for $\text{C}_{22}\text{H}_{20}\text{N}_6$: C 71.72, H 5.47, N 22.81; found: C 71.45, H 5.95, N 21.61. IR ν (cm^{-1}): 1589, 1563, 1558, 1516, 1436, 1410, 1328, 1297, 1258, 1148, 1076, 988, 783, 755, 606, 531, 334, 324.

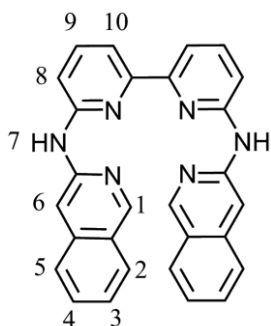
6: quinolin-2-amine (433 mg, 3 mmol) was used to give a yellow powder (295 mg, 45%).



$^1\text{H NMR}$ (300 MHz, $\text{DMSO-}d^6$): δ = 10.15 (s, 2H, H7), 8.46 (dd, J = 7.5, 1.6 Hz, 2H, H8), 8.22 (dd, J = 8.9, 3.8 Hz, 2H, H6), 8.02 – 7.92 (m, 4H, H9 + H10), 7.80 (t, J = 8.9 Hz, 6H, H1 + H4 + H5), 7.69 – 7.61 (m, 2H, H2), 7.37 (dd, J = 10.9, 4.0 Hz, 2H, H3). $^{13}\text{C NMR}$ (300 MHz, $\text{DMSO-}d^6$): 112.70(CH), 113.52(CH), 114.29(CH), 123.38(CH), 124.12(C), 126.47(CH), 127.61(CH), 129.59(CH), 137.33(CH), 138.75(CH), 146.68(C), 153.39(C), 153.45(C),

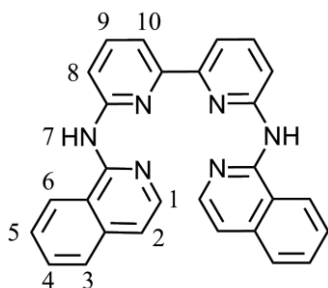
153.66(C). ES-MS (DMF): m/z (calc): 440.56 (440.17, $[M + \text{H}]^+$). Elemental analysis calcd (%) for $\text{C}_{28}\text{H}_{20}\text{N}_6 \cdot \text{H}_2\text{O}$: C 73.35, H 4.84, N 18.33; found: C 73.33, H 4.54, N 17.96. IR ν (cm^{-1}): 1652, 1576, 1558, 1532, 1506, 1463, 1436, 1394, 1371, 1305, 1248, 1141, 1076, 992, 789, 754, 668, 632, 608, 567, 542, 472, 328, 306.

7: isoquinolin-3-amine (250 mg, 1.73 mmol) was used. The resulting solid was purified by



dissolving in a DCM solution and then adding hexane dropwise until precipitation occurred. The white solid was filtered and dried under vacuum at 60 °C (240 mg, 16%). $^1\text{H NMR}$ (300 MHz, $\text{DMSO-}d^6$): δ = 10.01 (s, 2H, H7), 9.15 (s, 2H, H1), 8.81 (s, 2H, H6), 8.03 (M, J = 8.4 Hz, 4H, H2 + H8), 7.96 (t, J = 7.7 Hz, 2H, H9), 7.86 (d, J = 8.2 Hz, 2H, H5), 7.69 (t, J = 7.6 Hz, 2H, H4), 7.45 (t, J = 7.5 Hz, 2H, H3), 7.37 (d, J = 8.0 Hz, 2H, H10). $^{13}\text{C NMR}$ (300 MHz, $\text{DMSO-}d^6$): 154.82(C), 151.672(CH), 150.18(C), 138.955(CH), 138.29(C), 138.207(C),

131.73(CH), 128.209(CH), 126.394(CH), 125.902(C), 124.687(CH), 112.981(CH), 112.609(CH), 103.919(CH). ES-MS (DMF): m/z (calc): 440.17 (440.17, $[M + \text{H}]^+$). Elemental analysis calcd (%) for $\text{C}_{28}\text{H}_{20}\text{N}_6 \cdot 2\text{H}_2\text{O}$: C 70.57, H 5.08, N 17.64; found: C 71.70, H 4.47, N 17.30. IR ν (cm^{-1}): 1611, 1632, 1575, 1537, 1533, 1413, 1362, 1259, 1178, 1149, 986, 870, 783, 735, 686, 668, 638, 464.



8: isoquinolin-1-amine (433 mg, 3 mmol) was used. The resulting solid was purified by dissolving the ligand in a DCM solution and then hexane was added dropwise until precipitation occurred. The yellow solid was filtered and dried it under vacuum at 60 °C (108 mg, 15%). $^1\text{H NMR}$ (300 MHz, $\text{DMSO-}d^6$): δ 9.64 (s, 2H, H7), 8.64 (d, J = 8.5 Hz, 2H, H6), 8.29 (d, J = 8.2 Hz, 2H, H8), 8.10 (m, J =

13.1, 6.6 Hz, 4H, H1 + H10), 7.97 – 7.85 (t, 4H, H3 + H9), 7.77 (t, J = 7.5 Hz, 2H, H4), 7.70 – 7.60 (t, 2H, H5), 7.36 (d, J = 5.7 Hz, 2H, H9). ¹³C NMR (300 MHz, DMSO-*d*⁶): 153.72(C), 153.47(C), 151.77(C), 140.32(CH), 138.12(CH), 136.93(C), 130.36(CH), 126.80(CH), 126.59(CH), 123.89(CH), 119.04(C), 114.30(CH), 114.21(CH), 113.96(CH). ES-MS (DMF): *m/z* (calc): 440.10 (440.17, [M + H]⁺). Elemental analysis calcd (%) for C₂₈H₂₀N₆·H₂O: C 73.35, H 4.84, N 18.33; found: C 73.19, H 4.54, N 17.96. IR ν (cm⁻¹): 1652, 1588, 1558, 1494, 1436, 1330, 1240, 1270, 1240, 1165, 988, 834, 786, 638, 516, 468, 386, 344.

2.5.3. Synthesis of the iron complexes

General procedure: In a round bottom flask the suitable ligand (0.15 mmol), [Fe(NCS)₂] (1.6 mL of a 0.1 M methanolic solution, 1.1 eq.) and ascorbic acid (5 mg) were added. The flask was closed and the suspension was stirred overnight. The solid was collected by filtration over a micropore filter, thoroughly washed with methanol, and dried under vacuum.

Crystal growing: Single crystals suitable for X-ray diffraction study were obtained for compounds **11**, **12** and **15** as follows: the crude powder (50 mg) was dissolved in dry, degassed DMF (10 mL), affording a dark solution which became red after addition of a small amount of ascorbic acid (5 mg). Aliquots (1 mL) of this solution were put into 10 reaction tubes. Degassed methanol was layered on top of these samples, and the 10 tubes were stoppered and left untouched. Dark crystals were obtained within a few days by liquid-liquid diffusion. The crystals were collected, washed with MeOH, and dried under vacuum. For compound **10**: ligand **3** (20 mg) was dissolved in degassed DMF (4 mL). 1 mL aliquots of this solution were pipette-filtered over 1 cm Celite into five Corning tubes. To each tube 0.22 mL of the Fe(NCS)₂ solution was carefully added to create a two-layer system. Degassed methanol was then layered on top of these layers. The tubes were then stoppered and left untouched at room temperature, and if possible under sunlight, to allow slow liquid/liquid diffusion. Within 3 days, red crystals of **10** appeared at the wall of the vials. The tubes were immediately sent for single crystal X-ray structure determination.

9: The yellow compound was obtained with a yield of 77%. IR ν (cm⁻¹): 3344, 2056 (NCS⁻), 1636, 1606, 1590, 1534, 1418, 1456, 1436, 1224, 1174, 1000, 779, 753, 739, 697, 643, 514, 482, 324, 318. ¹H NMR (300 MHz, DMSO-*d*⁶): δ = 9.69 (s, 2H), 7.89 (d, J = 7.8 Hz, 2H), 7.82 (s, 4H), 7.71 – 7.49 (m, 4H), 6.77 (d, J = 6.6 Hz, 2H), 2.41 (s, 6H). HR-MS (DMF): *m/z* (calc): 482.0856 (482.0845, [M – NCS]⁺).

10: The orange compound was obtained with a yield of 76%. IR ν (cm^{-1}): 3294, 2093 (NCS^-), 2061 (NCS^-), 1627, 1616, 1582, 1531, 1496, 1461, 1440, 1436, 1237, 1177, 1048, 1012, 820, 792, 636, 638, 512, 430, 322. ^1H NMR (300 MHz, $\text{DMSO}-d^6$): δ = 78.34, 66.75, 58.73, 44.28, 23.37, 8.01, 7.83, 7.58, 7.55, 6.61. ES-MS (DMF): m/z (calc): 482.26 (482.09, $[\text{M} - \text{NCS}]^+$). Crystal data (at 110(2) K): $F_w = 540.45$, orange red irregular needle, $0.44 \times 0.15 \times 0.08 \text{ mm}^3$, triclinic, $P-1$ (no. 2), $a = 8.5705(3)$, $b = 10.9724(4)$, $c = 13.3111(4) \text{ \AA}$, $\alpha = 69.364(3)$, $\beta = 79.591(3)$, $\gamma = 80.737(3)^\circ$, $V = 1145.71(7) \text{ \AA}^3$, $Z = 2$, $D_x = 1.567 \text{ g cm}^{-3}$, $\mu = 0.873 \text{ mm}^{-1}$, abs. corr. range: 0.758–0.952. 13952 Reflections were measured up to a resolution of $(\sin \theta/\lambda)_{\text{max}} = 0.62 \text{ \AA}^{-1}$. 4624 Reflections were unique ($R_{\text{int}} = 0.0513$), of which 4034 were observed [$I > 2\sigma(I)$]. 326 Parameters were refined using 2 restraints. $R1/wR2$ [$I > 2\sigma(I)$]: 0.0301/0.0770. $R1/wR2$ [all refl.]: 0.0364/0.0798. $S = 1.030$. Residual electron density found between -0.30 and 0.37 e \AA^{-3} .

11: The rusty compound was obtained with a yield of 91%. Single crystals were obtained by liquid-liquid diffusion from MeOH into DMF. IR ν (cm^{-1}): 2853, 2923, 2362, 2075 (NCS^-), 1634, 1533, 1490, 1464, 1442, 1236, 1174, 1010, 790, 643, 449, 330, 325. ^1H NMR (300 MHz, $\text{DMSO}-d^6$): δ = 77.04, 67.63, 58.35, 44.35, 27.64, 24.26, 15.78, 9.68, 8.13, 7.84, 7.68, 6.77. ES-MS (DMF): m/z (calc): 481.86 (482.09, $[\text{M} - \text{NCS}]^+$). Crystal data (at 110(2) K): $F_w = 540.45$, orange irregular plate, $0.34 \times 0.24 \times 0.07 \text{ mm}^3$, monoclinic, $C2/c$ (no. 15), $a = 15.7947(6)$, $b = 12.1802(2)$, $c = 14.5597(5) \text{ \AA}$, $\beta = 122.729(5)^\circ$, $V = 2356.33(18) \text{ \AA}^3$, $Z = 4$, $D_x = 1.523 \text{ g cm}^{-3}$, $\mu = 0.849 \text{ mm}^{-1}$, abs. corr. range: 0.832–0.950. 8245 Reflections were measured up to a resolution of $(\sin \theta/\lambda)_{\text{max}} = 0.65 \text{ \AA}^{-1}$. 2684 Reflections were unique ($R_{\text{int}} = 0.0452$), of which 2210 were observed [$I > 2\sigma(I)$]. 164 Parameters were refined with 1 restraint. $R1/wR2$ [$I > 2\sigma(I)$]: 0.0343/0.0892. $R1/wR2$ [all refl.]: 0.0436/0.0913. $S = 1.036$. Residual electron density found between -0.32 and 0.33 e \AA^{-3} .

12: The rusty compound was obtained with a yield of 91%. Dark red single crystals were obtained by liquid-liquid diffusion from MeOH into DMF in 29% yield. IR ν (cm^{-1}): 3392, 2363, 2063 (NCS^-), 1620, 1587, 1530, 1469, 1436, 1229, 1174, 1005, 788, 648, 580, 325. ^1H NMR (300 MHz, $\text{DMSO}-d^6$): δ = 72.08, 58.24, 43.39, 30.04, 27.18, 19.07, 8.32, 8.13, 7.94, 7.87, 7.79, 7.57, 6.92, 2.33. ES-MS (DMF): m/z (calc): 481.88 (482.09, $[\text{M} - \text{NCS}]^+$). Elemental analysis calcd (%) for $\text{C}_{24}\text{H}_{20}\text{FeN}_8\text{S}_2$: C 53.34, H 3.73, N 20.73; found: C 52.98, H 3.98, N 20.68. Crystal data: **Phase I** (at 295 K): $F_w = 540.45$, dark red diamond, $0.64 \times 0.24 \times 0.20 \text{ mm}^3$, monoclinic, $C2/c$ (no. 15), $a = 13.2932(3)$, $b = 13.2099(2)$, $c = 14.3032(3) \text{ \AA}$, $\beta = 103.715(2)^\circ$, $V = 2440.05(8) \text{ \AA}^3$, $Z = 4$, $D_x = 1.471 \text{ g cm}^{-3}$, $\mu = 0.820 \text{ mm}^{-1}$, abs. corr. range: 0.710–0.874. 9143 Reflections were measured up to a resolution of $(\sin \theta/\lambda)_{\text{max}} =$

0.606 Å⁻¹. 2280 Reflections were unique ($R_{\text{int}} = 0.0190$), of which 2020 were observed [$I > 2\sigma(I)$]. 164 Parameters were refined with 1 restraint. $R1/wR2$ [$I > 2\sigma(I)$]: 0.0269/0.0735. $R1/wR2$ [all refl.]: 0.0311/0.0755. $S = 1.074$. Residual electron density found between -0.30 and 0.23 e Å⁻³. **Phase II** (at 110 K): $F_w = 540.45$, dark red diamond, $0.64 \times 0.23 \times 0.22$ mm³, monoclinic, $C2/c$ (no. 15), $a = 13.1548(2)$, $b = 13.21019(18)$, $c = 14.1638(2)$ Å, $\beta = 107.2514(16)^\circ$, $V = 2350.62(6)$ Å³, $Z = 4$, $D_x = 1.527$ g cm⁻³, $\mu = 0.851$ mm⁻¹, abs. corr. range: 0.697–0.868. 12820 Reflections were measured up to a resolution of $(\sin \theta/\lambda)_{\text{max}} = 0.65$ Å⁻¹. 2694 Reflections were unique ($R_{\text{int}} = 0.0447$), of which 2493 were observed [$I > 2\sigma(I)$]. 164 Parameters were refined with 1 restraint. $R1/wR2$ [$I > 2\sigma(I)$]: 0.0295/0.0821. $R1/wR2$ [all refl.]: 0.0314/0.0833. $S = 1.078$. Residual electron density found between -0.54 and 0.45 e Å⁻³.

13: The orange complex was obtained with a yield of 61%. IR ν (cm⁻¹): 3080, 2362, 2036 (NCS⁻), 1652, 1584, 1563, 1532, 1461, 1294, 1242, 794, 751, 473. ¹H NMR (300 MHz, DMSO-*d*⁶): $\delta = 10.16$ (s, 2H), 8.47 (d, $J = 5.6$ Hz, 2H), 8.24 (d, $J = 8.3$ Hz, 2H), 8.00 (s, 4H), 7.82 (t, $J = 8.1$ Hz, 6H), 7.71 – 7.60 (m, 2H), 7.41 (d, $J = 6.4$ Hz, 2H). HR-MS (DMF): m/z (calc): 554.0838 (554.0845, [M – NCS]⁺).

14: The red complex was obtained with a yield of 92%. IR ν (cm⁻¹): 3294, 2062 (NCS⁻), 1636, 1616, 1576, 1564, 1541, 1490, 1474, 1404, 1322, 1247, 1171, 1004, 866, 786, 664, 635, 459, 425. ¹H NMR (300 MHz, DMSO-*d*⁶): $\delta = 10.01$ (s, 2H), 9.15 (s, 2H), 8.81 (s, 2H), 8.03 (M, $J = 8.4$ Hz, 4H), 7.96 (t, $J = 7.7$ Hz, 2H), 7.86 (d, $J = 8.2$ Hz, 2H), 7.69 (t, $J = 7.6$ Hz, 2H), 7.45 (t, $J = 7.5$ Hz, 2H), 7.37 (d, $J = 8.0$ Hz, 2H). ES-MS (DMF): m/z (calc): 554.06 (554.08, [M – NCS]⁺).

15: The brown compound was obtained with yield of 81%. Dark brown single crystals were obtained by liquid-liquid diffusion from MeOH into DMF in 32% yield. IR ν (cm⁻¹): 2365, 2110 (NCS⁻), 2071 (NCS⁻), 1636, 1610, 1593, 1533, 1506, 1436, 1233, 796, 740, 668, 664, 581, 477. ¹H NMR (300 MHz, DMSO-*d*⁶): $\delta = 72.92$, 73.50, 28.19, 26.37, 25.66, 22.49, 10.47, 9.31, 8.64, 8.26, 8.10, 8.06, 7.91, 7.77, 7.66, 7.36. ES-MS (DMF): m/z (calc): 554.04 (554.08, [M – NCS]⁺).

Crystal data: **Phase I** (at 300 K): $F_w = 612.51$, dark brown block, $0.39 \times 0.24 \times 0.09$ mm³, monoclinic, $C2/c$ (no. 15), $a = 13.1139(3)$, $b = 13.9825(3)$, $c = 14.8988(4)$ Å, $\beta = 92.719(2)^\circ$, $V = 2728.84(11)$ Å³, $Z = 4$, $D_x = 1.491$ g cm⁻³, $\mu = 0.743$ mm⁻¹, abs. corr. range: 0.794–0.933. 8264 Reflections were measured up to a resolution of $(\sin \theta/\lambda)_{\text{max}} = 0.59$ Å⁻¹. 2413 Reflections were unique ($R_{\text{int}} = 0.0235$), of which 2070 were observed [$I > 2\sigma(I)$]. 190 Parameters were refined with 1 restraint. $R1/wR2$ [$I > 2\sigma(I)$]: 0.0347/0.0952. $R1/wR2$ [all

refl.]: 0.0410/0.0974. $S = 1.094$. Residual electron density found between -0.40 and $0.58 \text{ e } \text{Å}^{-3}$. **Phase II** (at 110 K): $F_w = 612.51$, dark brown block, $0.38 \times 0.28 \times 0.11 \text{ mm}^3$, monoclinic, $C2/c$ (no. 15), $a = 12.9785(2)$, $b = 13.9262(3)$, $c = 14.5637(3) \text{ Å}$, $\beta = 93.7103(17)^\circ$, $V = 2626.74(9) \text{ Å}^3$, $Z = 4$, $D_x = 1.549 \text{ g cm}^{-3}$, $\mu = 0.772 \text{ mm}^{-1}$, abs. corr. range: $0.795\text{--}0.927$. 8254 Reflections were measured up to a resolution of $(\sin \theta/\lambda)_{\max} = 0.62 \text{ Å}^{-1}$. 2579 Reflections were unique ($R_{\text{int}} = 0.0251$), of which 2224 were observed [$I > 2\sigma(I)$]. 190 Parameters were refined with 1 restraint. $R1/wR2$ [$I > 2\sigma(I)$]: $0.0290/0.0748$. $R1/wR2$ [all refl.]: $0.0352/0.0765$. $S = 1.034$. Residual electron density found between -0.46 and $0.44 \text{ e } \text{Å}^{-3}$.

X-Ray diffraction studies: All reflection intensities were measured using a KM4/Xcalibur (detector: Sapphire3) with enhance graphite-monochromated Mo $K\alpha$ radiation ($\lambda = 0.71073 \text{ Å}$) under the program CrysAlisPro (Version 1.171.33.55, Oxford Diffraction Ltd., 2010). The program CrysAlisPro was used to refine the cell dimensions. Data reductions were done using the program CrysAlisPro. The structures were solved with the program SHELXS-97 and were refined on F^2 with SHELXL-97.³⁵ Analytical numeric absorption corrections based on a multifaceted crystal model were applied using CrysAlisPro. The temperatures of the data collections were controlled using the system Cryojet (manufactured by Oxford Instruments). The H-atoms were placed at calculated positions (except for that located on N2) using the instructions AFIX 43, or AFIX 137 (only for **11** and **12**) with isotropic displacement parameters having values 1.2 or 1.5 times U_{eq} of the attached C atoms. The positions and the isotropic temperature factors of the H atoms located on N2 (*i.e.*, H2A) were refined freely. The distances N2–H2A were restrained to be $0.83(3) \text{ Å}$.

Magnetic susceptibility data were measured on a Quantum Design MPMS-XL squid magnetometer from powder samples for compounds **9**, **10**, **13** and **14**, and from recrystallized samples for compounds **11**, **12**, and **15**. In all cases, the $\sim 10\text{--}20 \text{ mg}$ sample was inserted in a plastic straw before introduction in the magnetometer. DC magnetization measurements were performed in a field of 0.5 T , from 300 to 3 K (cooling mode) and from 3 to 300 K (heating mode) with a rate of $0.3\text{--}1.1 \text{ K min}^{-1}$ for compounds **9–14**, and from 80 to 400 K (heating mode) and from 400 to 80 K (cooling mode) with a rate of $0.3\text{--}1.1 \text{ K min}^{-1}$ for compound **15**. The total measuring time was 20 h . The transition temperatures were obtained using the first derivative of $\chi_{MT} = f(T)$. Corrections for the diamagnetism of the sample were calculated using Pascal's constants.³⁶

Differential Scanning Calorimetry (DSC): Heat capacities were obtained by use of a differential scanning calorimeter Q1000 with the LNCS accessory from TA Instruments.

The temperature and enthalpy scales were calibrated with a standard sample of indium, using its melting transition (156.6 °C, 3296 J mol⁻¹). The measurements were carried out using 6 to 13 mg of samples sealed in aluminum pans with mechanical crimp, with an empty pan as reference. The zero-heat flow procedure described by TA Instruments was followed, using as reference compound a synthetic sapphire. Using this procedure, an overall accuracy of ca. 0.2 K in temperature and up to 5 to 10% in the heat capacity is estimated over the whole temperature range.

Optical microscopy: Optical microscopy images of single crystals of **1** and **12** were recorded in bright-field transmission mode using an Olympus BX51 microscope equipped with a 640×512 colour camera (Moticom), a halogen lamp (400-700 nm) and a 50× long-working-distance objective (NA=0.5). The sample was enclosed in a Linkam THMS600 liquid nitrogen cryostat equipped with glass windows. The heating and cooling rates were 5 K min⁻¹ and images were taken every 30 s.

2.6. References:

1. P. Gamez, J. S. Costa, M. Quesada and G. Aromi, *Dalton Trans.*, 2009, 7845-7853.
2. A. Bousseksou, G. Molnar and G. Matouzenko, *Eur. J. Inorg. Chem.*, 2004, 4353-4369.
3. J. F. Létard, P. Guionneau and L. Goux-Capes, *Top. Curr. Chem.*, 2004, 235, 221-249.
4. O. Kahn and C. J. Martinez, *Science*, 1998, 279, 44-48.
5. M. S. Alam, M. Stocker, K. Gieb, P. Muller, M. Haryono, K. Student and A. Grohmann, *Angew. Chem., Int. Ed.*, 2010, 49, 1159-1163.
6. M. Cavallini, I. Bergenti, S. Milita, G. Ruani, I. Salitros, Z. R. Qu, R. Chandrasekar and M. Ruben, *Angew. Chem., Int. Ed.*, 2008, 47, 8596-8600.
7. J.-F. Létard, N. Daro and S. Auffret, *Spin transition materials*, 2010, patent US 2010/0178511.
8. M. Ohba, K. Yoneda, G. Agusti, M. C. Munoz, A. B. Gaspar, J. A. Real, M. Yamasaki, H. Ando, Y. Nakao, S. Sakaki and S. Kitagawa, *Angew. Chem., Int. Ed.*, 2009, 48, 4767-4771.
9. P. D. Southon, L. Liu, E. A. Fellows, D. J. Price, G. J. Halder, K. W. Chapman, B. Moubaraki, K. S. Murray, J. F. Letard and C. J. Kepert, *J. Am. Chem. Soc.*, 2009, 131, 10998-11009.
10. L. Salmon, G. Molnar, D. Zitouni, C. Quintero, C. Bergaud, J. C. Micheau and A. Bousseksou, *J. Mater. Chem.*, 2010, 20, 5499-5503.
11. I. Salitros, N. T. Madhu, R. Boca, J. Pavlik and M. Ruben, *Monatsh. Chem.*, 2009, 140, 695-733.
12. M. Kepenekian, J. S. Costa, B. Le Guennic, P. Maldivi, S. Bonnet, J. Reedijk, P. Gamez and V. Robert, *Inorg. Chem.*, 2010, 49, 11057-11061.
13. S. Cobo, D. Ostrovskii, S. Bonhommeau, L. Vendier, G. Molnar, L. Salmon, K. Tanaka and A. Bousseksou, *J. Am. Chem. Soc.*, 2008, 130, 9019-9024.
14. O. Kahn, *Molecular Magnetism*, John Wiley & Sons, New York, 1993.
15. A. Bousseksou, J. Nasser, J. Linares, K. Boukheddaden and F. Varret, *J. Phys. I*, 1992, 2, 1381-1403.
16. W. Nicolazzi, S. Pillet and C. Lecomte, *Phys. Rev. B*, 2008, 78, 174401.

17. C. Enachescu, L. Stoleriu, A. Stancu and A. Hauser, *Phys. Rev. Lett.*, 2009, 102, 257204.
18. K. Boukheddaden, S. Miyashita and M. Nishino, *Phys. Rev. B*, 2007, 75, 094112.
19. H. Spiering, K. Boukheddaden, J. Linares and F. Varret, *Phys. Rev. B*, 2004, 70, 184106.
20. M. Kepenekian, B. Le Guennic and V. Robert, *J. Am. Chem. Soc.*, 2009, 131, 11498-11502.
21. S. Bonnet, M. A. Siegler, J. Sanchez Costa, G. Molnar, A. Bousseksou, A. L. Spek, P. Gamez and J. Reedijk, *Chem. Commun.*, 2008, 5619-5621.
22. S. Bonnet, G. Molnar, J. Sanchez Costa, M. A. Siegler, A. L. Spek, A. Bousseksou, W.-T. Fu, P. Gamez and J. Reedijk, *Chem. Mater.*, 2009, 21, 1123-1136.
23. S. Bedoui, G. Molnár, S. Bonnet, C. Quintero, H. Shepherd, W. Nicolazzi, L. Salmon and A. Bousseksou, *Chem. Phys. Lett.*, 2010, 499, 94-99.
24. X. L. Bai, X. D. Liu, M. Wang, C. Q. Kang and L. X. Gao, *Synthesis*, 2005, 458-464.
25. J. F. Létard, P. Guionneau, L. Rabardel, J. A. K. Howard, A. E. Goeta, D. Chasseau and O. Kahn, *Inorg. Chem.*, 1998, 37, 4432-4441.
26. M. Sorai, M. Nakano and Y. Miyazaki, *Chem. Rev.*, 2006, 106, 976-1031.
27. T. Nakamoto, Z. C. Tan and M. Sorai, *Inorg. Chem.*, 2001, 40, 3805-3809.
28. O. Roubeau, M. deVos, A. F. Stassen, R. Burriel, J. G. Haasnoot and J. Reedijk, *J. Phys. Chem. Solids*, 2003, 64, 1003-1013.
29. M. Sorai and S. Seki, *J. Phys. Chem. Solids*, 1974, 35, 555-570.
30. F. H. Herbstein, *Acta Crystallogr., Sect. B*, 2006, B62, 341-383.
31. C. Hansch, A. Leo and R. W. Taft, *Chem. Rev.*, 1991, 91, 165-195.
32. C. Atmani, F. El Hajj, S. Benmansour, M. Marchivie, S. Triki, F. Conan, V. Patinec, H. Handel, G. Dupouy and C. J. Gomez-Garcia, *Coord. Chem. Rev.*, 2010, 254, 1559-1569.
33. G. Dupouy, M. Marchivie, S. Triki, J. Sala-Pala, J. Sala n, C. J. Gomez-Garcia and P. Guionneau, *Inorg. Chem.*, 2008, 47, 8921-8931.
34. J. S. Costa, K. Lappalainen, G. de Ruiter, M. Quesada, J. K. Tang, I. Mutikainen, U. Turpeinen, C. M. Grunert, P. Gütllich, H. Z. Lazar, J. F. Létard, P. Gamez and J. Reedijk, *Inorg. Chem.*, 2007, 46, 4079-4089.
35. G. M. Sheldrick, *Acta Crystallogr., Sect. A*, 2008, 64, 112-122.
36. G. A. Bain and J. F. Berry, *J. Chem. Educ.*, 2008, 85, 532.

3

Effect of metal dilution on the thermal spin transition of $[\text{Fe}_x\text{Zn}_{1-x}(\text{bapbpy})(\text{NCS})_2]$

Abstract

This study reports on the effects of zinc dilution on the structure and magnetic properties of the mononuclear two-step spin-crossover compound $[\text{Fe}(\text{bapbpy})(\text{NCS})_2]$ (**1**; bapbpy = *N,N'*-di(pyrid-2-yl)-2,2'-bipyridine-6,6'-diamine). The zinc analogue of **1**, $[\text{Zn}(\text{bapbpy})(\text{NCS})_2]$ (**3**), was synthesized and characterized by X-ray powder diffraction, which suggests different structural features from **1**. The crystal structure of the related compound $[\text{Zn}(\text{bapbpy})(\text{NCS})]_2[\text{Zn}(\text{NCS})_4] \cdot 3\text{DMF}$ (**4**) was determined by single crystal X-ray diffraction. The Zn(II) ions in the cations of **4** are five-coordinated, with four N-donors of the bapbpy ligand and one thiocyanate. Nine samples $[\text{Fe}_x\text{Zn}_{1-x}(\text{bapbpy})(\text{NCS})_2]$ were prepared with iron fractions of $x = 0.89, 0.81, 0.76, 0.65, 0.60, 0.53, 0.44, 0.38,$ and 0.24 . According to powder X-ray diffraction and infrared spectroscopy, the structure of compound **1** is retained in the zinc-diluted samples when $x > 0.53$. At higher dilutions (i.e., when $x < 0.53$), the phase of compound **3** gradually takes over, but the SCO of the iron complexes in the zinc phase remains observable at an iron fraction as low as $x = 0.24$. Powder X-ray diffraction and infrared spectroscopy data indicate the presence of the zinc phase only (i.e., compound **3**) when $x \leq 0.24$. Magnetic susceptibility measurements on the diluted samples show that upon decreasing the iron fraction x , both hysteresis cycles become initially narrower, and then vanish to lead to a single-step SCO material at $x = 0.76$. Upon additional increase of the zinc contents, the cooperativity of the SCO gradually vanishes to lead to a non-cooperative SCO material at the lowest iron fraction studied ($x = 0.24$).

3.1. Introduction

The ability of metal complexes to undergo a transition between a low-spin state (hereafter, LS) and a high-spin state (hereafter, HS), *i.e.*, Spin Crossover (hereafter, SCO), is recognized as one of the most fascinating examples of molecular switching.¹ SCO can be achieved through modulation of an external stimulus, such as temperature, pressure, magnetic field, or light irradiation.² This phenomenon is accompanied by a dramatic and easily detectable change in the macroscopic properties associated to the different electronic states, such as colour, crystal size, and magnetism. In some cases both states are metastable in a given set of physical conditions, thus creating a hysteresis loop (memory effect).³ Such functional materials are therefore excellent candidates for permanent memory devices, which is reflected by the spectacular developments of the research dealing with size-reduction of memory devices.⁴ However, the detailed properties of the transition, like the steepness of the transition, the fraction of metal centres performing the transition, or the presence of two steps and/or of hysteresis cycles, do not depend only on the molecular formula of the compound, but also on intermolecular interactions.⁵ A few models have been proposed to take into account the interplay between short-range and long-range interactions between the spin-bearing metal centres. These models allowed for predicting, for example, the occurrence of two-step SCO.^{2, 6, 7} However, the relationship between the intermolecular interactions in the solid state and the cooperativity of a spin transition, which governs hysteretic behaviour, are not fully understood yet, in the sense that it still remains impossible to predict the detailed SCO properties of an Fe(II) octahedral compound, or to design new compounds achieving a set of target SCO properties.⁸

The synthesis, structural, and magnetic properties of the mononuclear compound [Fe(bapbpy)(NCS)₂] (**1**; bapbpy = *N,N'*-di(pyrid-2-yl)-2,2'-bipyridine-6,6'-diamine) was recently described.⁵ The spin transition of this compound is highly cooperative, showing a steep, two-step transition curve with two hysteresis cycles. Furthermore, this material has raised interest because of the occurrence of a crystallographically well-defined intermediate phase (hereafter, IP) stable over a wide temperature range, and that is different from the LS and HS phases. Although single crystal and powder X-ray diffraction studies, as well as Mössbauer and Raman spectroscopy, show that the HS and LS phases contain a single HS or LS iron(II) site, respectively,⁹ in the IP two thirds of the iron(II) centres are found in the LS state, whereas one third is in the HS state. Remarkably, X-ray crystallography demonstrated long-range ordering of the

[HS–LS–LS] motif in the IP, and the occurrence of strong supramolecular interactions (hydrogen bonds and π – π stacking interactions) along the crystallographic c axis of all three phases. Hydrogen bonded intermolecular interactions seem to be of paramount importance for the cooperativity in the spin transitions of compound **1**,⁹ since, for example, the solvate [Fe(bapbpy)(NCS)₂]·2DMF (compound **2**), which has two DMF molecules H–bonded to the N–H bridges of the bapbpy ligand, shows non-cooperative SCO. In Chapter 2 it was shown that hindering groups located near the N–H bridges weaken the N···S intermolecular interactions, resulting in non-cooperative SCO. These characteristics make of compound **1** a particularly attractive example for studying metal dilution effects. The effect of dilution of SCO complexes into a lattice of isostructural but magnetically silent analogues (typically FeL_n diluted in ZnL_n) has proved to deliver significant information on the relationship between intermolecular interactions and the degree of cooperativity of spin crossover in the solid state.¹⁰ This method was first introduced for the mixed crystal series [Fe_xZn_{1-x}(2-pic)₃]Cl₂·EtOH ($x = 1$ to 0.007, 2-pic = 2-picolyamine),¹¹ for which the SCO curve initially featured an abrupt step, but when became increasingly more gradual as the Zn:Fe ratio increased. Furthermore, the transition temperatures were shifted to lower values, which reflects an increasing stabilization of the HS state. These results supported the existence of cooperative elastic interactions between the SCO metal centres as the transition proceeds. Iron-based SCO compounds can also be diluted using other metal cations such as Ni(II), Co(II) or Mn(II), which, although not being magnetically silent, allow for probing the effects of metal ions having different sizes compared to Zn(II).¹² For example, a recent metal dilution study on [Fe_{0.02}Mn_{0.98}(terpy)₂](ClO₄)₂ (terpy = 2,2';6',2''-terpyridine) has shown that although the iron complexes remain in the LS state when incorporated into the lattice of the corresponding manganese(II) complexes, they can flip to the HS state by irradiation of the dilute phase at low temperature.¹³ The metastable HS state undergoes thermal relaxation to the LS state at elevated temperature, but very long life times were observed, *e.g.* several days when $T < 20$ K. Many metal dilution studies focused on studying the light-induced excited state spin trapping (LIESST),¹⁴⁻¹⁶ but there are, to our knowledge, very few metal dilution studies on the temperature-induced spin transition of mononuclear two-step SCO compounds.^{11, 17} Therefore, to further understand the cooperativity of the spin transition in compound **1**, we carried out a detailed investigation of the system [Fe_xZn_{1-x}(bapbpy)(NCS)₂].

3.2. Results

3.2.1. Sample preparation

Zn(bapbpy)(NCS)₂ (compound **3**) was prepared similarly to its iron(II) analogue **1** reported in the literature.⁵ The preparation method consisted in the impregnation of a methanolic suspension of the bapbpy ligand by a methanolic solution of [Zn(NCS)₂].¹⁸ Compound **3** is more soluble than **1** in methanol, and it was obtained as a yellowish powder in slightly lower yields than **1** (80% vs. 88%). The ¹H NMR of compound **3** at room temperature in DMSO-*d*⁶ shows well-resolved peaks of the coordinated bapbpy ligand in the 7.26 to 11.07 ppm region, consistent with the diamagnetic nature of the zinc ion. By contrast, at room temperature compound **1** is paramagnetic and its ¹H NMR spectrum shows broad signals across a broad ppm range (0 to 80 ppm) (Figure AI.1, Appendix I). Furthermore, the ¹³C NMR spectrum of **3** reveals a small broad resonance at 134.78 ppm consistent with reported values for isothiocyanates ions.¹⁹ The infrared spectrum of compound **3** clearly shows two characteristic thiocyanate vibrations at 2086 cm⁻¹ and 2053 cm⁻¹. The former lies in the same region as for the HS Fe(II) compound **1**, but the latter value is significantly lower and may correspond to a non-coordinated thiocyanate ion. Mass spectrometry of a DMF solution of **3** shows two characteristic peaks at *m/z* = 461.68 for [Zn(bapbpy)(NCS)]⁺ (calc. 462.05) and 534.73 for [Zn(bapbpy)(NCS)(DMF)]⁺ (calc. 535.10). Overall, results obtained from ¹H and ¹³C NMR, IR spectroscopy, and ES-MS analyses are consistent with the Zn(II) coordination by at least one thiocyanate ion and the bapbpy ligand in compound **3**. Finally, elemental analysis concludes on the chemical formula of C₂₂H₁₆ZnN₈S₂ of compound **3**, but all analyses were unable to confirm, in absence of crystal structure, whether one or two thiocyanate ions are coordinated to the metal centre in the solid state.

Comparison of the experimental powder X-ray diffractograms of compounds **1** and **3** at room temperature is shown in Figure 3.1. The two compounds clearly have different structures, which suggests that both compounds may have different packing geometry and/or molecular geometries. The major differences are: (i) the intense reflection at 2θ ≈ 22.5° for compound **1** (star), which is not present for **3**; (ii) some reflections of **3**, *e.g.* at 2θ ≈ 11°, 13.3° and 18.2° (circles), that are absent in **1**. Originally, zinc(II) ions were chosen for metal dilution studies because analogous zinc and iron complexes are expected to have the same crystal structure. As a consequence, solid solutions of

diluted complexes can often be obtained, *e.g.*, as reported for $[\text{Fe}(\text{2-pic})_3]\text{Cl}_2 \cdot \text{EtOH}$.¹¹ The powder X-ray diffraction data of compounds **1** and **3** suggest that this is not the case here.

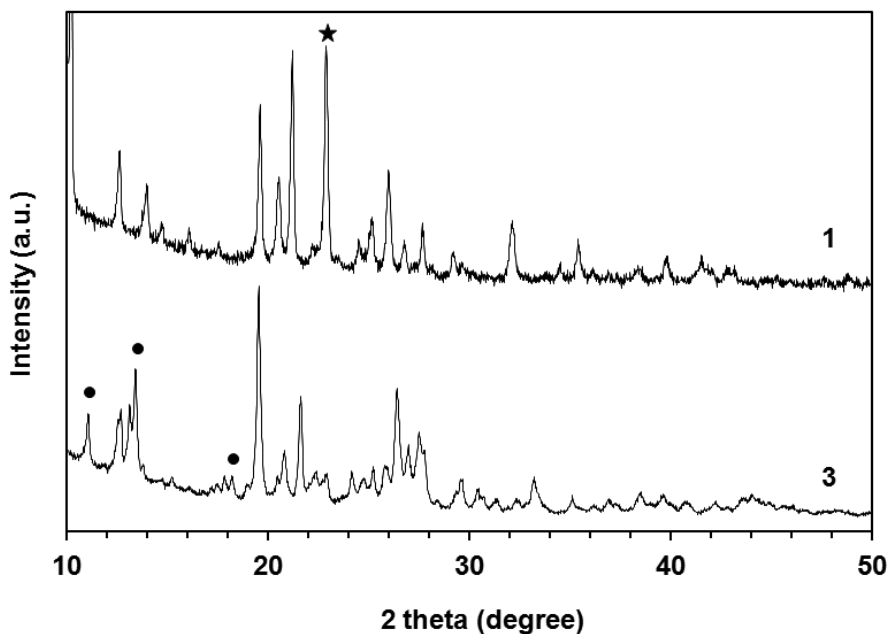


Figure 3.1. Experimental X-ray powder diffractograms of powder samples of **1** (top) and **3** (bottom) collected at room temperature.

Nine samples of $[\text{Fe}_x\text{Zn}_{1-x}(\text{bapbpy})(\text{NCS})_2]$, referred to as **(a)** to **(i)**, were synthesized according to the procedure described by Gütlich and co-workers.¹² The values of the experimental iron fractions in samples **(a)** to **(i)** were calculated from the iron and zinc concentrations determined by metal trace analysis (ICP-OES) for each sample. As shown in Figure 3.2, there are some discrepancies between the Fe:Zn ratios introduced during the synthesis and those found in the isolated solid powders. This is most probably due to the higher solubility of the zinc complex of bapbpy (**3**) in MeOH, compared to that of **1**. It should be noted that the different coordination modes of bapbpy toward Fe(II) and Zn(II) may also contribute to these discrepancies.

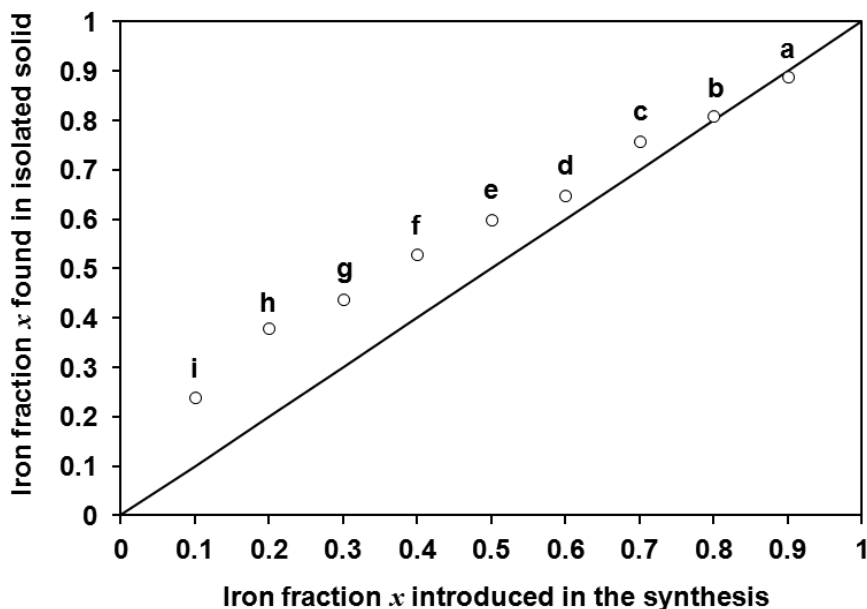


Figure 3.2. Iron fractions (x) obtained from metal trace analysis (ICP-OES) vs. that introduced during synthesis. The full line corresponds to the ideal situation where x (found) = x (introduced).

3.2.2. Magnetic measurements

Magnetic susceptibility measurements were aimed at investigating the effect of introducing Zn(II) in the crystal lattice of the iron-based compound **1** on its magnetic properties. Figure 3.3 shows the $\chi_M T$ vs. T plot for the metal diluted samples (**a**) to (**i**), as well as that of compound **1**, where χ_M stands for the molar magnetic susceptibility and T the temperature. Based on the measurements of $\chi_M T$ at 300 K (Table AI.1, Appendix I), the Fe(II) HS molar fraction γ_{HS} for each diluted sample at a given temperature was derived from the equation $\gamma_{HS} = \chi_M T / x(\chi_M T)_{300}$ where x stand for the iron fraction found by metal trace analysis. Figure 3.4 shows the evolution of γ_{HS} as a function of temperature (from 100 K to 250 K) in the cooling and heating modes for all diluted samples. When the iron fraction x decreased, the $\chi_M T$ values at 300 K decreased, which is expected with increasing amounts of the diamagnetic zinc(II) metal ion (Table AI.1, Appendix I). Second, the widths of the two hysteresis loops became narrower; the higher-temperature hysteresis cycle eventually disappeared at $x = 0.81$, while the lower-temperature hysteresis cycle disappeared at $x = 0.76$, which leads to a one-step SCO phase. Third, the one-step spin crossover became more gradual at iron

fractions lower than 0.76. Finally, no significant residual HS fraction was observed at low temperatures (Figure 3.3 and Table AI.1), and the last sample, characterized by an iron content as low as 0.24, still retained SCO properties.

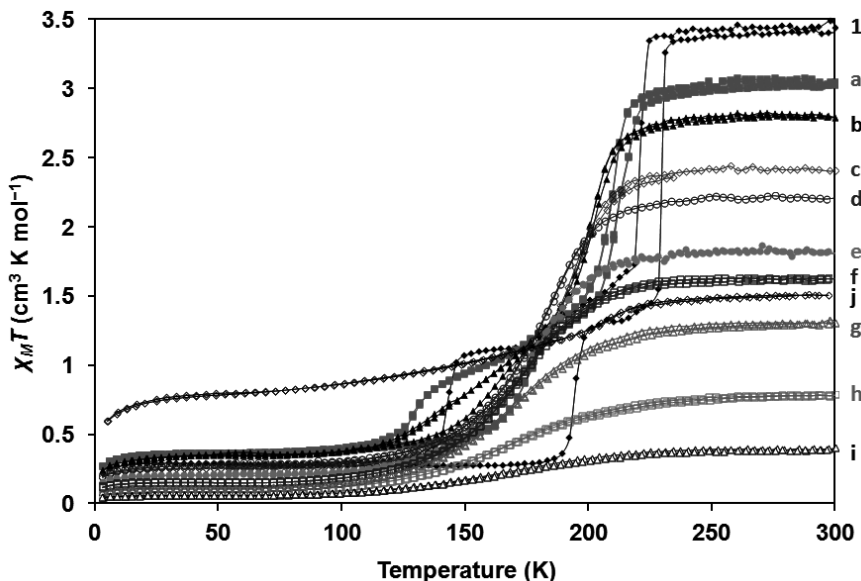


Figure 3.3. Evolution of the $\chi_M T$ curve for the powder samples (a) to (i) of $[\text{Fe}_x\text{Zn}_{1-x}(\text{bapbpy})(\text{NCS})_2]$. All data are shown in both cooling and heating modes. Sample (1) is a powder sample of $[\text{Fe}(\text{bapbpy})(\text{NCS})_2]$ synthesized as previously.⁵ Sample (j) is a 1:1 physical mixture of the Fe-only (1) and the Zn-only (3) powders.

From these data the evolution of the transition temperature $T_{1/2}$ as a function of the iron fraction x were calculated (see Figure 3.5 and Table 3.1). The transition temperatures $T_{1/2}$ are defined from the maximum of $d(\chi_M T)/dT$ (Figure AI.2, Appendix I). For the higher-temperature hysteresis cycle, named as $T_{1/2}^1$ (see Table 3.1), when the iron fraction x decreased then both transition temperatures in the cooling mode ($T_{1/2}^1 \downarrow$) and in the warming mode ($T_{1/2}^1 \uparrow$) decreased as well. As a consequence of the faster evolution of the latter compared to the former the hysteresis width also decreased to completely disappear at $x = 0.76$. Surprisingly, for the lower-temperature hysteresis cycle, $T_{1/2}^2$, both $T_{1/2}^2 \downarrow$ and $T_{1/2}^2 \uparrow$ were found to increase dramatically between $x = 0.89$ and $x = 0.76$ (Figure 3.5), which leads to the disappearance of both hysteresis cycles at $x = 0.76$. When $x < 0.76$, $T_{1/2} \downarrow$ and $T_{1/2} \uparrow$ are equal within experimental errors, and are

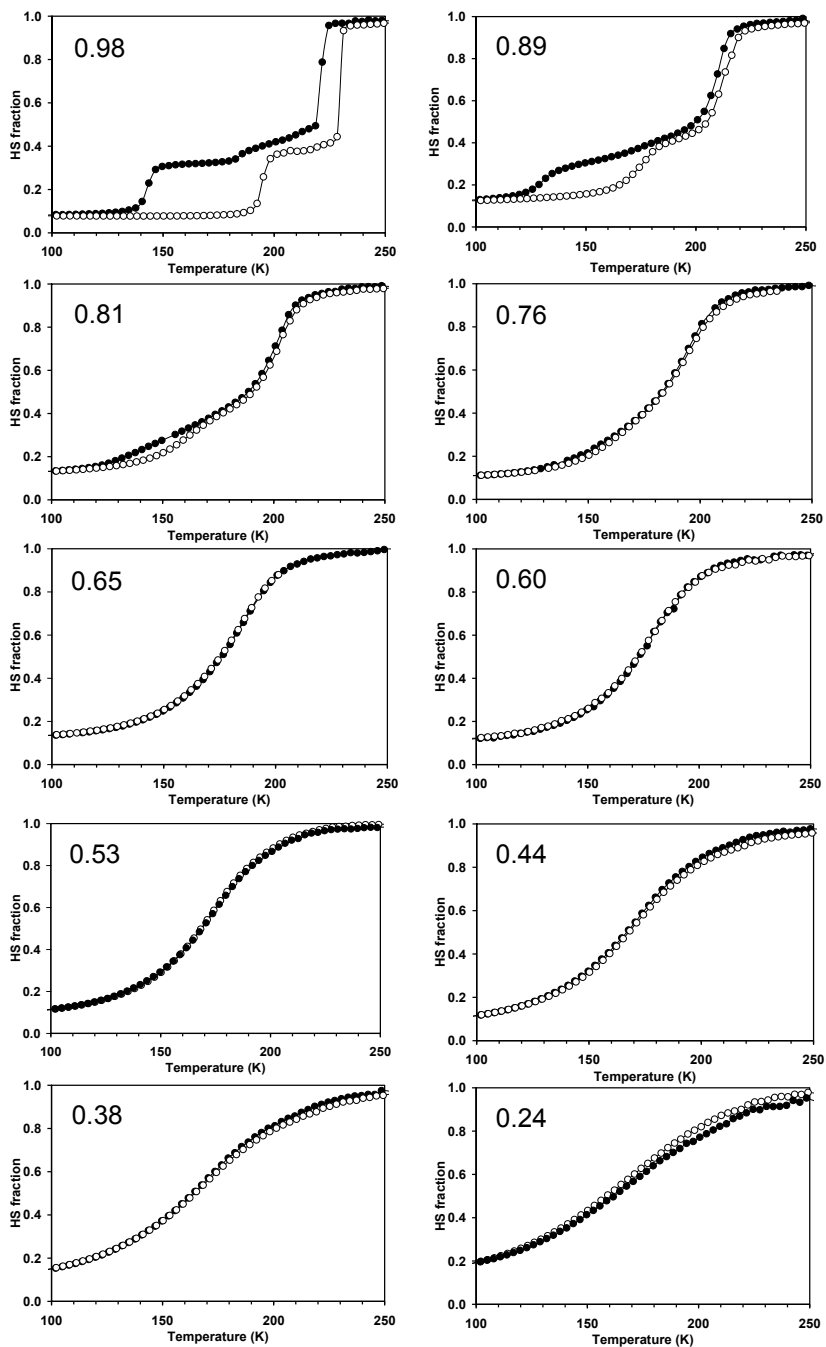


Figure 3.4. Plots of the HS fraction versus T for different samples $[\text{Fe}_x\text{Zn}_{1-x}(\text{bapppy})(\text{NCS})_2]$ with different iron fraction x . All data are shown in both cooling (\bullet) and heating modes (\circ).

found to decrease with decreasing iron content down to $T_{1/2} = 165$ K for $x = 0.24$. Interestingly, it was observed that when $x > 0.76$ the variation of $T_{1/2}$ with x was more pronounced, for both high- and low-temperature transitions, than when the samples were more dilute.

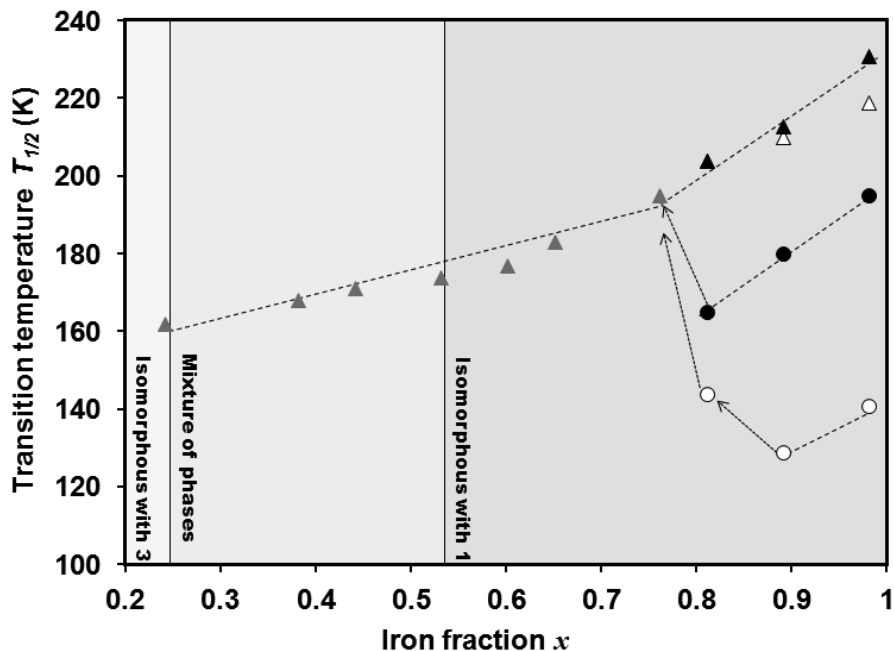


Figure 3.5. Evolution of the transition temperatures $T_{1/2}$ as a function of the iron fraction x in $[\text{Fe}_x\text{Zn}_{1-x}(\text{bapbpy})(\text{NCS})_2]$. The transition temperatures are indicated as triangles in the cooling mode (Δ) and in the heating mode (\blacktriangle) for the higher-temperature hysteresis cycle; as circles in the cooling mode (\circ) and in the heating mode (\bullet) for the lower-temperature hysteresis cycles. When $x \leq 0.76$, both hysteresis cycles disappear and both $T_{1/2\downarrow}$ and $T_{1/2\uparrow}$ are equal (indicated as grey triangular). $T_{1/2}$ values were derived from the maximum of $d(\chi_M T)/dT$ (Figure A1.2). Lines are guides for the eye, and the increase of grey colour in the background indicate three phases upon increase of iron fraction x .

Table 3.1. Transition temperatures (K) and hysteresis widths of diluted samples $[\text{Fe}_x\text{Zn}_{1-x}(\text{bapbpy})(\text{NCS})_2]$ as a function of iron fraction (x).

Sample number	Iron fraction	$T^1_{1/2\downarrow}$	$T^1_{1/2\uparrow}$	ΔT^1_{hyst}	$T^2_{1/2\downarrow}$	$T^2_{1/2\uparrow}$	ΔT^2_{hyst}
1	0.98	219 (3)	231 (3)	10 (3)	141 (3)	195 (3)	54 (3)
a	0.89	210 (3)	213 (3)	3 (3)	129 (3)	180 (3)	51 (3)
b	0.81	204 (3)	204 (3)	0 (4)	144 (3)	165 (3)	21 (3)
c	0.76	195 (3)	195 (3)	–	–	–	–
d	0.65	183 (3)	183 (3)	–	–	–	–
e	0.60	177 (3)	177 (3)	–	–	–	–
f	0.53	174 (3)	174 (3)	–	–	–	–
g	0.44	171 (3)	171 (3)	–	–	–	–
h	0.38	168 (3)	168 (3)	–	–	–	–
i	0.24	162 (3)	162 (3)	–	–	–	–

3.2.3. Powder X-ray diffraction

The powder X-ray diffractograms of compound **1** and compound **3** are different. The diffractogram of **1** is consistent with the calculated powder pattern obtained from the crystal structure of its HS phase.⁹ Figure 3.6 shows the evolution of the powder X-ray diffractograms of the diluted samples (**a**) to (**i**). The existence of well-defined peaks indicates that all samples are crystalline solids. For samples with an iron fraction $x \geq 0.53$, the diffractograms show no major differences as compared with that of the pure compound **1**, except for the gradual shift of a few reflections. We conclude, therefore, that the structure of the diluted samples remains mostly unchanged up to 53% of iron(II). However, structural changes seem to occur when $x \leq 0.44$ as shown by the appearance of new diffraction peaks at $2\theta = 21.6^\circ$ and 26.4° . Furthermore, it should be noted that the intensity of these new reflections increases with increasing zinc content. The reflections characteristic for the phase of compound **1**, notably the peak at $2\theta = 21.2^\circ$, persisted initially, but disappeared with iron fractions $x \leq 0.24$, where only the pattern of compound **3** could be observed. Consequently, the diluted samples in the composition region $0.24 < x < 0.53$ are likely to be a mixture of two phases, whereas the most diluted sample ($x = 0.24$) is fully in the phase of the zinc compound **3**. Thus, upon decreasing the iron:zinc ratio a gradual phase transition is observed in the

resulting solid powders, from the crystallographic phase of compound **1** to that of compound **3**.

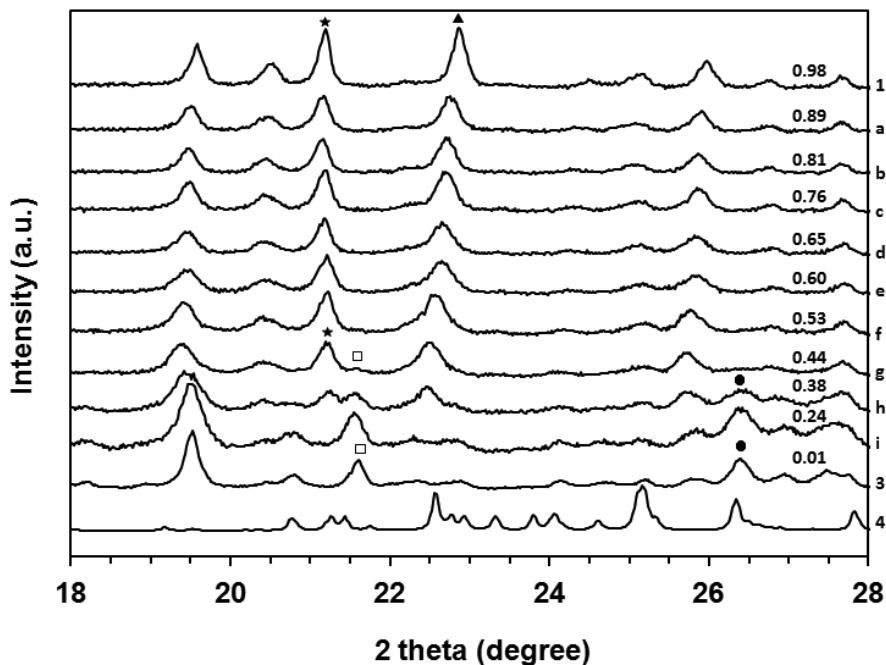


Figure 3.6. Powder X-ray diffractograms for $[\text{Fe}_x\text{Zn}_{1-x}(\text{bapbpy})(\text{NCS})_2]$ in the range $18\text{--}28^\circ$ (2θ) measured at room temperature. The calculated powder pattern derived from the crystal structure of $[\text{Zn}(\text{bapbpy})(\text{NCS})_2][\text{Zn}(\text{NCS})_4]\cdot 3\text{DMF}$ (**4**) at 110 K is also shown. The symbols are indicating the significant changes in diffraction peaks.

3.2.4. Infrared spectroscopy

In contrast to powder X-ray diffraction, which provides global information on the crystal structure but no details on the local structure of a molecule in the solid state, spectroscopic methods are more sensitive to local symmetry. Compound **1** has been characterized thoroughly by Raman and infrared spectroscopies in several studies;^{5,9} it shows a characteristic coordinated thiocyanate stretching vibration at 2090 cm^{-1} at room temperature (i.e., for the HS phase). The Raman signature of the LS Fe(II) complex appears at higher energies, either as a singlet at 2138 cm^{-1} (IP) or as a doublet at 2134 and 2139 cm^{-1} (LS phase). For the zinc compound **3**, infrared spectroscopy at room temperature showed two well-resolved absorption bands at 2053 and 2086 cm^{-1} .

The latter is consistent with a stretching vibration for a coordinated thiocyanate ion, whereas the former indicates either an uncoordinated thiocyanate ion, or a thiocyanate ion with coordination that is different from that found in the iron compound.

The infrared spectra of the diluted samples (**a**) to (**i**) are shown in Figure 3.7. With iron fractions higher than 0.53 the IR spectra were found to be identical to that of compound **1**. For x is 0.53, the IR spectrum shows a significant decrease in the intensity of the absorption band at 2090 cm^{-1} , and the appearance of two new bands at 2053 and 2092 cm^{-1} . As the iron content decreased below 0.53, the IR spectra showed a complete shift of the absorption band at 2090 cm^{-1} to slightly lower wavenumbers (2086 cm^{-1}), and an increase in the intensities of the band at 2053 cm^{-1} . As mentioned earlier, the absorption band at 2053 cm^{-1} was not present for $x > 0.53$, which is consistent with the powder X-ray data showing that the phases of samples (**a**) to (**e**) are identical to that of compound **1**.

A new sample was prepared [sample (**j**)] by physically mixing equimolar amounts of the solid powders of compounds **1** and **3**. Although the chemical composition of samples (**f**) and (**j**) were almost identical ($x \sim 0.5$) their IR spectra were found to be significantly different. For sample (**j**) the IR spectrum showed two well-resolved absorption bands at 2060 and 2086 cm^{-1} , whereas for sample (**f**) a strong absorption band is present at 2090 cm^{-1} , with a small shoulder at lower wavenumbers. Thus, the coordination environment of the thiocyanate ions in sample (**f**) is closer to that of compound **1** than to that of compound **3**. Overall, infrared spectroscopic and powder X-ray diffraction data are consistent with the idea that the phases for sample (**a**) to (**e**) are similar to that of compound **1**. Thus, impregnating a methanolic suspension of the bapbpy ligand with an iron/zinc mixture that is richer in iron does not lead to a pure phase mixture of compound **1** and **3**, but to diluted samples (**a**) to (**e**), in which the zinc and iron complexes have the same coordination mode. At iron fractions lower than 0.53, however, the same impregnation method leads to a mixture of both phases in which one of the two thiocyanate anions has a distinctive coordination environment.

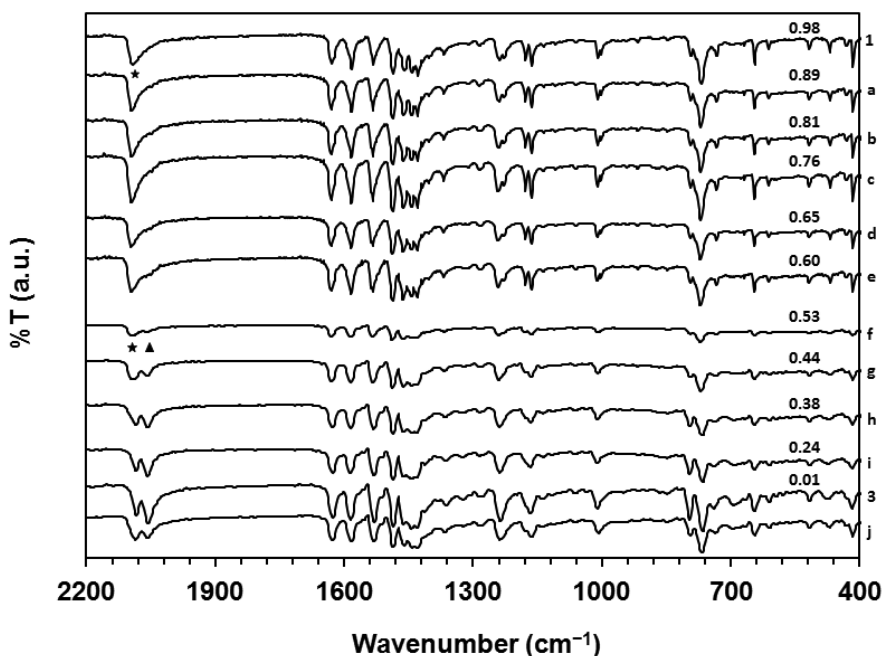


Figure 3.7. Infrared spectra of $[\text{Fe}_x\text{Zn}_{1-x}(\text{bapbpy})(\text{NCS})_2]$ (samples **(a)** to **(f)**), compound **1**, and compound **3**, in the 2200 to 400 cm^{-1} region. The iron fraction x is indicated for each spectrum. Sample **(j)** is a 1:1 physical mixture of the Fe-only (**1**) and the Zn-only (**3**) powdered compounds (see text). The symbols are indicating the significant changes in thiocyanate vibrations.

3.2.5. Single-crystal X-ray diffraction

Attempts were made to grow single crystals of $[\text{Fe}_x\text{Zn}_{1-x}(\text{bapbpy})(\text{NCS})_2]$ ($x = 0.99, 0.95, 0.90,$ and 0.50). Unfortunately no mixed crystals were obtained: when $x = 0.90$ single crystals were obtained, but single crystal X-ray diffraction was consistent with the published structure of $[\text{Fe}(\text{bapbpy})(\text{NCS})_2]$ (see Appendix I) and zinc could not be detected in the crystal lattice using X-ray diffraction or ICP. When the iron fraction was $x = 0.5$, two types of crystals were clearly formed: small colourless crystallites and red single crystals. The red crystals were found to be $[\text{Fe}(\text{bapbpy})(\text{NCS})_2]$ as well, with no detectable traces of Zn(II), whereas the colourless crystallites were too small for crystal structure determination. Although compound **1** crystallizes reproducibly from DMF/MeOH liquid-liquid diffusion,⁵ we were unable to obtain crystals of compound **3** under similar conditions. By changing the crystallization conditions, *i.e.*, using the slow vapour diffusion of diethyl ether into a DMF solution of compound **3** at room

temperature, single crystals (compound **4**) suitable for X-ray structure determination were obtained.

The asymmetric unit of compound **4** contains two crystallographically independent $[\text{Zn}(\text{bapbpy})\text{NCS}]^+$ cations, one $[\text{Zn}(\text{NCS})_4]^{2-}$ complex anion, and three uncoordinated DMF molecules. The $[\text{Zn}(\text{bapbpy})\text{NCS}]^+$ cations are almost perfectly aligned along the crystallographic *c* axis. The $\text{S1B}\cdots\text{Zn1}'$ and $\text{S1A}\cdots\text{Zn2}''$ intermolecular distances between two neighbouring $[\text{Zn}(\text{bapbpy})\text{NCS}]^+$ cations are 3.556(8) Å and 3.643(8) Å, respectively, which is significantly larger than the sum of the effective ionic radius of zinc(II) (0.74 Å)²⁰ and the van der Waals radius of the sulfur atom (1.80 Å). Therefore, there is no significant $\text{Zn}\cdots\text{S}$ intermolecular interactions, and the Zn1 and Zn2 centres from the $[\text{Zn}(\text{bapbpy})\text{NCS}]^+$ cations are penta-coordinated. The coordination sphere of each cation comprises the four N atoms of a bapbpy ligand in the equatorial plane and one nitrogen-bonded NCS^- ligand in the axial position. The Zn–N bond lengths (see Table 3.2) are consistent with those in other penta-coordinated zinc(II) centres found in the literature.²¹ The basal N–Zn–N coordination angles in $[\text{Zn}(\text{bapbpy})\text{NCS}]^+$ cation, which vary from 77.97(7)° to 101.56(7)° (Table 3.2), and the torsion angle $\text{N1A–N3A–N4A–N6A} = 25.61(8)^\circ$, are indicative of a distorted square pyramidal geometry. The third Zn(II) centre in the unit cell is coordinated by four thiocyanate ligands, thereby resulting in a distorted tetrahedral environment with N–Zn3–N angles that vary in the range 104.9°–115.4° (See Table 3.2), consistent with previously reported structure of this complex anion.^{22–24} Furthermore, as depicted in Figure 3.8 there are three non-equivalent DMF solvent molecules in the crystal lattice. One acts as a bifurcated hydrogen bond donor through O1, which is involved in two N–H \cdots O hydrogen bonding interactions with the N–H donor groups of the two crystallographically independent bapbpy ligands [$\text{N2B}\cdots\text{O1} = 2.943(4)$ Å, $\text{N2A}\cdots\text{O1} = 2.875(5)$ Å]. The other two DMF molecules are H-bonded in terminal mode *via* O2 and O3 with N5A–H5C and N5B–H5D , respectively, of the two crystallographically independent bapbpy ligands [$\text{N5A}\cdots\text{O2} = 2.794(3)$ Å, $\text{N5B}\cdots\text{O3} = 2.791(3)$ Å].

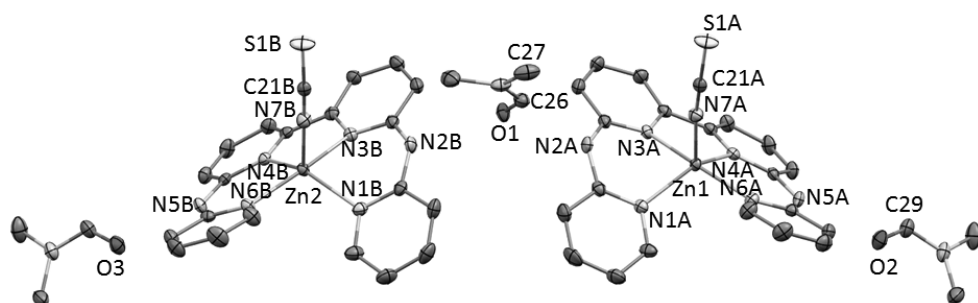


Figure 3.8. The hydrogen-bonded motif, for which the two crystallographically independent $[\text{Zn}(\text{babppy})(\text{NCS})]^+$ cations and the three independent DMF molecules are donors and acceptors, respectively. Hydrogen atoms and the disorder of the bifurcated DMF molecules (*i.e.*, O1) have been omitted for clarity.

Table 3.2. Relevant bond distances and angles (\AA , $^\circ$) for compound **4** at 110 K.

Bond distance (\AA)		Angles ($^\circ$)	
Zn1–N1A	2.079(2)	N6A–Zn1–N4A	88.92(7)
Zn1–N3A	2.087(2)	N4A–Zn1–N3A	77.97(7)
Zn1–N4A	2.095(2)	N3A–Zn1–N1A	85.07(7)
Zn1–N6A	2.069(2)	N1A–Zn1–N6A	101.56(7)
Zn1–N7A	1.998(2)	N7A–Zn1–N1A	103.12(8)
N2A \cdots O1	2.875(5)	N7A–Zn1–N3A	94.95(8)
N5A \cdots O2	2.794(3)	N7A–Zn1–N4A	118.68(8)
N2B \cdots O1	2.942(4)	N7A–Zn1–N6A	95.38(8)
S1B \cdots Zn1 $'$	3.556(8)	C21A–N7A–Zn1	173.70(2)
S1A \cdots Zn2 $''$	3.643(8)	N6A–N4A–N3A–N1A	-25.61(8)
Zn3–N8	1.948(3)	N10–Zn3–N9	111.9(1)
Zn3–N9	1.946(2)	N11–Zn3–N8	105.0(1)
Zn3–N10	1.947(2)	N8–Zn3–N9	115.4(2)
Zn3–N11	1.996(4)	N11–Zn3–N9	104.9(2)

Note: all distances and angles are given for Zn1 only, which those for Zn2 are similar. Symmetry operators: $' = -x, 1/2+y, 1/2-z$; $'' = x, 1/2-y, 1/2+z$

The powder pattern of compound **4** was calculated from the single crystal data using the program Mercury,²⁵ and it does not match with the experimental powder X-ray diffractogram of compound **3** (Figure AI.4). The major differences include: an intense singlet at $2\theta = 19^\circ$ for compound **3** (star) that is not present in **4**, and a doublet at $2\theta = 16^\circ$ in compound **4** that is not observed for compound **3** (circle). In addition, the chemical composition of the crystal of compound **4**, $[\text{Zn}(\text{bapbpy})(\text{NCS})_2][\text{Zn}(\text{NCS})_4] \cdot 3\text{DMF}$, does not correspond to the elemental analysis for compound **3**. Therefore, compound **3** (powder) and compound **4** (single crystal) must be considered as different materials. The presence of DMF in the crystal lattice of **4** certainly plays an important role during crystal growing, and the absence of DMF during the synthesis of compound **3** may explain, in part, why we were unable to grow crystals of this latter material. However, although single crystals of compound **3** could not be obtained, the crystal structure of compound **4** provided the important information that zinc(II) may favour a penta-coordinate geometry with the ligand set it is offered (bapbpy and two thiocyanates), whereas iron(II) prefers a hexa-coordinate geometry in $[\text{Fe}(\text{bapbpy})(\text{NCS})_2]$.

3.3. Discussion

As different preparation methods may lead to SCO compounds with different magnetic properties,⁹ any zinc-diluted sample should be prepared according to a known procedure, *i.e.*, a procedure that leads to a well-characterized iron-only SCO material. For $[\text{Fe}(\text{bapbpy})(\text{NCS})_2]$ we have developed two procedures: the first one, used in the present work, consists in the impregnation of the bapbpy methanolic suspension by a methanolic solution of the metal thiocyanate, which leads to the formation of a powder. The second method consists in growing single crystals by slow liquid-liquid diffusion of methanol into a solution of the iron compound in DMF. Thus far the latter technique remains unsuccessful at growing single crystals of the Zn-only compound or metal-diluted single crystals. Recrystallizing compound **3** in different conditions eventually allowed the growth of single crystals of compound **4**, which has different coordination geometries than those of the material ($[\text{Fe}(\text{bapbpy})(\text{NCS})_2] \cdot 2\text{DMF}$)⁹ obtained by recrystallization of compound **1** under the same conditions. Powder X-ray diffraction also showed evidence that compound **3** has different structural properties than those of compound **4** (see Appendix I).

As previously stated, zinc(II) was selected not only because of its diamagnetism and its similar size compared to iron(II), but also because of its ability to form hexa-coordinated complexes. However, in absence of a crystal structure of compound **3** it is not clear whether the zinc centre is in a hexa- or penta-coordinated environment for this material. The IR spectrum of **3** clearly shows two NCS⁻ vibrations at 2086 and 2053 cm⁻¹, indicating two different coordination environments for NCS⁻. By contrast, the highly symmetrical, hexa-coordinated HS iron(II) compound **1** shows only one single thiocyanate vibration at 2090 cm⁻¹. Powder X-ray diffraction indicates that the structures of **1** and **3** are different. X-ray structure determination of compound **4** suggests that the Zn(II) metal centres may favour a penta-coordinated geometry with the bapbpy ligand, rather than the hexa-coordinate geometry found with Fe(II). We hypothesize that this is the reason why the crystal structure of the diluted samples (**a**) to (**i**) changes at zinc content higher than 0.47, and why single crystals of the mixed-metal compounds could not be obtained.²⁶

Dilution studies have been realized on two-step SCO compounds²⁷ or one-step SCO compounds including hysteretic cycles.^{16, 28-30} To the best of our knowledge this report is the first metal dilution study on a two-step SCO Fe(II) system including two hysteresis loops. For compound **1**, cooperativity is mediated mainly *via* intermolecular N–H⋯S hydrogen-bonding networks.^{5, 31} With high iron fractions ($x = 1.00$ to $x = 0.53$) powder X-ray and infrared data of the mixed samples resemble those of compound **1**, and one may conclude that in these samples the zinc complex adopts the coordination geometry found in the HS iron(II) phase. In such a phase the transition between a two-step SCO and a one-step SCO occurs at $x = 0.76$. Magnetic susceptibility data show that upon further increasing the zinc concentration the cooperativity is further reduced to lead to a non-cooperative spin crossover at $x = 0.24$, with a lower transition temperature compared to $x = 0.76$.

These observations are mostly consistent with previously published dilution studies.^{11, 12, 29, 32} An exception is $T_{1/2}^2 \downarrow$, which increases dramatically between $x = 0.89$ and 0.76 ., leading to the quick disappearance of the IP at $x = 0.76$. This is a rare observation. Usually, the effects of metal dilution on the transition temperatures are based on two phenomena: (i) the average distance between neighbouring Fe(II) metal ions increases;³² (ii) the Zn(II) metal complexes interact with their analogous Fe(II) neighbours *via* intermolecular interactions that are similar to that between adjacent iron complexes. The first effect was first explained by J. P. Martin,³² and is based on

probability theory. To obtain a situation where an Fe(II) ion is far apart from another one with a probability of 0.9, the iron fraction x has to be as low as 0.03. Thus it is only at very low values of x that the Fe(II) ions may be considered as isolated. In this work, the lowest iron fraction was 0.24, therefore the first effect may be considered as negligible.

Regarding the second effect, the interactions between Fe(II) SCO centres and Zn(II) complexes have been explained by the influence of the sizes of the metal ions by Ganguli *et al*¹² and Hauser *et al*.³³ The ionic radius of the Zn(II) ion ($r = 0.74 \text{ \AA}$) is intermediate between that of the HS Fe(II) ion ($r = 0.78 \text{ \AA}$) and that of the LS Fe(II) ion ($r = 0.61 \text{ \AA}$). Thus, Fe(II) ions in the HS state are slightly larger than the Zn(II) ions, so that they feel in a zinc-diluted sample a “positive pressure” from their surroundings that stabilizes the LS state, *i.e.*, raises $T_{1/2}$ ↓. On the other hand, as LS Fe(II) ions are smaller than Zn(II) ions they feel a “negative pressure” in a zinc phase that tends to stabilize the HS state, *i.e.* decrease $T_{1/2}$ ↑. Thus the dilution effect tends to make hysteresis cycles thinner. This “chemical pressure” effect is less important when the Fe(II) HS ions are highly diluted, as illustrated in Figure 3.5: the steepness of the SCO transition temperature *vs.* x slope is lower in the region in which SCO is one-step relative to the region in which SCO is two-step.

The observation that no significant HS residual fractions remain at low temperatures is worth noticing, as it has been observed in a number of dilution studies that considerable residual HS fractions may remain in diluted samples at low temperatures.^{16, 28} Residual HS fractions at low temperatures typically occur in amorphous media or poorly crystallized systems,¹⁶ but recently Létard *et al* provided another possible explanation that is consistent with our experimental results. In fact these authors support the idea that when the temperature limit for information storage after light irradiation, known as T_{LIESST} ,^{14, 28} is higher than $T_{1/2}$, then the relaxation of the HS state becomes slow at temperatures lower than $T_{1/2}$, which leads to high residual HS fraction upon cooling.^{34, 35} In the case of the present study, for all diluted samples $[\text{Fe}_x\text{Zn}_{1-x}(\text{bapbpy})(\text{NCS})_2]$ the transition temperatures $T_{1/2}$ remain higher than 150 K. In comparison, the T_{LIESST} of compound **1** is 56 K,^{9, 36} and on the basis of previous work²⁸ the T_{LIESST} of the metal-diluted samples is expected to be close to that recorded for **1**. Thus, all transition temperatures $T_{1/2}$ of the zinc-diluted samples (**a**) to (**i**) are significantly higher than their expected T_{LIESST} . As a consequence, thermal relaxation of

the HS state to the LS state is fast compared to the cooling rates used in magnetic susceptibility measurements, which avoided residual HS fractions at low temperatures.

3.4. Conclusion

The present study addresses for the first time the effects of zinc dilution on a mononuclear two-step SCO compound with two hysteresis cycles. The unknown zinc analogue of compound **1**, compound **3**, was synthesized and characterized to have a different crystallographic structure than **1**. Although the crystal structure of **3** could not be obtained we hypothesize from that of compound **4** and from IR spectroscopy data that the coordination environment of Zn(II) in **3** may not be similar to that of Fe(II) in **1**, but that the zinc ions may prefer a penta-coordinated environment. The study of the diluted samples was completed using powder samples. According to powder X-ray diffraction, magnetic susceptibility measurements, and infrared spectroscopy data, it appears that in the zinc-diluted samples containing a majority of iron ($x > 0.53$) the phase of the iron compound is retained. At higher dilutions, the phase of the zinc compound **3** is gradually taking over, but the SCO of the iron compound remains observable at an iron fraction as low as $x = 0.24$, for which powder X-ray diffraction indicates no sign of the iron structure. Meanwhile, magnetic susceptibility measurements reveal that upon decreasing the iron fraction x , both hysteresis cycles become initially narrower, and then vanish at $x = 0.76$, to lead to a single-step SCO material with some degree of cooperativity. Upon further increase of the zinc contents, the cooperativity gradually vanishes to lead to a fully non-cooperative SCO material at the lowest iron fraction studied ($x = 0.24$). Despite the different coordination of the Fe(II) and Zn(II) bapbpy complexes the spin crossover of the hexa-coordinated Fe(II) complex is robust enough to withstand dilution into a magnetically silent Zn(II) phase that is structurally different from that of the iron compound. In the future it would be interesting to study dilution effects on $[\text{Fe}(\text{bapbpy})(\text{NCS})_2]$ with metals known to adopt an octahedral geometry, such as Ni(II). In the ideal case, the supramolecular hydrogen bonding network should not be modified by the diluting metal, which would, for example, allow us to study the LIESST effect at high dilutions.

3.5. Experimental

3.5.1. General information

Metal composition analysis was determined on a VARIAN VISTA MPX Inductively Coupled Plasma Optical Emission spectrometer (ICP-OES). For each product two different samples were individually measured, and only the average value is given. Elemental analysis was performed by Kolbe Mikroanalytisches Laboratorium, Mülheim an der Ruhr, Germany. Infrared spectra were measured on a Perkin Elmer PARAGON 1000 FT-IR spectrometer equipped with a diamond ATR device. X-ray powder diffraction data were collected on a Philips X'Pert PRO diffractometer equipped with the X'celerator using Cu-K α radiation. Magnetic susceptibility measurements were performed on samples of 6.30, 7.30, 5.96, 5.65, 6.87, 6.04, 12.26, 13.97, 14.30, and 14.72 mg of powder {for [Fe(bapbpy)(NCS) $_2$], and samples **(a)**-**(i)**, respectively}. Each sample was inserted in a plastic straw before introduction in a Quantum Design MPMS-XL SQUID magnetometer. DC magnetization measurements were performed in a field of 0.5 T, from 300 to 3 K (cooling mode) and from 3 to 300 K (heating mode). The total measuring time for each sample was 20 h. Corrections for the diamagnetism of the sample were calculated using Pascal's constants.³⁷

3.5.2. Sample preparation

Bapbpy and complex [Fe(bapbpy)(NCS) $_2$] (powder) **(1)** were prepared according to a literature procedure.⁵ Fe:Zn composition for [Fe(bapbpy)(NCS) $_2$] was found to be 98:2 by ICP-OES.

Zn(bapbpy)(NCS) $_2$ (3): A suspension of bapbpy (100 mg, 294 μ mol) in MeOH (7 mL) was prepared and stirred at 400 r.p.m. at room temperature. A 0.1 M solution of [Zn(NCS) $_2$] prepared by the Kahn method¹⁸ (3.00 mL, 300 μ mol,) was added to the suspension; the vial was stoppered and stirred for 16 h at room temperature. The yellow solid was filtered over Micropore membrane filter (RC 55, pore \varnothing 0.45 μ m), washed with MeOH (3 \times 10 mL), and dried under vacuum ($P \approx 10^{-2}$ torr) for 3 h to yield 122 mg of the product (80%). ^1H NMR (300 MHz, δ in ppm in DMF- d^7 , 300 K): 11.34 (s, 2H, N-H), 8.27 (d, 4H, 3.6 Hz), 8.17 (t, 2H, 7.5 Hz), 8.10 (d, 2H, 4.9 Hz), 7.55 (m, 4H), 7.34 (t, 2H, 6.1 Hz). ^1H NMR (300 MHz, δ in ppm in DMSO- d^6 , 300 K): 11.07 (s, 2H, N-H), 8.31–8.00 (m, 6H), 7.89 (s, 2H), 7.41 (t, 4H, 8.7 Hz), 7.27 (d, 2H, 8.6 Hz). ^{13}C NMR (600 MHz, δ in ppm in DMF- d^7 , 300 K): 155.96, 155.34, 147.74, 147.32, 143.28, 142.70, 134.78 (NCS $^-$), 119.35, 117.35, 117.13, 116.40. IR (cm^{-1}): 3278, 3192, 3103, 2086 (NCS $^-$), 2053 (NCS $^-$), 1626, 1585, 1532, 1486,

1461, 1447, 1433, 1362, 1324, 1277, 1239, 1178, 1167, 1137, 1062, 1013, 1004, 850, 797, 765, 691, 646, 613, 515, 418, 342. ES-MS in DMF m/z (calc): 534.73 (535.10, $[M-NCS+DMF]^+$), 461.68 (462.05, $[M-NCS]^+$). Fe:Zn composition found by ICP-OES: 1:99. Elemental analysis calcd (%) for $C_{22}H_{16}ZnN_8S_2$: C 50.62, H 3.09, N 21.48, S 12.26; found: C 50.46, H 3.28, N 21.23, S 11.29.

$[Fe_xZn_{1-x}(bapbpy)(NCS)_2]$ [samples (a) to (i)]: 0.1 M solutions of $[M(NCS)_2]$ ($M = Fe$ or Zn) were prepared as follows: Solution A: $FeSO_4 \cdot 7H_2O$ (1.38 g, 5.00 mmol), KNCS (972 mg, 10.0 mmol) and ascorbic acid (20 mg) were stirred in MeOH (40 mL) for 30 minutes. The suspension was filtered on a P4 frit; the solid was washed twice with MeOH (4 mL); the combined filtrates were transferred to a volumetric flask and the volume adjusted to 50.0 mL with MeOH. Solution A was used directly after preparation, as it turns purple by aerial oxidation within one hour. Solution B: $ZnSO_4 \cdot 7H_2O$ (2.87 g, 10.0 mmol) and KSCN (1.94 g, 20.0 mmol) were stirred in MeOH (80 mL) for 30 minutes. The suspension was filtered on a P4 frit; the solid was washed twice with MeOH (8 mL); the combined filtrates were transferred to a volumetric flask and the volume adjusted to 100.0 mL with MeOH.

Preparation of sample (a) to (i): the bapbpy ligand (20.0 mg, 59.0 μ mol) was weighed in 9 different vials (a) \rightarrow (i) each containing a small stirring bar. MeOH (4.0 mL) was added in each vial, and the resulting yellow suspension was stirred at 300 r.p.m for 10 min. Decreasing amounts of solution A ($[Fe(NCS)_2]$, $V = 540, 480, 420, 360, 300, 240, 180, 120,$ and 60μ L, respectively) and increasing volumes of solution B ($[Zn(NCS)_2]$, $V = 60, 120, 180, 240, 300, 360, 420, 480,$ and 540μ L, respectively) were added to vials (a) to (i) while stirring at room temperature. The total metal content was 60 μ mol, and the theoretical Fe:Zn ratio for samples (a) to (i) was 90:10, 80:20, ..., 20:80, and 10:90, respectively. All the vials were closed with a plastic cap and the 9 solutions were stirred at room temperature for 16 hrs. The suspension in each vial was filtered over Micropore membrane filter (RC 55, pore \varnothing 0.45 μ m), washed with MeOH (3×2 mL), and dried under vacuum ($P \approx 10^{-2}$ torr) for 3 hrs to yield the 9 samples (a) to (i). Yields: 22, 21, 21, 20, 18, 19, 18, 17, 19 mg, respectively. Characterization was performed using elemental analysis (ICP-OES), IR spectroscopy, powder X-ray diffraction, and magnetic susceptibility measurements.

Sample preparation for metal trace analysis (ICP-OES): 1-3 mg of the powder was precisely weighed in a 10.0 mL volumetric flask and dissolved in a concentrated nitric acid (extra pure, > 62% from Acros Organics). 1.0 mL of this solution and 4.0 mL of nitric acid were pipette-transferred into a 100 mL volumetric flask, the volume of the solution was completed to 100 mL with MilliQ water, the solution homogenized (final concentrations in $HNO_3 \approx 3\%$, total metal concentration ≈ 200 -700 ppb) and introduced in the spectrometer

for measurement. Fe:Zn compositions for **(a)** to **(i)** found by ICP-OES: 89:11, 81:19, 76:24, 65:35, 60:40, 53:47, 44:56, 38:62, 24:76, respectively.

Sample (j): the powder of compound **1** (5.00 mg, 9.80 μmol) and compound **3** (5.10 mg, 9.80 μmol) were added together in a small glass vial and mixed with a spatula. IR (cm^{-1}): 3278, 3192, 3110, 2086 (NCS^-), 2060 (NCS^-), 1627, 1584, 1532, 1487, 1462, 1445, 1430, 1367, 1324, 1286, 1238, 1178, 1164, 1137, 1062, 1010, 916, 849, 795, 768, 734, 679, 645, 613, 516, 470, 430, 417, 342, 323.

[Zn(bapbpy)(NCS)]₂[(Zn(NCS)₄)]·3DMF (4**):** Single crystals were grown by slow diffusion of diethyl ether vapour into a DMF solution of compound **3** (5.5 mg in 1 mL DMF). Yellowish plate-like crystals were obtained. Crystal data: Fw = 1444.65, pale yellow plate, $0.52 \times 0.37 \times 0.05 \text{ mm}^3$, monoclinic, $P2_1/c$ (no. 14), $a = 11.8288(3)$, $b = 33.5181(7)$, $c = 16.7009(4) \text{ \AA}$, $\beta = 110.287(3)^\circ$, $V = 6210.8(3) \text{ \AA}^3$, $Z = 4$, $D_x = 1.545 \text{ g cm}^{-3}$, $\mu = 1.413 \text{ mm}^{-1}$, abs. corr. range: 0.612–0.929. 42120 Reflections were measured up to a resolution of $(\sin \theta/\lambda)_{\text{max}} = 0.62 \text{ \AA}^{-1}$. 12231 Reflections were unique ($R_{\text{int}} = 0.0260$), of which 9970 were observed [$I > 2\sigma(I)$]. 863 Parameters were refined with 182 restraints. $R1/wR2$ [$I > 2\sigma(I)$]: 0.0344/0.0827. $R1/wR2$ [all refl.]: 0.0459/0.0871. $S = 1.021$. Residual electron density found between -0.55 and 0.78 e \AA^{-3} . IR (cm^{-1}): 3278, 3195, 2988, 2086 (NCS^-), 2059 (NCS^-), 1668, 1662, 1652, 1646, 1634, 1628, 1585, 1539, 1532, 1489, 1472, 1464, 1448, 1435, 1386, 1286, 1241, 1168, 1118, 1062, 1012, 797, 772, 668, 646, 612, 516, 488, 429, 418, 344, 314. No CHN analysis was obtained due to the limited amount.

3.6. References:

1. P. Gütllich and H. A. Goodwin, *Top. Curr. Chem.*, 2004, 233, 1-47.
2. A. Bousseksou, G. Molnar, L. Salmon and W. Nicolazzi, *Chem. Soc. Rev.*, 2011, 40, 3313-3335.
3. O. Kahn and C. J. Martinez, *Science*, 1998, 279, 44-48.
4. P. Gamez, J. Sanchez Costa, M. Quesada and G. Aromi, *Dalton Trans.*, 2009, 7845-7853.
5. S. Bonnet, M. A. Siegler, J. S. Costa, G. Molnar, A. Bousseksou, A. L. Spek, P. Gamez and J. Reedijk, *Chem. Commun.*, 2008, 5619-5621.
6. M. Kepenekian, B. Le Guennic and V. Robert, *Phys. Rev. B*, 2009, 79.
7. H. J. Shepherd, S. Bonnet, P. Guionneau, S. Bedoui, G. Garbarino, W. Nicolazzi, A. Bousseksou and G. Molnar, *Phys. Rev. B*, 2011, 84.
8. G. A. Craig, J. S. Costa, O. Roubeau, S. J. Teat and G. Aromi, *Chem. Eur. J.*, 2012, 18, 11703-11715.
9. S. Bonnet, G. Molnar, J. S. Costa, M. A. Siegler, A. L. Spek, A. Bousseksou, W.-T. Fu, P. Gamez and J. Reedijk, *Chem. Mater.*, 2009, 21, 1123-1136.
10. P. Gütllich, A. Hauser and H. Spiering, *Angew. Chem. Int. Ed.*, 1994, 33, 2024-2054.
11. M. Sorai, J. Ensling and P. Gütllich, *Chem. Phys.*, 1976, 18, 199-209.
12. P. Ganguli, P. Gütllich and E. W. Muller, *Inorg. Chem.*, 1982, 21, 3429-3433.

-
13. F. Renz, H. Oshio, V. Ksenofontov, M. Waldeck, H. Spiering and P. Gütllich, *Angew. Chem. Int. Ed.*, 2000, 39, 3699-3700.
 14. C. Balde, C. Desplanches, A. Wattiaux, P. Guionneau, P. Gütllich and J.-F. Létard, *Dalton Trans.*, 2008, 2702-2707.
 15. C. Balde, C. Desplanches, M. Grunert, Y. L. Wei, P. Gütllich and J. F. Létard, *Eur. J. Inorg. Chem.*, 2008, 5382-5389.
 16. I. Krivokapic, P. Chakraborty, C. Enachescu, R. Bronisz and A. Hauser, *Inorg. Chem.*, 2011, 50, 1856-1861.
 17. I. Sanner, E. Meissner, H. Koppen, H. Spiering and P. Gütllich, *Chem. Phys.*, 1984, 86, 227-233.
 18. H. Daubric, C. Cantin, C. Thomas, J. Kliava, J. F. Letard and O. Kahn, *Chem. Phys.*, 1999, 244, 75-88.
 19. H.-O. Kalinowski, *Carbon-13 NMR spectroscopy*, John Wiley & Sons Ltd., 1988.
 20. R. D. Shannon, *Acta Crystallogr., Sect. A*, 1976, 32, 751-767.
 21. M. Liu and S. K. Arora, *Acta Crystallogr., Sect. C*, 1993, 49, 372-374.
 22. S. Chattopadhyay, K. Bhar, S. Das, S. Chantrapromma, H.-K. Fun and B. K. Ghosh, *J. Mol. Struct.*, 2010, 967, 112-118.
 23. M. Alexiou, E. Katsoulakou, C. Dendrinou-Samara, C. P. Raptopoulou, V. Psycharis, E. Manessi-Zoupa, S. P. Perlepes and D. P. Kessissoglou, *Eur. J. Inorg. Chem.*, 2005, 1964-1978.
 24. O. V. Pryma, S. R. Petrusenko, V. N. Kokozay, B. W. Skelton, O. V. Shishkin and T. S. Teplytska, *Eur. J. Inorg. Chem.*, 2003, 1426-1432.
 25. C. F. Macrae, I. J. Bruno, J. A. Chisholm, P. R. Edgington, P. McCabe, E. Pidcock, L. Rodriguez-Monge, R. Taylor, J. van de Streek and P. A. Wood, *J. Appl. Crystallogr.*, 2008, 41, 466-470.
 26. *The notation $[\text{Fe}_x\text{Zn}_{1-x}(\text{bapbpy})(\text{NCS})_2]$ assumes that the zinc centre is in the same phase as the iron centre, which is only true when $x > 0.53$. This notation is incorrect for $x < 0.53$, but we use it for all Fe:Zn ratios for commodity reasons.*
 27. C. P. Kohler, R. Jakobi, E. Meissner, L. Wiehl, H. Spiering and P. Gütllich, *J. Phys. Chem. Solids*, 1990, 51, 239-247.
 28. C. Balde, C. Desplanches, P. Gütllich, E. Freysz and J. F. Létard, *Inorg. Chim. Acta*, 2008, 361, 3529-3533.
 29. A. Rotaru, M. M. Dirtu, C. Enachescu, R. Tanasa, J. Linares, A. Stancu and Y. Garcia, *Polyhedron*, 2009, 28, 2531-2536.
 30. J. P. Martin, J. Zarembowitch, A. Bousseksou, A. Dworkin, J. G. Haasnoot and F. Varret, *Inorg. Chem.*, 1994, 33, 6325-6333.
 31. Z. Arcis-Castillo, S. Zheng, M. A. Siegler, O. Roubeau, S. Bedoui and S. Bonnet, *Chem. Eur. J.*, 2011, 17, 14826-14836.
 32. J. P. Martin, J. Zarembowitch, A. Dworkin, J. G. Haasnoot and E. Codjovi, *Inorg. Chem.*, 1994, 33, 2617-2623.
 33. A. Hauser, P. Gütllich and H. Spiering, *Inorg. Chem.*, 1986, 25, 4245-4248.
 34. P. Chakraborty, C. Enachescu, C. Walder, R. Bronisz and A. Hauser, *Inorg. Chem.*, 2012, 51, 9714-9722.
 35. N. Paradis, G. Chastanet and J.-F. Létard, *Eur. J. Inorg. Chem.*, 2012, 2012, 3618-3624.
 36. S. Pillet, E.-E. Bendeif, S. Bonnet, H. J. Shepherd and P. Guionneau, *Phys. Rev. B*, 2012, 86, 4106-4106.
 37. G. A. Bain and J. F. Berry, *J. Chem. Educ.*, 2008, 85, 532.

4



Influence of selenocyanate ligands on the transition temperature and cooperativity of bapbpy-based Fe(II) spin-crossover compounds

Abstract

Coordination of the ligand bapbpy (**1**) or of one of its derivatives (**2-8**) to $\text{Fe}(\text{NCSe})_2$ afforded eight new iron(II) compounds of the type $[\text{Fe}(\text{R}_2\text{bapbpy})(\text{NCSe})_2]$ (**9-16**). Compounds **11**, **13**, and **16** were structurally characterized by single crystal X-ray diffraction. The crystal structures of these compounds revealed packing and intermolecular interactions similar to their thiocyanate analogues. Magnetic susceptibility measurements were carried out for all iron compounds and revealed thermal spin-crossover (SCO) behaviour for compounds **9**, **11**, **13**, **15** and **16**. Compounds **11**, **13**, **15** and **16**, indeed show the expected increase in the transition temperature $T_{1/2}$ of the SCO upon replacement of NCS^- by NCSe^- . Compound **9**, however, shows a gradual, one-step SCO revealing a much lower cooperativity than that of the two-step SCO compound $[\text{Fe}(\text{bapbpy})(\text{NCS})_2]$. Heat capacity measurements were carried out for compounds **9**, **11**, **13**, **15** and **16**, and were fitted to the Sorai domain model. The number n of like-spin SCO centres per interacting domain, which is related to the cooperativity of the spin transition, was found to be high for compounds **11** and **15**, and low for compounds **9**, **11** and **13**. Altogether, X-ray, DSC, and magnetic data give a consistent structure-property relationship: hydrogen-bonding networks made of intermolecular $\text{N}-\text{H}\cdots\text{Se}$ interactions are vital for the cooperativity of $[\text{Fe}(\text{L})(\text{NCSe})_2]$ SCO compounds ($\text{L} = \text{bapbpy}$ and derivatives).

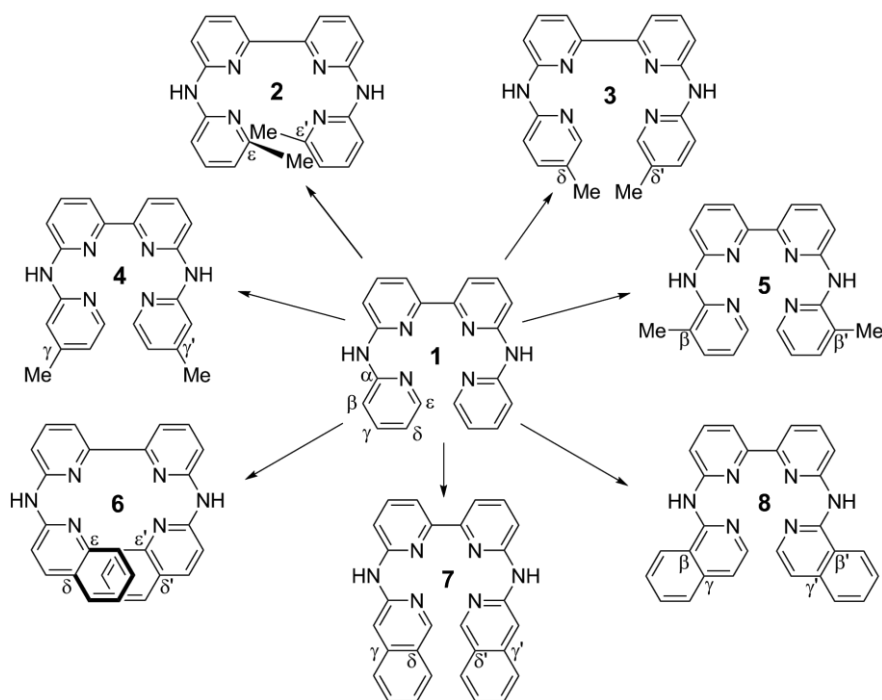
4.1. Introduction

There is a large scientific and technological interest in finding new molecular switches, as they might be used in the building of nano-sized gas sensors,^{1, 2} temperature sensors,³ electronic information processing devices, and data storage devices.^{4, 5} Spin-crossover (SCO) iron(II) complexes are typical prototypes of molecular switches,^{6, 7} as they transit between the low spin (LS) and high spin (HS) states upon temperature or pressure variations, upon light irradiation, or under the influence of strong magnetic or electric fields.⁸ Next to the temperature at which the SCO occurs, the cooperativity of the transition is an important aspect of SCO that is the result of short- and long-range intermolecular interactions in the crystal lattice. However, it still remains very challenging to design SCO materials featuring predefined properties, *e.g.*, with cooperative SCO transitions occurring near room temperature.

The thermal SCO phenomenon is usually rationalized within the frame of the ligand field theory.⁹ In this model a better ligand set around the metal ion generates a higher ligand field splitting (hereafter, LFS), as a result of which the LS state should be favoured and hence the transition temperature $T_{1/2}$ of the SCO compound should be higher. Within the widely used series of cyanate-derived ligands NCX^- ($\text{X}=\text{O}, \text{S}, \text{Se}$) selenocyanate ligands must increase the LFS compared to thiocyanates because the less electronegative selenium atom removes less electron density from the nitrogen atom than sulfur, thus resulting in a stronger ligand field for N-bound metal complexes. Consistently, from the first studies on the classical systems $[\text{Fe}(\text{L})_2(\text{NCX})_2]$ (where L = phen or 2,2'-bipy and $\text{X} = \text{S}, \text{Se}$),¹⁰⁻¹² to the more recent examples based on the 1,2,4-triazole ligand,^{13, 14} it has been shown that with the increase of the LFS along the NCX^- spectrochemical series, the $T_{1/2}$ indeed shifts towards higher temperatures. However, in these examples the effect on cooperativity has not been rationalized due to either single crystal structures that were not always available or to the involvement of solvent molecules in the crystal lattice, which led to a lack of information on changes in supramolecular interactions involving the Se vs. S atom replacement.

Recently we reported the two-step mononuclear SCO compound $[\text{Fe}(\text{bapbpy})(\text{NCS})_2]$ ¹⁵ (bapbpy = *N,N'*-di(pyrid-2-yl)-2,2'-bipyridine-6,6'-diamine, **1** in Scheme 4.1) and its derivatives $[\text{Fe}(\text{R}_2\text{bapbpy})(\text{NCS})_2]$ (Chapter 2). The crystal structures available for this family of compounds show the central role of the thiocyanate sulfur atom for the cooperativity of the SCO, which relies on strong intermolecular N–H \cdots S hydrogen

bonding interactions. This central role opened a unique opportunity to systematically study the influence of exchanging S by Se on the cooperativity in this family of compounds. Modifying the chemical structure of the ligands $R_2\text{bapbpy}$ in $[\text{Fe}(R_2\text{bapbpy})(\text{NCS})_2]$ allowed for increasing the transition temperature of the SCO near to room temperature, but at the cost of cooperativity (Chapter 2).¹⁶ Designing SCO materials is notoriously difficult and minor chemical changes of the ligands lead, *via* small differences in the crystal lattice of the iron complex, to significant changes in the SCO properties. We considered replacing the NCS^- ligands in $[\text{Fe}(R_2\text{bapbpy})(\text{NCS})_2]$ complexes by NCSe^- , to increase the LFS while hopefully maintaining the overall crystal packing. Last but not least, with new SCO compounds added to the $[\text{Fe}(R_2\text{bapbpy})(\text{NCX})_2]$ family we intend to deepen our understanding of the structure-function relationship for bapbpy-based iron(II) compounds, which may represent one step further towards the “rational design” of mononuclear SCO compounds.



Scheme 4.1. Ligand bapbpy **1** and its derivatives **2-8**.

4.2. Results

4.2.1. Synthesis of the complexes

The ligand bapbpy (**1**) and seven derivatives **2-8** were synthesized by palladium-catalyzed Buchward-Hartwig cross-coupling between 6,6'-dibromo-2,2'-bipyridines and different arylamines (see Chapter 2).^{15, 16} Coordination of these ligands to iron(II) selenocyanate was achieved using three different methods, hereafter called methods **a-c**. Method **a** has been previously described (see Chapter 2 and reference 15) and consists in impregnating a methanolic suspension of the ligand by a methanol solution of $\text{Fe}(\text{NCSe})_2$. The advantage of this method is that the materials are obtained in high yields (> 80%). Its disadvantage is that the materials may contain variable amounts of the free ligand, as indicated by the inconsistency between the calculated and experimental values found by elemental analyses. In method **b** the ligand was first dissolved in DMF, before addition of 1.1 eq. of $\text{Fe}(\text{NCSe})_2$ as a methanolic solution without stirring. Because the metal compounds are poorly soluble in pure methanol, their solubility is lowered as methanol slowly diffuses into the DMF solution, leading to precipitation of the complexes. This method usually results in a higher chemical purity compared to method **a**, unless the starting ligand is poorly soluble in DMF. Finally, method **c** is similar to method **b**, but methanol diffusion is slowed down to obtain single crystals of the iron compounds, whereas both methods **a** and **b** produce polycrystalline powders. In this work, compounds **9a-16a** were synthesized *via* method **a**, and compounds **9b**, **11b**, **13b**, **15b** were synthesized by method **b**. Compounds **10b**, **12b**, **14b** and **16b** could not be obtained due to the low solubility or rapid precipitation of the ligands **2**, **4**, **6** and **8** in DMF, respectively. Finally, three ligands led to the formation of single crystals of **11c**, **13c** and **16c** suitable for X-ray diffraction.

All new materials were analyzed with IR spectroscopy and mass spectrometry. The expected $[\text{Fe}(\text{R}_2\text{bapbpy})(\text{NCSe})]^+$ monocationic peak was found by electron-spray mass spectrometry (calculated at m/z 502 for **9**, 530 for **10-13**, and 602 for **14-16**; see Table 4.1), which confirmed coordination of the ligands to Fe(II). Consistently, the IR spectra of the thirteen solids showed the characteristic stretching vibrations of the coordinated selenocyanate ligands in the range 2060 to 2100 cm^{-1} (Table 4.1). For compounds **9a**, **11a**, **11b**, **13a**, **13b**, **16a** and **16c**, another NCSe^- stretching vibration was observed in the range 2052 to 2074 cm^{-1} . It is worth noticing that **9b** shows an intense absorption band at 1661 cm^{-1} , which is not present in the infrared spectrum of

9a. This absorption band is most likely due to the presence of DMF molecules in the crystal lattice of **9b**. Elemental analyses indeed account for two DMF molecules per iron complex in the crystal lattice of **9b**, whereas compounds **11b**, **13b**, and **15b** do not have any lattice solvent molecule.

Table 4.1. Numbering, formulae, infrared selenocyanate stretching vibrations, and HR-MS $[\text{Fe}(\text{R}_2\text{bapbpy})(\text{NCSe})]^+$ monocationic peak, for compounds **9-16**.

Compound/Method	Formula	NCSe ⁻ vibrations (cm ⁻¹)	<i>m/z</i>
9a	<i>trans</i> -[Fe(1)(NCSe) ₂]	2090, 2057	501.9978
9b	<i>trans</i> -[Fe(1)(NCSe) ₂] \cdot 2DMF	2067	501.9973
10a	<i>trans</i> -[Fe(2)(NCSe) ₂]	2057	530.0288
11a	<i>trans</i> -[Fe(3)(NCSe) ₂]	2094, 2060	530.1 ^a
11b	<i>trans</i> -[Fe(3)(NCSe) ₂]	2093, 2052	530.0290
12a	<i>trans</i> -[Fe(4)(NCSe) ₂]	2080	530.1 ^a
13a	<i>trans</i> -[Fe(5)(NCSe) ₂]	2100, 2070	530.0282
13b	<i>trans</i> -[Fe(5)(NCSe) ₂]	2100, 2066	530.0294
14a	<i>trans</i> -[Fe(6)(NCSe) ₂]	2078	602.1 ^a
15a	<i>trans</i> -[Fe(7)(NCSe) ₂]	2061	602.0287
15b	<i>trans</i> -[Fe(7)(NCSe) ₂]	2060	602.0286
16a	<i>trans</i> -[Fe(8)(NCSe) ₂]	2108, 2072	602.0290

^a Measured by standard ESI-MS.

4.2.2. Single crystal and powder X-ray diffraction studies

Single crystals of compounds **11**, **13** and **16** suitable for X-ray structure determination were obtained *via* method **c**. A mixture of dark orange and dark red crystals was obtained for compound **11**. X-ray structure determination showed that the dark red crystals are solvent free (compound **11c**), whereas the dark orange crystals (compound **11c'**) contain one methanol molecule per iron complex. When crystals of **11c** were flash cooled to 110 K, crystal damage occurred that was too significant to collect a full data set, most likely due to a phase transition occurring between 200 and 110 K. Thus, the structure of **11c** was determined at 200 K only. The structure of the solvated compound $[\text{Fe}(\mathbf{3})(\text{NCSe})_2]\cdot\text{MeOH}$ (**11c'**) could be determined at 110 K as no crystal damage occurred upon cooling. Dark red and almost black single crystals of

compounds **13c** and **16c**, respectively, were also obtained. X-ray structure determination showed that the crystal lattices of both **13c** and **16c** are solvent free. The structure of **13c** was determined both at 110 and 300 K since no significant loss of crystallinity occurred upon cooling. The structure of **16c** was only determined at 110 K, since the temperature of the HS state is too high for collecting data with the temperature controller that was used for single crystal X-ray crystallography. The crystal structures of **11c**, **11c'**, **13c** and **16c** are shown in Figure 4.1. In all cases, the tetradentate R₂babppy ligand was found coordinated to iron(II) in the basal plane, leaving the two selenocyanate ligands in *trans* positions of the octahedron (Figure 4.1). Selected bond lengths and angles are provided in Table 4.2.

Compounds **11c** and **11c'** crystallized in the triclinic space group *P*-1 at 200 K and 110 K, respectively. For **11c**, the average Fe–N bond length is *ca.* 2.16 Å, which is typical of an HS Fe(II) complex in an FeN₆ octahedral environment. The *cis* N–Fe1–N basal coordination angles vary from 77.15(7)° to 115.48(7)° (Table 4.2), which together with the torsion angle [N1–N3–N4–N6 = 23.52(8)°] is indicative of a strong distortion of the octahedral geometry. For the solvated compound **11c'**, the average Fe–N bond length is found to be 2.13 Å, which is slightly shorter than that found in **11c** but still suggests an HS Fe(II) complex. The *cis* N–Fe1–N angles in the basal plane of the ligand babppy lies between 77.51(7)° and 113.04(7)° (Table 4.2), which is comparable to the molecular conformation found for the solvent-free compound **11c**. In the structure of the solvated compound **11c'** the solvent molecules are H-bonded as acceptor to the NH bridges of the R₂babppy ligand *via* N–H⋯O hydrogen bond [N⋯O = 2.863(3) Å], and act as donors to a neighbouring NCS[–] ligand in an intermolecular O–H⋯Se interaction [O⋯Se = 3.338(3) Å] (Figure AII.1, Appendix II).

The compounds **13c** and **16c** crystallized in the centrosymmetric *C*2/*c* space group, and the iron complexes are found at two fold rotation axes. For compound **13c**, the average Fe–N bond length was found to be 1.96 Å at 102(2) K, which is typical of an LS Fe(II) complex in an FeN₆ octahedral environment. At 300(2) K, the average Fe–N bond length for **13c** was found to be 2.13 Å, which indicates an HS state. For compound **16c**, the average Fe–N bond length is 1.97 Å at 110(2) K, which suggests an LS Fe(II) complex in an FeN₆ octahedral environment. Furthermore, the *cis* N–Fe1–N basal coordination angles of **13c** and **16c** are very similar in their LS state (Table 4.2). In summary, the crystal structures of compounds **13c** and **16c** are very similar to each

other, but also with the one observed for the compound $[\text{Fe}(\text{bapbpy})(\text{NCS})_2]$.¹⁵ In contrast the crystal structures of **11c** and **11c'** have a more distorted octahedron.

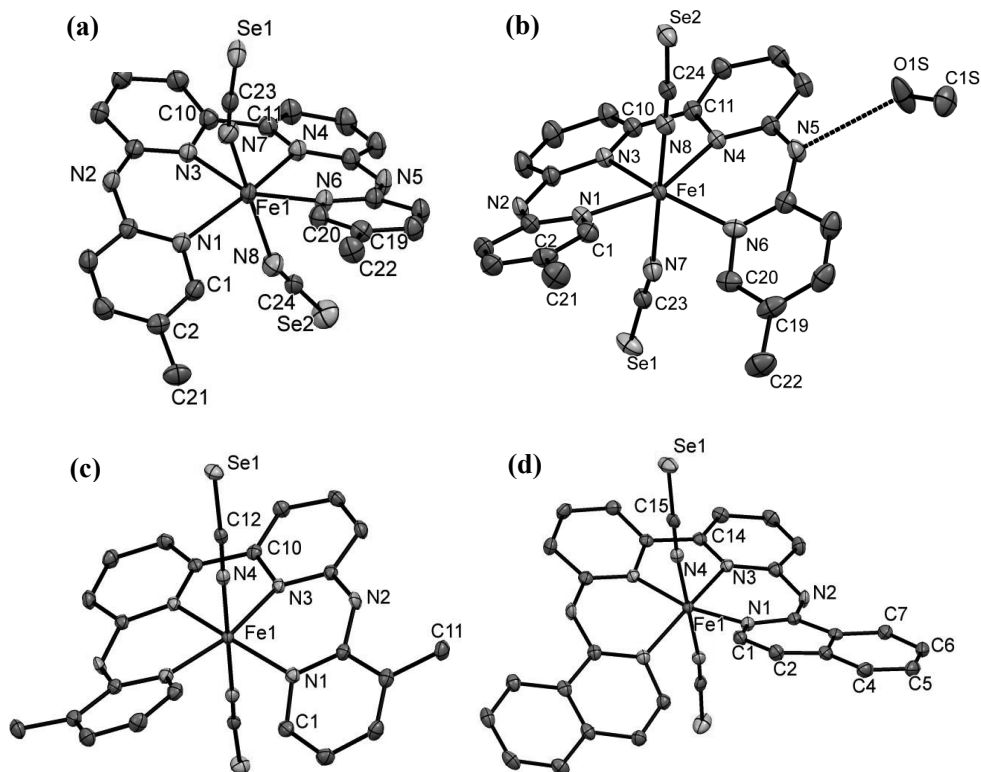


Figure 4.1. Displacement ellipsoid plots (50% probability level) (a) for compound **11c** at 200(2) K (HS phase), (b) for **11c'** at 110(2) K (HS phase), (c) for compound **13c** at 102(2) K (LS phase), (d) for compound **16c** at 110(2) K (LS phase). Hydrogen atoms were omitted for clarity. Selected atom labelling is only shown for crystallographically independent atoms.

The crystal packing of compounds **11c**, **13c**, and **16c** are characterized by two sets of supramolecular interactions as shown in Figure 4.2. The first set includes N–H \cdots Se intermolecular interactions between two adjacent iron complexes along the crystallographic *c* axis. Unlike the N–H \cdots S interactions found in the compound $[\text{Fe}(\text{bapbpy})(\text{NCS})_2]$ where each sulfur atom is involved in a single H-bond interaction, but similar to the thiocyanate analogue $[\text{Fe}(\mathbf{3})(\text{NCS})_2]$ (see Chapter 2), in compound **11c** the Se atom (e.g., Se1 in Figure 4.2a) on one selenocyanate ligand is accepting two

Table 4.2. Selected bond lengths (Å) and angles (°) for the crystal structures of **11c**, **11c'**, **13c**, and **16c**.

	11c	11c'		13c		16c
T (K)	200(2)	110(2)		300(2)	102(2)	110(2)
Phase	HS	HS		HS	LS	LS
Fe1–N1	2.152(2)	2.134(2)	Fe1–N1	2.126(3)	2.022(2)	2.002(2)
Fe1–N3	2.157(2)	2.130(2)	Fe1–N3	2.108(2)	1.950(2)	1.947(2)
Fe1–N4	2.155(2)	2.122(2)	Fe1–N4	2.145(3)	1.947(2)	1.951(2)
Fe1–N6	2.163(2)	2.130(2)	N1–Fe1–N1	110.1(1)	97.49(8)	96.51(9)
Fe1–N7	2.183(2)	2.153(2)	N1–Fe1–N4	93.4(1)	94.08(8)	96.00(1)
Fe1–N8	2.152(2)	2.132(2)	N3–Fe1–N1	160.9(1)	168.20(8)	167.10(9)
N1–Fe–N6	115.48(7)	113.04(7)	N3–Fe1–N3	78.82(9)	82.68(7)	82.98(9)
N3–Fe1–N1	85.43(7)	86.60(7)	N3–Fe1–N4	82.8(1)	83.54(8)	84.0(1)
N4–Fe1–N3	77.15(7)	77.51(7)	N1–N3–N3–N1	18.11(1)	13.97(8)	–16.38(9)
N6–Fe1–N4	85.20(7)	85.62(7)				
N1–N3–N4–N6	–23.52(8)	–21.47(8)				

N–H \cdots Se hydrogen bonds of the NH bridges from two neighbouring molecules (Figure 4.2). The N \cdots Se interatomic distance [3.538(2) Å] is very close to the sum of the van der Waals radii (3.45 Å), which confirms the strong hydrogen-bonding interactions in **11c**. In contrast, the N–H \cdots Se intermolecular distances for compounds **13c** [4.058(2) Å] and **16c** [3.968(2) Å] at 102 K and 110 K, respectively, are significantly longer than 3.45 Å, which suggests relatively weak N–H \cdots Se intermolecular interactions for these compounds.

The second set of intermolecular interactions is caused by π – π stacking between the terminal pyridine rings of two adjacent molecules. The centroid-centroid distance is 4.074(12) Å for compound **11c** at 200 K, while the corresponding distance is 3.846(2) Å and 3.818(6) Å for **13c** at 300 K and 102 K, respectively. For compound **16c**, each ring of the bipyridine fragment is involved in π – π stacking with the two fused aromatic rings of the isoquinoline groups of the neighbouring molecules, with centroid-centroid distances of 3.757(16) Å and 3.858(16) Å. Overall, π – π stacking interactions are weak but similar within this family of compounds (**11c**, **13c**, and **16c**). In summary,

compound **11c** shows stronger hydrogen bonding interactions than **13c** and **16c**, and therefore it is expected to show higher cooperativity – if it happens to have SCO properties.

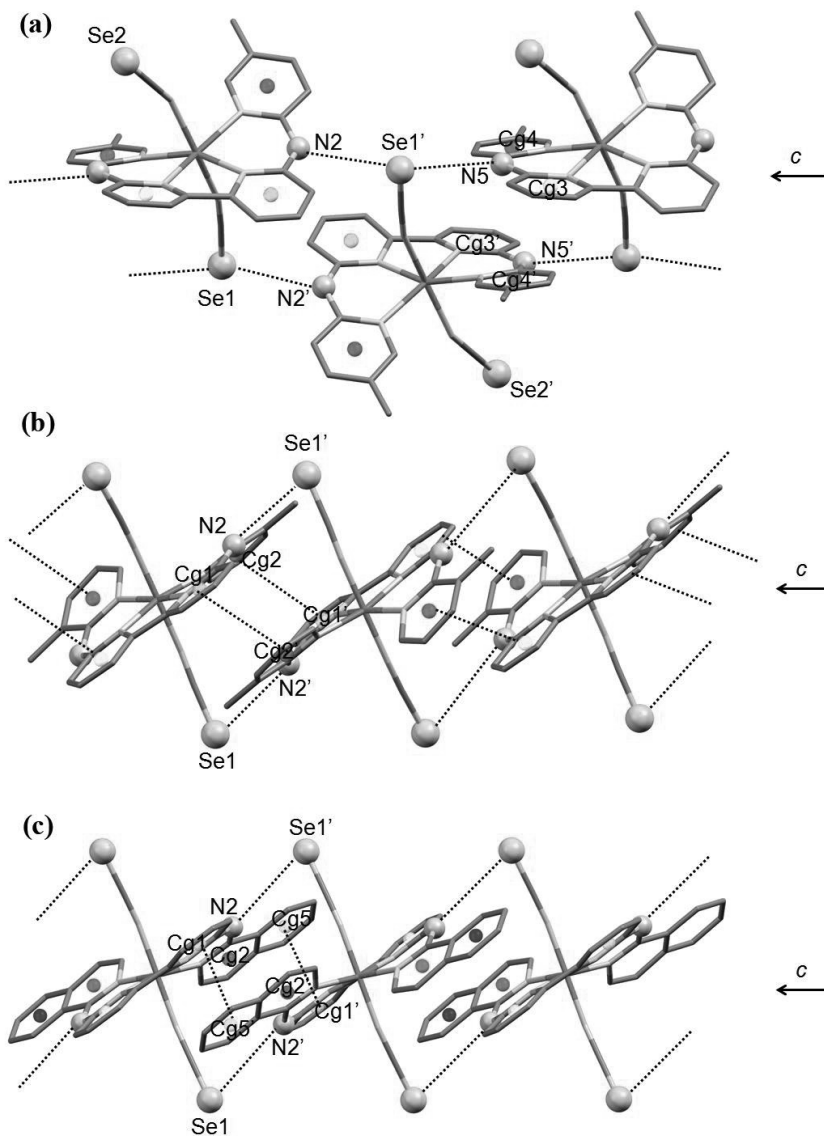


Figure 4.2. Crystal packing along the crystallographic *c* axis for compounds (a) **11c** at 200(2) K, (b) **13c** at 102(2) K, and (c) **16c** at 110(2) K. Symmetry operator $\bar{1} = -x, -y, -z$.

Table 4.3. N...Se and π - π interactions (\AA , $^\circ$) found in complexes **11c**, **13c** and **16c** at different spin states.

	11c	13c	16c
T (K)	200(2)	300(2)	110(2)
Phase	HS	HS	LS
N2...Se1 [']	3.538(2)	4.237(3)	4.058(2)
N5...Se1 [']	3.540(2)	n.a.	n.a.
N2-H2A...Se1 [']	171.15(2)	165.36(2)	160.95(2)
N5-H5A...Se1 [']	174.08(2)	n.a.	n.a.
Cg2...Cg1 [']	7.549(14)	3.846(2)	3.818(6)
Cg3...Cg4 [']	4.074(12)	3.846(2)	3.818(6)
Cg5...Cg1 [']	n.a.	n.a.	n.a.

n.a. = non-applicable. Symmetry operator ['] = -x,-y,-z

For the compounds obtained by method **a**, **b**, or **c**, mass spectrometry indicated the presence of chemically identical complexes. However, SCO is utterly sensitive to polymorphism or lattice solvent inclusion.¹⁴ For example, two different materials [Fe(bapbpy)(NCS)₂] and [Fe(bapbpy)(NCS)₂].2DMF are known to form depending on the crystallization conditions.¹⁷ Thus, molecular characterization methods are not enough, and the influence of the sample preparation method on the structural phase and purity of compounds **9**, **11**, **13**, **15**, and **16** was studied by powder X-ray diffraction (PXRD). The powder diffractograms for compounds **9a**, **9b** (Figure 4.3), **11a**, **11b**, **13a**, **13b** (Appendix II, Figure AII.3), **15a**, and **15b** (Appendix II, Figure AII.3), and **16a** (Figure 4.3) were measured at room temperature and compared to calculated diffractograms from the available crystal structures. For compounds **11**, **13**, and **15** the experimental (**11a** vs. **11b**, **13a** vs. **13b**, and **15a** vs. **15b**) and calculated (**11c** or **13c**) powder diffractograms show no major differences, thus demonstrating that for ligands **3**, **5**, and **7** all preparation methods lead to the same chemical compound. For compound **16a**, the powder diffractogram was measured at both 110 K and 300 K (Figure 4.3). The diffractogram of **16a** at 300 K shows some significant changes compared to 110 K, for example, a single peak at $2\theta \approx 17.3^\circ$ (triangles in Figure 4.3) at 300 K turns to two close peaks at low temperatures; and two peaks at $2\theta \approx 22.6^\circ$ becomes a single peak at 110 K (stars). These changes suggest that the compound is

undergoing a phase transition upon cooling. In addition, there were no major differences between the calculated spectrum from the crystal structure of **16c** (LS phase) and the measured diffractogram of **16a** at 110 K, which concluded that compounds **16a** and **16c** are identical materials.

In contrast, comparison of the experimental X-ray powder diffractograms of compounds **9a** and **9b** at room temperature clearly shows different structures (Figure 4.3). The major differences are: (i) the intense reflection at $2\theta \approx 21.5^\circ$ for compound **9a**, which is shifted slightly in **9b**; (ii) some reflections of **9a**, e.g. at $2\theta \approx 19.1^\circ$, 16.7° and 17.8° , that are absent in **9b**; (iii) multiple reflection peaks between $2\theta \approx 26.3^\circ$ and 27.6° in **9a** appears to be a single peak for **9b**. Thus, **9a** and **9b** are clearly two different materials. This result is consistent with the elemental analysis for **9b**, which showed the best fit with two DMF solvent molecules per iron complex in the crystal lattice, whereas **9a** has not been in contact with DMF at all. Additionally, the powder diffractogram of **9a** is clearly different from that of its thiocyanate analogue $[\text{Fe}(\mathbf{1})(\text{NCS})_2]^{15}$ (also prepared *via* method **a**), which shows that for the bapbpy complex changing the thiocyanate ligands to selenocyanates leads to a change of the structure of the material. Unfortunately, all efforts to grow single crystals of **9c** were unsuccessful. In conclusion, PXRD indicate that for compounds **11**, **13**, **15**, and **16**, the different methods of preparation produce the same material, whereas for compound **9** materials prepared by methods **a** and **b** show different structures.

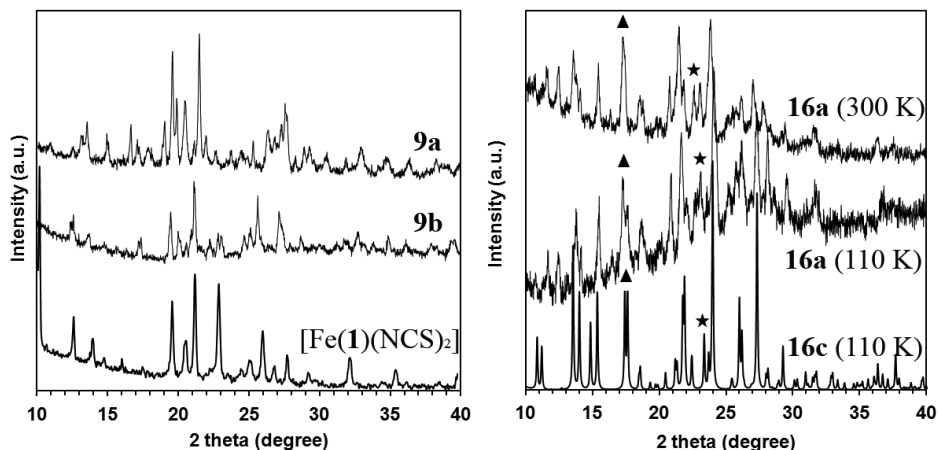


Figure 4.3. Left: powder X-ray diffractograms for compounds **9a**, **9b** and $[\text{Fe}(\mathbf{1})(\text{NCS})_2]$ at room temperature prepared by method **a**.¹⁵ Right: of compound **16a** at 300 K, and 110 K, to that of the calculated from the single X-ray structure of compound **16c** at 110 K.

4.2.3. Magnetic susceptibility measurements

Magnetic susceptibility measurements were carried out to investigate the SCO properties of compounds **9** to **16** as shown by $\chi_M T$ vs. T plots in Figure 4.4 (χ_M stands for the molar magnetic susceptibility and T the temperature). Compounds **10a**, **12a** and **14a** have $\chi_M T$ values close to $3 \text{ cm}^3 \text{ K mol}^{-1}$ (Appendix II, Figure AII.2) between 30 K and 300 K, which compares well with an HS state described in an octahedral coordination environment ($\chi_M T = 3.0 \text{ cm}^3 \text{ mol}^{-1} \text{ K}$). Therefore there is no spin crossover for **10a**, **12a** and **14a**. On the other hand, compounds **9a**, **11a**, **13a**, **15a** and **16a** all show SCO properties. For compound **9a** the $\chi_M T$ value of $3.0 \text{ cm}^3 \text{ K mol}^{-1}$ at 300 K gradually decreases until it reaches $0.1 \text{ cm}^3 \text{ K mol}^{-1}$ at 5 K, a gradual SCO without hysteresis cycle. The transition temperature of **9a**, measured as the maximum of $d(\chi_M T)/dT$, was found to be 195(4) K (Table 4.4). For compound **11a** the $\chi_M T$ value of $3.2 \text{ cm}^3 \text{ K mol}^{-1}$ at 300 K diminishes down to $0.3 \text{ cm}^3 \text{ K mol}^{-1}$ at 5 K, in a complete and abrupt SCO. The transition temperatures of 113(4) K in the cooling mode and 137(4) K in the heating mode (Table 4.4) reveal a hysteresis cycle of 24(6) K indicative of high cooperativity. For compound **13a** $\chi_M T$ gradually decreased from $3.0 \text{ cm}^3 \text{ K mol}^{-1}$ at 350 K down to $0.1 \text{ cm}^3 \text{ K mol}^{-1}$ at 5 K, with a gradual SCO. At 300 K, the SCO is not complete with a $\chi_M T$ value of $2.8 \text{ cm}^3 \text{ K mol}^{-1}$. The transition temperature for **13a** is 214(20) K. For **15a** the $\chi_M T$ value of $2.5 \text{ cm}^3 \text{ K mol}^{-1}$ at 300 K is low compared to the expected $3.0 \text{ cm}^3 \text{ K mol}^{-1}$ for an octahedral HS iron(II) centre, which might indicate the presence of uncoordinated ligand in the material. For this material there is an abrupt SCO with transition temperatures of 141(4) K in the cooling mode and 149(4) K in the heating mode showing a hysteresis cycle of 8(6) K width. For compound **16a** a $\chi_M T$ value of $1.2 \text{ cm}^3 \text{ K mol}^{-1}$ was measured at 300 K indicating a mixture of HS and LS state. An oven was used to probe the magnetic susceptibility of compound **16a** between 300 K and 500 K. At 500 K the $\chi_M T$ value of 2.9 is close to the expected value of $3.0 \text{ cm}^3 \text{ K mol}^{-1}$ so that the SCO can be estimated as being almost complete. The $\chi_M T$ value gradually decreases from 500 K to 100 K, with a transition temperature estimated to be 357(19) K. This value is significantly higher than that found for the thiocyanate analogue [Fe(**8**)(NCS)₂] (288 K, Chapter 2). Compound **16a** has the highest reported transition temperature of all iron(II) bapbpy-based SCO materials.

The magnetic susceptibility measurements of the SCO compounds **11b**, **13b**, and **15b**, were essentially similar to that of **11a**, **13a**, and **15a**, which confirmed that the

materials obtained by method **a** or **b** were similar for ligands **3**, **5**, and **7** (Figure 4.4). Minor variation in the transition temperatures (Table 4.4) and $\chi_M T$ values at room or low temperatures were attributed to the higher chemical purity of samples prepared by method **b**. In contrast, for **9b** a dramatic decrease in the transition temperature [$\Delta T_{1/2}=82(4)$ K] was observed compared to compound **9a**, concomitant with a less abrupt variation of $\chi_M T$ vs. T . This observation is consistent with elemental analyses and PXRD data, which all point to the different nature of the SCO materials **9a** and **9b**. The difference between **9a** and **9b** is similar to what was observed with the thiocyanate analogue, where two crystallographically characterized compounds [Fe(babppy)(NCS)₂] and [Fe(babppy)(NCS)₂] \cdot 2DMF are obtained by two different preparation methods.¹⁷

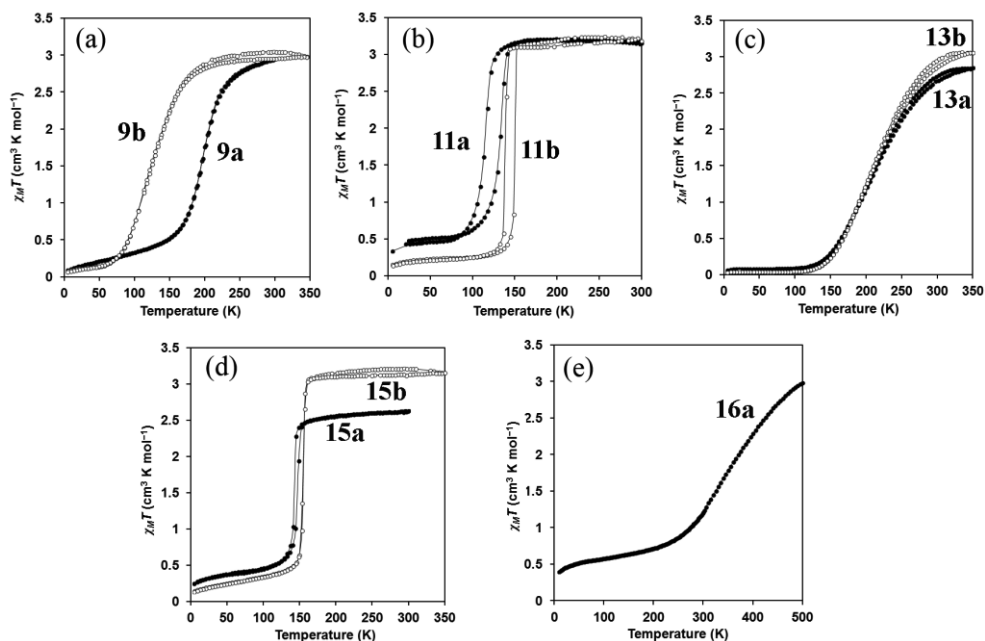


Figure 4.4. Comparison of the $\chi_M T$ vs. T curves for (a) **9a** and **9b**; (b) **11a** and **11b**; (c) **13a** and **13b**; (d) **15a** and **15b**, and (e) **16a**, in both heating and cooling modes with a rate of 0.3-1.1 K min⁻¹.

4.2.4. DSC measurements

Calorimetric measurements on SCO compounds provide important thermodynamic parameters such as the enthalpy and entropy variations accompanying a spin transition,

Table 4.4. Transition temperatures and hysteresis widths for the SCO compounds [Fe(L)(NCSe)₂]. Heating / cooling rate = 0.3-1.1 K min⁻¹.

Compound	$T_{1/2\downarrow}$ (K)	$T_{1/2\uparrow}$ (K)	ΔT_{hyst} (K) ^a
9a	193(4)	196(4)	–
9b	113(4)	113(4)	–
11a	113(4)	137(4)	24(6)
11b	136(4)	153(4)	17(6)
13a	213(16)	214(20)	–
13b	201(4)	202(4)	–
15a	141(4)	149(4)	8(6)
15b	153(4)	158(4)	5(6)
16a	358(22)	355(15)	–

^a Only indicated when $T_{1/2\uparrow} - T_{1/2\downarrow}$ is larger than the uncertainty on $T_{1/2}$

the transition temperature, and they provide indications on the order of the transition. Thus, the molar heat capacities at constant pressure C_p , were measured for compounds **9a**, **11a**, **13a**, **15a**, **15b** and **16a**, by differential scanning calorimetry (DSC, see Figure 4.5). Compounds **15a** and **15b** are the same material, but **15b** is higher in purity therefore DSC data are shown for **15b** only. The excess heat capacity, ΔC_p , due to the spin crossover in the above-mentioned compounds was obtained by estimating normal heat-capacity curve with the high- and low-temperature data, which are shown as dashed lines in Figure 4.5, and subtracting it from the total heat capacity (Figure 4.6). In this estimation, no heat-capacity step at the transition temperature was considered. Compound **9a** showed a broad heat capacity anomaly between 150 and 300 K, culminating at 200 K. This temperature matches well with that determined by the magnetic susceptibility measurements ($T_{1/2} = 195(4)$ K). For compound **11a**, the DSC measurements were performed in the heating mode only but not in the cooling mode due to the closeness of the transition temperature $T_{1/2\downarrow}$ to the low temperature limit of the DSC setup (measurements upon cooling can typically be made down to only 120 K). Compound **11a** showed a broad heat capacity anomaly between 100 K and 150 K, with a maximum estimated at 125 K, which is slightly lower than that given by magnetic susceptibility measurements ($T_{1/2\uparrow} = 137(4)$ K). For compound **13a**, a very broad heat capacity anomaly is observed between 150 and 300 K, with its maximum

estimated at 220 K. This is again consistent with the magnetic susceptibility measurements of **13a**, which shows a gradual SCO curve with $T_{1/2}$ estimated at about 214(20) K. For compound **15b**, DSC measurements in both cooling and heating modes exhibited sharp heat-capacity peaks centred at *ca.* 146 K and 153 K, respectively. These temperatures are in excellent agreement with the magnetic measurements of **15b**. Finally, for compound **16a**, a broad heat capacity anomaly was observed between 300 and 450 K, the maximum being at 350 K. Overall, DSC data are in good agreement with the magnetic susceptibility measurements for all tested compounds.

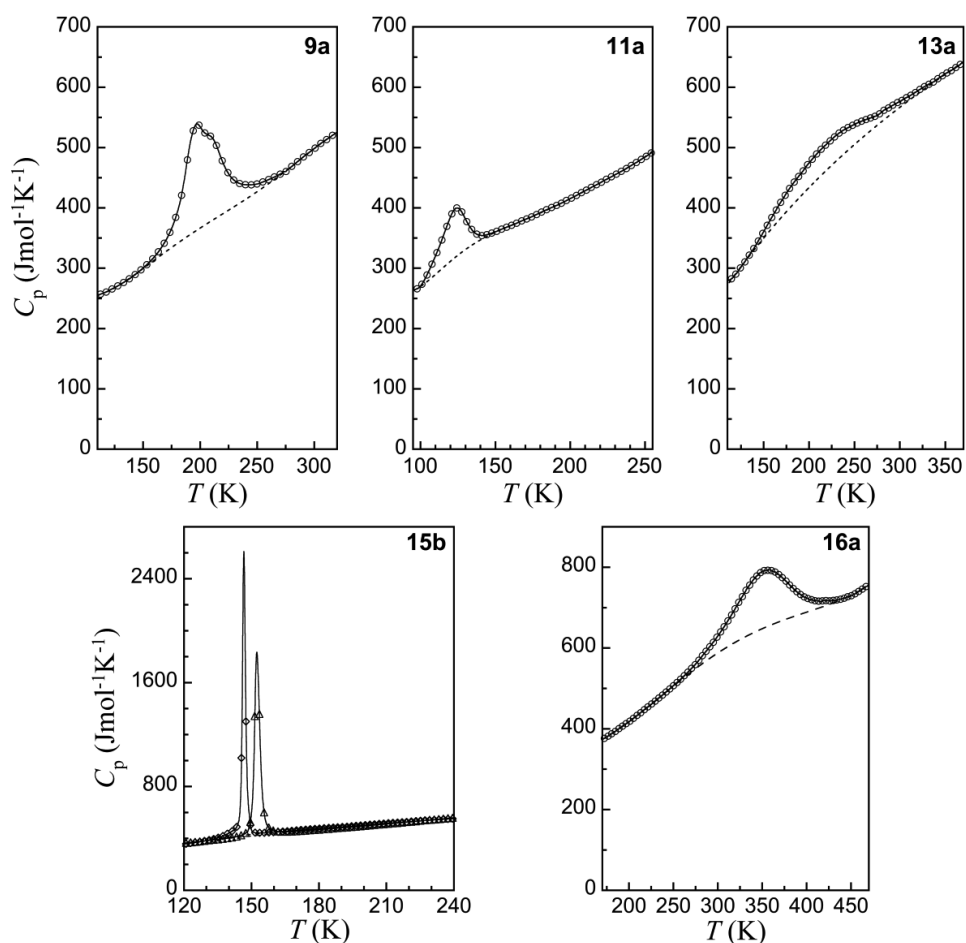


Figure 4.5. Molar heat capacities of compounds **9a**, **11a**, **13a**, **15b** and **16a**, as derived from differential scanning calorimetry. Data in both warming and cooling are shown for **15b**. Dashed lines are estimated normal heat capacities used for ΔC_p determination. Heating/cooling rate is 10 K min^{-1} .

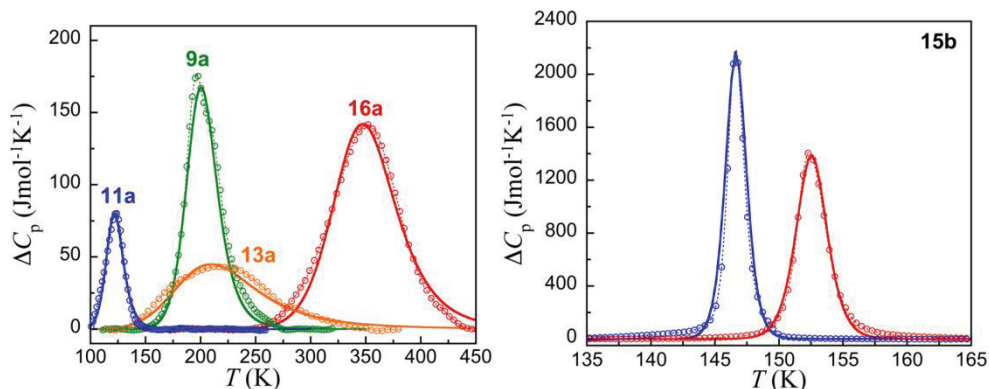


Figure 4.6. Excess molar heat capacities of compounds **9a**, **11a**, **13a** and **16a** upon warming (left) and **15b** in both warming and cooling modes (right, respectively in red/blue). Full lines are fits to the domain model (see text and Table 4.5).

Table 4.5. Excess enthalpy and entropy due to the SCO, and parameters describing the SCO ($T_{1/2}$) and its cooperativity (n) in compounds **9a**, **11a**, **13a**, **15b** and **16a** as derived from Sorai's domain model (see text).

Compound	9a	11a	13a	15b	16a
$\Delta_{SCO}H$ (kJ mol^{-1})	6.24	1.66	4.73	4.43 / 4.69	10.9
$\Delta_{SCO}S$ ($\text{J mol}^{-1} \text{K}^{-1}$)	31.0	13.7	22.0	30.2 / 30.7	31.5
n	5.8	14.4	3.1	54.8 / 70.5	4.8
$T_{1/2}$ (K)	202	123	222	153 / 147	351

As done previously for the thiocyanate series (see Chapter 2), the phenomenological domain model proposed by Sorai^{18, 19} was used to quantify and compare the cooperative character of the SCO compounds presented in this chapter, through the number of interacting SCO molecules per domain, n . Thus, the experimental excess heat capacity data were fitted to Eq. 4.1 (full lines in Figure 4.6), fixing the excess enthalpy due to the SCO, $\Delta_{SCO}H$, to the value derived experimentally (see Table 4.5). The resulting best-fit parameters n and $T_{1/2}$ are gathered in Table 4.5. Clearly the values for n correlate with the differences in abruptness of the SCO curves in magnetic susceptibility measurements or sharpness of heat capacity peaks in DSC. Both compounds **11** and **15** can be considered as cooperative SCO compounds with values

of n of 14.4 and 54.8 / 70.5 (in cooling / warming mode), respectively, whereas compounds **9**, **13**, and **16** have low n values (5.8, 3.1, and 4.8 respectively) and can be considered as poorly cooperative.

$$\Delta C_p = \frac{n(\Delta_{SCO}H)^2}{RT^2} \frac{\exp\left[\frac{n\Delta_{SCO}H}{R}\left(\frac{1}{T} - \frac{1}{T_{1/2}}\right)\right]}{\left\{1 + \exp\left[\frac{n\Delta_{SCO}H}{R}\left(\frac{1}{T} - \frac{1}{T_{1/2}}\right)\right]\right\}^2} \quad \text{Eq. 4.1}$$

4.3. Discussion

To the best of our knowledge, this work is one of the few comprehensive studies on the systematical replacement of NCS^- anion by NCSe^- in a family of related SCO compounds. As selenium is less electronegative than sulfur, the LS state of $[\text{Fe}(\text{R}_2\text{bapbpy})(\text{NCX})_2]$ compounds is expected to be stabilized with $\text{X}=\text{Se}$ ligands compared to $\text{X}=\text{S}$, and the transition temperature of the corresponding SCO compound should increase. However, considering the high sensitivity of the SCO phenomenon to minute changes in the ligand structure (Chapter 2), to the presence of lattice solvent molecules (this Chapter), or to crystallization methods (Chapter 5), one should first demonstrate that replacing S by Se does not significantly change the chemical nature, *i.e.*, the molecular formula and the crystal structure, of the SCO materials. This is demonstrated in the present work: for ligands **3**, **5**, and **8**, the bis-thiocyanate and bis-selenocyanate iron(II) compounds have strikingly similar crystal structures (Figure AII.4, Appendix II), and indeed materials **11**, **13** and **16** have higher transition temperatures than their thiocyanate analogues (Figure 4.7), which is consistent with previous studies.^{11, 12, 20-23} The case of ligand **3** is interesting, as the thiocyanate complex did not show any SCO properties whereas replacement of S by Se leads to a SCO compound (**11**) with a $T_{1/2}$ of 125 K. Overall, the substitution of thiocyanate by selenocyanate thus appears as a means to tune the transition temperature of bapbpy-based SCO compounds.

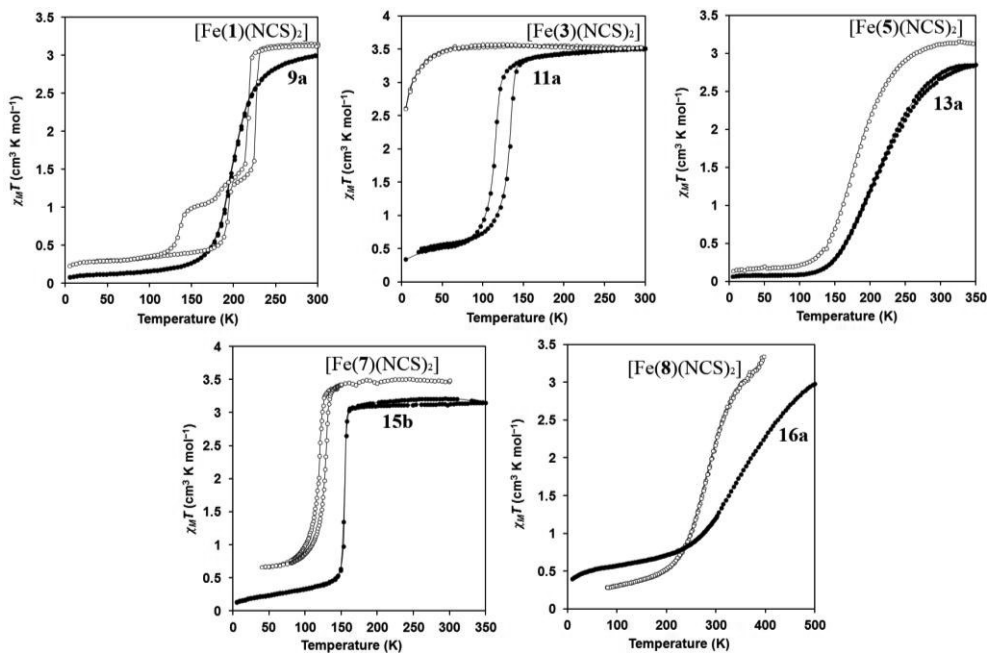


Figure 4.7. Comparison of $\chi_M T$ vs. T curves for compounds **9a**, **11a**, **13a**, **15b** and **16a**, and their thiocyanate analogues.¹⁶

These additional data mostly confirm the qualitative model for cooperativity developed with thiocyanate compounds (Chapter 2). In absence of substituents in β, β' -positions on the terminal pyridine rings of the tetradentate ligand, the SCO remains cooperative (compounds **11** and **15**) due to the N–H \cdots S/Se hydrogen bonding interactions characterized crystallographically in **11c**. In contrast, the N–H \cdots Se intermolecular distances for **13c** and **16c** are significantly longer than those found in **11c**, which in our model is due to the hindering substituents located near the NH bridges of the R₂babppy ligand. Such weakened N–H \cdots Se interactions correlate with the non-cooperative SCO observed for these compounds. The fact that compounds **10a**, **12a**, and **14a** do not show SCO behaviour is consistent with observation on their thiocyanate analogues (Chapter 2). For compounds **10a** and **14a** the sterically hindering substituent in ϵ or δ position of the terminal pyridyl nitrogen atom results in intramolecular steric hindrance, which is believed to increase the distortions of the organic backbone, thus to weaken the LFS of the complex and prevent SCO to occur. Although the replacement of S by Se might increase the LFS as in **11**, this increase seems not be large enough to allow SCO to occur. On the other hand, compound **12a** would have been expected to show

cooperative SCO behaviour as there are no substituents in ϵ or δ positions. Its thiocyanate analogue $[\text{Fe}(\text{4})(\text{NCS})_2]^{16}$ did not show any SCO either, and for this ligand additional distortions due to packing effects may be the reason for the destabilization of the LS state.

More importantly, the number of interacting SCO molecules per domain, n , between the selenocyanate and thiocyanate SCO complexes (Chapter 2) for ligands **5**, **7** and **8** are comparable based on the DSC data (that is, replacing S by Se does not significantly change the cooperativity of these SCO materials). Remarkably, the n values for the gradual SCO compounds based on ligands **5** (**13a**, 3.1) and **8** (**16a**, 4.8) remain similar to those of their thiocyanate analogues (2.8 and 5.3 respectively). In contrast, for a hysteretic SCO compound based on ligand **7**, a large increase of n value was obtained (**15a**, 54.8) compared to that of its thiocyanate analogue (16.8). Thus, for the gradual SCO compounds the replacement of NCS^- by NCSe^- does not increase the cooperativity, whereas for cooperative SCO compounds, by replacing NCS^- with NCSe^- , not only the transition temperature can be increased, but also higher cooperativity in the solid state can be obtained.

Compound **9a** clearly represents an exception as its SCO is non cooperative whereas the bapbpy ligand has no hindering substituent on the terminal pyridine rings. In this case the replacement of thiocyanate by selenocyanate has a dramatic effect on the magnetic behaviour of the complex, leading to a gradual one-step SCO for **9a**, whereas $[\text{Fe}(\text{bapbpy})(\text{NCS})_2]$ is a two-step hysteretic SCO compound.¹⁵ Such decrease in cooperativity upon replacement of S by Se has been reported previously.²¹ However, a direct comparison cannot be made here as the crystal structure of the sulfur and selenium analogues are different according to powder XRD (Figure 4.3). The changes in cooperativity might be a result of the different crystal structures in this case, rather than of the mere replacement of S by Se. Compound **9a** is a typical case showing that subtle changes in the ligands may lead to drastic variations of the SCO properties.

4.4. Conclusion

A series of materials of the general formula $[\text{Fe}(\text{L})(\text{NCSe})_2]$ based on the bapbpy ligand and seven derivatives thereof have been synthesized and structurally characterized. Five new selenocyanate-containing materials **9**, **11**, **13**, **15**, and **16** showed SCO behaviour, two being cooperative (**11** and **15**) whereas the others are non-cooperative. The striking structural similarity between the thiocyanate and

selenocyanate compounds, and the central position of the chalcogenide atoms in the hydrogen-bonding network responsible for cooperativity, provided a unique opportunity to probing the effect of exchanging the sulfur atoms by selenium on the SCO behaviour of the compounds. For most compounds (**11a**, **13a**, **15a**, and **16a**) the expected stabilization of the LS state was observed, and **11a** even showed SCO whereas its thiocyanate analogue did not. Compound **9a** appears as an exception, as its dramatically lower cooperativity compared to the thiocyanate analogue seems to be due to a structural change.

4.5. Experimental

4.5.1. General information

All reactions were performed under argon atmosphere using standard Schlenk line techniques. Toluene was dried over sodium and degassed, diethylether was dried over sodium and benzophenone, DMF was dried over CaH_2 . Degassed solvents were obtained by bubbling argon through 50 mL solvent in a Schlenk flask for one hour. For all complex syntheses, degassed solvents were used. The reagent 6,6'-dibromo-2,2'-bipyridine was synthesized in two steps according to the literature,²⁴ and the syntheses of the bapbpy derivatives **1-8** followed previously described procedures (see Chapter 2).¹⁶ All other reagents obtained from commercial sources were used without further purification. Filtration of the iron(II) compounds was done on Whatman membrane filters (regenerated cellulose RC55) with 1 μm pores. ^1H NMR and ^{13}C NMR spectra were recorded at room temperature using a Bruker DPX300 (300 MHz) spectrometer. Chemical shifts are indicated in ppm relative to TMS. Infrared spectra (IR) were taken on a Perkin Elmer FT-IR Spectrometer Paragon 1000 equipped with a Golden Gate ATR device, using the reflectance technique (4000-300 cm^{-1} , resolution 4 cm^{-1}). Mass spectrometry was performed on a Finnigan Mat 900 spectrometer equipped with an electrospray interface. HR Mass spectra were measured using direct injection (2 μL of a 2 μM solution in DMF and 0.1% formic acid on a Thermo Finnigan LTQ Orbitrap mass spectrometer equipped with an electrospray ion source in positive mode (source voltage 3.5 kV, sheath gas flow 10, capillary temperature 275 $^\circ\text{C}$) with resolution $R = 60.000$ at $m/z = 400$ (mass range = 150-2000) and dioctylphthalate ($m/z=391.28428$) as "lock mass". Elemental analyses (C,H,N,S) were obtained from a Perkin-Elmer 2400 Series II analyzer.

X-ray powder diffraction data were collected on a Philips X'Pert PRO diffractometer equipped with the X'celerator using $\text{Cu-K}\alpha$ radiations. Single crystal X-Ray diffraction data

were collected by measure all reflection intensities using a KM4/Xcalibur (detector: Sapphire3) with enhance graphite-monochromated Mo $K\alpha$ radiation ($\lambda = 0.71073 \text{ \AA}$) under the program CrysAlisPro (Version 1.171.35.11 Oxford Diffraction Ltd., 2011). The program CrysAlisPro was used to refine the cell dimensions. Data reduction was done using the program CrysAlisPro. The structure was solved with the program SHELXS-97²⁵ and was refined on F^2 with SHELXL-97.²⁵ Analytical numeric absorption corrections based on a multifaceted crystal model were applied using CrysAlisPro. The temperature of the data collection was controlled using the system Cryojet (manufactured by Oxford Instruments). The H atom (except when specified) were placed at calculated positions using the instructions AFIX 43 with isotropic displacement parameters having values 1.2 times U_{eq} of the attached C atoms. The H atoms attached to N2 was found from difference Fourier maps, and its coordinates/isotropic factor were refined freely [the N–H distance was restrained to 0.88(3) \AA using the DFIX command].

Magnetic susceptibility measurements were performed using a Quantum Design MPMS-5S SQUID magnetometer for compounds **9a**, **10a**, **11a**, **12a**, **13a**, **14a**, **15a**, **9b**, **11b**, **13b** and **15b**. In each case, the ~10-20 mg sample was mounted on a plastic straw before introduction in the magnetometer. DC magnetization measurements were performed in a field of 0.1 T, from 300 to 5 K (cooling mode) and from 5 to 300 K (heating mode) with a rate of 0.3 to 1.1 K min^{-1} . The total measuring time for each sample was 20 h. Compound **16a** was measured using a Quantum Design MPMS-XL magnetometer at the Physical Measurements unit of the Servicio de Apoyo a la Investigación-SAI, Universidad de Zaragoza. The measurements in the range 300-500 K were performed with the oven option. For these the powder sample (15.25 mg) was mounted in a piece of Al foil (22.66 mg) that was folded in a round shape, and held/trapped into the knot formed by 4 constantan fibres. Corrections for the sample holder assemblies were applied, as well as corrections for the diamagnetism of the sample, calculated using Pascal's constants.²⁶ Heat capacities were obtained by use of a differential scanning calorimeter Q1000 with the LNCS accessory from TA Instruments. The temperature and enthalpy scales were calibrated with a standard sample of indium, using its melting transition (156.6 $^{\circ}\text{C}$, 3296 J mol^{-1}). The measurements were carried out using 6 to 13 mg of samples sealed in aluminium pans with mechanical crimp, with an empty pan as reference. The zero-heat flow procedure described by TA Instruments was followed, using as reference compound a synthetic sapphire. Using this procedure, an overall accuracy of ca. 0.2 K in temperature and up to 5 to 10% in the heat capacity is estimated over the whole temperature range.

4.5.2. Preparations of iron(II) complexes

The 0.1 M methanolic solution of $[\text{Fe}(\text{NCSe})_2]$ used for the synthesis of the iron complexes was prepared as follows: $\text{FeSO}_4 \cdot x\text{H}_2\text{O}$ (99.999% trace metals basis, CAS nr. 13463-43-9) (151 mg, 1.0 mmol) and KSeCN (288 mg, 2.0 mmol) were mixed in degassed methanol (6 mL) and stirred for 40 min. Ascorbic acid (5 mg) was added to prevent aerial oxidation. K_2SO_4 was removed by filtration on filter paper (Whatman 597) into a 10 mL volumetric flask. The flask was filled up to 10 mL with methanol, resulting in a clear, colourless iron(II) solution, which must be used within one hour. Oxidation of the iron solution upon aging was visible due to a change of colour (from colourless to dark violet).

Three methods were used to synthesize the iron(II) complexes $[\text{Fe}(\text{L})(\text{NCSe})_2]$: (the compounds number with notation **a**, **b** or **c**, are indicated for the corresponding synthetic methods)

Method a: in a two-necked round-bottom flask the tetrapyrrolyl ligand (0.1 mmol) and 3 mL of degassed methanol were added to form a suspension. 0.1 M methanolic solution of $[\text{Fe}(\text{NCSe})_2]$ (1.1 eq.) was then added resulting in an immediate colour change. The suspension was stirred at room temperature under argon for 16 hrs. The solids were filtered through a membrane filter, thoroughly washed with methanol, and dried under vacuum for 3 hours.

Method b: in a two-necked round bottom flask the tetrapyrrolyl ligand (0.05 mmol) was dissolved in an appropriate amount of degassed DMF (in case of **15b**, ligand **7** was heated in DMF to 130 °C to be dissolved and then cooled down to room temperature). A 0.1 M methanolic solution of $[\text{Fe}(\text{NCSe})_2]$ (1.1 eq.) was added at room temperature. The resultant solution was left unstirred overnight under argon. In case of ligands **1**, **3**, and **5**, solids appeared at the bottom of the flask within a day. For ligand **7** this was not the case, and excess MeOH was carefully layered on top of the DMF solution, to obtain a precipitate the next day. In all cases, the excess solution was removed by canula, and the solid was thoroughly washed with methanol, dried under high vacuum for 3 h to obtain compounds **9b**, **11b**, **13b** or **15b**.

During the synthesis of compounds **10b**, **12b**, and **14b**, no solid appeared overnight after addition of $\text{Fe}(\text{NCSe})_2$. However with addition of excess MeOH (20 mL), solids appeared within 3 days. In each case, the IR spectrum was identical to that of free ligand **2**, **4**, and **6**, respectively. Compound **16b** could not be prepared since ligand **8** has very low solubility in DMF, even when heated.

Method c: the ligand **3** or **5** (20 mg) was dissolved in dry and degassed DMF (4 mL), affording a clear yellow/orange solution to which a small amount (~5 mg) of ascorbic acid was added to prevent oxidation. In case of ligand **8** (24 mg), the DMF suspension (5 mL) was heated to 80 °C and cooled down to room temperature, however the ligand was still not fully dissolved. 1 mL aliquots of ligand solution were pipette-filtered over 1 cm Celite into a Corning tube. [Fe(NCSe)₂] (0.1 M methanolic solution, 136 μL for ligand **3** or **5**, 114 μL for ligand **8**, 1.1 eq.) was carefully layered on top of the ligand solution. Degassed methanol was then layered on top of these two layers. The 4 tubes were then sealed and left untouched, if possible in a sunny place. Red/dark crystals were obtained for compounds **11c**, **11c'**, **13c**, and **16c** within a week by liquid-liquid diffusion.

Important note on crystal growing: visible light seems to play a role in the crystallization of this family of compounds. For example, sunny weeks were systematically followed by significantly increased yield and crystal quality, whereas control crystal growing experiments performed in the dark or during weeks of bad weather, always led to much lower crystal quality or no crystals at all. Crystal growth should be best realized during sunny periods.

[Fe(1)(NCSe)₂] (9a): The red powder was obtained with a yield of 83%. IR spectroscopy (cm⁻¹): 3188, 3101, 2090 (NCSe⁻), 2057 (NCSe⁻), 1622, 1582, 1558, 1527, 1482, 1460, 1441, 1436, 1345, 1237, 1175, 1165, 1134, 1074, 1060, 1010, 1004, 915, 862, 794, 765, 734, 668, 645, 630, 614, 599, 512, 482, 418, 342, 324. High resolution ES-MS from DMF solution *m/z* (calc): 501.9978 (501.9978 [M–NCSe]⁺). Elemental analysis calcd (%) for C₂₂H₁₆FeN₈Se₂·0.6C₂₀H₁₆N₆: C 50.39, H 3.18, N 20.05; found: C 51.06, H 2.21, N 19.95.

[Fe(1)(NCSe)₂]·2DMF (9b): The small red polycrystals were obtained with a yield of 67%. IR spectroscopy (cm⁻¹): 3313, 3205, 3077, 3014, 2928, 2067 (NCSe⁻), 1661 (DMF), 1652, 1646, 1582, 1558, 1538, 1482, 1462, 1436, 1428, 1387, 1368, 1281, 1242, 1173, 1159, 1134, 1102, 1057, 1006, 868, 843, 797, 768, 681, 666, 645, 614, 578, 516, 488, 422, 414, 355, 324. High resolution ES-MS from DMF solution *m/z* (calc): 501.9973 (501.9978 [M–NCSe]⁺). Elemental analysis calcd (%) for C₂₈H₃₀FeN₁₀O₂Se₂: C 44.68, H 4.02, N 18.62; found: C 44.30, H 4.03, N 18.65.

[Fe(2)(NCSe)₂] (10a): The brown powder was obtained with a yield of 93%. IR spectroscopy (cm⁻¹): 3052, 2806, 2057 (NCSe⁻), 1664, 1630, 1610, 1576, 1560, 1534, 1514, 1465, 1442, 1383, 1341, 1296, 1270, 1245, 1176, 1158, 1091, 1039, 1000, 988, 960, 890, 861, 805, 774, 746, 725, 720, 670, 640, 570, 495, 428. High resolution ES-MS from DMF solution *m/z* (calc): 530.0288 (530.0291 [M–NCSe]⁺).

[Fe(3)(NCSe)₂] (11a): The orange powder was obtained with a yield of 82%. IR spectroscopy (cm⁻¹): 3278, 3197, 3108, 2094 (NCSe⁻), 2060 (NCSe⁻), 1626, 1616, 1581, 1558, 1527, 1496, 1456, 1436, 1410, 1374, 1236, 1177, 1149, 1048, 1002, 894, 821, 791, 736, 668, 654, 638, 512, 483, 425, 323. ESI-MS (DMF) *m/z* (calc): 530.1 (530.0 [M–NCSe]⁺). Elemental analysis calcd (%) for C₂₄H₂₀FeN₈Se₂: C 45.45, H 3.18, N 17.67; found: C 43.50, H 2.08, N 16.20.

[Fe(3)(NCSe)₂] (11b): The small red polycrystals were obtained with a yield of 28%. IR spectroscopy (cm⁻¹): 3277, 3193, 3103, 2093 (NCSe⁻), 2052 (NCSe⁻), 1652, 1625, 1581, 1558, 1526, 1496, 1456, 1436, 1410, 1373, 1226, 1176, 1148, 1047, 1001, 894, 820, 790, 736, 652, 638, 512, 484, 452, 418, 319. High resolution ES-MS from DMF solution *m/z* (calc): 530.0290 (530.0291 [M–NCSe]⁺). Elemental analysis calcd (%) for C₂₄H₂₀FeN₈Se₂: C 45.43, H 3.18, N 17.67; found: C 45.06, H 2.65, N 17.34.

[Fe(3)(NCSe)₂] and [Fe(3)(NCSe)₂]·MeOH (11c and 11c’): Two types of single crystals were obtained upon using method **c**, with a total yield of 51%.

Crystal data for **11c**: Fw = 634.25, red plate, 0.34 × 0.25 × 0.11 mm³, triclinic, *P*-1 (no. 2), *a* = 8.6403(3), *b* = 11.2005(4), *c* = 13.5845(5) Å, α = 68.946(3), β = 79.002(3), γ = 80.171(3)°, *V* = 1196.84(8) Å³, *Z* = 2, *D*_x = 1.760 g cm⁻³, μ = 8.782 mm⁻¹, abs. corr. range: 0.193–0.501. 14037 Reflections were measured up to a resolution of (sin θ/λ)_{max} = 0.62 Å⁻¹. 4684 Reflections were unique (*R*_{int} = 0.0187), of which 4561 were observed [*I* > 2 σ (*I*)]. 327 Parameters were refined using 2 restraints. *R*1/*wR*2 [*I* > 2 σ (*I*)]: 0.0248/0.0652. *R*1/*wR*2 [all refl.]: 0.0255/0.0656. *S* = 1.015. Residual electron density found between –0.60 and 0.46 e Å⁻³.

Crystal data for **11c’**: Fw = 666.29, dark red plate, 0.34 × 0.16 × 0.06 mm³, triclinic, *P*-1 (no. 2), *a* = 9.0074(3), *b* = 11.3214(3), *c* = 13.6382(3) Å, α = 75.312(2), β = 89.534(2), γ = 81.410(2)°, *V* = 1329.59(7) Å³, *Z* = 2, *D*_x = 1.664 g cm⁻³, μ = 7.965 mm⁻¹, abs. corr. range: 0.163–0.639. 17736 Reflections were measured up to a resolution of (sin θ/λ)_{max} = 0.62 Å⁻¹. 5202 Reflections were unique (*R*_{int} = 0.0246), of which 5015 were observed [*I* > 2 σ (*I*)]. 350 Parameters were refined using 3 restraints. *R*1/*wR*2 [*I* > 2 σ (*I*)]: 0.0282/0.0744. *R*1/*wR*2 [all refl.]: 0.0293/0.0755. *S* = 1.041. Residual electron density found between –0.69 and 0.68 e Å⁻³.

[Fe(4)(NCSe)₂] (12a): The reddish orange powder was obtained with a yield of 90%. IR spectroscopy (cm⁻¹): 3289, 3192, 3100, 2080 (NCSe⁻), 1634, 1593, 1580, 1558, 1532, 1490, 1463, 1442, 1436, 1418, 1371, 1290, 1236, 1224, 1193, 1174, 1137, 1031, 1010, 934, 866,

815, 802, 788, 734, 690, 668, 644, 624, 588, 543, 487, 453, 425, 330. ESI-MS (DMF) m/z (calc): 530.1 (530.03 [M–NCSe]⁺).

[Fe(5)(NCSe)₂] (13a): The brown powder was obtained with a yield of 68%. IR spectroscopy (cm⁻¹): 3386, 3072, 2100 (NCSe⁻), 2070 (NCSe⁻), 1616, 1586, 1576, 1558, 1532, 1520, 1506, 1471, 1447, 1436, 1418, 1362, 1312, 1227, 1191, 1176, 1118, 1076, 1006, 920, 813, 788, 750, 668, 648, 624, 584, 542, 425, 327. High resolution ES-MS from DMF solution m/z (calc): 530.0282 (530.0291 [M–NCSe]⁺). Elemental analysis calcd (%) for C₂₄H₂₀FeN₈Se₂: C 45.43, H 3.18, N 17.67; found: C 45.56, H 2.51, N 17.58.

[Fe(5)(NCSe)₂] (13b): The dark brown powder was obtained with a yield of 44%. IR spectroscopy (cm⁻¹): 3382, 3074, 2100 (NCSe⁻), 2066 (NCSe⁻), 1668, 1652, 1646, 1616, 1586, 1558, 1531, 1520, 1506, 1464, 1447, 1436, 1418, 1361, 1312, 1225, 1190, 1175, 1117, 1074, 1030, 1006, 920, 896, 812, 787, 749, 734, 668, 648, 623, 582, 541, 487, 450, 426, 327. High resolution ES-MS from DMF solution m/z (calc): 530.0294 (530.0291 [M–NCSe]⁺). Elemental analysis calcd (%) for C₂₄H₂₀FeN₈Se₂: C 45.43, H 3.18, N 17.67; found: C 45.05, H 2.47, N 17.52.

[Fe(5)(NCSe)₂] (13c): Dark single crystals were obtained with a yield of 40%. Crystal data for **13c: Phase I** (102(2) K): Fw = 634.25, dark red irregular shape crystal, 0.31 × 0.09 × 0.06 mm³, monoclinic, C2/c (no. 15), $a = 13.2071(3)$, $b = 13.3999(3)$, $c = 14.0838(3)$ Å, $\beta = 105.467(2)^\circ$, $V = 2402.20(9)$ Å³, $Z = 4$, $D_x = 1.754$ g cm⁻³, $\mu = 3.689$ mm⁻¹, abs. corr. range: 0.534–0.858. 10051 Reflections were measured up to a resolution of $(\sin \theta/\lambda)_{\max} = 0.62$ Å⁻¹. 2429 Reflections were unique ($R_{\text{int}} = 0.0288$), of which 2181 were observed [$I > 2\sigma(I)$]. 164 Parameters were refined using 1 restraint. $R1/wR2$ [$I > 2\sigma(I)$]: 0.0240/0.0596. $R1/wR2$ [all refl.]: 0.0289/0.0615. $S = 1.076$. Residual electron density found between -0.33 and 0.53 e Å⁻³. **Phase II** (300(2) K): Fw = 634.25, dark red irregular shape crystal, 0.31 × 0.09 × 0.06 mm³, monoclinic, C2/c (no. 15), $a = 13.4237(3)$, $b = 13.3663(4)$, $c = 14.2028(5)$ Å, $\beta = 101.916(3)^\circ$, $V = 2493.43(13)$ Å³, $Z = 4$, $D_x = 1.690$ g cm⁻³, $\mu = 3.554$ mm⁻¹, abs. corr. range: 0.549–0.839. 7254 Reflections were measured up to a resolution of $(\sin \theta/\lambda)_{\max} = 0.59$ Å⁻¹. 2193 Reflections were unique ($R_{\text{int}} = 0.0279$), of which 1820 were observed [$I > 2\sigma(I)$]. 164 Parameters were refined using 1 restraint. $R1/wR2$ [$I > 2\sigma(I)$]: 0.0351/0.0841. $R1/wR2$ [all refl.]: 0.0459/0.0894. $S = 1.039$. Residual electron density found between -0.35 and 0.49 e Å⁻³.

[Fe(6)(NCSe)₂] (14a): The rusty yellow powder was obtained with a yield of 88%. IR spectroscopy (cm⁻¹): 3301, 3214, 3066, 2078 (NCSe⁻) 1652, 1616, 1600, 1582, 1558, 1538, 1506, 1483, 1464, 1456, 1436, 1404, 1299, 1255, 1174, 1146, 1004, 824, 798, 780, 753,

668, 644, 618, 524, 486, 418, 398, 328. ESI-MS (DMF) m/z (calc): 602.1 (602.03 [M–NCSe]⁺).

[Fe(7)(NCSe)₂] (15a): The reddish orange powder was obtained with a yield of 83%. IR spectroscopy (cm⁻¹): 3258, 3058, 2061 (NCSe⁻), 1634, 1612, 1576, 1558, 1538, 1490, 1456, 1445, 1418, 1404, 1362, 1322, 1280, 1259, 1248, 1219, 1188, 1172, 1149, 1004, 986, 962, 866, 784, 758, 735, 685, 668, 638, 544, 462, 423, 397, 357, 328. High resolution ES-MS from DMF solution m/z (calc): 602.0287 (602.0292 [M–NCSe]⁺), 730.9380 (730.9390 [M+Na]⁺).

[Fe(7)(NCSe)₂] (15b): The brown powder was obtained with yield of 35%. IR spectroscopy (cm⁻¹): 3290, 3058, 2060 (NCSe⁻), 1634, 1615, 1576, 1539, 1490, 1445, 1404, 1361, 1322, 1279, 1245, 1218, 1189, 1171, 1148, 1003, 986, 913, 866, 785, 743, 685, 662, 635, 540, 461, 427, 356, 309. High resolution ES-MS from DMF solution m/z (calc): 602.0286 (602.0292 [M–NCSe]⁺). Elemental analysis calcd (%) for C₃₀H₂₀FeN₈Se₂: C 51.02, H 2.85, N 15.86; found: C 52.98, H 2.83, N 15.96.

[Fe(8)(NCSe)₂] (16a): The brown powder was obtained with yield of 81%. IR spectroscopy (cm⁻¹): 3364, 3058, 2108 (NCSe⁻), 2072 (NCSe⁻), 1635, 1611, 1592, 1576, 1558, 1532, 1506, 1496, 1471, 1464, 1456, 1436, 1418, 1394, 1347, 1303, 1256, 1232, 1169, 1148, 1077, 1026, 986, 860, 794, 739, 684, 668, 662, 618, 581, 524, 492, 468, 412, 398, 340, 314. High resolution ES-MS from DMF solution m/z (calc): 602.0290 (602.0292 [M–NCSe]⁺).

[Fe(8)(NCSe)₂] (16c): Dark crystals were obtained and sent immediately for single crystal X-ray structure determination. IR spectroscopy (cm⁻¹): 3368, 3066, 2108 (NCSe⁻), 2074 (NCSe⁻), 1635, 1610, 1591, 1576, 1558, 1538, 1532, 1506, 1464, 1436, 1418, 1394, 1312, 1286, 1232, 1168, 1029, 983, 858, 807, 793, 739, 668, 662, 581, 538, 492, 469, 418, 375, 350, 336, 322, 313.

Crystal data for **16c**: Fw = 706.31, black block, 0.28 × 0.17 × 0.15 mm³, monoclinic, C2/c (no. 15), $a = 13.0310(2)$, $b = 14.0929(3)$, $c = 14.6490(3)$ Å, $\beta = 94.4729(15)^\circ$, $V = 2682.02(9)$ Å³, $Z = 4$, $D_x = 1.749$ g cm⁻³, $\mu = 3.315$ mm⁻¹, abs. corr. range: 0.510–0.673. 8173 Reflections were measured up to a resolution of $(\sin \theta/\lambda)_{\max} = 0.62$ Å⁻¹. 2703 Reflections were unique ($R_{\text{int}} = 0.0465$), of which 2338 were observed [$I > 2\sigma(I)$]. 190 Parameters were refined using 1 restraints. $R1/wR2$ [$I > 2\sigma(I)$]: 0.0340/0.0929. $R1/wR2$ [all refl.]: 0.0407/0.0964. $S = 1.044$. Residual electron density found between –0.81 and 1.07 e Å⁻³.

4.6. References:

1. P. D. Southon, L. Liu, E. A. Fellows, D. J. Price, G. J. Halder, K. W. Chapman, B. Moubaraki, K. S. Murray, J. F. Letard and C. J. Kepert, *J. Am. Chem. Soc.*, 2009, 131, 10998-11009.
2. M. Ohba, K. Yoneda, G. Agusti, M. C. Munoz, A. B. Gaspar, J. A. Real, M. Yamasaki, H. Ando, Y. Nakao, S. Sakaki and S. Kitagawa, *Angew. Chem. Int. Ed.*, 2009, 48, 4767-4771.
3. L. Salmon, G. Molnar, D. Zitouni, C. Quintero, C. Bergaud, J. C. Micheau and A. Bousseksou, *J. Mater. Chem.*, 2010, 20, 5499-5503.
4. M. S. Alam, M. Stocker, K. Gieb, P. Müller, M. Haryono, K. Student and A. Grohmann, *Angew. Chem. Int. Ed.*, 2010, 49, 1159-1163.
5. M. Cavallini, I. Bergenti, S. Milita, G. Ruani, I. Salitros, Z. R. Qu, R. Chandrasekar and M. Ruben, *Angew. Chem. Int. Ed.*, 2008, 47, 8596-8600.
6. J. F. Létard, P. Guionneau and L. Goux-Capes, *Top. Curr. Chem.*, 2004, 235, 221-249.
7. O. Kahn and C. J. Martinez, *Science*, 1998, 279, 44-48.
8. M. A. Halcrow, *Chem. Soc. Rev.*, 2011, 40, 4119-4142.
9. P. Gütllich and H. A. Goodwin, *Top. Curr. Chem.*, 2004, 233, 1-47.
10. W. A. Baker and H. M. Bobonich, *Inorg. Chem.*, 1964, 3, 1184-1188.
11. E. König, K. Madeja and K. J. Watson, *J. Am. Chem. Soc.*, 1968, 90, 1146-1153.
12. E. König and K. Madeja, *Chem. Commun.*, 1966, 61-62.
13. A. Ozarowski, S. Z. Yu, B. R. McGarvey, A. Mislankar and J. E. Drake, *Inorg. Chem.*, 1991, 30, 3167-3174.
14. J. A. Real, A. B. Gaspar and M. C. Munoz, *Dalton Trans.*, 2005, 2062-2079.
15. S. Bonnet, M. A. Siegler, J. S. Costa, G. Molnar, A. Bousseksou, A. L. Spek, P. Gamez and J. Reedijk, *Chem. Commun.*, 2008, 5619-5621.
16. Z. Arcis-Castillo, S. Zheng, M. A. Siegler, O. Roubeau, S. Bedoui and S. Bonnet, *Chem. Eur. J.*, 2011, 17, 14826-14836.
17. S. Bonnet, G. Molnár, J. S. Costa, M. A. Siegler, A. L. Spek, A. Bousseksou, W. T. Fu, P. Gamez and J. Reedijk, *Chem. Mater.*, 2009, 21, 1123-1136.
18. M. Sorai and S. Seki, *J. Phys. Chem. Solids*, 1974, 35, 555-570.
19. M. Sorai, Y. Nakazawa, M. Nakano and Y. Miyazaki, *Chem. Rev.*, 2013, 113, PR41-122.
20. N. Brefuel, S. Shova, J. Lipkowski and J.-P. Tuchagues, *Chem. Mater.*, 2006, 18, 5467-5479.
21. J. A. Real, I. Castro, A. Bousseksou, M. Verdaguer, R. Burriel, M. Castro, J. Linares and F. Varret, *Inorg. Chem.*, 1997, 36, 455-464.
22. J. A. Real, H. Bolvin, A. Bousseksou, A. Dworkin, O. Kahn, F. Varret and J. Zarembowitch, *J. Am. Chem. Soc.*, 1992, 114, 4650-4658.
23. N. Moliner, M. C. Munoz, P. J. van Koningsbruggen and J. A. Real, *Inorg. Chim. Acta*, 1998, 274, 1-6.
24. X. L. Bai, X. D. Liu, M. Wang, C. Q. Kang and L. X. Gao, *Synthesis*, 2005, 458-464.
25. G. M. Sheldrick and T. R. Schneider, *Methods Enzymol.*, 1997, 277, 319-343.
26. G. A. Bain and J. F. Berry, *J. Chem. Educ.*, 2008, 85, 532-536.

5

Synthesis and magnetic properties of bapphen-based mononuclear Fe(II) spin-crossover complexes

Abstract

The new rigid ligand bapphen and its iron(II) complexes $[\text{Fe}(\text{bapphen})(\text{NCX})_2]$ ($X = \text{S}$, or Se) were synthesized. The complex $[\text{Fe}(\text{bapphen})(\text{NCS})_2]$ was obtained in two different forms (**1a** and **1d**) *via* two different preparative methods. The magnetic susceptibility measurement revealed that **1a** is HS at room temperature and has a three-step incomplete spin transition, while **1d** has no SCO properties and remains HS state over the full temperature range of 5-300 K. The magnetic behaviour of $[\text{Fe}(\text{bapphen})(\text{NCSe})_2]$ (**2a**) shows an incomplete and gradual spin transition over the full temperature range of 5-350 K, the cooperativity of the transition is lost upon substitution of S by Se.

5.1. Introduction

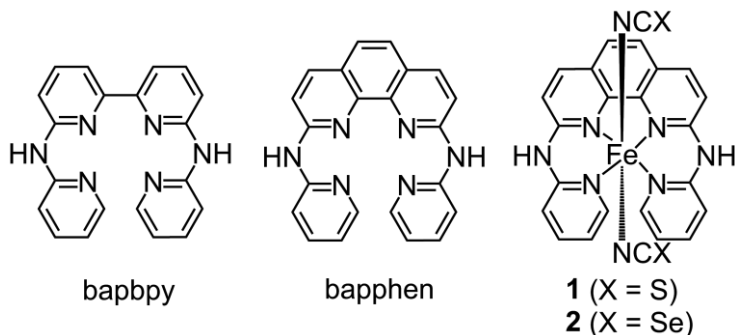
As discussed in Chapter 1, the spin crossover (SCO) phenomenon in octahedral d^4 - d^7 transition metals represents a prototype of molecular switches,¹⁻³ which might be used for the building of nano-sized gas^{4,5} or temperature sensors⁶ and electronic information processing or data storage devices.^{7,8} Iron(II)-based SCO compounds have been actively investigated for several decades, as they can switch between a diamagnetic low-spin (LS) state and a paramagnetic high-spin (HS) state upon temperature variation, upon application of high pressures, upon light radiation, or under the influence of strong magnetic or electric fields.⁹ However, in order to reach a real technological impact, it is imperative that the SCO transition should occur near room temperature.¹⁰ Furthermore, the occurrence of cooperative SCO with hysteresis loops is critical for information storage application.³ Cooperativity originates from the combination of short- and long-range interactions in the solid state.¹¹ These interactions depend on many parameters such as the crystal structure, the inclusion of guest molecules in the crystal lattice, or the size and crystallinity of the crystallites. As a result, it still remains challenging to design molecular compounds combining these two properties. *e.g.*, cooperative SCO with transition temperatures around room temperature.

One approach to tune the transition temperature of a SCO material is to make use of the ligand field strength of the ligand.⁹ The SCO properties of a compound depend on the ligand field strength imposed on the metal ion by all surrounding donor atoms. Basically, a higher ligand field splitting (LFS) results in an increase of the temperature $T_{1/2}$ at which half of the material has gone through SCO.¹² However, in Chapter 2 it was shown that the mere occurrence of SCO, as well as the transition temperatures at which it occurs, seems rather erratic and therefore difficult to predict. Packing effects, for example, play a very important role in solid-state SCO compounds.¹³ Structural changes should be kept to a minimum if one hopes to keep the crystal packing of a new compound similar to that of a known SCO compound.

Inspired by earlier investigations on the SCO compounds $[\text{Fe}(\text{bapbpy})(\text{NCS})_2]$ ¹⁴ and $[\text{Fe}(\text{phen})_2(\text{NCX})_2]$ ($X=\text{S}, \text{Se}$, phen = 1,10-phenanthroline),¹⁵ a new rigid N_4 -donor ligand was designed, namely *N,N'*-bis(pyrid-2-yl)-1,10-phenanthroline-2,9-diamine (bapphen, Scheme 5.1). This tetradentate ligand consists of two amino-pyridines connected by a phenanthroline backbone. On the one hand the ligands bapphen and bapbpy are structurally similar: (i) both must coordinate to the metal centre at the basal

plane of an octahedron, leaving the axial positions for the binding of two *trans* thiocyanate or selenocyanate ions; (ii) both contain two non-coordinating N–H bridges aimed at forming intermolecular hydrogen bonds with neighbouring molecules. These hydrogen bonds have been shown to play a critical role in the cooperativity of the SCO compounds $[\text{Fe}(\text{bapbpy})(\text{NCS})_2]$ and its derivatives, and they must be kept untouched in the design of any new cooperative bapbpy-based SCO compounds.^{13, 16} On the other hand, the ligand bapphen is in principle more conjugated and more rigid than bapbpy because of the phenanthroline backbone, which might enhance the ligand field strength, and therefore increase the transition temperature of its iron(II) complexes compared to $[\text{Fe}(\text{bapbpy})(\text{NCS})_2]$.

In this Chapter, the two new compounds $[\text{Fe}(\text{bapphen})(\text{NCX})_2]$ are described with $X = \text{S}$ or Se . Their magnetic properties have been investigated and are compared to their bapbpy-based analogues $[\text{Fe}(\text{bapbpy})(\text{NCS})_2]$ (**3**) and $[\text{Fe}(\text{bapbpy})(\text{NCSe})_2]$ (**4**).

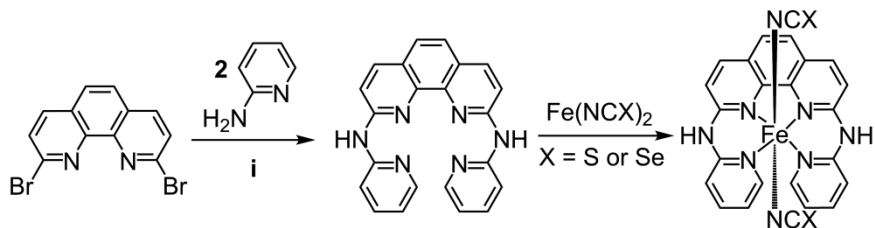


Scheme 5.1 Schematic representations of the ligands bapbpy, bapphen, and $[\text{Fe}(\text{bapphen})(\text{NCX})_2]$ ($X = \text{S}$ for **1**, or $X = \text{Se}$ for **2**).

5.2. Results

5.2.1. Synthesis and characterization

The synthesis of the ligand bapphen was performed by the previously described¹⁴ palladium-catalyzed Buchward-Hartwig cross-coupling reaction between 2-aminopyridine and 2,9-dibromo-1,10-phenanthroline (see Scheme 5.2), which are commercially available or can be prepared following literature procedures.^{17, 18} Coordination of the ligand bapphen to either iron(II) thiocyanate or iron(II)



Scheme 5.2. Synthetic route towards the ligand bapphen, and its complexes $[\text{Fe}(\text{bapphen})(\text{NCX})_2]$ ($\text{X} = \text{S}$ for **1** or $\text{X} = \text{Se}$ for **2**). Conditions for **i**: 2 mol% $\text{Pd}(\text{dba})_2$, 4 mol% (*S*)-BINAP, 4 equivalent $\text{KO}t\text{Bu}$, 80 °C in dry and degassed toluene, 3 d, yield: 68%.

selenocyanate, to prepare compounds **1a-d**, or **2a-c**, was achieved using the three different synthesis methods **a**, **b**, and **c** that are extensively described in Chapter 4, plus method **d** that consisted in the slow diffusion of MeOH and $\text{Fe}(\text{NCS})_2$ into a DCM solution of the ligand. As described in Chapter 4, different preparative methods with the same molecular building blocks may lead to materials with different SCO properties, and extreme care was taken to fully characterize the materials obtained by the different methods. The new compounds **1a-d** and **2a-b** were analyzed with IR spectroscopy and mass spectrometry. They all showed the expected $[\text{Fe}(\text{bapphen})(\text{NCX})]^+$ monocationic peak by electron-spray mass spectrometry (calculated at m/z 478.0532 for **1** and 525.9978 for **2**, see Table 5.1), which confirms coordination of the ligand bapphen to the Fe(II) ion. Consistently, the IR spectra of all iron compounds show the characteristic stretching vibrations of the coordinated thiocyanate ligands for **1**, and of the selenocyanate ligands for **2** in the range of 2080 to 2100 cm^{-1} (See Table 5.1).

Elemental analyses were performed for compounds **1b**, **1c**, **1d**, **2b**, and **2c** after thorough vacuum drying, and fitted to the formula $[\text{Fe}(\text{bapphen})(\text{NCX})_2] \cdot n\text{DMF}$ with $n = 0, 1, \text{ or } 2$ (Table AIII.1, Appendix III), but not for method **a** as explained in Chapter 4. The analyses of **1b** and **1d** suggested that no DMF molecules were trapped in the crystal lattice. The samples of both **1c** and **1d** were crystalline, they had been obtained using liquid-liquid diffusion of MeOH into DMF or DCM respectively. For **1c** elemental analysis was not very conclusive on the value of n ; however, powder X-ray diffraction showed the same phase as **1d** (Figure AIII.1, Appendix III). For **2c**, the single crystal X-ray structure determination showed two DMF solvent molecules per iron complex, but once the crystals were taken out of the mother liquor they

immediately became a reddish brown powder, which indicates the escape of solvent molecules from the crystal lattice. Elemental analyses for **2b** and **2c** after drying the crystals under vacuum for two hours, clearly showed that both compounds contained no DMF molecules in their crystal lattices (Table AIII.1). Thus the two lattice DMF molecules in **2c** are loosely bound, to form after exposure to air or vacuum a solid of the same composition as **2b**.

Table 5.1. Numbering, formulae, yields, m/z ratio for the $[\text{Fe}(\text{bapphen})(\text{NCX})]^+$ monocationic peak observed by mass spectrometry, and infrared thiocyanate/selenocyanate stretching vibrations for compounds **1** and **2**.

Compound	Formula	Yield (%)	m/z	NCX^- vibrations (cm^{-1})
1a	<i>trans</i> - $[\text{Fe}(\text{bapphen})(\text{NCS})_2]$	67	478.0525	2082
1b	<i>trans</i> - $[\text{Fe}(\text{bapphen})(\text{NCS})_2]$	52	478.0527	2084
1c	<i>trans</i> - $[\text{Fe}(\text{bapphen})(\text{NCS})_2]$	64	478.0532	2082
1d	<i>trans</i> - $[\text{Fe}(\text{bapphen})(\text{NCS})_2]$	42	478.0532	2081
2a	<i>trans</i> - $[\text{Fe}(\text{bapphen})(\text{NCSe})_2]$	68	525.9975	2086
2b	<i>trans</i> - $[\text{Fe}(\text{bapphen})(\text{NCSe})_2]$	81	525.9985	2090
2c ^a	<i>trans</i> - $[\text{Fe}(\text{bapphen})(\text{NCSe})_2] \cdot 2\text{DMF}$	–	–	–

^a Single crystals of **2c** were analyzed by single crystal X-ray structure determination and elemental analysis only.

5.2.2. Description of X-ray structures

A number of attempts to grow single crystals of **1** using method **c** were undertaken, with different concentrations and volumes. However, the resultant crystallites were not of an acceptable quality for crystal structure analysis. Changing the solvent from DMF to DCM resulted in red square-shaped single crystals, **1d**, suitable for X-ray diffraction techniques. The experimental powder X-ray diffractogram of **1c** was found to be identical to the calculated diffractogram from the single crystal X-ray structure of **1d** (Figure AIII.1, Appendix III), suggesting that **1c** and **1d** are the same phase of the same material. Overall, it is worth mentioning that although the ligands bapphen and bapbpy are structurally very similar, the crystallization of their iron complexes are very different: complex $[\text{Fe}(\text{bapbpy})(\text{NCS})_2]$ can be easily crystallized using diffusion of

MeOH into DMF in a Corning tube (method **c**), while **1** only crystallized in more specific conditions using DCM instead of DMF. The X-ray crystal structure of **1d** was determined at 100, 240 and 300 K. Remarkably the same X-ray diffraction patterns were obtained at the three temperatures, giving identical cell dimensions from 110 to 300 K. Thus, no phase transitions occurred upon variation of the temperature, suggesting that **1d** may not have SCO properties. Therefore, only the crystal structure obtained at 100 K for **1d** is presented below. The X-ray crystal structure of **2c** was determined both at 110 and 250 K. The molecular geometries of **1d** and **2c** are shown in Figure 5.1, and selected bond lengths and angles for **1d** and **2c** are provided in Table 5.2. Both **1d** and **2c** show a similar coordination environment as for the compound [Fe(bapbpy)(NCS)₂]:^{14, 16} the tetradentate ligand bapphen is coordinated to iron(II) in the basal plane, leaving the two thiocyanate (**1d**) or selenocyanate (**2c**) ligands in *trans* positions on the octahedron (Figure 5.1). Two independent DMF molecules are present per iron complex in **2c**.

Compound **1d** crystallized in the triclinic space group *P*-1. The average Fe–N bond length was found to be 2.15 Å at 100 K, which is typical of a HS Fe(II) complex in an FeN₆ octahedral environment. The basal N–Fe–N coordination angles, which vary from 78.31(7)° to 85.53(7)° (Table 5.2), and the torsion angle N1–N3–N4–N6 = 18.98(8)°, are indicative of a distorted octahedral geometry. As expected, the phenanthroline backbone is flat, and the torsion angle N4–C13–C14–N3 = 6.39(3)° is significantly smaller than the one found for the bipyridine-based complex [Fe(bapbpy)(NCS)₂] in the HS phase [N3–C10–C10B–N3B = 12.90(3)°]¹⁴ Furthermore, the angle between the two planes of the two terminal pyridine rings is 34.77° in **1d**, which is very similar compared to the one found in HS [Fe(bapbpy)(NCS)₂] (33.08°),¹⁴ which thus seems to be the result of the steric clash between facing hydrogen atoms on the terminal pyridines.

Compound **2c** crystallizes in the monoclinic space group *P*2₁/*c* both at 250 K and 110 K. The average Fe–N bond length for **2c** is 2.15 Å at 250 K and 2.08 Å at 110 K, indicating that compound **2c** is in the HS state at 250 K while it is most likely in a mixed HS/LS state at 110 K. In the structure of **2c**, the two DMF molecules are bound *via* relatively strong N–H⋯O [N2⋯O2S = 2.761(4) Å, N5⋯O1S = 2.786(4) Å] hydrogen bonding interactions between the two N–H donor groups of the ligand bapphen and the acceptor carbonyl group of DMF. The packing in **2c** is built from one-

dimensional chains with the repetitive motif $\text{DMF}\cdots\mathbf{1}\cdots\text{DMF}$ along $[1\ 1\ 0]$, via the $\text{N}-\text{H}\cdots\text{O}$ interactions. The structure is different to that of $[\text{Fe}(\text{bapbpy})(\text{NCS})_2]\cdot 2\text{DMF}$ ¹⁶ due to different space group and packing.

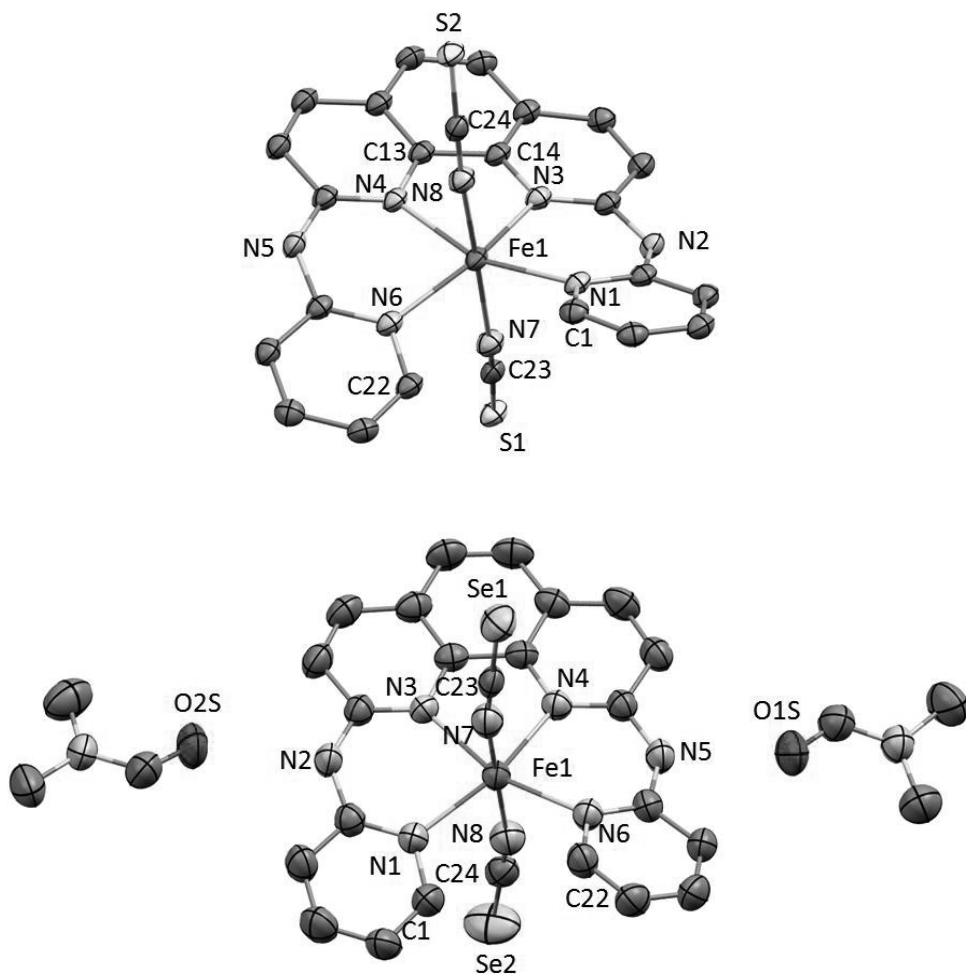


Figure 5.1. Displacement ellipsoid plots (50% probability level) for compound **1d** (HS) at 100(2) K (top) and for compound **2c** (HS) at 250(2) K (bottom). Hydrogen atoms were emitted for clarity.

Table 5.2. Selected bond lengths (Å) and angles (°) for the crystal structures of **1d** and **2c**.

	1d	2c	
T (K)	100(2)	110(2)	250(2)
Spin state	HS	HS+LS	HS
Fe1–N1	2.144(2)	2.098(3)	2.156(3)
Fe1–N3	2.126(2)	2.070(3)	2.144(3)
Fe1–N4	2.137(2)	2.051(3)	2.118(3)
Fe1–N6	2.142(2)	2.111(3)	2.174(3)
Fe1–N7	2.184(2)	2.068(4)	2.145(5)
Fe1–N8	2.155(2)	2.075(4)	2.158(5)
N2–O2S	–	2.761(4)	2.779(5)
N5–O1S	–	2.786(4)	2.798(5)
N6–Fe1–N4	85.29(7)	86.9(1)	85.3(1)
N4–Fe1–N3	78.31(7)	80.4(1)	78.7(1)
N3–Fe1–N1	85.53(7)	86.7(1)	85.2(1)
N8–Fe1–N4	84.99(7)	88.0(1)	88.0(2)
N7–Fe1–N3	82.43(7)	85.8(1)	86.0(1)
N7–Fe1–N8	177.19(7)	177.1(1)	175.3(2)
N4–C13–C14–N3	–6.39(3)	0.57(5)	0.97(6)
N6–N4–N3–N1	–18.98(8)	–12.1(1)	–13.4(2)
C1–N1–N6–C22	–42.00(2)	–38.2(3)	–34.1(4)

In the crystal packing of **1d** at 100 K, each molecule interacts with two adjacent iron complexes *via* N–H \cdots S intermolecular interactions along the crystallographic *b* axis (Figure 5.2a). The intermolecular N \cdots S distance are N2 \cdots S2 = 3.370(2) Å and N5 \cdots S1 = 3.404(2) Å, indicating strong hydrogen bond interactions that are comparable to the ones found in [Fe(bapbpy)(NCS)₂].¹⁴ Regarding π – π stacking interactions, the Fe1–S1–Fe1 intermolecular angle between the adjacent molecules *via* sulfur atom on the thiocyanate ligand is 103.89° (Figure 5.2a). The centroid-centroid distance in **1d** was found to be Cg1–Cg2 = 7.195 Å at 100 K (Cg1 and Cg2 are defined as the terminal pyridine ring between two neighbouring complexes), *i.e.*, there is no π – π stacking interaction in the direction of the N–H \cdots S hydrogen bonding network. As a

result, the intermolecular distance between the two iron centres of two closest neighbouring molecules in **1d** is much longer (Fe–Fe = 9.262(5) Å) (Figure 5.2a) than in [Fe(bapbpy)(NCS)₂]. However, two layers of the one dimensional chains of **1d** are held together by strong π – π stacking of the phenantroline backbones following the direction [1 0 $\bar{1}$] (Cg3–Cg4 = 3.599 Å, Figure 5.2b). Overall, whereas the N–H \cdots S hydrogen bonding network in **1d** seems similar to that found in [Fe(bapbpy)(NCS)₂], the π – π stacking interactions are organized in a very different manner, resulting in large iron-to-iron intermolecular distances, which seems to play a role in SCO.

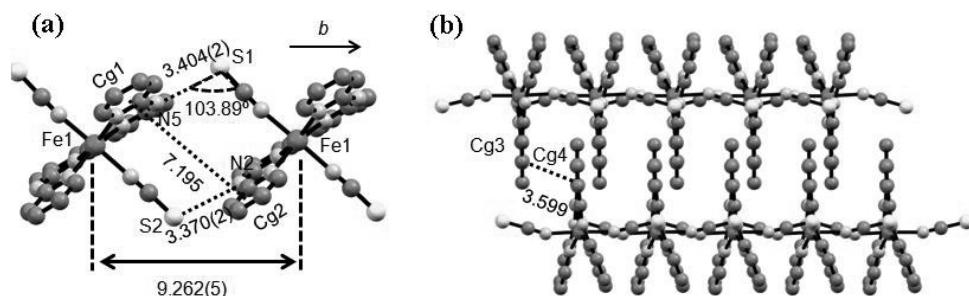


Figure 5.2. (a) N–H \cdots S hydrogen bonding network along the crystallographic *b* axis. (b) A 2D array of two layers of **1d** interact *via* π – π stacking following the direction [1 0 $\bar{1}$] at 100(2) K.

5.2.3. Magnetic properties

The temperature dependence of $\chi_M T$ was measured for samples **1a**, **1b**, **2a** and **2b**, and crystalline samples **1c** and **1d**, in both the heating and the cooling modes (Figure 5.3), where χ_M is the molar magnetic susceptibility and *T* the temperature. Samples **1c** and **1d** show room-temperature $\chi_M T$ values of 3.51 and 3.57 cm³ K mol^{−1}, respectively, in agreement with a HS iron(II) centre in an octahedral FeN₆ environment. However, no significant change in $\chi_M T$ values was observed between 30 K and 300 K for both samples: both **1c** and **1d** stay in the high-spin (HS) state. This result is consistent with the X-ray single crystal studies of **1d** at 110, 240, and 310 K, and confirms that **1c** and **1d** are identical materials. Unexpectedly, compounds **1a** and **1b** show complicated SCO behaviour across the same temperature range. The magnetic susceptibility measurement for the powder sample **1a** shows two gradual transitions at low temperature and one abrupt transition with hysteresis around 280 K (Figure 5.3). The $\chi_M T$ value of 3.0 cm³ K mol^{−1} remains constant from 300 K to 280 K, where it abruptly

decreases to a value of $2.3 \text{ cm}^3 \text{ K mol}^{-1}$ at 260 K. Then the value of $\chi_M T$ gradually decreases from $2.3 \text{ cm}^3 \text{ K mol}^{-1}$ down to $1.3 \text{ cm}^3 \text{ K mol}^{-1}$ at 61 K. The further decrease of $\chi_M T$ below 50 K is a typical feature of a kinetically frozen spin transition (see Discussion). The transition temperatures for the first transition of **1a**, measured as the maximum of $d(\chi_M T)/dT$ vs. T (Figure AIII.2), was found to be 268(4) K in the cooling mode and 280(4) K in the heating mode, which defines a hysteresis width of 12 K (Table 5.3). The second and third transitions occur at 152(8) K and 77(4) K, respectively, and do not show any hysteresis. For compound **1b**, the magnetic susceptibility measurements showed similar SCO behaviour compared to **1a**, with a less complete first transition and a higher residual HS fraction at low temperatures, *i.e.*, higher $\chi_M T$ values across the whole temperature range.

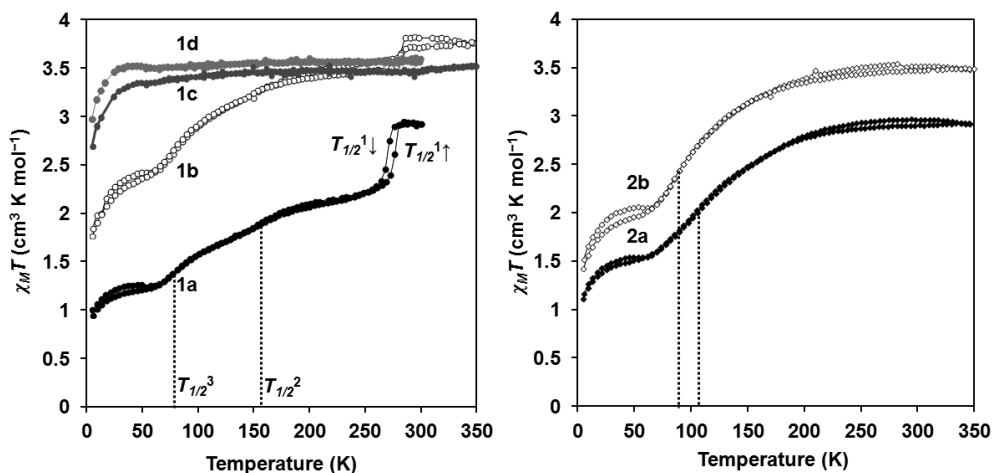


Figure 5.3. Thermal variation of $\chi_M T$ for compounds **1a**, **1b**, **1c**, and **1d** (left); **2a**, and **2b** (right). Scan rate 0.3-1.1 K min^{-1} . The cooling and heating curves are identical for **1c** and **1d**, therefore only the heating curve is shown respectively.

The remarkable difference between the magnetic properties of samples **1a**, **1b**, and **1d** (**1c**) suggests that packing effects play a critical role in the SCO behaviour of $[\text{Fe}(\text{bapphen})(\text{NCS})_2]$. The power X-ray diffractograms of the three materials **1a**, **1b**, and **1d**, was thus measured as it can provide global information on phase/crystal structure in the solid state. Sample **1a** clearly shows a diffractogram that is different from **1d**, which suggests that both samples have different structures. As shown in

Figure 5.4, the major differences between **1a** and **1d** are: (i) the intense reflection peaks at $2\theta \approx 19^\circ$ and 21° for **1a** (circle), which are not present in **1d**; (ii) other reflections of **1a**, e.g. at $2\theta \approx 24^\circ$ (diamond), and 25° (triangle) that are absent in **1d**. The powder X-ray diffractogram for **1b**, although poorly resolved, however shows some resemblance to the calculated diffractogram for **1d**. In combination with the magnetic susceptibility measurement of **1b**, these data suggest that **1b** is a mixture between **1a** and **1d** in an amorphous phase. Overall, compound **1** shows at least two forms **1a** and **1d** with remarkably different magnetic properties, which are obtained depending on the preparation methods.

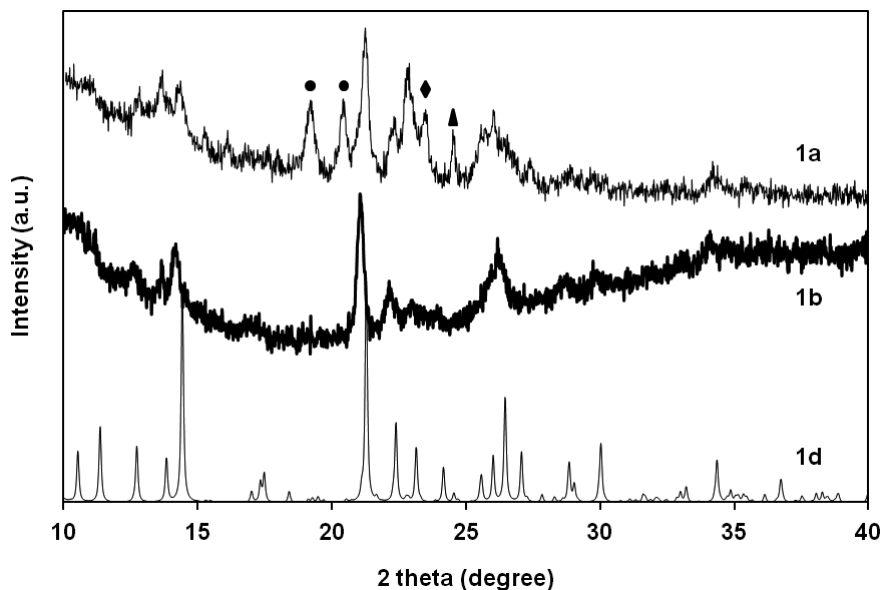


Figure 5.4. Experimental powder X-ray diffractograms for **1a** and **1b** in the range $10\text{-}40^\circ$ (2θ) measured at room temperature. The calculated powder pattern derived from the crystal structure of **1d** at 240 K using program Mercury¹⁹ is also shown. The symbols in **1a** indicate the most significant differences with samples **1b** and **1d**.

The magnetic susceptibility measurements for **2a** and **2b** show SCO behaviour for both compounds. The $\chi_M T$ values for both compounds gradually decrease from 350 K to 60 K, and after a short plateau decrease again due to a kinetically frozen spin transition (Figure 5.3). As for compound **1** the $\chi_M T$ values are higher in **2b** compared to **2a** across the whole temperature range, indicating a higher degree of metallation with method **b**.

A single transition temperature can be defined for **2a** and **2b**; its value is 101(4) K and 85(4) K for **2a**, and **2b** respectively (see Appendix III). Comparing the magnetic susceptibility measurements for compounds **1a**, **1b** and **2a**, **2b**, it appears that the spin crossover in **2a** and **2b** is more gradual, and that the hysteresis loop is lost with NCSe⁻ ligands compared to thiocyanate ligands, in which the SCO was found to be cooperative in **1a** and **1b** (Figure 5.3).

Table 5.3. Transition temperatures for compounds **1a**, **1b**, **2a**, and **2b** as determined by magnetic susceptibility measurements.

Compound	$T_{1/2}^1(\text{K})^a$	$T_{1/2}^1 \downarrow (\text{K})^b$	$T_{1/2}^1 \uparrow (\text{K})$	$\Delta T_{\text{hys}}^1(\text{K})$	$T_{1/2}^2(\text{K})$	$T_{1/2}^3(\text{K})$
1a	274(4)	268(4)	280(4)	12(6)	152(8)	77(4)
1b	282(4)	277(4)	286(4)	9(6)	–	–
2a	101(4)	–	–	–	–	–
2b	85(4)	–	–	–	–	–

^a $T_{1/2}^1$ is defined as $(T_{1/2}^1 \uparrow + T_{1/2}^1 \downarrow) / 2$. ^b $T_{1/2} \downarrow$ and $T_{1/2} \uparrow$ are defined as the temperatures where $d(\chi_M T)/dT$ has a maximum in the cooling mode or in the heating mode (Appendix III).

5.3. Discussion

The $\chi_M T$ vs. T plots for **1a** and its analogue [Fe(bapbpy)(NCS)₂] (**3a**), as well as for **2a** and [Fe(bapbpy)(NCSe)₂] (**4a**) (Figure 5.5), show very different SCO behaviours. This is remarkable since bapbpy and bapphen are structurally very similar ligands, thus showing the sensitivity of the SCO phenomenon to small changes in the molecular structure of the metal complex. Upon careful observation, however, the $\chi_M T$ vs. T plot for **1a** shows multi-step spin transitions, which is rather similar to [Fe(bapbpy)(NCS)₂] even if three steps are observed instead of two, and even if the residual HS fraction remains high at low temperature for **1a** whereas for [Fe(bapbpy)(NCS)₂] the SCO is complete. Similarly, the $\chi_M T$ vs. T plot for **2a** shows a gradual transition, which was also found for [Fe(bapbpy)(NCSe)₂] (see Chapter 4).

The fact that the transitions in **1a** and **2a** are incomplete might be explained by the interplay between thermal spin-crossover and spin-trapping.²⁰⁻²² In thermal SCO, for both LS and HS states the electronic energies can be calculated as a function of the

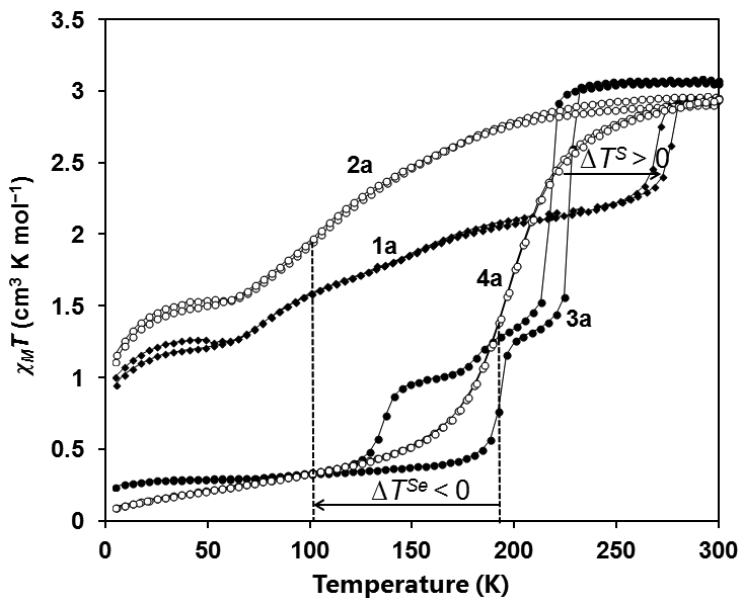


Figure 5.5. Comparison of $\chi_M T$ vs. T curves for compounds **1a**, **2a**, **3a** ($[\text{Fe}(\text{bapbpy})(\text{NCS})_2]$), and **4a** ($[\text{Fe}(\text{bapbpy})(\text{NCSe})_2]$). ΔT^{S} and ΔT^{Se} indicate the change in the SCO transition temperature $T_{1/2}$ ¹ between $X = \text{S}$ and $X = \text{Se}$ for $[\text{Fe}(\text{L})(\text{NCX})_2]$ compounds ($\text{L} = \text{bapbpy}$ or bapphen).

average metal-to-ligand distance (Figure 5.6a). The difference between the zero-point energies of the two states can be expressed as $\Delta E_{HL}^0 = \Delta E_{HS}^0 - \Delta E_{LS}^0$ (Figure 5.6a). In general, all complexes will be in the LS state at low temperatures, whereas at elevated temperatures an entropy-driven HS state can be observed.²³ An energy barrier (ΔE_{act}) must be overcome before the HS \rightarrow LS transition can take place (Figure 5.6a). Under normal conditions, the energy needed for overcoming this barrier (ΔE_{act}) is provided by thermal energy (kT). Upon lowering the temperature rapidly, however, if the HS \rightarrow LS relaxation is slow, *i.e.* $kT \ll \Delta E_{act}$, it is possible to ‘freeze’ the metastable HS species.^{24, 25} This is typically realized in quench-cooling experiments, where the sample is cooled down to 5 K within seconds, or in a T_{LIESST} (LIESST = Light-Induced Spin-State Trapping) experiment, in which the SCO compound first undergoes a slow and complete spin-crossover to the LS state upon cooling, followed by radiation of the LS state material at low temperatures to photochemically produce the HS state at low temperature (Figure 5.6b). When the laser is switched off, the compound remains HS until it is warmed above the T_{LIESST} temperature where the thermal energy becomes high enough to overcome the activation barrier that is necessary to relax from the HS

state to the LS state ($kT \geq \Delta E_{act}$). However if T_{LIESST} approaches $T_{1/2}$ as shown in Figure 5.6c, the HS state becomes metastable and may not undergo the complete transition to the LS state, because the thermal relaxation of HS to LS becomes too slow near $T_{1/2}$, *i.e.*, near T_{LIESST} . This case is similar to thermal spin trapping. For compounds $[\text{Fe}(\text{bapbpy})(\text{NCX})_2]$ the transition temperatures $T_{1/2}$ are high compared to T_{LIESST} ($T_{LIESST} = 56 \text{ K}$ for $[\text{Fe}(\text{bapbpy})(\text{NCS})_2]$),¹⁶ leading to low residual HS fraction in the LS phase. In contrast, for $[\text{Fe}(\text{bapphen})(\text{NCX})_2]$ the low $T_{1/2}$ leads to high residual HS fractions even at 5 K.

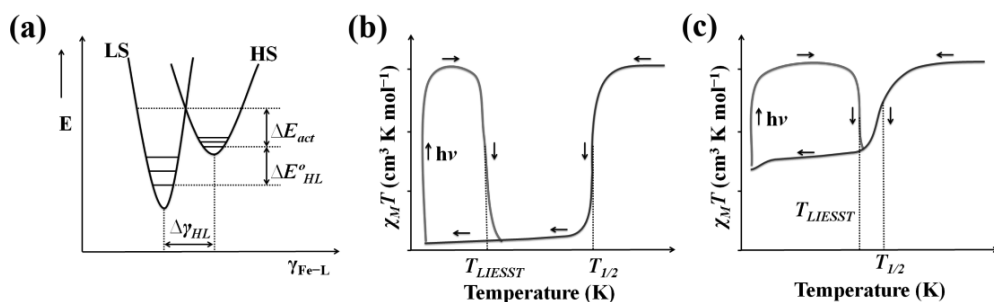


Figure 5.6. (a) Schematic representation of the potential wells for the LS and HS states of an iron(II) SCO compound; (b) and (c) schematic representations of relaxation processes when slow thermal spin-crossover and LIESST are followed by slow warming above T_{LIESST} , in the case of an abrupt SCO system and with $T_{LIESST} \ll T_{1/2}$ (b) or when $T_{LIESST} \approx T_{1/2}$ (c).

Furthermore, striking differences were observed between the magnetic behaviour of $[\text{Fe}(\text{L})(\text{NCS})_2]$ and $[\text{Fe}(\text{L})(\text{NCSe})_2]$ (L = bapphen or bapbpy). For compound $[\text{Fe}(\text{bapphen})(\text{NCS})_2]$ a higher $T_{1/2}$ was found for **1a** than for $[\text{Fe}(\text{bapbpy})(\text{NCS})_2]$ (**3a**, $\Delta T^S > 0$, see Figure 5.5). This is indeed what was expected since the more conjugated and more rigid phenantroline backbone was thought to give a higher ligand field strength, and therefore increase the transition temperature of its iron(II) complexes compared to **3a**. However, for compound $[\text{Fe}(\text{bapphen})(\text{NCSe})_2]$, the transition temperature $T_{1/2}$ in **2a** is more than 90 K lower than that of $[\text{Fe}(\text{bapbpy})(\text{NCSe})_2]$ (**4a**, $\Delta T^{Se} < 0$, see Figure 5.5). Thus, the simple model based on the ligand field strength cannot be used to predict the evolution of transition temperatures in SCO. Indeed, it does not take into account crystal packing effects and supramolecular interactions, which play a critical role in the SCO phenomenon.

This role is best demonstrated by the effect of different preparative methods on the SCO behaviour of compound **1**. Previous studies have shown that different polymorphs arising from different preparative methods can have very different SCO properties.²⁶⁻²⁸ The first form of compound **1**, obtained *via* method **a**, exhibits cooperative spin crossover. It was obtained from a methanol suspension that was stirred with Fe(NCS)₂ overnight leading to impregnation of the ligand suspension by the metal to form the complex. In contrast, the second form, **1d**, was obtained from slow crystallization from MeOH–DCM mixtures after three days. This difference in preparation crystallization results in two distinctive crystal structures for compound **1** (Figure 5.4), which strongly affects the FeN₆ coordination sphere and decides whether SCO can occur or not.

Comparing the crystal structures of **1c/1d** and **3c** ([Fe(bapbpy)(NCS)₂]) may help understanding why **1d** has lost SCO properties (Figure AIII.3, Appendix III). Although the ligand sets with bapphen and bapbpy are almost identical, there are small deviations of the orientation of the thiocyanate ligands, which has been suggested as a possible reason for the absence of SCO (see Chapter 2). Furthermore, the crystal packing in **1d** is very different from that of **3c**. For example, although the 1D chains of N–H⋯S intermolecular interactions exist in both crystal structures, the π – π stacking interactions do not occur between dipyridylamine units along the infinite 1D chain in **1d**, but rather between phenantroline moieties following the direction [1 0 –1]. The fact that **1d** does not have SCO properties may thus either be attributed to the different orientation of the NCS[–] ligands or to the absence of π – π stacking interaction along the direction of the N–H⋯S network.

5.4. Conclusion

The new rigid ligand bapphen was synthesized, and a series of new iron(II) complexes based on bapphen was prepared. The complex [Fe(bapphen)(NCS)₂] appears to exist as two different forms, **1a** and **1d**. In **1a** a three-step incomplete SCO is observed with a hysteresis loop occurring near 280 K. Although the intermediate phases in **1a** are not fully characterized yet, our hypothesis is that T_{LIESST} might be very close to $T_{1/2}$ ³ for this compound, causing very slow relaxation from the second intermediate phase to the fully LS state. Further characterization of the two intermediate phases is ongoing. The crystal structure of **1d** was obtained, but this form of [Fe(bapphen)(NCS)₂] has no SCO properties. The magnetic behaviour of [Fe(bapphen)(NCSe)₂] (**2a**) shows that the cooperativity of the transition is lost upon substitution of S by Se, which is consistent

with the trend found for babppy. Overall, this case study demonstrates that the mere occurrence of SCO, as well as the transition temperatures, are impossible to predict based on ligand field strength, as packing effects play a critical role in the magnetic properties of solid-state SCO compounds.

5.5. Experimental

5.5.1 General information

All reactions were performed under argon using standard Schlenk line techniques. The applied vacuum was about 10^{-3} mbar. Toluene was dried over sodium. Degassed solvents were obtained by bubbling argon through 50 mL solvent in a Schlenk flask for one hour. Degassed solvents were used for all complex syntheses. The reagent 2,9-dibromo-1,10-phenanthroline was synthesized using literature procedures.^{17, 18} All other chemicals were obtained from commercial sources and used without further purification. Filtration of complexes was carried out using Whatman RC60 membrane filters. NMR Spectra were measured on a Bruker DPX-300 spectrometer at room temperature. Chemical shifts are indicated in *ppm* relative to TMS. Mass spectra were obtained using soft electron-spray from a Thermoquest Finnagen AQA. High resolution mass spectra were measured using direct injection (2 μ L of a 2 μ M solution in DMF and 0.1% formic acid on a mass spectrometer (Thermo Finnigan LTQ Orbitrap) equipped with an electron-spray ion source in positive mode (source voltage 3.5 kV, sheath gas flow 10, capillary temperature 275 °C) with resolution $R=60.000$ at $m/z=400$ (mass range = 150-2000) and dioctylphtalate ($m/z=391.28428$) as "lock mass". Infrared spectra were acquired on a Perkin Elmer FT-IR spectrometer PARAGON 1000 at room temperature. Elemental analyses (C,H,N,S) were obtained from a Perkin-Elmer 2400 Series II analyzer.

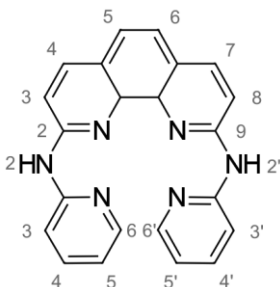
Single crystal X-Ray diffraction data of **1d** and **2c** were collected by measuring all reflection intensities using a KM4/Xcalibur (detector: Sapphire3) with enhance graphite-monochromated Mo $K\alpha$ radiation ($\lambda = 0.71073$ Å) under the program CrysAlisPro (Version 1.171.35.11 Oxford Diffraction Ltd., 2011). The program CrysAlisPro was used to refine the cell dimensions. Data reduction was done using the program CrysAlisPro. The structure was solved with the program SHELXS-97²⁹ and was refined on F^2 with SHELXL-97.²⁹ Analytical numeric absorption corrections based on a multifaceted crystal model were applied using CrysAlisPro. The temperature of the data collection was controlled using the system Cryojet (manufactured by Oxford Instruments). The H atoms (except when specified) were placed at calculated positions using the instructions AFIX 43 with isotropic displacement parameters having values 1.2 times U_{eq} of the attached C atoms. The H

atoms attached to N1 and N2 were found from difference Fourier maps, and its coordinates/isotropic factor were refined freely [the N–H distance was restrained to 0.88(3) Å using the DFIX command].

For magnetic susceptibility measurements, each sample was mounted in a plastic straw before introduction in a Quantum Design MPMS–XL SQUID magnetometer. DC magnetization measurements were performed in a field of 0.1 T, from 5 to 350 K (heating mode) and from 350 to 5 K (cooling mode) with a rate of 0.3–1.1 K min⁻¹ for compounds **1b**, **1c**, **2a**, and **2b**; from 5 to 300 K (heating mode) and from 300 to 5 K (cooling mode) with a rate of 0.3–1.1 K min⁻¹ for compounds **1a** and **1d**. For each sample the total measuring time was ~20 h. Corrections for the diamagnetism of the samples were calculated using Pascal's constants.³⁰

5.5.2 Preparation of *N,N'*-bis(pyrid-2-yl)-1,10-phenanthroline-2,9-diamine (bapphen):

2-Aminopyridine (280 mg, 2.97 mmol), 2,9-dibromo-1,10-phenanthroline (500 mg, 1.48 mmol), Pd(dba)₂ (20.9 mg, 0.0363 mmol), (S)-BINAP (36.6 mg, 0.0587 mmol) and KO^tBu (666 mg, 5.94 mmol) were weighed into a two-neck round-bottom flask, placed under argon atmosphere, and suspended in distilled and degassed toluene (30 mL). The brown suspension was heated to 80 °C and stirred under argon for 40 hours. The red/brown suspension was then cooled to room temperature and demineralized water (30 mL) was added. The mixture was



stirred vigorously for 1.5 hours, filtered, and washed three times with water, diethyl ether, and hexanes. The yellow solids were collected, dried in vacuum for two hours, to yield 68% of bapphen (368 mg, 1.01 mmol). ¹H NMR (DMSO-*d*⁶): δ= 10.12 (s, 2 H; 2 NH), 9.26 (d, J = 6 Hz, 2H, pyH^{3,3'}), 8.31 (m, 2H, pyH^{6,6'}), 8.23 (d, J = 6 Hz, 2H, phenH^{3,8}), 7.64 (s, 2H, phenH^{5,6}), 7.56 (d, ³J (H,H)= 9 Hz, 2 H, phenH^{4,7}), 7.49 (m, 2 H, pyH^{4,4'}), 6.98 ppm (m, 2 H, pyH^{5,5'}). ¹³C NMR (DMSO-*d*⁶): δ=154.11 (Cq), 153.14 (Cq), 147.76 (pyC^{6,6'}), 143.26 (phenC^{11,12}), 137.98 (pyC^{4,4'}), 137.46 (phenC^{3,8}), 124.06 (phenCq), 122.87 (phenC^{5,6}), 116.59 (pyC^{5,5'}), 114.62 (phenC^{4,7}), 111.58 (pyC^{3,3'}). MS (MeOH) *m/z* (calc): 364.4 (365.0, [M+H]⁺). HR–MS (DMF): *m/z* (calc): 365.1506 (365.1509, [M+H]⁺). EA calc (%) for C₂₂H₁₆N₆H₂O: C 69.10, H 4.74, N 21.97; found: C 70.54, H 3.61, N 21.53. IR spectroscopy (cm⁻¹): 3012, 1622, 1576, 1560, 1516, 1472, 1452, 1340, 1311, 1230, 1142, 1089, 994, 840, 770, 729, 616, 594, 514, 486, 414.

5.5.3 Preparation of complexes [Fe(bapphen)(NCX)₂] (X=S or Se):

Preparation of 0.1 M [Fe(NCX)₂] solution (X=S or Se): FeSO₄ (152 mg, 1.00 mmol), ascorbic acid (5 mg), and KNCS (194 mg, 2.00 mmol) or, respectively, KNCSe (288 mg, 2.00 mmol), were mixed in MeOH (6 mL) and stirred under argon for half an hour. The white, respectively slightly orange, suspension was filtered over Celite on filter paper into a 10 mL volumetric flask. The flask was filled up to 10 mL with MeOH, resulting in a clear solution, which was prepared fresh every time.

Four methods noted **a**, **b**, **c**, or **d** were used to synthesize the iron(II) complexes [Fe(bapphen)(NCX)₂] (X=S or Se). The compounds are designated **a**, **b**, **c** or **d**, depending on their preparation method.

Method a: bapphen (40 mg, 0.11 mmol for **1a**; 50 mg, 0.14 mmol for **2a**) was suspended in degassed MeOH (3 mL) and stirred under argon to form a yellow suspension. 1.1 equivalent of Fe(NCS)₂ or Fe(NCSe)₂ (0.12 mmol for **1a**; 0.15 mmol for **2a**, 0.1 M stock solution) was added to the mixture, and an immediate colour change to red was observed. The suspension was stirred under argon for 18 hours, filtered over a micropore filter, washed with degassed MeOH, and finally dried *in vacuo* for 3 hours.

Method b: bapphen (20 mg, 0.05 mmol for **1b**; 51 mg, 0.14 mmol for **2b**) was dissolved in degassed DMF (3 mL) under argon. To the clear yellow solution, 1.1 equivalent of Fe(NCS)₂ or Fe(NCSe)₂ (0.06 mmol for **1b**; 0.15 mmol for **2b**, 0.1 M stock solution) was added and an immediate colour change to red was observed. The solution was stirred under argon for 18 hours, upon which a dark precipitate appeared. The precipitate was filtered over a micropore filter, washed with MeOH, and finally dried in vacuum for 3 h.

Method c: to grow crystals of compound **1** (**1c**): 10 mg of bapphen was dissolved in 2 mL degassed DMF, affording a clear yellow solution. A small amount of ascorbic acid (5 mg) was added to prevent oxidation. 1 mL aliquots of this solution were pipette-filtered over 1 cm Celite into the vertical compartment of two Y-shaped glass tubes, 1.0 mL of the 0.1 M Fe(NCS)₂ solution was carefully added into the other compartment of the glass tube. Then both solutions were frozen by dipping each Y-shaped glass tube into liquid nitrogen. Then an additional layer of pure DMF (1 mL) was added on top of the frozen bapphen solution, and finally degassed MeOH was carefully added to fill the entire glass tube. The glass tubes were then stoppered and kept under argon using balloons at room temperature, and if possible under sun light, to allow slow liquid/liquid diffusion. Single crystals were obtained typically within a week once formed. The crystals of **1c** or **1d** were not vacuum or air sensitive and therefore could be handled under ambient conditions for several weeks.

To grow crystals of compound **2** (**2c**), bapphen (25 mg) was dissolved in degassed DMF (5 mL). 1 mL aliquots of this solution were pipette-filtered over 1 cm Celite into five Corning tubes. To each tube 0.15 mL of the Fe(NCSe)₂ solution was carefully added to create a two-layer system. Degassed methanol was then layered on top of these layers. The tubes were then stoppered and left untouched at room temperature, and if possible under sunlight, to allow slow liquid/liquid diffusion. Within 3 days, dark crystals of **2c** appeared at the wall of the vials. The tubes were immediately sent for single crystal X-ray structure determination. Once the crystals left the mother liquor they immediately became reddish brown powder.

Method d: to grow single crystals of **1d**, the procedure of **1c** (above) was followed using DCM instead of DMF. The quantities of chemicals were followed with exact same amounts.

[Fe(bapphen)(NCS)₂] (**1a**): the red solid was obtained with a yield of 67% (40 mg, 0.074 mmol). IR spectroscopy (cm⁻¹): 3278, 3206, 3080, 3134, 2082 (NCS⁻), 1630, 1600, 1581, 1543, 1516, 1472, 1428, 1370, 1244, 1149, 1105, 1009, 847, 773, 731, 647, 592, 500, 418, 316. HR-MS (DMF): *m/z* (calc): 478.0525 (478.0532, [M-NCS]⁺).

[Fe(bapphen)(NCS)₂] (**1b**): the red solid was obtained with a yield of 52% (15 mg, 0.029 mmol). IR spectroscopy (cm⁻¹): 3278, 3190, 3132, 3040, 2084 (NCS⁻), 1630, 1600, 1582, 1542, 1472, 1418, 1369, 1266, 1244, 1147, 1104, 1010, 848, 773, 732, 668, 648, 527, 500, 418, 336, 322. HR-MS (DMF): *m/z* (calc): 478.0527 (478.0532, [M-NCS]⁺). EA calc (%) for C₂₄H₁₆FeN₈S₂: C 53.74, H 3.01, N 20.90, S 11.93; found: C 52.57, H 1.97, N 20.49, S 11.05. ¹H NMR (DMSO-*d*⁶): δ = 84.43, 78.55, 38.76, 27.67, 12.22, 11.51, 9.76.

[Fe(bapphen)(NCS)₂] (**1c**): dark red crystallites were obtained with a yield of 64%, however the crystals were not good enough for single crystal X-ray structure determination. IR spectroscopy (cm⁻¹): 3278, 3192, 3132, 3052, 2082 (NCS⁻), 1629, 1600, 1582, 1540, 1472, 1418, 1368, 1244, 1147, 1104, 1009, 848, 722, 730, 668, 648, 500, 470, 418, 321. HR-MS (DMF): *m/z* (calc): 478.0532 (478.0532, [M-NCS]⁺). EA calc (%) for C₂₄H₁₆FeN₈S₂: C 53.74, H 3.01, N 20.89, S 11.95; found: C 52.87, H 3.59, N 20.01, S 10.24.

[Fe(bapphen)(NCS)₂] (**1d**): small red square-shaped blocks were obtained with a yield of 42%. IR spectroscopy (cm⁻¹): 3276, 3190, 3130, 3055, 2081 (NCS⁻), 1629, 1599, 1580, 1542, 1473, 1422, 1368, 1243, 1147, 1103, 1008, 848, 772, 729, 667, 647, 499, 469. HR-MS (DMF): *m/z* (calc): 478.0532 (478.0532, [M-NCS]⁺). EA calc (%) for C₂₄H₁₆FeN₈S₂: C 53.74, H 3.01, N 20.89, S 11.95; found: C 53.36, H 2.74, N 20.11, S 11.15.

Crystal data: Fw = 536.42, small red block, 0.11 × 0.08 × 0.08 mm³, triclinic, *P*-1 (no. 2), *a* = 8.6588(3), *b* = 9.2618(3), *c* = 14.2198(4) Å, α = 101.113(2)°, β = 96.671(3)°, γ =

90.935(3)°, $V = 1110.54(6) \text{ \AA}^3$, $Z = 2$, $D_x = 1.604 \text{ g cm}^{-3}$, $\mu = 7.472 \text{ mm}^{-1}$, abs. corr. range: 0.541–0.667. 15376 Reflections were measured up to a resolution of $(\sin \theta/\lambda)_{\max} = 0.62 \text{ \AA}^{-1}$. 4361 Reflections were unique ($R_{\text{int}} = 0.0321$), of which 4037 were observed [$I > 2\sigma(I)$]. 324 Parameters were refined using 2 restraints. $R1/wR2$ [$I > 2\sigma(I)$]: 0.0354/0.0938. $R1/wR2$ [all refl.]: 0.0390/0.0967. $S = 1.035$. Residual electron density found between -0.40 and 0.72 e \AA^{-3} .

[Fe(bapphen)(NCSe)₂] (**2a**): the red solids were obtained with a yield of 68% (59 mg, 0.094 mmol). IR spectroscopy (cm^{-1}): 3277, 3188, 3132, 3040, 2086 (NCSe⁻), 1628, 1600, 1580, 1542, 1472, 1424, 1368, 1266, 1243, 1148, 1104, 1009, 844, 768, 731, 668, 647, 616, 513, 499, 418, 322. HR-MS (DMF): m/z (calc): 525.9975 (525.9978, [M–NCSe]⁺).

[Fe(bapphen)(NCSe)₂] (**2b**): the red solids were obtained with a yield of 81% (57 mg, 0.11 mmol). IR spectroscopy (cm^{-1}): 3277, 3189, 3132, 3056, 2090 (NCSe⁻), 1629, 1600, 1581, 1542, 1516, 1472, 1423, 1390, 1369, 1351, 1266, 1243, 1148, 1104, 1009, 846. HR-MS (DMF): m/z (calc): 525.9985 (525.9978, [M–NCSe]⁺). EA calc (%) for C₂₄H₁₆FeN₈Se₂: C 45.72, H 2.56, N 17.78; found: C 45.15, H 1.76, N 17.45. ¹H NMR (DMSO-*d*⁶): $\delta = 83.76$, 78.09, 44.09, 38.35, 27.27, 12.28, 11.31, 9.44.

[Fe(bapphen)(NCSe)₂] \cdot 2DMF (**2c**): crystal data: **Phase I** (110(2) K): $F_w = 776.41$, black irregular shape crystal, $0.36 \times 0.15 \times 0.14 \text{ mm}^3$, monoclinic, $P2_1/c$ (no. 14), $a = 13.8105(4)$, $b = 16.6679(4)$, $c = 14.6516(5) \text{ \AA}$, $\beta = 112.851(4)^\circ$, $V = 3107.99(18) \text{ \AA}^3$, $Z = 4$, $D_x = 1.659 \text{ g cm}^{-3}$, $\mu = 2.874 \text{ mm}^{-1}$, abs. corr. range: 0.566–0.755. 16892 Reflections were measured up to a resolution of $(\sin \theta/\lambda)_{\max} = 0.59 \text{ \AA}^{-1}$. 5481 Reflections were unique ($R_{\text{int}} = 0.0321$), of which 4446 were observed [$I > 2\sigma(I)$]. 448 Parameters were refined using 134 restraints. $R1/wR2$ [$I > 2\sigma(I)$]: 0.0420/0.0972. $R1/wR2$ [all refl.]: 0.0556/0.1029. $S = 1.045$. Residual electron density found between -1.09 and 1.18 e \AA^{-3} . **Phase II** (250(2) K): $F_w = 776.41$, dark red irregular shape crystal, $0.36 \times 0.15 \times 0.14 \text{ mm}^3$, monoclinic, $P2_1/c$ (no. 14), $a = 14.0472(7)$, $b = 16.6733(6)$, $c = 14.9392(7) \text{ \AA}$, $\beta = 113.775(6)^\circ$, $V = 3202.0(2) \text{ \AA}^3$, $Z = 4$, $D_x = 1.611 \text{ g cm}^{-3}$, $\mu = 2.790 \text{ mm}^{-1}$, abs. corr. range: 0.525–0.743. 14132 Reflections were measured up to a resolution of $(\sin \theta/\lambda)_{\max} = 0.58 \text{ \AA}^{-1}$. 5206 Reflections were unique ($R_{\text{int}} = 0.0346$), of which 3900 were observed [$I > 2\sigma(I)$]. 446 Parameters were refined using 146 restraints. $R1/wR2$ [$I > 2\sigma(I)$]: 0.0456/0.1141. $R1/wR2$ [all refl.]: 0.0656/0.1221. $S = 1.032$. Residual electron density found between -0.44 and 0.50 e \AA^{-3} . Once the crystals left the mother liquor they immediately became reddish brown powder. EA calc (%) for C₂₄H₁₆FeN₈Se₂: C 45.72, H 2.56, N 17.78; found: C 45.73, H 2.63, N 17.64.

5.6 References:

1. A. Bousseksou, G. Molnar and G. Matouzenko, *Eur. J. Inorg. Chem.*, 2004, 4353-4369.
2. J. F. Létard, P. Guionneau and L. Goux-Capes, *Top. Curr. Chem.*, 2004, 235, 221-249.
3. O. Kahn and C. J. Martinez, *Science*, 1998, 279, 44-48.
4. M. Ohba, K. Yoneda, G. Agustí, M. C. Muñoz, A. B. Gaspar, J. A. Real, M. Yamasaki, H. Ando, Y. Nakao, S. Sakaki and S. Kitagawa, *Angew. Chem.*, 2009, 121, 4861-4865.
5. P. D. Southon, L. Liu, E. A. Fellows, D. J. Price, G. J. Halder, K. W. Chapman, B. Moubaraki, K. S. Murray, J. F. Létard and C. J. Kepert, *J. Am. Chem. Soc.*, 2009, 131, 10998-11009.
6. L. Salmon, G. Molnar, D. Zitouni, C. Quintero, C. Bergaud, J. C. Micheau and A. Bousseksou, *J. Mater. Chem.*, 2010, 20, 5499-5503.
7. M. S. Alam, M. Stocker, K. Gieb, P. Müller, M. Haryono, K. Student and A. Grohmann, *Angew. Chem. Int. Ed.*, 2010, 49, 1159-1163.
8. M. Cavallini, I. Bergenti, S. Milita, G. Ruani, I. Salitros, Z.-R. Qu, R. Chandrasekar and M. Ruben, *Angew. Chem.*, 2008, 120, 8724-8728.
9. P. Gütllich and H. A. Goodwin, *Top. Curr. Chem.*, 2004, 233, 1-47.
10. I. Šalitroš, N. T. Madhu, R. Boča, J. Pavlik and M. Ruben, *Monatsh. Chem.*, 2009, 140, 695-733.
11. H. Spiering, T. Kohlhaas, N. Romstedt, A. Hauser, C. Bruns-Yilmaz, J. Kusz and P. Gütllich, *Coord. Chem. Rev.*, 1999, 192, 629-647.
12. J. Klingele, D. Kaase, M. Schmucker, Y. Lan, G. Chastanet and J.-F. Létard, *Inorg. Chem.*, 2013, 52, 6000-6010.
13. Z. Arcis-Castillo, S. Zheng, M. A. Siegler, O. Roubeau, S. Bedoui and S. Bonnet, *Chem. Eur. J.*, 2011, 17, 14826-14836.
14. S. Bonnet, M. A. Siegler, J. S. Costa, G. Molnar, A. Bousseksou, A. L. Spek, P. Gamez and J. Reedijk, *Chem. Commun.*, 2008, 5619-5621.
15. E. Konig and K. Madeja, *Chem. Commun.*, 1966, 61-62.
16. S. Bonnet, J. b. Molnar, J. Sanchez Costa, M. A. Siegler, A. L. Spek, A. Bousseksou, W.-T. Fu, P. Gamez and J. Reedijk, *Chem. Mater.*, 2009, 21, 1123-1136.
17. J. Frey, T. Kraus, V. Heitz and J.-P. Sauvage, *Chem. Eur. J.*, 2007, 13, 7584-7594.
18. T. Ishii, R. Hirashima, N. Tsutsumi, S. Amemori, S. Matsuki, Y. Teshima, R. Kuwahara and S. Mataka, *J. Org. Chem.*, 2010, 75, 6858-6868.
19. C. F. Macrae, I. J. Bruno, J. A. Chisholm, P. R. Edgington, P. McCabe, E. Pidcock, L. Rodriguez-Monge, R. Taylor, J. van de Streek and P. A. Wood, *J. Appl. Crystallogr.*, 2008, 41, 466-470.
20. J. F. Létard, *J. Mater. Chem.*, 2006, 16, 2550-2559.
21. M. A. Halcrow, *Chem. Soc. Rev.*, 2008, 37, 278-289.
22. F. Varret, K. Boukheddaden, G. Chastanet, N. Paradis and J.-F. Létard, *Eur. J. Inorg. Chem.*, 2013, 2013, 763-769.
23. A. Hauser, *Top. Curr. Chem.*, 2004, 233, 49-58.
24. H. A. Goodwin and K. H. Sugiyarto, *Chem. Phys. Lett.*, 1987, 139, 470-474.
25. A. Hauser, *Top. Curr. Chem.*, 2004, 234, 155-198.
26. A. Ozarowski, B. R. McGarvey, A. B. Sarkar and J. E. Drake, *Inorg. Chem.*, 1988, 27, 628-635.
27. G. S. Matouzenko, A. Bousseksou, S. Lecocq, P. J. van Koningsbruggen, M. Perrin, O. Kahn and A. Collet, *Inorg. Chem.*, 1997, 36, 5869-5879.
28. N. Moliner, M. C. Munoz, S. Letard, J. F. Letard, X. Solans, R. Burriel, M. Castro, O. Kahn and J. A. Real, *Inorg. Chim. Acta*, 1999, 291, 279-288.

29. G. M. Sheldrick, *Acta Crystallogr. Sect. A*, 2008, 64, 112-122.
30. G. A. Bain and J. F. Berry, *J. Chem. Educ.*, 2008, 85, 532-536.

6

High-temperature cooperative spin crossover of an iron(II) amine-bridged bis-bipyridine complex

Abstract

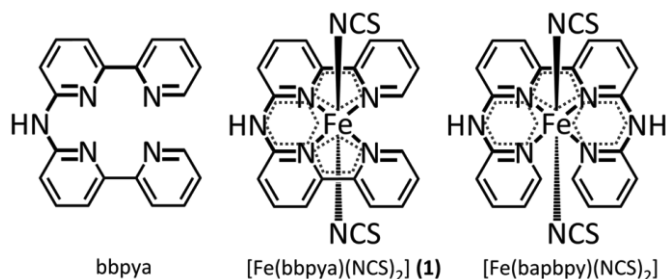
The new mononuclear spin-crossover complex [Fe(bbpya)(NCS)₂] was synthesized. It is in the low-spin state at room temperature and, according to magnetic susceptibility and DSC measurements, exhibits abrupt and complete spin crossover to the high-spin state at an unusually high temperature of $T_{1/2} = 418$ K with a 21 K wide hysteresis cycle. This cooperative behaviour correlates with the intermolecular interactions observed in the X-ray crystal structure.

6.1. Introduction

Spin crossover (SCO) is one of the most fascinating phenomena in coordination chemistry.¹ It can occur for $3d^4$ - $3d^7$ transition metal ions in a pseudo-octahedral environment, *i.e.*, when the *d*-electrons can occupy either a high-spin (HS) or a low-spin (LS) state configuration. Spin crossover can be triggered by temperature variations, light irradiation, or by the application of pressure, of a magnetic field, or of an electric field.² Cooperativity is a very important aspect for SCO, and for molecular compounds it is a consequence of intermolecular interactions in the crystal lattice.³ SCO complexes have long been considered for their potential applications in, for example, displays or memory devices,⁴ provided that a hysteretic bistable domain is present near room temperature. However, it remains very challenging to design a SCO material with predefined magnetic properties.⁵ Iron(II) 1,2,4-triazole coordination polymers⁶ and Hofmann coordination networks of the type $[\text{Fe}(\mu\text{-}N,N'\text{-bis-diimine})\text{M}(\mu\text{-CN})_4]$ ⁷ (M = Cu, Ni, Pt, Au, Ag) have highly cooperative spin-switching properties near or above room temperature, and for this reason are the most intensely studied SCO systems. The only drawback of these coordination polymers is that the iron centres situated at the boundaries of a crystalline domain may feel a different environment compared to the metal centres in the bulk, which for example influences the SCO properties of nanomaterials based on such compounds.⁸ On the other hand, mononuclear SCO systems may not exhibit those limitations as the ligand set around the metal centre is well defined throughout the whole crystallite. However, molecular systems with abrupt and complete spin transition occurring near room temperature or above, and showing hysteretic behaviour, remain scarce.^{5, 9-11}

Inspired by earlier investigations on $[\text{Fe}(\text{bapbpy})(\text{NCS})_2]$ ¹² and $[\text{Fe}(\text{bpy})_2(\text{NCS})_2]$,¹³ a new rigid N_4 -donor ligand was designed, namely *N,N*-bis(2,2'-bipyrid-6-yl)amine (bbpya, Scheme 6.1). This tetradentate ligand consists of two bipyridines connected by one N–H bridge aimed at forming intermolecular hydrogen bond interactions, which have been shown to be critical for the cooperativity of SCO complexes based on the bapbpy ligand (also see Chapter 2).¹⁴ The ligand bbpya is similar to bapbpy and is expected to coordinate in a tetradentate fashion at the basal plane of an octahedral iron(II) centre, leaving the two *trans* axial positions for the binding of thiocyanate ions. However, bbpya is also quite different from bapbpy, as the former has only one N–H bridge and will form upon coordination to a metal ion two 5-membered and one 6-membered chelate rings, whereas the latter has two N–H bridges and forms one 5-

membered and two 6-membered rings upon coordination (Scheme 6.1). The presence of two bipyridine chelates instead of one, and the overall more open structure of bbpya is expected to result in a reduced distortion of the octahedral coordination sphere, and therefore in an increase of the ligand field splitting and stabilization of the LS state. In the present study, we report a new mononuclear Fe(II) SCO complex based on the bbpya ligand, $[\text{Fe}(\text{bbpya})(\text{NCS})_2]$; its spin transition takes place at remarkably high temperatures, but still with strong cooperativity.

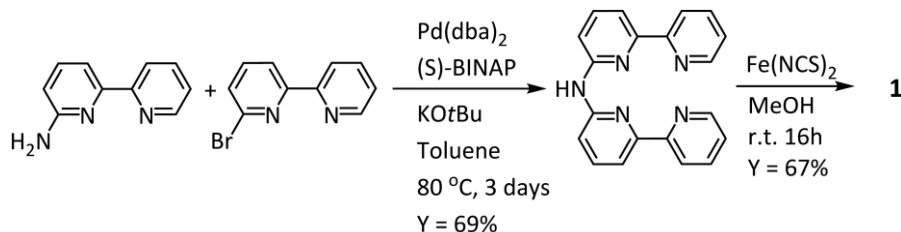


Scheme 6.1. Schematic drawing of the ligand bbpya, of its iron complex **1**, and of $[\text{Fe}(\text{bapbpy})(\text{NCS})_2]$.¹²

6.2. Results and discussion

6.2.1. Synthesis of bbpya and complex **1**

The synthesis of the ligand bbpya was carried out using a Buchwald-Hartwig cross-coupling reaction between 6-amino-2,2'-bipyridine^{15, 16} and 6-bromo-2,2'-bipyridine (see Scheme 6.2). The ligand was obtained in a yield of 69%. The reaction of bbpya with 1.1 eq. of $\text{Fe}(\text{NCS})_2$ in MeOH resulted in a deep purple suspension, which was stirred overnight and filtered to eventually afford complex **1** as a deep purple powder. The very dark colour of the compound suggested a low-spin state at room temperature. Single crystals suitable for X-ray structure determination were grown in a Y-shaped tube using liquid-liquid diffusion of a methanolic solution of $[\text{Fe}(\text{NCS})_2]$ into a DMF solution of the ligand bbpya. The powder X-ray diffraction pattern of compound **1** was calculated from the single crystal data using the program Mercury,¹⁷ and matches the experimental powder X-ray diffractogram of compound **1**. Furthermore, identical IR spectra indicate the same structural composition for the crude powder and crushed single crystals of complex **1** (Figure AIV.1, AIV.2, see Appendix IV).



Scheme 6.2. Synthetic route towards the ligand bbpya and its iron complex **1**.

6.2.2. Description of crystal structure and packing of **1**

The crystal structure of **1** was determined at 110(2) K. Complex **1** crystallizes in the triclinic space group *P*-1. As anticipated, the Fe(II) ion is in an octahedral geometry with four N-donors of the ligand bbpya in the equatorial plane, and two N-donors of the thiocyanate anions in the axial positions. The crystal lattice does not contain any solvent molecules. A projection of complex **1** is shown in Figure 6.1a (see Table 6.1 for bond lengths and angles). At 110 K the average Fe–N bond length is 1.96 Å, which is typical of an LS Fe(II) complex in an octahedral environment, and comparable to those found for [Fe(bapbpy)(NCS)₂] in the LS phase (Fe–N_{avg} = 1.95 Å).¹² The angle between the two planes of the two terminal pyridine rings is 23.3° in **1**, significantly smaller than that found in [Fe(bapbpy)(NCS)₂] (44.8°).¹² The more planar orientation of the coordinated bbpya ligand is likely due to the replacement of a six-membered ring in bapbpy by a five-membered ring in bbpya, which opens the tetradentate ligand compared to bapbpy and keeps the hydrogen atoms on the terminal pyridine rings away from each other. Moreover, the angles between the nitrogen donors of the thiocyanate ligands and the four nitrogen atoms N1–N2–N4–N5 in the basal plane of bbpya, vary from 87.00(2)° to 92.63(2)°, *i.e.*, the axial thiocyanate ligands are almost perpendicular to the mean molecular plane of bbpya, whereas in [Fe(bapbpy)(NCS)₂] those angles vary from 84.19(1)° to 97.18(1)°. The comparison of crystal structures of **1** and [Fe(bapbpy)(NCS)₂] at 110 K is shown in Figure 6.1b, indeed showing that **1** has the less distorted octahedron. In the structure of **1**, the complex is disordered over a pseudo-twofold rotation axis, forming two orientations [occupancy factor of the major component: 0.671(3)]. The coordination geometry and bond distances in the two orientations are highly similar, but the different orientations have a major impact on the long-range hydrogen bonding interactions.

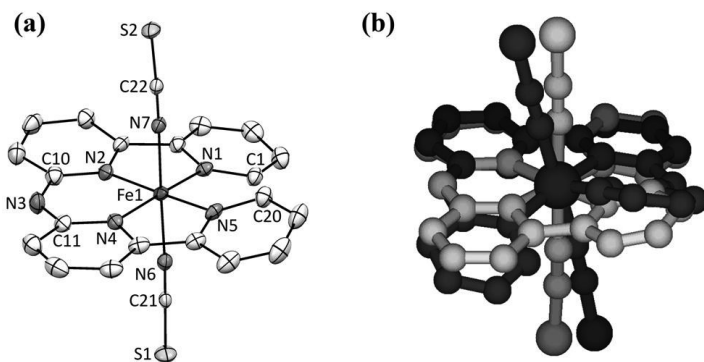


Figure 6.1. a) Displacement ellipsoid plot (50% probability level) of compound **1** at 110 K. b) a MOLDEN-generated superposition of the structures of $[\text{Fe}(\text{bbpya})(\text{NCS})_2]$ (**1**) (light grey) and $[\text{Fe}(\text{bapbpy})(\text{NCS})_2]^{12}$ (dark) in the LS state. Hydrogen atoms and disorder are omitted for clarity.

The crystal packing in **1** comprises H-bonding and π - π stacking interactions. Because of the presence of the inversion centre in *P*-1, hydrogen-bonded dimers are formed with two strong N-H \cdots S hydrogen bonds with intermolecular distances N3 \cdots S2' and N3' \cdots S2 of 3.331(5) Å (Figure 6.2a). In this major orientation it thus appears that due to the absence of a second N-H group in the ligand bbpya the formation of hydrogen-bonded infinite 1D chains is not possible. However, when the minor disorder component is taken into account a different hydrogen-bonding pattern appears. For example, when one of the molecules in each 'dimer' is in its minor disorder orientation a 1D chain is formed comprising single hydrogen bonds with N3 \cdots S1" distances of 3.073(7) Å (Table 6.1 and Figure 6.2b). Two different N-H \cdots S contacts modes between adjacent molecules thus occur in the crystal. As a result, the propagation of N-H \cdots S hydrogen bonds is found along the crystal following the direction [1 0 1], but the hydrogen-bonded chain has defects because of the statistical distribution of the molecules over their disorder components. Finally, π - π stacking interactions are also present in **1**, as shown by the short distances between the terminal pyridine rings of two neighbouring molecules (Cg1 \cdots Cg2' = 4.28 Å). Overall, despite the disorder complex **1** maintains relatively strong intermolecular interactions in the crystal packing over long distances, suggesting that compound **1** may show cooperative SCO behaviour.

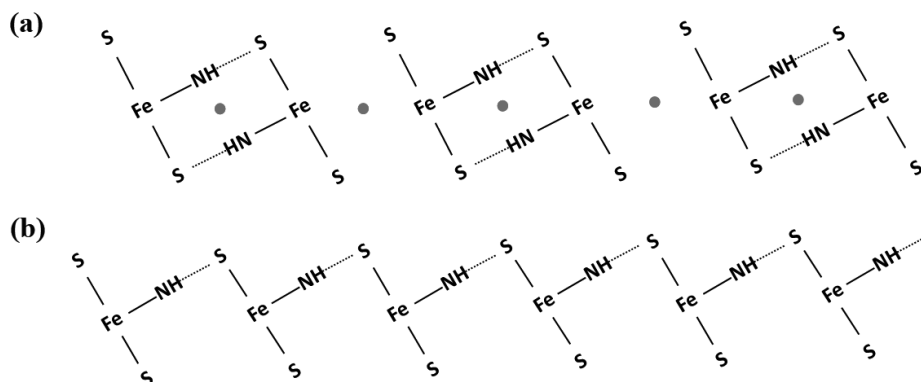


Figure 6.2. Schematic representations of the two limiting contact modes between adjacent molecules in the crystal packing of **1**. The reality is somewhere between these two extreme forms. Inversion centre is indicated with a dot.

Table 6.1. Selected bond lengths (Å) and angles (°) for the crystal structure of complex **1** at 110 K. Short intermolecular interactions (Å) of complex **1** in the crystal packing at 110 K are also included.

Bond distance (Å)		Angles (°)		Torsions (°)	
Fe1–N1	1.998(5)	N1–Fe1–N2	81.9(2)	N4–N2–N1–N5	7.4(3)
Fe1–N2	1.926(5)	N2–Fe1–N4	94.5(2)	C1–N1–N5–C20	27.9(3)
Fe1–N4	1.928(5)	N4–Fe1–N5	81.1(2)	N2–C10–C11–N4	4.9(4)
Fe1–N5	2.011(4)	N5–Fe1–N1	102.8(2)	C20–C11–C10–C1	12.08(7)
Fe1–N6	1.946(5)	N6–Fe1–N7	178.63(18)		
Fe1–N7	1.936(5)				
N3...S2'	3.331(5)				
N3...S1''	3.073(7)				

Symmetry operations: ' = -x, -y, -z; '' = 1-x, 1-y, -z

6.2.3. Magnetic properties of **1**

To investigate the magnetic properties of compound **1** the temperature dependence of $\chi_M T$ was measured in the range 300–550 K for a powder sample of **1** (χ_M is the molar magnetic susceptibility, Figure 6.3a). Magnetic susceptibility measurements show that compound **1** undergoes a complete and cooperative SCO. At room temperature and up to *ca.* 330 K the $\chi_M T$ value of 0.01–0.02 cm³ mol⁻¹ K is clearly indicative of an LS state, consistent with the dark colour of the compound and the average Fe–N distance

in the X-ray crystal structure. Further heating of the sample to 550 K using an oven was necessary to reach the $\chi_M T$ value of $3.02 \text{ cm}^3 \text{ mol}^{-1} \text{ K}$ expected for an Fe(II) ion in its HS state. The cooperative character of the SCO in **1** is evidenced by a rather abrupt transition and the presence of a reproducible but dissymmetric hysteresis cycle of 21 K at its widest point. The spin transition occurs at $T_{1/2\uparrow} = 428(1)$ and $T_{1/2\downarrow} = 407(3)$ K upon warming and cooling, respectively, as derived from the maximum of $d(\chi_M T)/dT$ (Figure AIV.3). The average transition temperature $T_{1/2}$ is 418 K, and represents one of the highest transition temperatures reported for SCO compounds. It is remarkably higher than that of $[\text{Fe}(\text{bapbpy})(\text{NCS})_2]$, which, in spite of its seemingly similar chemical formula, is HS at room temperature and exhibits a 2-step transition at low temperatures.¹² Attempts of structural characterization of the HS state of **1** are ongoing. Challenge arises as the SCO temperature occurs at a temperature not reachable with the temperature controller of a common single crystal X-ray diffractometer.

To support the results of magnetic measurements differential scanning calorimetry (DSC) measurements were undertaken for a powder sample of **1** in the range of 150–500 K. The calorimetric data reveal anomalies both in warming and cooling modes at the temperatures $T_{1/2\uparrow} = 434(1)$ and $T_{1/2\downarrow} = 415(1)$ K, respectively, as defined by heat capacity maxima (Figure 6.3b). These temperatures match those of the transition in the $\chi_M T$ vs. T plot and can thus be ascribed to the SCO phenomenon in **1**. The excess enthalpy and entropy associated with the SCO in **1** can be derived from integration of ΔC_p (Figure 6.4a) over T and $\ln T$, respectively, and arise to $\Delta_{\text{SCO}}H = 12.9 / 15.6 \text{ kJ mol}^{-1}$ and $\Delta_{\text{SCO}}S = 29.9 / 37.4 \text{ J mol}^{-1} \text{ K}^{-1}$, respectively, upon warming and cooling. These relatively large values are in agreement with a cooperative SCO in **1**.^{18, 19} To quantify cooperativity the excess heat capacity was fitted to Sorai's domain model (full lines in Figure 6.4a, see Appendix IV for details).²⁰ The fit yielded the number $n = 10.2$ and 6.5, respectively, of like-spin SCO centres per interacting domain upon warming and cooling. The former value is consistent with that obtained for the lower temperature transition observed in $[\text{Fe}(\text{bapbpy})(\text{NCS})_2]$, and with the cooperative transition of other reported SCO complexes $[\text{Fe}(\text{L})(\text{NCS})_2]$, where L is a disubstituted bapbpy derivative (see Chapter 2). The latter, smaller value is consistent with gradual transition / broader excess heat capacity peak observed in other Fe(II) bapbpy-derivative complexes upon cooling (see Chapter 2). For a direct comparison, HS fractions can be derived from both magnetic and calorimetric data (Appendix IV), showing an excellent agreement (Figure 6.4b). Another quantification of the

cooperative character of the SCO in **1** can be obtained from these data with the so-called Slichter and Drickamer model.²¹ The best agreement is obtained (Appendix IV) with a mean-field interaction term $\Gamma = 8.15 \text{ kJ mol}^{-1}$. This result, corresponding to $\Gamma/RT_{1/2} = 2.34$, is perfectly consistent with the experimental observations, since in this model bistability is predicted for values of $\Gamma/RT_{1/2} > 2$, and the width of the resulting hysteresis cycle in the SCO curve increases with $\Gamma/RT_{1/2}$. Overall, magnetic and calorimetric data provide a consistent view of the spin transition of compound **1**. The observed hysteresis cycle, which is a sign of efficient cooperativity in compound **1**, is in agreement with the intermolecular interactions observed in the crystal packing.

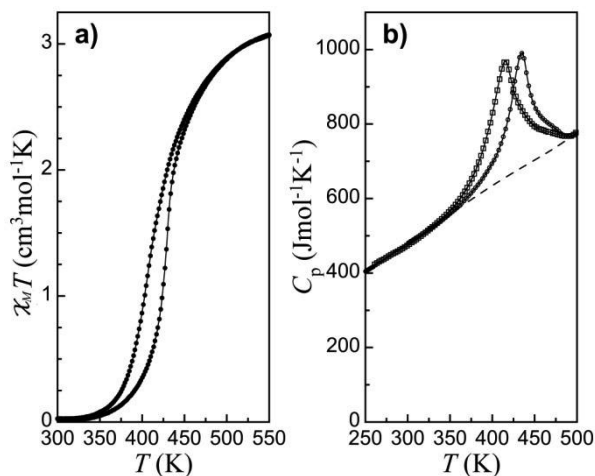


Figure 6.3. a) Thermal variation of $\chi_M T$ for complex **1**, measured at 10 K min^{-1} . b) Molar heat capacities for compound **1** upon warming (empty circles) and cooling (empty squares). The dashed line is the estimated normal heat capacity used for ΔC_p determination (see Appendix IV).

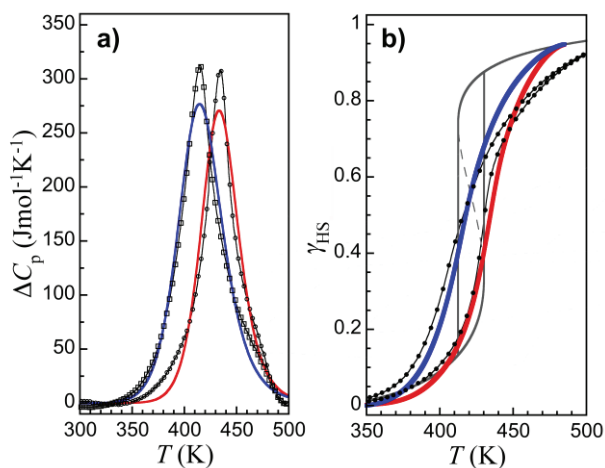


Figure 6.4. a) Excess molar heat capacities associated with the SCO in **1**. Full red and blue lines are fits of the data upon warming (empty circles) and cooling (empty squares) to the domain model of Sorai (see Appendix IV and reference 20) with $n = 10.2$ and 6.5 respectively. b) The spin crossover of **1** shown as the high-spin fraction γ_{HS} vs. T (full red and blue lines are derived from calorimetric data, black dots are from magnetic data), and the simulation with the Slichter-Drickamer model (full grey line).

6.3. Conclusion

The new rigid amine-bridged bis-bipyridine ligand bbpya was designed and synthesized, aiming at increasing the transition temperature of bapbpy-based SCO complexes while maintaining intermolecular interactions between the mononuclear complexes. Its solvent-free iron(II) bithiocyanate complex **1**, $[\text{Fe}(\text{bbpya})(\text{NCS})_2]$, is indeed a new SCO compound with H-bonding and π - π stacking interactions in the solid state. Remarkably, compound **1** is LS at room temperature in the solid state, and shows one of the highest transition temperatures recorded among mononuclear SCO complexes, while keeping a large hysteresis cycle of 21 K. The uncommon features of compound **1** validate the strategy of replacing 6-membered chelate rings by 5-membered ones to increase the transition temperature. Although the obtained transition temperature may even be too high for information storage applications, it may allow studying mechanistic and microscopic aspects of cooperative SCO that were more difficult to study in cooled environments.

6.4. Experimental

6.4.1. General information

All chemicals were obtained from commercial sources and used without further purification, unless otherwise mentioned. 6-Bromo-2,2'-bipyridine was purchased from Sigma-Aldrich (CAS 10495-73-5), and 6-amino-2,2'-bipyridine was synthesized according to previously reported procedures.^{15, 16} Experiments that needed an inert environment were performed using standard Schlenk line techniques. The applied vacuum was about 10^{-3} mbar. Degassed solvents were obtained by bubbling argon through the solvent in a Schlenk flask for at least one hour. For all ligand and complex syntheses, degassed solvents were used; for ligand purifications solvents were used without further purification. Filtration of complexes was carried out using Whatman RC 60 membrane filters. For other filtrations Whatman 597 filters were used. NMR Spectra were measured on a Bruker DPX-300 Spectrometer at room temperature. Mass spectra were obtained using soft electron spray from a Thermoquest Finnagen AQA. High-resolution mass spectra were measured using direct injection (2 μ L of a 2 μ M solution in DMSO on a (Thermo Finnigan LTQ Orbitrap) mass spectrometer equipped with an electron spray ion source in positive mode (source voltage 3.5 kV, sheath gas flow 10, capillary temperature 275 °C) with resolution $R = 60,000$ at $m/z = 400$ (mass range = 150-2000) and dioctylphthalate ($m/z = 391.28428$) as "lock mass". IR spectra were acquired on a PerkinElmer FT-IR Spectrometer Spectrum Two at room temperature. Elemental analysis (C,H,N,S) were obtained from a Perkin-Elmer 2400 Series II analyzer.

6.4.2. Preparation of the ligand bbpya

A mixture of 6-bromo-2,2'-bipyridine (250 mg, 1.07 mmol), [Pd(dba)₂] (13 mg, 0.022 mmol), (S)-BINAP (27 mg, 0.043 mmol) and KO^tBu (483 mg, 4.30 mmol) was put under argon and partially dissolved in degassed toluene (20 mL) in a dry round-bottom flask. The mixture was stirred for 10 min and 6-amino-2,2'-bipyridine (220 mg, 1.28 mmol) was added, followed by heating the reaction mixture to 80 °C. After 3 days, the brown mixture was cooled down with an ice bath. Deionized water (25 mL) was added and the mixture was stirred for 1 hour. No solid appeared and the resultant mixture was then extracted with DCM (3 \times 40 mL). The organic layers were combined and dried over MgSO₄, followed by filtration to remove MgSO₄ and evaporation of solvent DCM under reduced pressure, giving a brown oil. Adding cold MeOH to the oil resulted in the formation of solids which were filtered, washed with cold

MeOH and dried under high vacuum, to afford bbpya as a white solid (241 mg, 69%). $R_f = 0.09$ (SiO₂: MeOH/DCM: 1/9). ¹H NMR (DMSO-*d*⁶): $\delta = 9.90$ (s, 1H, NH), 8.69 (ddd, $J = 4.8, 1.9, 0.9$ Hz, 2H, H-7), 8.38 (dt, $J = 8.0, 1.1$ Hz, 2H, H-4), 7.99 (td, $J = 7.7, 1.8$ Hz, 2H, H-6), 7.93 (dt, $J = 5.4, 2.7$ Hz, 2H, H-3), 7.89 (d, $J = 2.9$ Hz, 4H, H-1, H-2), 7.45 (ddd, $J = 7.5, 4.7, 1.2$ Hz, 2H, H-5). ¹³C NMR (DMSO-*d*⁶): $\delta = 155.5$ (Cq), 153.9 (Cq), 153.4 (Cq), 149.3 (C-7), 138.9 (C-1), 137.3 (C-6), 124.0 (C-5), 120.4 (C-4), 112.8 (C-3), 112.3 (C-2) ppm. ¹H NMR (CD₂Cl₂): $\delta = 8.72 - 8.61$ (m, 2H), 8.40 (d, $J = 8.0$ Hz, 2H), 8.07 – 7.97 (m, 2H), 7.90 – 7.77 (m, 4H), 7.71 (d, $J = 8.2$ Hz, 2H), 7.54 (s, 1H), 7.32 (ddd, $J = 7.4, 4.7, 1.1$ Hz, 2H). IR spectroscopy (cm⁻¹): 3390, 2922, 2852, 1582, 1558, 1520, 1472, 1447, 1418, 1340, 1296, 1271, 1230, 1152, 1091, 1073, 1050, 990, 963, 902, 818, 774, 738, 679, 668, 644, 620, 572, 402, 341, 317. Elemental analysis calcd (%) for C₂₀H₁₅N₅: C 73.82, H 4.65, N 21.53; found: C 73.21, H 5.36, N 20.39. ES-MS (MeOH) m/z (calc): 326.1 (326.4, [M+H]⁺), 348.0 (348.4, [M+Na]⁺), 673.2 (673.7, [2M+Na]⁺).

6.4.3. Preparation and crystallization of complex [Fe(bbpya)(NCS)₂] (1)

An Fe(NCS)₂ solution was prepared by weighing KSCN (195 mg, 2.00 mmol) and ascorbic acid (6.1 mg, 0.035 mmol) under argon into a round-bottom flask. FeSO₄ (152 mg, 1.00 mmol) was added and the mixture was suspended in degassed methanol (6.0 mL). The suspension was stirred for 40 min, followed by filtration and the filtrate was transferred into a volumetric flask. The volume was adjusted to 10.0 mL with degassed methanol and the volumetric flask was well shaken, yielding a 0.1 M [Fe(NCS)₂] solution in methanol. Since the filtration and the iron solution were not kept under argon, the iron solution had to be prepared fresh for every synthesis. The oxidation of the iron solution was visible by a change of colour (from colourless to dark violet).

Synthesis of **1**: The ligand bbpya (30 mg, 0.093 mmol) was dissolved in degassed methanol (3 mL) in a round-bottom flask and stirred under argon, to give a yellow solution. 1.1 Eq. of the 0.1 M iron solution (0.1 mmol) was added to the dissolved ligand, resulting in a purple suspension. The mixture was stirred 16 hours under argon. The purple solid was collected by filtration and washed with degassed methanol (3 × 5 mL). The purple solid was dried under high vacuum for 3 hours (31 mg, 67%). IR spectroscopy (cm⁻¹): 3269, 3184, 3130, 3099, 3047, 2125 (NCS⁻), 2109 (NCS⁻), 1625, 1601, 1582, 1529, 1478, 1464, 1451, 1416, 1406, 1302, 1250, 1172, 1164, 1139, 1090, 1022, 949, 870, 800, 759, 725, 685, 661, 643, 629, 495, 478. HR-MS (DMSO): m/z (calc): 497.0170 (497.0174, [M]⁺), 439.0420 (439.0423, [M-NCS]⁺). ¹H NMR (DMSO-*d*⁶): $\delta = 9.92$ (s, 1H), 8.68 (d, $J=3.9$, 2H), 8.38 (d, $J=7.7$, 2H), 8.06 – 7.80 (m, 6H), 7.46 (dd, $J=6.8, 4.7$, 2H), 6.34 (s, 1H). Integration of the peaks was difficult due to the low solubility of the complex. Elemental analysis calcd (%)

for C₂₂H₁₅FeN₇S₂: C 53.13, H 3.04, N 19.73, S 12.87; found: C 52.56, H 2.93, N 19.73, S 12.77.

Single crystals suitable for X-ray diffraction were obtained as follows: the ligand bbpya (15 mg) was dissolved in degassed DMF (3 mL) to afford a clear yellow solution. A small amount of ascorbic acid (5 mg) was added to prevent aerial oxidation. 1 mL aliquots of this solution were pipette-filtered over 1 cm Celite into the vertical compartment of a Y-shape glass tube, Fe(NCS)₂ (0.5 mL of a 0.1 M solution) was carefully added into the other compartment of the glass tube. Liquid nitrogen was used to freeze both compartments before degassed MeOH was added to fill the Y-shaped tubes. Each tube was then stoppered and kept at room temperature under argon using balloons, if possible in a sunny place. Single crystals were obtained within a week. Yield: 90%. The crystals were not air-sensitive and did not indicate loss of solvent therefore could be handled out of the mother liquor and at ambient conditions for several weeks. Crystal data: Fw = 497.38, black irregular lath, 0.43 x 0.12 x 0.08 mm³, triclinic, *P*-1 (no. 2), *a* = 8.8024(4), *b* = 8.8862(4), *c* = 13.7229(5) Å, α = 100.637(3), β = 103.916(3), γ = 95.972(3)°, *V* = 1011.52(8) Å³, *Z* = 2, *D*_x = 1.633 g cm⁻³, μ = 8.134 mm⁻¹, abs. corr. range: 0.195-0.596. 12241 Reflections were measured up to a resolution of (sin θ/λ)_{max} = 0.62 Å⁻¹. 3945 Reflections were unique (*R*_{int} = 0.0215), of which 3502 were observed [*I* > 2σ(*I*)]. 578 Parameters were refined using 1152 restraints. *R*1/*wR*2 [*I* > 2σ(*I*)]: 0.0294/0.0796. *R*1/*wR*2 [all refl.]: 0.0335/0.0830. *S* = 1.074. Residual electron density found between -0.29 and 0.24 e Å⁻³.

6.5. References:

1. P. Gütllich and H. A. Goodwin, *Top. Curr. Chem.*, 2004, 233, 1-47.
2. M. A. Halcrow, *Chem. Soc. Rev.*, 2011, 40, 4119-4142.
3. H. Spiering, T. Kohlhaas, N. Romstedt, A. Hauser, C. Bruns-Yilmaz, J. Kusz and P. Gütllich, *Coord. Chem. Rev.*, 1999, 192, 629-647.
4. O. Kahn and C. J. Martinez, *Science*, 1998, 279, 44-48.
5. B. Schafer, C. Rajnak, I. Salitros, O. Fuhr, D. Klar, C. Schmitz-Antoniak, E. Weschke, H. Wende and M. Ruben, *Chem. Commun.*, 2013, 49, 10986-10988.
6. O. Roubeau, *Chem. Eur. J.*, 2012, 18, 15230-15244.
7. M. C. Muñoz and J. A. Real, *Coord. Chem. Rev.*, 2011, 255, 2068-2093.
8. Y. Raza, F. Volatron, S. Moldovan, O. Ersen, V. Huc, C. Martini, F. Brisset, A. Gloter, O. Stephan, A. Bousseksou, L. Catala and T. Mallah, *Chem. Commun.*, 2011, 47, 11501-11503.
9. I. Šalitroš, N. T. Madhu, R. Boča, J. Pavlik and M. Ruben, *Monatsh. Chem.*, 2009, 140, 695-733.
10. L. Zhang, G.-C. Xu, H.-B. Xu, T. Zhang, Z.-M. Wang, M. Yuan and S. Gao, *Chem. Commun.*, 2010, 46, 2554-2556.
11. B. Weber, W. Bauer and J. Obel, *Angew. Chem. Int. Ed.*, 2008, 47, 10098-10101.
12. S. Bonnet, M. A. Siegler, J. S. Costa, G. Molnar, A. Bousseksou, A. L. Spek, P. Gamez and J. Reedijk, *Chem. Commun.*, 2008, 5619-5621.

-
13. E. W. Müller, H. Spiering and P. Gülich, *Chem. Phys. Lett.*, 1982, 93, 567-571.
 14. Z. Arcis-Castillo, S. Zheng, M. A. Siegler, O. Roubeau, S. Bedoui and S. Bonnet, *Chem. Eur. J.*, 2011, 17, 14826-14836.
 15. T. Norrby, A. Börje, L. Zhang and B. Åkermark, *Acta Chem. Scand.*, 1998, 52, 77-85.
 16. J. Yin, B. Xiang, M. A. Huffman, C. E. Raab and I. W. Davies, *J. Org. Chem.*, 2007, 72, 4554-4557.
 17. C. F. Macrae, I. J. Bruno, J. A. Chisholm, P. R. Edgington, P. McCabe, E. Pidcock, L. Rodriguez-Monge, R. Taylor, J. van de Streek and P. A. Wood, *J. Appl. Crystallogr.*, 2008, 41, 466-470.
 18. M. Sorai and S. Seki, *J. Phys. Chem. Solids*, 1974, 35, 555-570.
 19. M. Sorai, *Top. Curr. Chem.*, 2004, 235, 153-170.
 20. M. Sorai, Y. Nakazawa, M. Nakano and Y. Miyazaki, *Chem. Rev.*, 2012, 113, PR41-PR122.
 21. C. P. Slichter and H. G. Drickamer, *J. Chem. Phys.*, 1972, 56, 2142-2160.

7

Synthesis, magnetic properties, and STM imaging of an iron(II) bapphen complex functionalized with a long alkyl chain

Abstract

In this chapter, the syntheses of a new tetradentate ligand bearing a long alkyl chain (C_{12}) and two N–H bridges based on the ligand bapphen (compound **1**), and of its iron(II) complex $[\text{Fe}(\mathbf{1})(\text{NCS})_2]$ (**2**), are presented. Compound **1** was synthesized in 10 steps with an overall yield of 1%. The evolution of the magnetic susceptibility vs. T of **2** revealed a gradual SCO behaviour in the bulk. The self assembly of **1** and **2** on HOPG surfaces was investigated by Scanning Tunnelling Microscopy (STM). Both compounds **1** and **2** formed ordered patterns after deposition by drop casting. The patterns of the two compounds are very different, which is attributed to the fundamentally different hydrogen bonding networks before and after coordination of $\text{Fe}(\text{NCS})_2$ to the tetradentate chelate. Two possible models for the self assembly of **1** and **2** are provided.

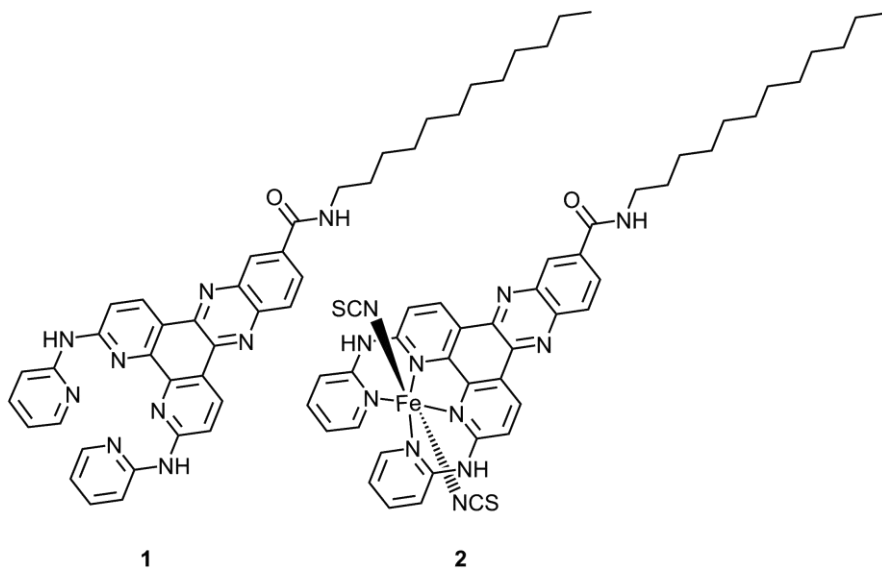
7.1. Introduction

The design of molecular switches that can be utilized for information processing and data storage is an attractive goal in material science. Spin-crossover (SCO) compounds hold considerable potential in this field. Spin crossover can occur for $3d^4$ - $3d^7$ transition metal ions in a pseudo-octahedral environment, *i.e.*, when the *d*-electrons can occupy either a high-spin (HS) or a low-spin (LS) state configuration. SCO can be triggered by temperature variations, light irradiation, or by the application of pressure, of a magnetic field, of an electric field.¹ Cooperativity where the SCO of one iron complex in the crystal lattice induces the SCO of a neighbouring complex, is a very important aspect of SCO that is a consequence of intermolecular interactions in the crystal lattice.² For example, if intermolecular interactions are sufficiently strong they may induce abrupt SCO and hysteresis loops, which is usually considered as required for information storage applications.³ However, up to now it still remains very challenging to control the cooperativity of molecular SCO compounds in order to make real devices that can store information.⁴

The state-of-the-art in spin-crossover research is to study SCO in nanosystems. Nanoparticles, thin films, liquid crystals and surface patterns of spin-crossover materials have all been described.⁵ More recently, metal complexes with long alkyl chains were shown to allow for the construction of nano-structured multifunctional materials,^{6,7} *i.e.*, materials in which several properties are combined, such as SCO and liquid crystal behaviour^{6, 8-10} or magnetic exchange interactions,¹¹ as well as single-molecule magnet (SMM) properties.¹² In all cases, examples have shown that the self assembly of such molecules to surfaces using the bottom-up approach was a new and powerful tool to prepare devices,^{13, 14} which might be complementary to more traditional top-down microfabrication techniques.¹³ However, the bottom-up self-assembly of one- or two-dimensional arrays of molecules with controlled magnetic properties requires the detailed understanding and control of intermolecular forces.

Recently, we reported the mononuclear SCO compound $[\text{Fe}(\text{bapbpy})(\text{NCS})_2]$ (bapbpy = *N,N'*-di(pyrid-2-yl)-2,2'-bipyridine-6,6'-diamine) to be highly cooperative.¹⁵ Intermolecular interactions are well characterized for this compound, in which hydrogen bonding interactions play a critical role in cooperativity. Intermolecular N–H \cdots S hydrogen bonds between neighbouring molecules are indeed correlated with the occurrence of hysteretic SCO. Based on these studies, and inspired by parallel

investigations on the SCO compound $[\text{Fe}(\text{bapphen})(\text{NCS})_2]$ (see Chapter 5), a new N_4 -donor ligand **1** was designed (Scheme 7.1). This tetradentate ligand consists of a bapphen ligand to which a long alkyl chain (C_{12}) is attached, *via* aromatic rings in positions 5 and 6 of the phenanthroline ring. The iron(II) complex of ligand **1**, complex **2**, has been prepared and characterized in the bulk. The compounds have been deposited on highly oriented pyrolytic graphite (HOPG) surface by drop casting, and the self assembly of ligand **1** and of its iron complex **2** on HOPG surfaces is studied by using scanning tunnelling microscopy (STM) techniques.

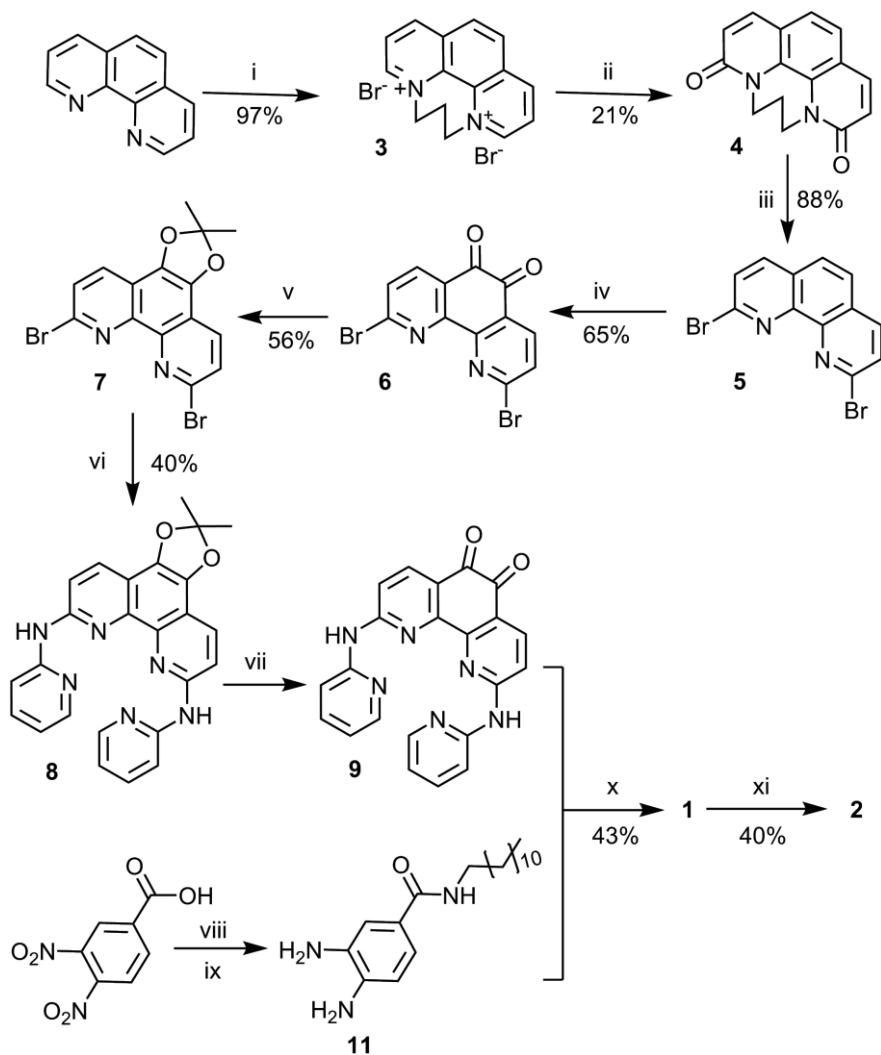


Scheme 7.1. Chemical structures of ligand **1** and its iron(II) complex **2**.

7.2. Results

7.2.1. Synthesis

The synthesis of 2,9-dibromophenanthroline (**5**) was done according to literature procedures.^{16, 17} The positions α to the nitrogens were activated towards nucleophilic attack by quaternizing the nitrogen atoms with a propane bridge (compound **3**). Subsequent oxidation with $\text{K}_3[\text{Fe}(\text{CN})_6]$ afforded compound **4** in 21% yield. Bromination of the 2 and 9 positions was realized with a $\text{PBr}_3/\text{POBr}_3$ mixture yielding compound **5** in 88% yield.



Scheme 7.2. Synthetic route towards compounds **1** and **2**. (i) 1,3-dibromopropane, PhNO_2 , 120 °C, 4 h. (ii) $\text{K}_3[\text{Fe}(\text{CN})_6]$, NaOH, H_2O , RT, 4 h. (iii) POBr_3 , PBr_3 , 192 °C, 18 h. (iv) KBr, conc. H_2SO_4 , conc. HNO_3 , 80 °C, 4 h. (v) 2-nitropropane, MeCN, H_2O , Na_2CO_3 , 55 °C, 8 h. (vi) 2-Aminopyridine, 2.7 mol% $\text{Pd}(\text{dba})_2$, 2.7 mol% (S)-BINAP, 2 eq. Cs_2CO_3 , dry toluene, 110 °C, 4 d. (vii) TFA/ H_2O (2:1), 50 °C, 12 h, solid used without further purification. (viii) 1.1 eq. oxalylchloride, 20 mol% DMF, DCM, RT, 1 h. (ix) 1.1 eq. dodecylamine, Et_3N , RT, 12 h. (x) MeOH, 85 °C, 18 h. (xi) 1.1 eq. 0.1 M $\text{Fe}(\text{NCS})_2$, MeOH, 80 °C, 18 h, under argon atmosphere.

The 5,6-dione functional groups were then introduced according to a method described by Ishi-i *et al*¹⁷ using a mixture of H_2SO_4 , HNO_3 and KBr. Compound **6** was obtained

in a reasonable yield of 65%. When the Buchwald-Hartwig cross-coupling was performed with the unprotected compound **6** (and 2-aminopyridine), the coupled product could not be obtained pure, and compound **6** was aminated (that is, the two bromides were substituted by two NH₂ groups), as confirmed by mass spectrometry. Thus, protecting the dione functional groups was realized by using 2-nitropropane to form a ketal group (compound **7**) according to a method described by Frey et al,¹⁶ which gave the air-stable compound **7** with a yield of 56%.

The Buchwald-Hartwig cross-coupling reaction between compound **7** and 2-aminopyridine afforded compound **8** with a yield of 40%. Several attempts were necessary to optimize this reaction (Table 7.1). For example, the reaction time was varied between 1 and 6 days, and the reaction temperature was also varied between 80 and 110 °C. The influence of the catalyst and the base on the product yield was also investigated. It was found that an increased amount of catalyst did not improve the yield significantly (Entry 1, Table 7.1), and that the nature of the base was critical in this reaction: a strong base (KO^tBu) only gave traces of **8** (10%) and a number of by-products, whereas the weaker base Cs₂CO₃ was more tolerant towards the protective group,¹⁸ giving **8** in reasonable yields. Being an important intermediate, compound **8** was fully characterized by mass spectrometry, NMR spectroscopy, and elemental analysis. It is worth noticing that the ¹H NMR spectrum of **8** at room temperature shows broad peaks in which almost no *J*-coupling could be observed (Figure AV.1, Appendix V). It was assumed that these broad peaks were caused by supramolecular interactions between the amine bridges and the pyridine rings of the ligand. Increasing the temperature to 50 °C and the number of scans improved the spectra (Appendix V), allowing full characterization of **8** by 2D NMR.

The last step of the synthesis involved the attachment of an alkyl chain to the 5 and 6 positions of the phenanthroline moiety of compound **9**. The diamine compound **11** which contained a 12-carbon alkyl chain, was successfully synthesized by modifying a two-step procedure described by Ikeda et al (Scheme 7.2).¹⁹ For the formation of the pyrazine ring of **1**, the dione **8** was first deprotected to give **9** (Scheme 7.2) following a procedure reported by Frey et al.¹⁶ Then, nucleophilic attack of **11** to **9** was realized in refluxing methanol at 85 °C for 18 h according to Antun,²⁰ leading to the precipitation of compound **1** that was collected by filtration and obtained with a yield of 43%.

Table 7.1. Investigated conditions for the Buchwald-Hartwig cross-coupling reaction between compound **7** and 2-aminopyridine to form compound **8**.

Entry	Pd(dba) ₂ (%)	BINAP (%)	Base	Time (days)	Temp (°C)	Yield 8
1	3.2	6.4	KOtBu	3	80	traces ^a
2	2.5	2.5	KOtBu ^b	4	80	traces ^a
3	2.5	2.5	Cs ₂ CO ₃	6 ^c	80 to 110 ^c	20% ^d
4	2.5	2.5	Cs ₂ CO ₃	4	110 ^e	40% ^d
5	2.5	2.5	Cs ₂ CO ₃	1	110 ^f	45% ^d

Reaction conditions: dry toluene, argon atmosphere. ^a Indicated by ¹H NMR and mass spectrometry analysis. ^b Purified by sublimation. ^c After reacting at 80 °C for 3 days, nothing had happened and the temperature was increased to 110 °C for another 3 days. ^d Isolated yield. ^e Increased temperature gradually from RT to 110 °C. ^f Directly increased temperature to 110 °C.

Ligand **1** was thus synthesized in 10 steps and 1% overall yield. It was fully characterized by mass spectrometry, NMR spectroscopy, and elemental analysis.

The coordination of compound **1** to iron(II) thiocyanate to form complex **2** was achieved by adding a slight excess of a methanolic solution of Fe(NCS)₂ to a methanol suspension of **1** (Scheme 7.2). Initial attempts of complexation were performed at room temperature for 18 h under argon. In these conditions a yellow solid was obtained that later proved to be lower in purity and contained some uncoordinated NCS⁻ ligands as shown by their stretching vibrations at 2051 cm⁻¹ in the IR spectrum of the product (see Appendix V).²¹ It appeared that heating to 80 °C was necessary for the coordination reaction to go to completion. After refluxing the mixture at 80 °C for 18 h under argon, a brown solid was obtained 40% yield. The new iron(II) complex **2** was analyzed with mass spectrometry and IR spectroscopy. It showed the expected [Fe(**1**)]²⁺ dicationic peak by electron-spray mass spectrometry (calculated at *m/z* 366.6465 for [Fe(**1**)]²⁺), which confirmed coordination of the ligand to the Fe(II) ion. Consistently, the IR spectrum showed the characteristic stretching vibrations of the coordinated thiocyanate ligands at 2077 cm⁻¹ for **2**. The multiple absorption bands between 3000 and 3300 cm⁻¹ are weak, but they appear in the region typical for N–H stretching frequencies, and the two intense absorption bands between 2800 and 2900 cm⁻¹ can be attributed to C–H stretching vibrations. In addition, the N–H⋯S intramolecular hydrogen bonding in **2** was studied by IR spectroscopy using an early

recognized correlation between the N...S distance and the change in stretching frequency of the N–H bond reported by Bellamy and Owen.²² Unfortunately, in this case the correlation between the N–H stretch in the IR and the N...S distance was not very clear based on the calculations (see Appendix V).

7.2.2. Magnetic susceptibility measurement of **2** in the bulk

In order to investigate the magnetic properties of compound **2** the temperature dependence of $\chi_M T$ was measured in both the heating and the cooling modes (Figure 7.1, where χ_M = the molar magnetic susceptibility, T = temperature). Compound **2** shows a gradual and incomplete SCO behaviour in the measured temperature range (5 to 350 K), with no hysteresis cycle. The $\chi_M T$ value of $2.5 \text{ cm}^3 \text{ K mol}^{-1}$ at 300 K gradually decreases to $1.5 \text{ cm}^3 \text{ K mol}^{-1}$ at 100 K, where it reaches a plateau. The further decreasing of $\chi_M T$ below 50 K is due to the zero-field splitting. The $\chi_M T$ value of $2.5 \text{ cm}^3 \text{ K mol}^{-1}$ at 300 K is low compared to the expected value of $3.0 \text{ cm}^3 \text{ K mol}^{-1}$ for an HS iron(II) centre in an octahedral FeN_6 environment, which might indicate the presence of uncoordinated ligand in the material. The transition temperature of **2**, measured as the maximum of $d\chi_M T/dT$ vs. T (see Appendix V), is 182(25) K in both the heating and the cooling modes.

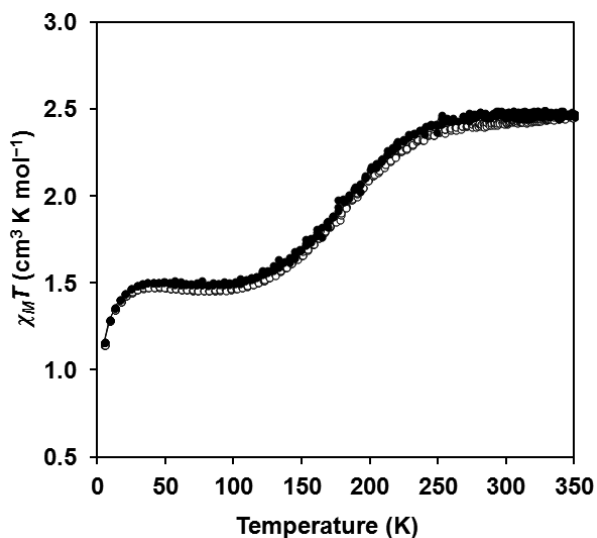


Figure 7.1. Plot of $\chi_M T$ versus T for compound **2** in both heating (empty circle) and cooling mode (filled circle). The measurement was performed with steps of 5 K in the low temperature range and with steps of 2 K in the 250 and 350 K temperature range, with a scan rate of 0.3-1.1 K min^{-1} .

7.2.3. STM spectroscopy of compounds **1** and **2** on HOPG surfaces

Highly oriented pyrolytic graphite (HOPG) was chosen as a surface for the study of the self assembly of **1** and **2**. The deposition of **1** or **2** on a HOPG surface was realized by adding a drop of a DMF solution of compound **1** or **2** (80 nM) and evaporating the solvent under a flow of argon. The self assembly of compound **1** or **2** on HOPG was then studied using STM. In both cases, highly ordered structures were observed (Figure 7.2), characterized by alternating bright and slightly darker stripes, whereas these stripes were absent from a control sample that was prepared in absence of both compounds. For **1** on HOPG, the periodicity of the stripes was estimated at 4.0 nm with the bright stripes exhibiting a width of 1.6 nm, and the darker stripes a width of 2.3 nm (Figure 7.3). In STM images a brighter colour represents higher electron density,¹³ thus the bright stripes are assigned to the aromatic unit of **1** (the bapphen part) because of the presence of π -electrons in aromatic rings.^{23, 24} The darker stripes are assigned to the alkyl chains in **1**, which have low-lying sigma orbitals that poorly contribute to the observed current. These observations are consistent with other reports showing similar patterns for aromatic compounds with long alkyl tails.^{13, 25, 26}

Compound **2** also self assembles on HOPG forming small islands of highly ordered structures (Figure AV.5, Appendix V). Images of smaller scan size (Figure 7.2d) showed alternating bright and slightly darker stripes just like for **1**. However, the periodicity of **2** seems smaller than that of **1** (Figure 7.2b vs. 7.2d), which was confirmed by analyzing the width of the stripes (Figure 7.3). Although the signal-to-noise ratio appears to be higher than for **1**, the periodicity of the stripes was estimated to be 2.0 nm, with one bright stripe of 1.0 nm and one dark stripe of 1.0 nm. Like for **1**, the bright stripes are assigned to the aromatic unit of **2** (the bapphen part), and the darker stripes are assigned to the alkyl chains in **2**. The shortening of the width of both bright and dark stripes in **2** on HOPG remains intriguing (see Discussion).

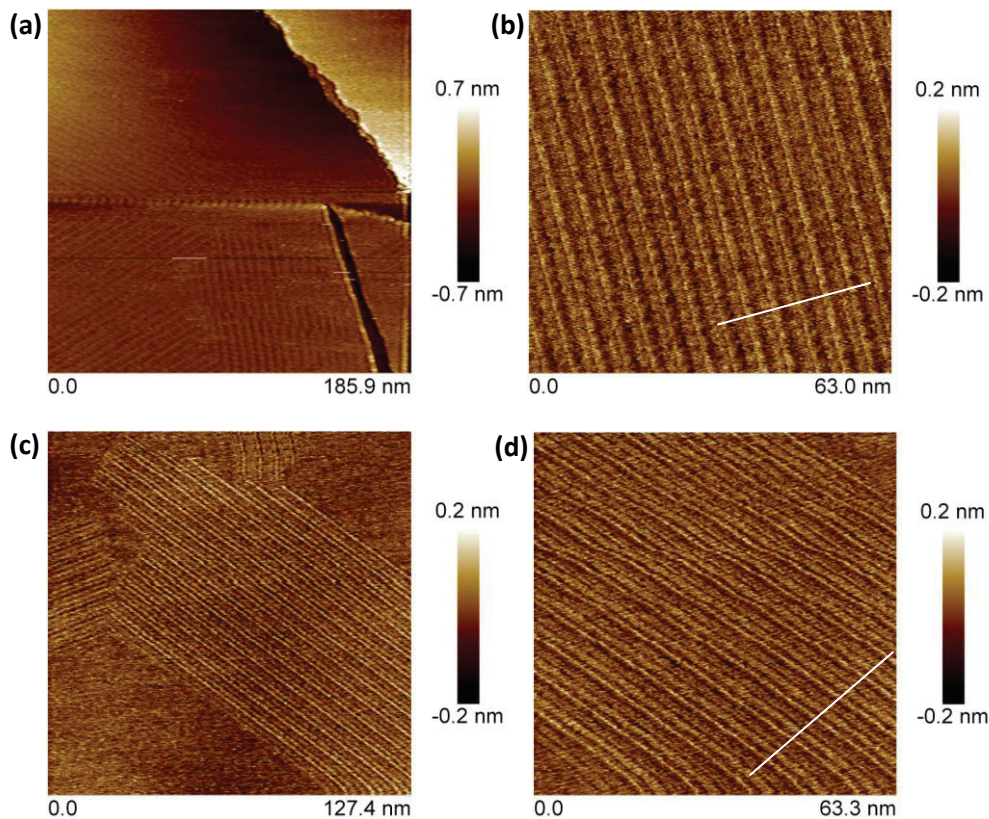


Figure 7.2. STM images of molecular submonolayers adsorbed on HOPG surface for: (a) compound **1**, 185.9 nm \times 185.9 nm; (b) compound **1**, 63 nm \times 63 nm, a separate STM image taken after a zoom-in of (a); (c) compound **2**, 127.4 nm \times 127.4 nm; (d) compound **2**, 63.3 nm \times 63.3 nm, a separate STM image taken after a zoom-in of (c). The brightness is proportional to the height at constant current mode. Both **1** and **2** on HOPG show ordered 2D domains, the white lines indicated in (b) and (d) are for stripe-width analysis in Figure 7.3. All images were taken under the same conditions: $V_{\text{bias}} = +500$ mV, $I_{\text{set}} = 1$ nA.

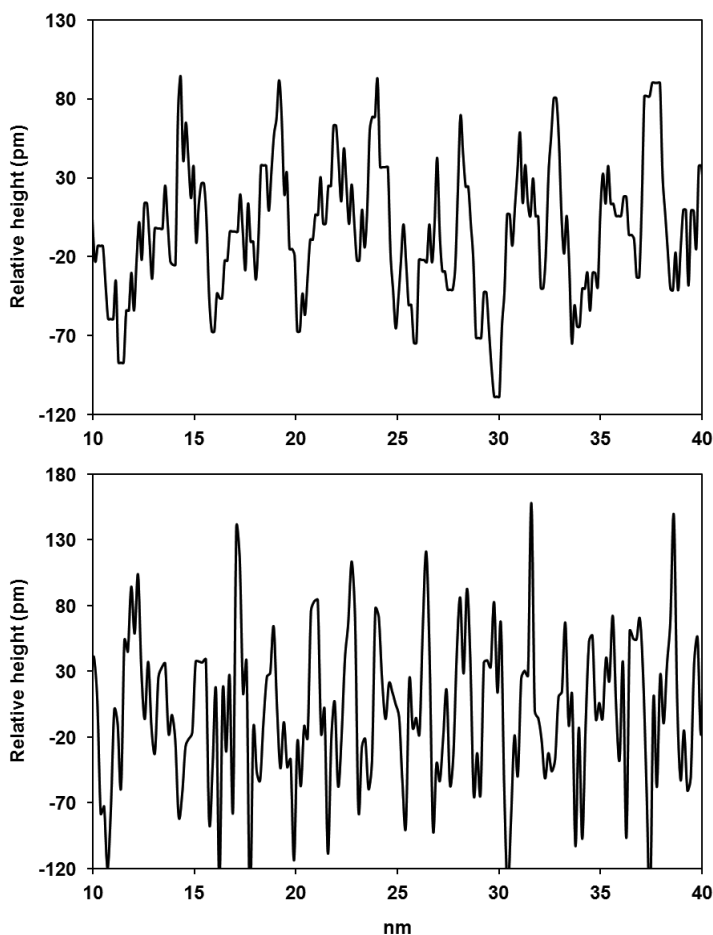


Figure 7.3. Stripe-width analyses for ligand **1** (top, from Figure 7.2b) and complex **2** (bottom, from Figure 7.2d) on HOPG along the white lines in Figures 7.2b and 7.2d.

7.3. Discussion

The $\chi_M T$ vs. T plot for compound **2** in the bulk shows gradual and incomplete spin transition behaviour, with a relatively high residual HS fraction at low temperature. As explained in Chapter 5, high residual HS fractions are expected for non-cooperative SCO with low $T_{1/2}$. The gradual spin transition indicates rather weak intermolecular interactions between the iron complexes,²⁷ which is unexpected as compound **2** possesses two N–H bridges susceptible to engage in N–H \cdots S hydrogen bonding networks. From the IR spectra for the cooperative SCO compounds such as

[Fe(bapbpy)(NCS)₂], which shows short N···S distances and strong N–H···S hydrogen bonds, multiple absorption bands for the stretching vibrations of the N–H bond are observed between 3000 and 3300 cm⁻¹. In contrast, for gradual SCO compounds such as [Fe(Me₂bapbpy)(NCS)₂] (Figure AV.6, Appendix V) the N···S distances are longer and the N–H···S hydrogen bonds are weaker, which translates in the IR spectrum of the solid into a single, stronger absorption band around 3400 cm⁻¹. Therefore, the multiple absorption bands in **2** may indicate that N–H···S interactions be present in the bulk. However, the lower cooperativity of the SCO in **2** might be ruled by other intermolecular interactions, for example π – π stacking between the large aromatic rings and/or Van der Waals interactions between the long alkyl tails, which may result in large iron-to-iron intermolecular distances. This is similar to the case of metal dilution effect shown in Chapter 3, where increasing concentrations of the magnetic inert Zn ions in the crystal lattice causes the iron centres to become further away from each other, resulting lowering the cooperativity of the SCO.

Following the deposition of free ligand **1** and complex **2** on HOPG, it is immediately clear from the STM images that the molecules of **1** and **2** are poorly mobile and diffuse on the surface over short distances to form submonolayers, as their positions are non-randomly distributed and as they form complex and highly ordered structures. Comparing with the STM image obtained from a freshly cleaved HOPG surface (Appendix V), the formation of these structures is not associated to, and does not follow, the underlying step edges of the HOPG surface. These features are somewhat reminiscent of the ordered structures reported recently for other alkyl-functionalized compounds.¹³

In a possible model for the arrangement of **1** on HOPG, the bright stripes are formed by the aromatic part of **1**, which may lay flat on the surface and interact *via* hydrogen bonding interactions between the neighbouring molecules. Indeed, the terminal pyridine rings in **1** can rotate in such a way that the nitrogen atom acts as hydrogen-bond acceptor, with the N–H bridge of the neighbouring molecule acting as a hydrogen-bond donor (Figure 7.5). Then, the alkyl chains lie also flat on the surface and form interdigitated domains that correspond to the dark stripes observed by STM. To evaluate the relevance of this model, the molecular structure of **1** was calculated by DFT in vacuum using the B3LYP functional and the LANL2DZ basis set as implemented in the GAMESS-UK package (Figure 7.4).²⁸ From the 3D structure of ligand **1** the calculated width of the aromatic part of the 2D network is about 1.6 nm, a

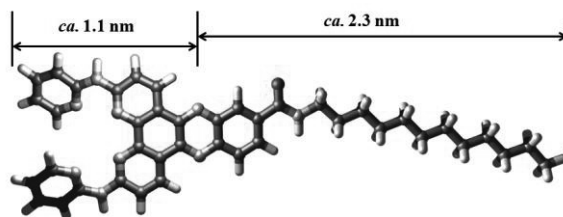


Figure 7.4. DFT-minimized molecular structure of **1**. The dimensions of the molecule are calculated using the program Mercury.³¹

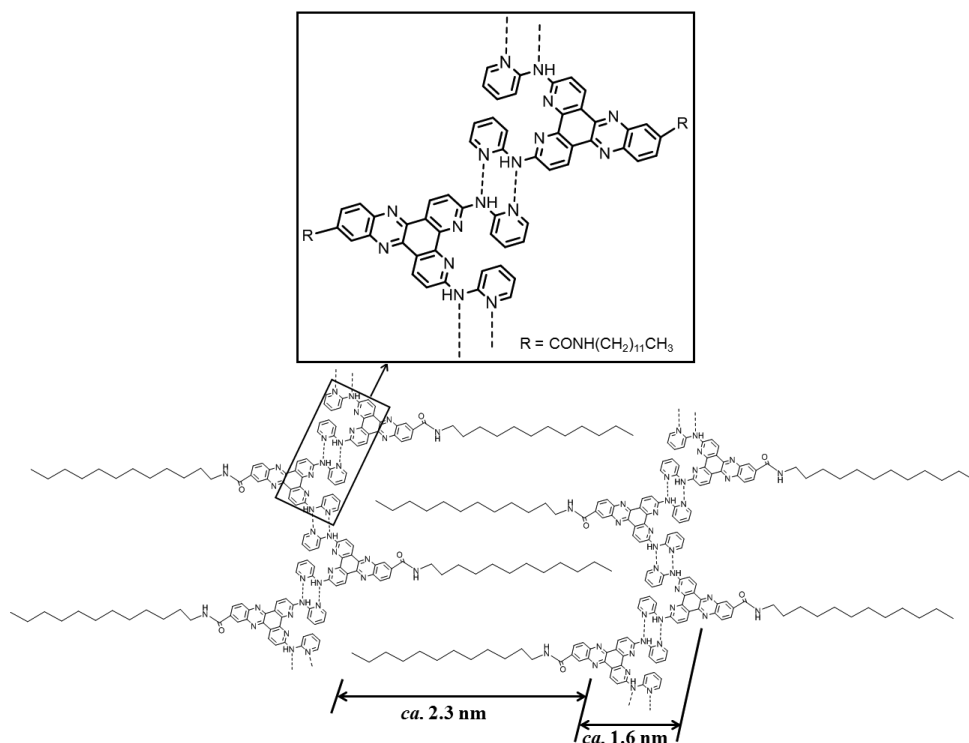


Figure 7.5. Proposed model for the self assembly of **1** on HOPG. Distances are calculated using Mercury,³¹ and the molecular structure of **1** is based on DFT. The 1D supramolecular chains are stabilized by H-bonding between the N–H bridge and the N atom on the terminal pyridine of the neighbouring molecule (insert); These chains then form a 2D motif stabilized by van der Waals interactions between the alkyl tails.

distance measured from projections of the nitrogen atom on the central pyrazine ring to the nitrogen atom on the pyrazine ring of a neighbouring molecule (Figure 7.5). This

value fits well with the experimental width analysis of the bright stripe (*ca.* 1.6 nm, Figure 7.3). The length of the alkyl chain in **1**, in which the distance measured from the tip of the tail to the nitrogen atom on the central pyrazine ring, is also close to the observed width of the dark stripes (2.3 nm, Figure 7.5). Overall, ligand-to-ligand hydrogen bonding and strong interactions with the surface create an interdigitated 2D-assembly of the flat ligands on HOPG, which is also consistent with previously reported adsorption of the pyridines on the carbon layer of HOPG.^{29, 30}

A shorter periodicity was found for the self assembly of **2** on HOPG. To understand this observation, a model was built for the arrangements of **2** on the surface based on the molecular structure of **2** in the LS state obtained by DFT (Figure 7.6). The structure of **2** is built from the X-ray structure of [Fe(bapbpy)(NCS)₂] complex in the LS state.^{15, 32} The tetradentate ligand **1** coordinates to iron(II) in the equatorial plane, leaving the two thiocyanate ligands in the axial positions of the octahedron (Figure 7.6). Thus, on HOPG the tetradentate ligand cannot lie flat because of the axial thiocyanate ligands that create a vacant space underneath **2**. As observed in crystal structures, each iron complex may thus interact with two neighbouring iron complexes via N–H···S hydrogen bonds to form one-dimensional supramolecular chains (Figure 7.7). In addition, because of these N–H···S intermolecular interactions the molecules are forced to tilt with respect to the surface in order to optimize the contact between the monolayer and the basal plane of graphite. As a result, the alkyl chains might enter the vacant space created by the axial thiocyanate ligands and the tilt, to ensure a close contact between the surface and the molecular network (Figure 7.7). In such a model, the periodicity would be shorter than the length of one molecule of **2**. From geometrical estimations the calculated widths of both the aromatic part and of the alkyl chains would fit well with the shorter observed width of the stripes of the network (Figure 7.7 and 7.8). Overall, although the results of the magnetic measurements suggested that N–H···S hydrogen bonding interactions in the bulk are poor, the STM images suggested that once deposited on a surface the N–H···S hydrogen interactions might occur and form ordered supramolecular structures. This would in turn suggest that if such domains of **2** on HOPG surfaces would have SCO properties, the SCO might be cooperative. Whether these 2D networks of **2** have SCO properties or not is unknown yet. We interpret the fact that bonding of **2** on HOPG forms 2D domains as a demonstration that N–H···S hydrogen interactions might rule intermolecular contacts in a monolayer domain, whereas recent examples of other iron based compounds showing

intercalation of C_{12} ligand chains and π - π interactions but lack of $N-H\cdots S$ hydrogen interactions were shown to form isolated 1D nanostructures on surface.^{33, 34}

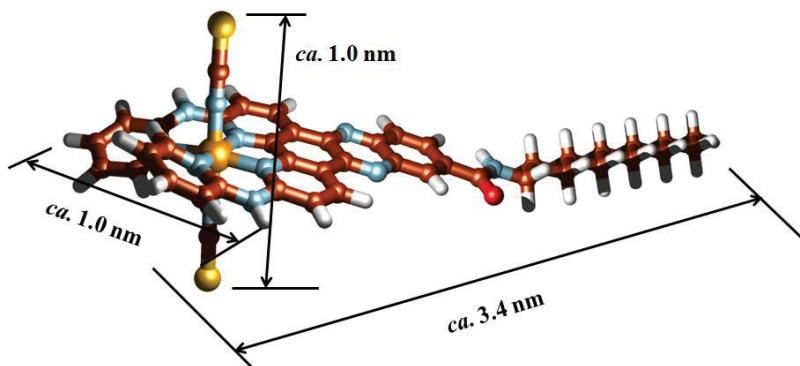


Figure 7.6. Molecular structure of **2** in the LS state as calculated by DFT. The dimensions of the molecule were calculated using the program Mercury.³¹

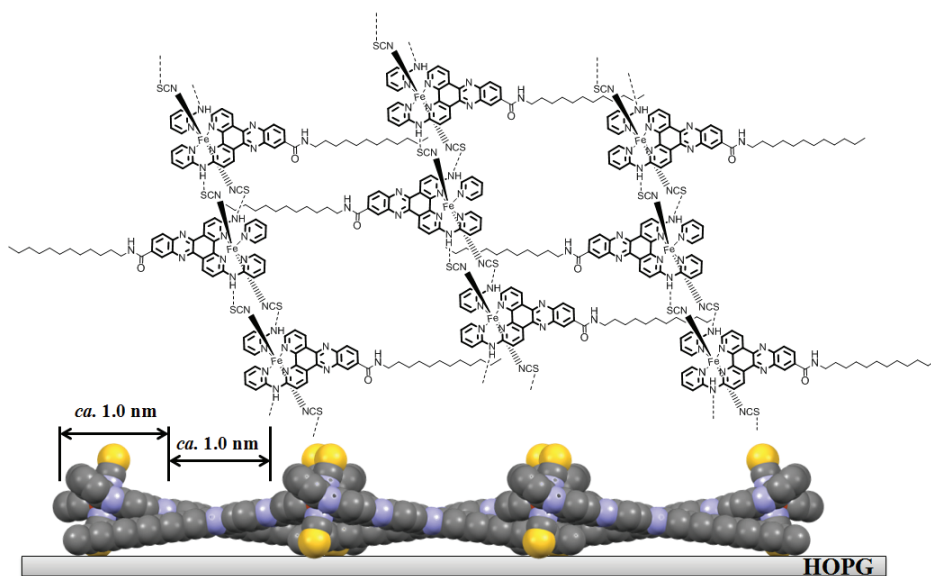


Figure 7.7. Proposed model for the arrangement of **2** on HOPG: (top) schematic representation of intermolecular $N-H\cdots S$ interactions between neighbouring iron(II) complexes; (bottom) side view of the arrangement of **2** parallel to the graphite surface. The two thiocyanate ions are modelled roughly perpendicular to the basal graphite plane. The distances are calculated using the program Mercury³¹ and the molecular structure of **2** calculated by DFT (colour code: grey, carbon; red, oxygen; yellow, sulfur; blue, nitrogen).

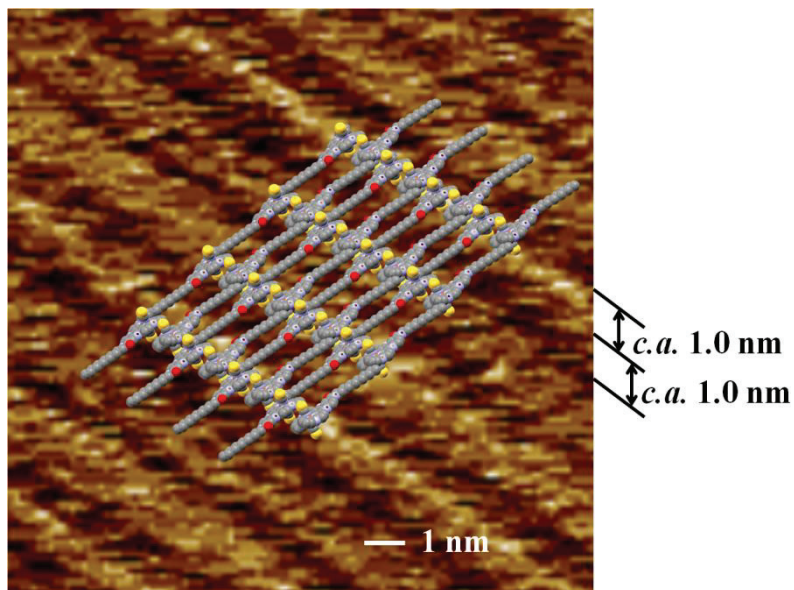


Figure 7.8. A zoom-in STM image from Figure 7.2d, with an overlay of the proposed model highlighting the positions of the 1D supramolecular chains (colour code: grey, carbon; red, oxygen; yellow, sulfur; blue, nitrogen).

7.4. Conclusion

The new bapphen-based ligand **1**, bearing a 12-carbon chain at the back of the phenanthroline backbone, was designed to self-assemble a SCO iron complex on surfaces. Its iron(II) complex **2** shows a gradual spin transition with no hysteresis cycle in the bulk. STM images of both ligand **1** and complex **2** on HOPG revealed stable and highly ordered arrangements on the surface. The different periodicities observed in STM images are attributed to the two different types of intermolecular interactions in **1** and **2**: N–H \cdots N hydrogen bonding for **1** vs. N–H \cdots S hydrogen bonding for **2**. As the resolution of STM images at ambient pressure and room temperature do not give enough information on the exact ordering and conformation of **2** on HOPG, further characterization using an ultra-high vacuum STM machine is ongoing. Overall, the present results suggest that the introduction of long alkyl chains into the ligand bapphen without blocking the N–H bridges is a valid strategy to deposit and organise SCO molecules onto surfaces. Ultimately, changing the temperature of the STM set-up might allow for observing whether SCO occurs in these 2D domains of complex **2**, and check whether it is cooperative or not.

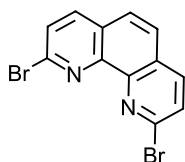
7.5. Experimental

7.5.1. General information

All reactions were performed under argon atmosphere using standard Schlenk line techniques. The applied vacuum was about 10^{-3} mbar. Dry solvents were collected from a Pure Solvent's MD5 dry solvent dispenser from Demaco. Degassed solvents were obtained by bubbling argon through 50 mL solvent in a Schlenk flask for one hour. For all complex syntheses, degassed solvents were used. The compounds **3**, **4**, and 2,9-dibromo-1,10-phenanthroline-5,6-dione (**6**) were synthesized using literature procedures^{16, 17} All other chemicals were obtained from commercial sources and used without any further purification. Thin-layer chromatography was carried out on silica TLC Al foils N/UV₂₅₄ from Sigma Aldrich or on pre-coated TLC-sheets Alugram[®] Alox N/UV₂₅₄. Flash chromatography was performed using silica gel (Sigma Aldrich, silica gel 60 Å 230-400 mesh) or aluminium oxide (Sigma Aldrich, activated, neutral, Brockmann I, 58 Å). Filtrations of ligands and complexes were carried out using Whatman RC60 membrane filters. NMR Spectra were measured on a Bruker DPX-300 Spectrometer at room temperature unless otherwise specified. Chemical shifts are indicated in *ppm* relative to TMS. Mass spectra were obtained using soft electron-spray from a Thermoquest Finnagen TSQ-quantum instrument. HR Mass spectra were measured using direct injection (2 μ L of a 2 μ M solution in DMF and 0.1% formic acid on a mass spectrometer (Thermo Finnigan LTQ Orbitrap) equipped with an electron-spray ion source in positive mode (source voltage 3.5 kV, sheath gas flow 10, capillary temperature 275 °C) with resolution $R=60.000$ at $m/z=400$ (mass range = 150-2000) and dioctylphthalate ($m/z=391.28428$) as "lock mass". IR spectra were acquired with a Perkin-Elmer Spectrum Two FT-IR spectrometer. Elemental analyses (C,H,N,S) were obtained from a Perkin-Elmer 2400 Series II analyzer.

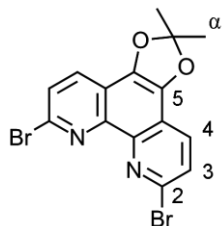
7.5.2. Ligand synthesis

2,9-dibromo-1,10-phenanthroline (**5**) was synthesized using a slightly modified literature procedure:³⁵ Compound **4** (1.0 g, 4.0 mmol), POBr₃ (5.0 g, 17 mmol) and PBr₃ (2.0 mL, 21 mmol) were added together and put under an argon atmosphere. After refluxing for 18 h, the black reaction mixture was cooled down to room temperature and poured onto ice/H₂O. A solution of 1 M NaOH was added until a pH of 7 was reached and the resulting brown solution was extracted with DCM. After evaporating the solvent under reduced pressure and subsequently drying the remaining solid in a vacuum oven, the product was obtained as a light brown solid (88%, 1.1 g). The ¹H NMR spectrum was



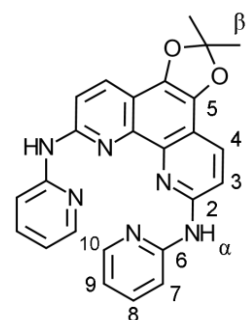
identical to that reported in the literature.³⁵ ¹H NMR (300 MHz, CDCl₃) δ 8.09 (d, *J* = 8.4 Hz, 2H), 7.83 (s, 2H), 7.80 (d, *J* = 8.4 Hz, 2H).

Compound 7: 2-Nitropropane (3.6 mL, 40 mmol) was added to a suspension of 2,9-dibromo-1,10-phenanthroline-5,6-dione (0.15 g, 0.36 mmol) in MeCN and H₂O (20 mL, 1:1). The mixture was degassed and a degassed solution of aqueous Na₂CO₃ (1.0 mL, 0.4 M) was added. The reaction mixture was refluxed for 8 h under an argon atmosphere. It was then cooled to room temperature, and extracted with DCM. Further evaporation of the solvent gave a brown solid.



The solid was subjected to column chromatography (silica gel, 200 mL DCM) using DCM as eluent. The second fraction was collected (*R*_f = 0.5, DCM) and after evaporation of the solvent the pure product was obtained as a yellow solid (56%, 83 mg). ESI-MS *m/z* (calc): 432.9 (433.0 [M+Na]⁺), 448.9 (449.0 [M+K]⁺). ¹H NMR (300 MHz, CDCl₃) δ 8.08 (d, *J* = 8.5 Hz, 2H; H-4), 7.75 (d, *J* = 8.6 Hz, 2H; H-3), 1.87 (s, 6H; H-α). ¹³C NMR (75 MHz, CDCl₃) δ 141.22 (Cq), 140.27 (Cq), 137.19 (Cq), 130.46 (C-4), 128.11 (C-3), 121.97 (Cq), 117.21 (Cq), 26.14 (C-α). Elemental analysis calcd (%) for C₁₅H₁₀Br₂N₂O₂: C 43.94, H 2.46, N 6.83; found: C 43.75, H 2.12, N 6.95.

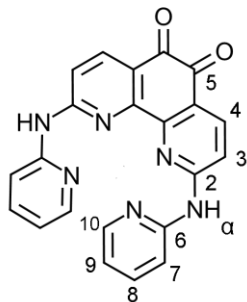
Compound 8: Pd(dba)₂ (7.5 mg, 13 μmol, 2.7 mol%), (S)-BINAP (8.2 mg, 13 μmol, 2.7 mol%) and Cs₂CO₃ (2 eq., 0.32 g, 0.98 mmol) were added together, put under argon, and dissolved in dry toluene (15 mL). After stirring for approximately 10 minutes at room temperature, compound 7 (0.20 mg, 0.48 mmol) and 2-aminopyridine (94 mg, 0.98 mmol) were added. Another 5.0 mL of dry toluene was added to the reaction mixture to ensure that all the substrates were in solution. After refluxing for 4.5 days at 110 °C the reaction was quenched with H₂O (20 mL) and stirred for another hour. After evaporating the solvents under reduced pressure, 266 mg of crude product was obtained.



The crude solid was subjected to column chromatography (silica gel, 10% MeOH/DCM). Using a 10% MeOH/DCM mixture as eluent for the column as well as for the TLC, the third fraction was collected (*R*_f = 0.3) to obtain the pure product as an orange solid (40%, 86 mg). ESI-MS *m/z* (calc): 437.1 (437.5 [M+H]⁺), 459.0 (459.5 [M+Na]⁺). ¹H NMR (300 MHz, MeOD, 40 °C) δ 8.21 (d, 2H; H-7), 8.19 (d, *J* = 4.8 Hz, 2H; H-10), 8.11 (d, *J* = 9.0 Hz, 2H; H-4), 7.57 (t, *J* = 7.9 Hz, 4H; H-3, 8), 6.94 (m, 2H; H-9), 1.84 (s, 6H; H-β). ¹³C NMR (75 MHz, MeOD, 40 °C) δ 155.70 (Cq), 152.52 (Cq), 148.50 (C-10), 143.9 (Cq), 139.83 (C-8), 136.86 (Cq), 131.44 (C-4), 121.69 (Cq), 118.13 (C-9), 116.51 (C-3), 114.28 (Cq), 113.90 (C-7), 25.91 (C-β). The signals corresponding to the

quaternary carbons were very weak. Elemental analysis calcd (%) for $C_{25}H_{20}N_6O_2$: C 68.80, H 4.62, N 19.25; found: C 67.75, H 4.35, N 19.27.

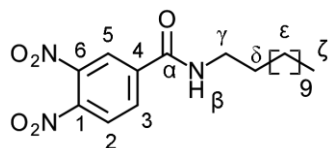
Compound 9: Compound **8** (81 mg, 0.18 mmol) was dissolved in a $H_2O:TFA$ mixture (1:2,



6.0 mL). After stirring for 5 h at 50 °C the reaction was worked up by two different methods. **Method A:** the solution was neutralized with saturated sodium hydrogen carbonate. A red compound slowly precipitated from the solution and was collected by filtration. After washing with water and drying under high vacuum, the product was obtained in a yield of 33%. **Method B:** The solution was neutralized with 2 M NaOH and extraction with ethyl acetate followed. The organic layer was

collected and after evaporation a reddish brown solid was obtained. This solid (352 mg) was used without further purification. The compound collected by method A was less soluble but more pure and it was used for the characterizations. The compound collected by method B was used further for the synthesis of compound **1**. ES-MS m/z (calc): 416.9 (417.4 $[M+Na]^+$), 511.8 (511.4 $[M+DMSO+K]^+$). 1H NMR (300 MHz, $DMSO-d_6$) δ 10.61 (s, 2H; H- α), 8.56 (d, $J = 8.4$ Hz, 2H: H-7) 8.36 (m, 2H; H-10), 8.22 (d, $J = 8.7$ Hz, 2H: H-4), 7.56 (d, $J = 8.7$ Hz, 2H: H-3), 7.49 (m, 2H: H-8), 7.05 (ddd, $J = 7.3, 4.9, 1.0$ Hz, 2H: H-9). ^{13}C NMR (400 MHz, $DMSO-d_6$) δ 177.82 (C-5), 158.10 (Cq), 153.63 (C-6), 153.54 (Cq), 148.36 (C-10), 138.96 (C-9), 137.54 (C-4), 122.21 (C-2), 118.38 (C-8), 113.87(C-3), 113.63 (C-7). Elemental analysis calcd (%) for $C_{22}H_{14}N_6O_2 \cdot H_2O$: C 64.07, H 3.91, N 20.38; found: C 64.67, H 3.44, N 20.29.

Compound 10: To an ice-cold suspension of 3,4-dinitrobenzoic acid (1.0 g, 4.7 mmol) and

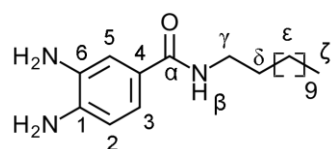


oxalylchloride (0.45 mL, 5.2 mmol) in dry DCM (40 mL), DMF (0.1 mL, 20 mol%) was added drop wise, which gas evolution was observed. After stirring for 1 h at room temperature the solvent was evaporated to remove the

excess of oxalylchloride. The remaining solid was redissolved in dry DCM (25 mL) and added slowly at 0 °C to a solution of dodecylamine (961 mg, 5.18 mmol) and triethylamine (0.98 mL, 7.1 mmol) in dry DCM (25 mL). The reaction mixture was stirred overnight at room temperature, and a clear yellow solution was obtained. Then the yellow solution was washed with brine (2×25 mL), the organic layer was dried over $MgSO_4$, after filtration to remove $MgSO_4$, and subsequently evaporated the solvent under reduced pressure, an orange solid was obtained. The solid was subjected to column chromatography (silica gel, 0.5% MeOH/DCM, 200 mL) eluting with 2% MeOH/DCM. The third fraction was collected (R_f

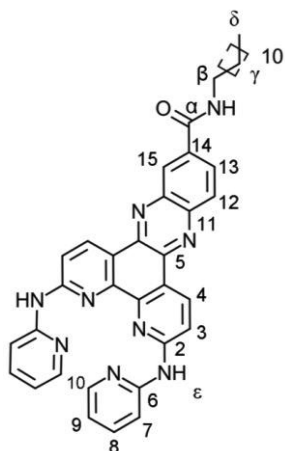
= 0.2, 2% MeOH/DCM) and compound **10** was obtained as a yellow solid (41%, 731 mg). ESI-MS m/z (calc): 380.21 (380.4 $[M+H]^+$). 1H NMR (300 MHz, MeOD) δ 8.48 (d, $J = 1.8$ Hz, 1H; H-5), 8.28 (dd, $J = 8.4, 1.8$ Hz, 1H; H-3), 8.15 (d, $J = 8.4$ Hz, 1H; H-2), 3.40 (m, 2H; γ), 1.62 (d, $J = 7.1$ Hz, 2H; δ), 1.32 (d, $J = 24.1$ Hz, 18H; H- ϵ), 0.88 (m, 3H; H- ζ). ^{13}C NMR (75 MHz, MeOD) δ 165.56 (Cq), 140.95 (Cq), 133.70 (C-2), 126.84 (C-5), 125.40 (C-3), 106.00 (Cq), 41.46 (C- γ), 33.07 (C- ϵ), 30.76 (C- ϵ), 30.71 (C- ϵ), 30.67 (C- ϵ), 30.47(C- ϵ), 30.42 (C- ϵ), 30.24 (C- δ), 28.07 (C- ϵ), 14.44 (C- ζ). Not all quaternary carbons could be detected. Elemental analysis calcd (%) for $C_{19}H_{29}N_3O_5$: C 60.14, H 7.70, N 11.10; found: C 60.40, H 6.60, N 10.90.

Compound 11: Under an argon atmosphere, compound **10** (0.20 g, 0.53 mmol) and Pd/C



10% (30 mg, 0.28 mmol) were suspended in degassed methanol (25 mL). The solution was put under an H_2 atmosphere using a balloon filled with H_2 , and stirred at room temperature for 5 h. After filtration over Celite and evaporation of the solvent, 171 mg of crude product was obtained. The solid was subjected to column chromatography (silica gel, 10% MeOH/DCM, 100 mL). By using 10% MeOH/DCM as eluent for the column as well for the TLC, the last spot ($R_f = 0.1$) was collected which contained the pure product as a grey solid (62%, 105 mg). ESI-MS m/z (calc): 320.1 (320.5 $[M+H]^+$), 342.1 (342.5 $[M+Na]^+$), 374.2 (374.5 $[M+MeOH+Na]^+$). 1H NMR (300 MHz, MeOD) δ 7.14 (d, $J = 2.0$ Hz, 1H; H-5), 7.08 (dd, $J = 8.1, 2.1$ Hz, 1H; H-3), 6.65 (d, $J = 8.1$ Hz, 1H; H-2), 1.57 (t, $J = 7.0$ Hz, 2H; H- γ), 1.30 (d, $J = 16.6$ Hz, 20H; H- δ, ϵ), 0.87 (m, 3H; H- ζ). ^{13}C NMR (75 MHz, MeOD) δ 170.83 (C- α), 140.60 (C-4), 134.82 (C-6), 125.38 (C-1), 120.30 (C-3), 116.41 (C-5), 115.66 (C-2), 40.90 (C- γ), 33.09 (C- ϵ), 30.79 (C- δ), 30.78 (C- ϵ), 30.74 (C- ϵ), 30.70 (C- ϵ), 30.52 (C- ϵ), 30.49 (C- ϵ), 28.13 (C- ϵ), 23.75 (C- ϵ), 14.45 (C- ζ). Elemental analysis calcd (%) for $C_{19}H_{33}N_3O$: C 71.43, H 10.41, N 13.15; found: C 71.62, H 9.20, N 13.09.

Compound 1: Compound **9** (36 mg, 92 μ mol) and compound **11** (35 mg, 0.11 mmol) were dissolved in degassed methanol (15 mL) and stirred for 18 h at 85 $^\circ C$. The precipitate formed during the reaction was collected by filtration. After washing the solid with methanol the product was obtained as a yellow solid (43%, 27 mg). ESI-MS m/z (calc): 678.1 (678.3 $[M+H]^+$), 751.4 (751.4 $[M+DMF+H]^+$). 1H NMR (300 MHz, $DMSO-d_6$, 40 $^\circ C$) δ 10.63 (s, 2H; H- ϵ), 9.20 (t, $J = 7.9$ Hz, 2H; H-4), 8.80 (t, $J = 4.9$ Hz, 1H; H-15), 8.65 (s, 1H; H-13), 8.39 (s, 1H; NH), 8.29 (m, 2H; H-9), 8.20 (m, 3H; H-10, 12), 7.79 (t, $J = 9.1$ Hz, 2H; H-3), 7.64 (t, $J = 6.8$ Hz, 2H; H-7), 7.07 (m, 2H; H-8), 1.62 (m, 2H; H- β), 1.29 (d, $J = 38.7$ Hz, 20H; H- γ), 0.83 (t, $J = 5.8$ Hz, 3H; H- δ). ^{13}C NMR (75 MHz, $DMSO-d_6$) δ 164.98 (C- α), 154.89 (Cq), 153.01 (Cq), 146.83 (C-9), 141.85 (Cq), 140.30 (Cq),

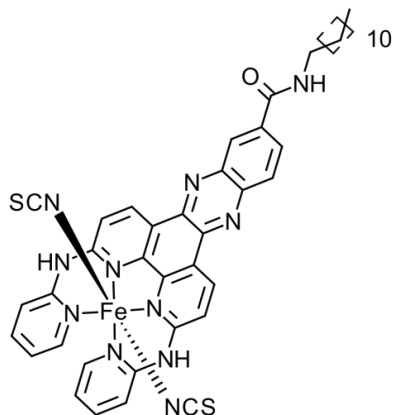


139.99 (C α), 138.82 (C-7), 135.45 (C α), 135.01 (C-4), 134.70, 128.62 (C-10), 128.38 (C-13), 127.64 (C-12), 120.12 (C α), 120.09 (C α), 117.48 (C-8), 114.95 (C-3), 112.89 (C-15), 31.15 (C- γ), 28.93 (C- γ), 28.89 (C- β), 28.67 (C- γ), 28.56 (C- γ), 26.43 (C- γ), 21.92 (C- γ), 13.75 (C- δ). IR ν (cm⁻¹): 3250, 3075, 2923, 2851, 1652, 1576, 1520, 1437, 1371, 1324, 1306, 1199, 1119, 996, 834, 768, 717, 611, 590, 511. Elemental analysis calcd (%) for C₄₁H₄₃N₉O·2H₂O: C 68.99, H 6.64, N 17.66; found: C 68.53, H 6.58, N 16.91.

7.5.3. Complex synthesis

Preparation of an 0.1 M iron(II) stock solution: KSCN (195 mg, 2.00 mmol) and ascorbic acid (6.1 mg, 0.035 mmol) were placed under argon in a round-bottom flask. FeSO₄·7H₂O (152 mg, 1.00 mmol) was added and the mixture was suspended in degassed methanol (6.0 mL). The suspension was stirred for 40 min, filtered, and the filtrate was transferred into a volumetric flask. The volume was adjusted to 10.0 mL with degassed methanol and the volumetric flask was well shaken, which resulted in an 0.1 M [Fe(NCS)₂] solution in methanol. Since the filtration and the solution were not kept under argon, the solution had to be prepared fresh for every synthesis. Aerial oxidation of the iron-containing solution was visible due to a change of colour (from colourless to dark violet).

[Fe(1)(NCS)₂] (2): Compound **1** (8.0 mg, 12 μ mol) was put under argon and degassed MeOH (2.0 mL) and Fe(NCS)₂ (0.13 mL of 0.1 M stock solution, 13 μ mol) were added successively. After refluxing under argon for 12 h at 80 °C the brown precipitate was collected and was washed extensively with MeOH. Compound **2** was obtained as a brown solid (40%, 5.7 mg). HR-MS *m/z* (calc): 366.6464 (366.6465 [M-2NCS]²⁺), 846.2788 (846.2786 [M-2NCS+TFA]⁺). IR ν (cm⁻¹): 3249, 3074, 2922, 2852, 2077 (NCS⁻), 1628, 1594, 1545, 1521, 1469, 1417, 1386, 1356, 1242, 1141, 1008, 837, 768, 753, 648, 604, 509.



7.5.4. Magnetic susceptibility measurement

Magnetic susceptibility measurements were recorded on a Quantum Design MPMS-XL SQUID magnetometer. Prior to the measurements 3.12 mg of compound **2** was centred in a field of 0.1 T at 300 K, then DC magnetization measurements were performed in a field of 0.1 T, from 5 to 350 K (heating mode) and from 350 to 5 K (cooling mode) with a rate of 0.3–1.1 K.min⁻¹. The measuring time was 20 h, and corrections for the diamagnetism were calculated using Pascal's constants.³⁶ The measurement was performed within a temperature range of 5 to 350 K with steps of 5 K in the low temperature range and with steps of 2 K in the 250 and 350 K temperature range. At each temperature, the magnetic susceptibility was measured 4 times, to compensate for any measuring errors.

7.5.5. General procedure for molecule deposition on HOPG and STM imaging

Sample preparation: a drop (9 μL) of a solution of compound **1** or **2** in distilled and degassed DMF (concentration 8×10⁻⁸ M) was carefully placed on a freshly cleaved HOPG surface under argon. The HOPG surface had been imaged with atomic resolution for reference. The functionalized substrate was then dried under a gentle stream of argon in a Schlenk flask, for over 16 h in the dark. Then the sample was directly probed by STM under ambient conditions.

STM spectroscopy: a PicoSPM I (Agilent Technologies) equipped with an E-scanner (8048 EV) and a Digital Instruments Multimode Microscope (Veeco) with Nanoscope IIIa controller were used to carry out all measurements under ambient conditions. Mechanical vibration was minimized using active vibration isolation table in a home-made sound box. The highly oriented pyrolytic graphite (HOPG, SPI-3, from SPI Supplies) was freshly cleaved using Scotch tape. The graphite surface was then imaged by STM to confirm the high resolution of the tip, and the flatness of the substrate. Mechanically cut Pt-Ir tips (90/10, from Goodfellow Cambridge Limited) of diameter 0.25 mm were used. Typically, the tunneling current set point was 1 nA. The bias voltage was +500 mV. The scan frequency was varied between 0.5 and 3 Hz depending on the scan size. Obtained STM images were flattened to eliminate unwanted features from scan lines (*e.g.*, noise, bow and tilt), and this image analysis command was carried out by using the program NanoScope Analysis (Version 1.40, Bruker Corporation, 2012).

DFT calculations: molecular structures of **1** and **2** were built with MOLDEN and minimized in vacuum using the B3LYP functional and the LANL2DZ basis set for all atoms as implemented in the GAMESS-UK package.

7.6. References

1. P. Gütllich and H. A. Goodwin, *Top. Curr. Chem.*, 2004, 233, 3-35.
2. H. Spiering, T. Kohlhaas, N. Romstedt, A. Hauser, C. Bruns-Yilmaz, J. Kusz and P. Gütllich, *Coord. Chem. Rev.*, 1999, 192, 629-647.
3. O. Kahn and C. J. Martinez, *Science*, 1998, 279, 44-48.
4. D. Wiedemann and A. Grohmann, *Dalton Trans.*, 2014, 43, 2406-2417.
5. A. Bousseksou, G. Molnar, L. Salmon and W. Nicolazzi, *Chem. Soc. Rev.*, 2011, 40, 3313-3335.
6. S. Hayami, M. R. Karim and Y. H. Lee, *Eur. J. Inorg. Chem.*, 2013, 2013, 683-696.
7. S. Schlamp, P. Thoma and B. Weber, *Eur. J. Inorg. Chem.*, 2012, 2759-2768.
8. M. Seredyuk, A. B. Gaspar, V. Ksenofontov, Y. Galyametdinov, J. Kusz and P. Gütllich, *Adv. Funct. Mater.*, 2008, 18, 2089-2101.
9. M. Seredyuk, A. B. Gaspar, V. Ksenofontov, S. Reiman, Y. Galyametdinov, W. Haase, E. Rentschler and P. Gütllich, *Chem. Mater.*, 2006, 18, 2513-2519.
10. S. Hayami, Y. Komatsu, T. Shimizu, H. Kamihata and Y. H. Lee, *Coord. Chem. Rev.*, 2011, 255, 1981-1990.
11. J. A. Real, A. B. Gaspar and M. C. Munoz, *Dalton Trans.*, 2005, 34, 2062-2079.
12. D. Gatteschi and R. Sessoli, *Angew. Chem., Int. Ed.*, 2003, 42, 268-297.
13. A. Mourran, U. Ziener, M. Moller, E. Breuning, M. Ohkita and J. M. Lehn, *Eur. J. Inorg. Chem.*, 2005, 2641-2647.
14. G. G. Condorelli, A. Motta, I. L. Fragalà, F. Giannazzo, V. Raineri, A. Caneschi and D. Gatteschi, *Angew. Chem., Int. Ed.*, 2004, 43, 4081-4084.
15. S. Bonnet, M. A. Siegler, J. S. Costa, G. Molnar, A. Bousseksou, A. L. Spek, P. Gamez and J. Reedijk, *Chem. Commun.*, 2008, 5619-5621.
16. J. Frey, T. Kraus, V. Heitz and J.-P. Sauvage, *Chem. Eur. J.*, 2007, 13, 7584-7594.
17. T. Ishi-i, R. Hirashima, N. Tsutsumi, S. Amemori, S. Matsuki, Y. Teshima, R. Kuwahara and S. Mataka, *J. Org. Chem.*, 2010, 75, 6858-6868.
18. D. S. Surry and S. L. Buchwald, *Chem. Sci.*, 2011, 2, 27-50.
19. M. Ikeda, H. Nakagawa, T. Suzuki and N. Miyata, *Bioorg. Med. Chem. Lett.*, 2012, 22, 1949-1952.
20. A. Greguric, I. D. Greguric, T. W. Hambley, J. R. Aldrich-Wright and J. G. Collins, *Dalton Trans.*, 2002, 31, 849-855.
21. S. Bonnet, G. Molnar, J. Sanchez Costa, M. A. Siegler, A. L. Spek, A. Bousseksou, W.-T. Fu, P. Gamez and J. Reedijk, *Chem. Mater.*, 2009, 21, 1123-1136.
22. L. J. Bellamy and A. J. Owen, *Spectrochim. Acta, Part A*, 1969, A 25, 329-333.
23. J. P. Rabe and S. Buchholz, *Phys. Rev. Lett.*, 1991, 66, 2096-2099.
24. J. P. Rabe and S. Buchholz, *Science*, 1991, 253, 424-427.
25. T. Nakanishi, H. Takahashi, T. Michinobu, M. Takeuchi, T. Teranishi and K. Ariga, *Colloids Surf., A*, 2008, 321, 99-105.
26. A. Stabel and J. P. Rabe, *Synth. Met.*, 1994, 67, 47-53.
27. C. P. Kohler, R. Jakobi, E. Meissner, L. Wiehl, H. Spiering and P. Gütllich, *J. Phys. Chem. Solids*, 1990, 51, 239-247.
28. M. F. Guest, I. J. Bush, H. J. J. Van Dam, P. Sherwood, J. M. H. Thomas, J. H. Van Lenthe, R. W. A. Havenith and J. Kendrick, *Mol. Phys.*, 2005, 103, 719-747.
29. E. N. Voloshina, D. Mollenhauer, L. Chiappisi and B. Paulus, *Chem. Phys. Lett.*, 2011, 510, 220-223.
30. J. D. Wuest and A. Rochefort, *Chem. Commun.*, 2010, 46, 2923-2925.

-
31. C. F. Macrae, I. J. Bruno, J. A. Chisholm, P. R. Edgington, P. McCabe, E. Pidcock, L. Rodriguez-Monge, R. Taylor, J. van de Streek and P. A. Wood, *J. Appl. Crystallogr.*, 2008, 41, 466-470.
 32. Z. Arcis-Castillo, S. Zheng, M. A. Siegler, O. Roubeau, S. Bedoui and S. Bonnet, *Chem. Eur. J.*, 2011, 17, 14826-14836.
 33. P. N. Martinho, T. Lemma, B. Gildea, G. Picardi, H. Müller-Bunz, R. J. Forster, T. E. Keyes, G. Redmond and G. G. Morgan, *Angew. Chem., Int. Ed.*, 2012, 51, 11995-11999.
 34. A. M. Ako, M. S. Alam, M. Rahman, J. P. Hill, N. M. Sanchez-Ballester, K. Ariga, G. Buth, C. E. Anson and A. K. Powell, *Chem. Eur. J.*, 2012, 18, 16419-16425.
 35. H. C. Guo, R. H. Zheng and H. J. Jiang, *Org. Prep. Proced. Int.*, 2012, 44, 392-396.
 36. G. A. Bain and J. F. Berry, *J. Chem. Educ.*, 2008, 85, 532-536.

8



Conclusions and outlook

8.1 Ligand modifications and new spin-crossover materials

Cooperative spin-crossover Fe(II) compounds showing thermal hysteresis exhibit magnetic and colourmetric bistability, which is of interest for a number of applications such as information storage and optical displays.¹ Mononuclear iron(II) complexes hold considerable potential in this field, and their properties may suffer less from size reduction effects than polymeric SCO materials because the coordination environment remains well defined throughout the material. However, the ideal mononuclear SCO complex is still rare as a high transition temperature and high cooperativity require strong ligands for Fe(II) *and* strong intermolecular interactions. One of the goals of this project was to design new mononuclear Fe(II) compounds based on the bapbpy ligand, *i.e.*, derivatives of the highly cooperative SCO compound [Fe(bapbpy)(NCS)₂] (**1**),² with higher transition temperatures. Four Chapters of this thesis focus hence on increasing the transition temperature of **1** while maintaining a hysteresis cycle (see Chapters 2, 4, 5 and 6, and Table 8.1).

The ligand bapbpy is a rigid, embracing N₄ ligand leaving two *trans* positions on the coordination sphere for coordination of axial ligands.² By adding electron-donating methyl groups on the four different positions of the terminal pyridine rings, only one SCO compound [Fe(Me₂bapbpy)(NCS)₂] was obtained (Chapter 2, **2**, see Table 8.1). However, its transition temperature is low (170 K) and the compound shows no hysteresis cycle. On the other hand, when more conjugated quinoline or isoquinoline substituents were used instead of the terminal pyridine rings, two new SCO compounds were obtained. One remains cooperative as in **1** (*i.e.*, with hysteresis cycle), but has a low transition temperature (**3**, Table 8.1); the other one shows a promising near room-temperature transition (288 K, **4** in Table 8.1), but no hysteresis cycle. The X-ray crystallography data of SCO compounds **2** and **4** show similar crystal packing, which features N–H⋯S hydrogen-bond networks. However, because of the substituents at the β, β' positions on the terminal pyridine rings (Figure 8.1), these N–H⋯S intermolecular interactions are weaker compared to those in compound **1**. Overall, for bapbpy-based SCO compounds the strength of these N–H⋯S hydrogen bonds correlates well with the cooperativity of the spin transition, and it appears to be important to keep the β positions on the bapbpy ligand vacant in order to maintain cooperativity. Strikingly, different isomers of the same mononuclear iron(II) complex give materials of very different SCO properties. Overall, by modifying the chemical structure of the bapbpy

ligand the transition temperature of the SCO compounds was increased to near room temperature, but unfortunately at the cost of cooperativity.

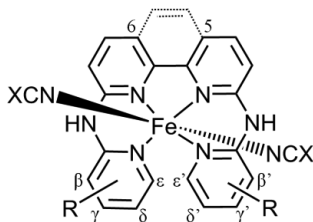


Figure 8.1. General schematic drawing of the iron(II) SCO complexes studied in this thesis based on the bapbpy ligand. X=S or Se.

Because minor chemical changes on the bapbpy ligand led to significant changes in the SCO properties of its Fe(II) compound, another approach was tried, which consisted in replacing the axial NCS^- ligand by more electron donating NCSe^- ligands (Chapter 4). Five new iron(II) SCO compounds **5-9** (Table 8.1) were obtained with the same R_2bapbpy derivatives as described in Chapter 2. Two were found to be cooperative SCO materials (**6** and **8**), whereas the others showed non-cooperative SCO. For **6** and **8**, although the transition temperatures are still far lower than room temperature, a trend was observed: their transition temperature is increased compared to the NCS^- analogues. In particular, compound **6** does show SCO whereas its thiocyanate analogue does not. Consistently, for the non-cooperative SCO compounds **7** and **9**, the same trend was also observed, with the transition temperature of **9** (357 K) being the highest of all bapbpy-based compounds reported to date. By comparing the X-ray structures of compounds **7** and **9** with those of **2** and **4**, a striking structural similarity was found between the thiocyanate and selenocyanate compounds, indicating that the increase of the transition temperature has a purely electronic origin. Compound **5** appears to be an exception, as its dramatically lower cooperativity compared to compound **1** seems to be the result of a change in X-ray structure of the Fe(II) compound when going from NCS^- to NCSe^- axial ligands, rather than an electronic effect.

By using a phenanthroline backbone instead of a bipyridine, not only the rigidity of the ligand is increased, but also the ligand field strength, since phen is a stronger ligand than bpy in the spectrochemical series (Chapter 5). Two new iron(II) SCO compounds were obtained with the new bapphen ligand (**10** and **11**, Table 8.1). Interestingly,

different forms exist for compound **10**, which are obtained by different preparation methods. The first form could not be crystallized but shows a three-step, incomplete SCO with a hysteresis cycle just below room temperature (280 K), whereas the second form crystallizes more easily but has no SCO properties. In compound **11**, in which the NCS^- ligands were replaced with NCSe^- ligands, the cooperativity was lost, similar to what was observed for the bapbpy complexes (e.g., **5** vs. **1**).

Finally, the most promising SCO compound described in this thesis, $[\text{Fe}(\text{bbpya})(\text{NCS})_2]$ (**12**, Table 8.1), was designed by a very different approach consisting in replacing one of the 6-membered rings found in bapbpy-based metal complexes, by a 5-membered ring (Chapter 6). The new ligand bbpya is a rigid and almost flat ligand in which two bipyridines are connected by a single amine bridge. Its iron(II) complex **12** indeed shows a decreased distortion of the octahedral coordination environment compared to **1**. As a result, **12** is low-spin (LS) at room temperature in the solid state and shows one of the highest transition temperatures recorded among known mononuclear SCO complexes. Most interestingly, it keeps a large hysteresis cycle of 21 K although each bbpya ligand has only one NH bridge to build hydrogen bonding networks. Crystal data revealed that cooperativity is maintained due to the disorder in the structure, which results in infinite supramolecular chains *via* hydrogen-bonding and π - π stacking interactions. Overall, the uncommon features of **12** validate the strategy of replacing 6-membered chelate rings by 5-membered ones to increase the transition temperature.

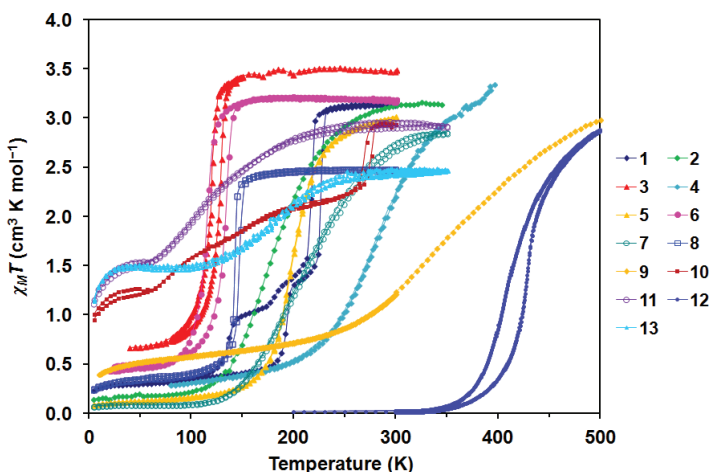


Figure 8.2. Summary of $\chi_M T$ vs. T curves for all SCO compounds **1-13** described in this thesis. The number codes are referred to Table 8.1 (see next page).

Table 8.1. Summary of transition temperatures ($T_{1/2}$), hysteresis widths (ΔT_{hyst}) and the number n of like-spin SCO centres per interacting domain of all new SCO compounds [Fe(L)(NCX)₂] described in this thesis (2-13) and, for comparison, of the reference compound [Fe(babpy)(NCS)₂] (1).

Entry	Chapter	Ligand L	NCX	$T_{1/2}$ (K) ^a	ΔT_{hyst} (K)	n	Special observation
1	–	babpy	NCS	235↓ / 239↑(1 st) 172↓ / 194↑(2 nd)	4 / 22	11.6 / 22.5	2-step SCO, with distinctive IP
2	2	β, β' - Me ₂ babpy	NCS	170(2)	–	2.8	
3	2	R ₂ babpy ^b	NCS	113(2)↓ / 125(2)↑	11(3)	16.8	
4	2	R' ₂ babpy ^c	NCS	288(5)	–	5.3	
5	4	babpy	NCSe	195(4)	–	5.8	Gradual transition
6	4	δ, δ' - Me ₂ babpy	NCSe	113(4)↓ / 137(4)↑	24(6)	14.4	Replace NCS by NCSe leads to SCO
7	4	β, β' - Me ₂ babpy	NCSe	214(20)	–	3.1	
8	4	R ₂ babpy ^b	NCSe	141(4)↓ / 149(4)↑	8(6)	54.8 / 70.5	
9	4	R' ₂ babpy ^c	NCSe	357(19)	–	4.8	
10	5	bapphen ^d	NCS	268(4)↓ / 280(4)↑ ^e	12(6)		2 forms, one showing multi-step transition
11	5	bapphen	NCSe	101(4)	–		Gradual transition
12	6	bbpya	NCS	407(3)↓ / 428(1)↑	21(3)	10.2 / 6.5	LS at RT
13	7	bapphen-C ₁₂	NCS	182(25)	–		Gradual transition, self assembly on HOPG

^a $T_{1/2}$ values were obtained based on magnetic susceptibility measurements on samples prepared by method a, ↓ and ↑ indicate $T_{1/2}$ in cooling and in the heating mode respectively, the errors are also given in the brackets. ^b R₂babpy contains isoquin-3-oline substituents. ^c R'₂babpy contains isoquin-1-oline substituents. ^d Transition temperatures are given based on the SCO form of [Fe(bapphen)(NCS)₂]. ^e Only the transition temperatures for the hysteresis (first-step transition) are given.

8.2 Understanding the cooperativity in [Fe(bapbpy)(NCS)₂]

In the research described in this thesis, the cooperativity of the SCO of [Fe(bapbpy)(NCS)₂] (**1**) was studied by diluting the iron complex with increasing amounts of its magnetically inert Zn(II) analogue (Chapter 3). The initial idea was to investigate to which extent the two-step SCO and hysteresis cycles remain when the average Fe–Fe distance becomes larger. However, the zinc analogue of **1** shows a different crystallographic structure compared to **1**, due to the different geometric preferences of the Zn(II) ion. Single crystals of cocrystallized [Fe_xZn_{1-x}(bapbpy)(NCS)₂] could not be obtained, as a result of which the study of the diluted compounds was completed using powder samples. Based on powder X-ray diffraction, magnetic susceptibility measurements, and infrared spectroscopy data, it appeared that in the zinc-diluted samples containing a majority of iron ($x > 0.53$) the phase of the iron compound was retained. At higher dilutions, the phase of the zinc analogue gradually took over, but the SCO of the iron compound remained observable at an iron fraction as low as $x = 0.24$. Upon decreasing the iron fraction x the two hysteresis cycles initially became narrower, and then vanished at $x = 0.76$, to lead to a single-step SCO material with some degree of cooperativity. Further increasing the zinc content led to the gradual loss of the cooperativity and to a fully non-cooperative SCO material at the lowest iron fraction studied ($x = 0.24$). Overall, this study clearly shows that the two steps and the hysteresis cycles of the SCO are two consequences of the same phenomenon: intermolecular interactions between spin-switching molecules. These two different manifestations of cooperativity are both lost simultaneously upon dilution.

8.3 SCO material on a surface

For nanomemory applications, the major goal is to perform spin switching of a single molecule at a surface. The current challenge includes controlling the self-organization and addressability of SCO molecules at surfaces. In this thesis, a new bapphen-based ligand bearing a 12-carbon chain at the back of the tetrapyrrolyl ligand is described. Although such functionalization represents extensive modifications of the polypyridyl ligand, the iron complex **13** (Table 8.1) still shows spin transition in the bulk material, although it is gradual and does not show a hysteresis cycle. The long alkyl chain helps the complex to self-assemble on a highly oriented pyrolytic graphite (HOPG) surface, where the molecules appear to form stable and highly ordered 2D patterns. The

periodicity of these patterns as observed by STM is different from the periodicity of similar patterns made by the free ligand on HOPG. A model was built that suggests that the N–H···S intermolecular interactions still exist at the HOPG surface for the iron complex **13**. This in turn suggests that molecules of **13** might show cooperative SCO once deposited on HOPG. Variable temperature STM is not a straightforward technique though, and collaboration on this topic is currently ongoing with the group of Atomic and Molecular Conductors (AMC) at the Leiden Institute of Physics. Overall, the introduction of long alkyl chains on the bapphen ligand without blocking the N–H bridges appears to be a valid strategy to deposit and organise SCO molecules onto surfaces.

8.4 Outlook and future perspectives

One of the major goals in the field of spin crossover is to “rationally design” mononuclear SCO compounds with high transition temperature and high cooperativity. “Rational design” involves understanding of the SCO phenomenon and being able to predict the properties of a given compound. This goal was pursued by making use of the ligand-field theory (see Chapter 1). Many different ligands were investigated for their abilities to increase the ligand field strength around the Fe(II) ion, to increase the transition temperature of the SCO of their iron complexes. Regarding cooperativity a model was built that predicts cooperative SCO when the N–H···S hydrogen bonds are strong, *i.e.*, when there is no substituent hampering hydrogen-bond interactions and when the intermolecular N···S distances are short (~ 3.4 Å), whereas non-cooperative SCO occurs when a substituent weakens the N–H···S hydrogen bonds by elongating the intermolecular N···S distances (3.9 to 4.1 Å). We are able to show that indeed mononuclear SCO compounds with high transition temperature and high cooperativity can be obtained.

However, it was found that extreme small changes, for example, replacing the S atom of the NCS anion with less electronegative Se atom in NCSe, represents a modification that is important enough to radically change the SCO properties of the complex. This extreme sensitivity of SCO to minute changes of the compound culminates in sample preparation, where the same compound prepared with different methods gives different forms with different SCO properties. The mere occurrence of SCO, as well as the transition temperatures, are still impossible to link in a straightforward manner to the

ligand field strength, as other parameters such as packing effects play a critical role in the magnetic properties of these SCO compounds.

For the high-temperature, cooperative SCO compound [Fe(bbpya)(NCS)₂] (**12**, Table 8.1), the strategy of decreasing the distortion of the octahedral coordination environment was a very successful approach. A high cooperativity remains even with only one NH bridge presents per complex, which could open a new door for the design of new rigid N₄ ligands. In practice indeed, the transition temperature of this compound may even be too high for information storage applications. Transition temperatures situated around 298 K are preferred, which may be obtained by replacing the axial NCS⁻ ligands in this compound by the less electron-donating NCO⁻ ligands. However, the high transition temperature of compound **12** allows for studying mechanistic and microscopic aspects of cooperative SCO that are more difficult to study in a cooled environment. Collaboration in this direction has been started with the group of Azzedine Bousseksou and Gabor Molnar in Toulouse.

It is worth mentioning that many SCO compounds described in this thesis have relatively low molecular weights, are neutral, and do not contain any solvent molecules in the crystal lattice. Therefore, they are in principle suitable for evaporation under ultra-high vacuum conditions to obtain clean, well-organized monolayers or sub-monolayers on surfaces. The transition temperatures of these compounds in the bulk are ranging from 113 K to 428 K. Thus, if it were possible to vary the temperature of an STM setup, it might be possible to observe whether SCO occurs for these complexes, either at the single-molecule level or at the level of a cluster of a few molecules, and to check whether such small clusters show cooperative SCO properties or not.

The initial results of compound **13** self-assembled on HOPG by dip coating are very promising, as this compound seems to form infinite 1D chains connected *via* the alkyl tails into large 2D domains. However, for practical applications both the transition temperature and synthetic availability of such compounds have to be improved. One of the reasons for the low transition temperature and high residual HS fraction at low temperature for this compound is most likely due to the extensive modification of the organic backbone of the bapphen ligand. It might be interesting to attach two alkyl chains at the 5,6 positions on the bapphen ligand, as shown in Figure 8.3. Such a ligand

potentially would be significantly easier to prepare than the ligand used in compound **13**.

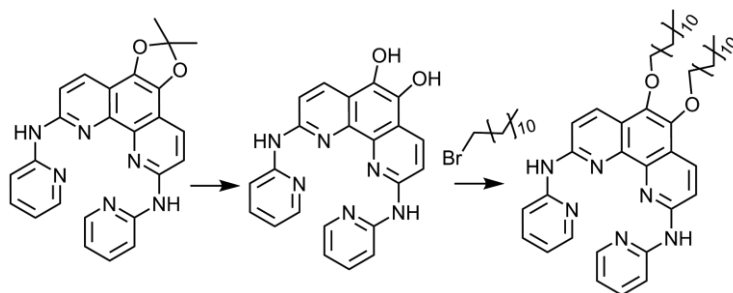


Figure 8.3. Proposed synthetic route towards a two-tailed bapphen-based iron(II) compound.

Even with compounds showing high cooperativity in the bulk, it is not guaranteed that the SCO molecules would remain cooperative on surfaces. The SCO will indeed depend on substrate-molecule interactions as well. It would be interesting to immobilize compound **13** onto a self-assembled monolayer (SAM) of alkanethiols on a gold surface (Figure 8.4). By doing so, the molecules are expected to hold roughly perpendicularly to the surface due to supramolecular interactions (van der Waals force).³ It is thus conceivable that hydrogen bonding and π - π stacking interactions may occur in such a system, thereby allowing cooperativity. Another advantage of using SAMs on gold surfaces is that defects and pollutants on the surface may be readily displaced by the thiols. This may lead to very flat surfaces, which would help the detection and characterization of the SCO molecules by STM. Overall, the question of the minimal size at which 2D clusters of SCO molecules show cooperative behaviour, is not resolved yet.

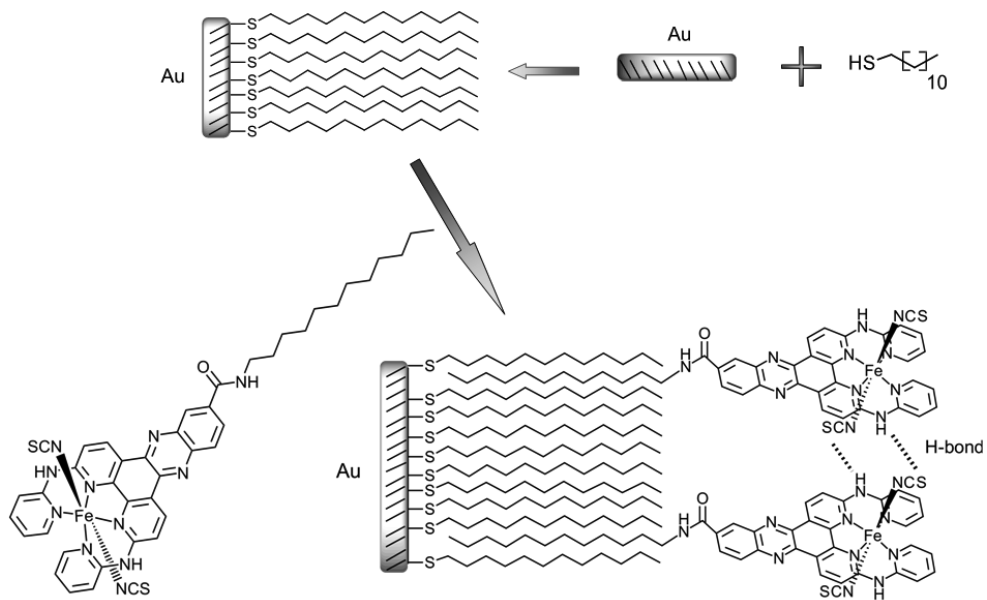


Figure 8.4. Immobilizing molecules of compound **13** to a self-assembled monolayer of alkanethiols on a gold surface.

8.5 References:

1. O. Kahn and C. J. Martinez, *Science*, 1998, 279, 44-48.
2. S. Bonnet, M. A. Siegler, J. Sanchez Costa, G. Molnar, A. Bousseksou, A. L. Spek, P. Gamez and J. Reedijk, *Chem. Commun.*, 2008, 5619-5621.
3. L. Srisombat, A. C. Jamison and T. R. Lee, *Colloids Surf., A*, 2011, 390, 1-19.

Appendix I

Supplementary information on Chapter 3

- ^1H NMR spectra of $[\text{Fe}(\text{bapbpy})(\text{NCS})_2]$ (**1**) and $\text{Zn}(\text{bapbpy})(\text{NCS})_2$ (**3**)
- Calculated and observed $\chi_M T$ values at 300 K for the diluted samples $[\text{Fe}_x\text{Zn}_{1-x}(\text{bapbpy})(\text{NCS})_2]$
- $d\chi_M T/dT$ vs. T plots for compound **1** and for the diluted samples (**a**) to (**i**)
- MOLDEN-generated superposition of the crystal structures for compound **1** and that of a mixture of bapbpy, $[\text{Fe}(\text{NCS})_2]$ and $[\text{Zn}(\text{NCS})_2]$ (10:9:1)
- X-ray powder diffractograms of a crude powder sample of **3** and the calculated powder pattern derived from the crystal structure of **4**.

AI.1 ^1H NMR spectra of $[\text{Fe}(\text{bapbpy})(\text{NCS})_2]$ (**1**) and $\text{Zn}(\text{bapbpy})(\text{NCS})_2$ (**3**)

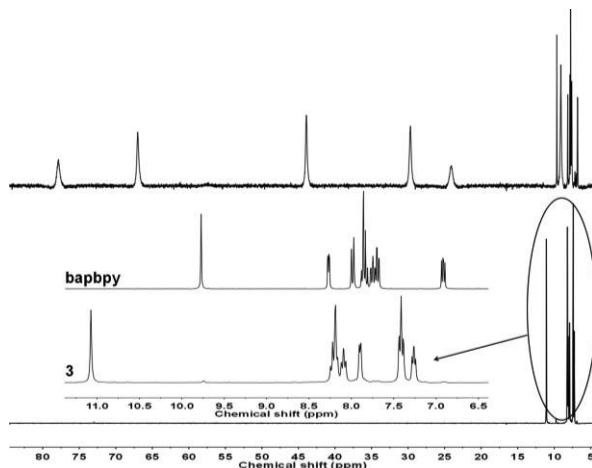


Figure AI.1. ^1H NMR of compound **1** (top) and **3** (bottom) in the 5 to 85 ppm region ($\text{DMSO}-d^6$). The insert diagram shows the ^1H NMR spectra of compound **3** compared to that of ligand bapbpy in the 6.4 to 11.4 ppm region.

AI.2 Calculated and observed $\chi_M T$ values at 300 K for the diluted samples $[\text{Fe}_x\text{Zn}_{1-x}(\text{bapbpy})(\text{NCS})_2]$

Table AI.1. Calculated and observed $\chi_M T$ values at 300 K for the diluted samples $[\text{Fe}_x\text{Zn}_{1-x}(\text{bapbpy})(\text{NCS})_2]$. The calculated values assume a magnetic susceptibility value of 3.5 for Fe ($\chi_{\text{Fe}T}$) and 0 for Zn ($\chi_{\text{Zn}T}$) at 300 K.

x	$\chi_M T$ (calc)	$\chi_M T$ at T = 300 K (obs)	$\chi_M T$ at T = 3 K (obs)
0.98	3.43	3.44	0.22
0.89	3.12	3.04	0.26
0.81	2.84	2.79	0.23
0.76	2.66	2.41	0.19
0.65	2.28	2.21	0.19
0.60	2.10	1.80	0.15
0.53	1.86	1.63	0.12
0.44	1.54	1.31	0.08
0.38	1.33	0.79	0.06
0.24	0.84	0.40	0.04

AI.3 $d\chi_M T/dT$ vs. T plots for compound 1 and for the diluted samples (a) to (i)

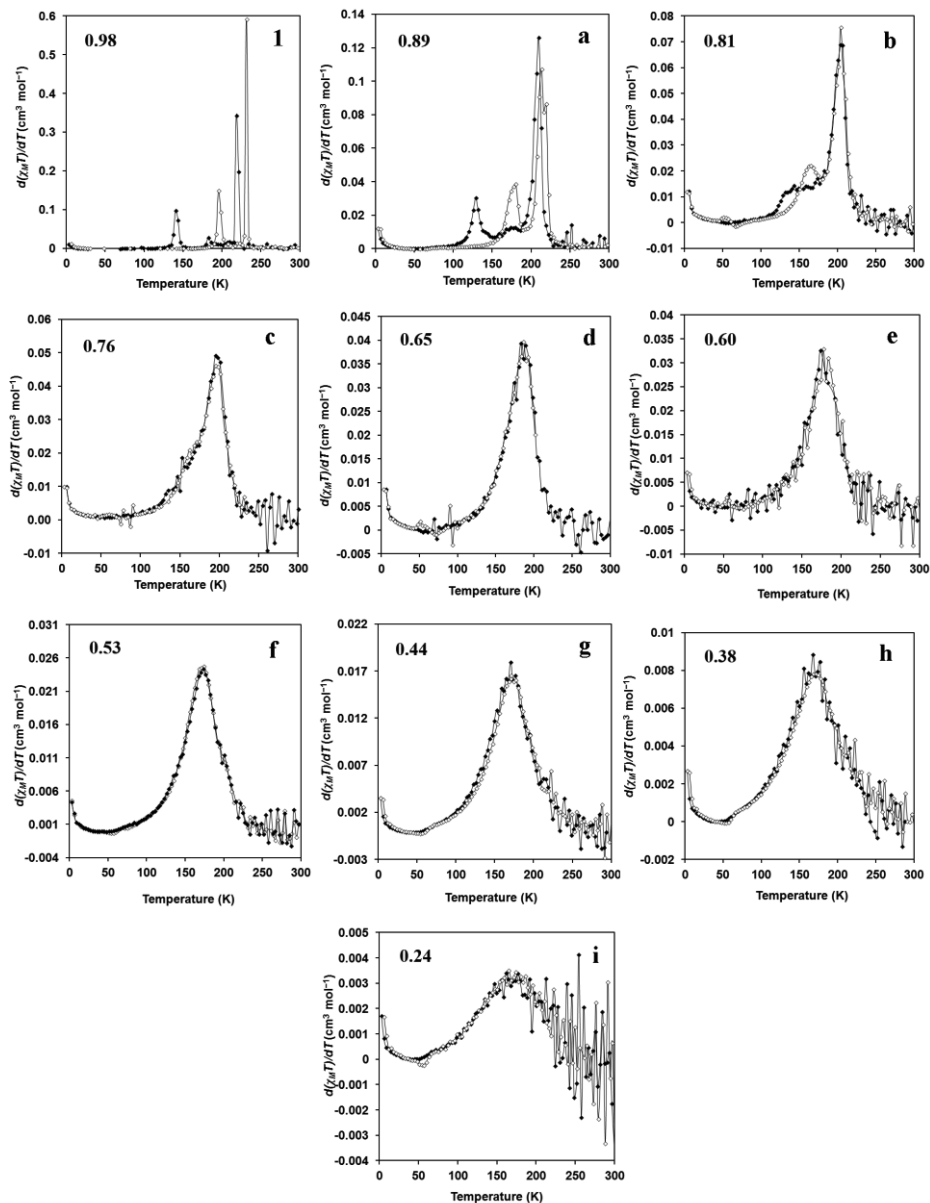


Figure AI.2. $d\chi_M T/dT$ vs. T plots for compound 1 (top left) and for the diluted samples (a) to (i), respectively, in the cooling (\blacklozenge) and heating (\diamond) modes.

AI.4 MOLDEN-generated superposition of the crystal structures for compound **1** and that of a mixture of bapbpy, $[\text{Fe}(\text{NCS})_2]$ and $[\text{Zn}(\text{NCS})_2]$ (10:9:1).



Figure AI.3. Comparison of single crystal structures of Fe only compound **1** (dark)¹ and that of a single crystal grown from a 10:9:1 mixture of bapbpy, $\text{Fe}(\text{NCS})_2$ and $\text{Zn}(\text{NCS})_2$ in DMF/MeOH (grey). No diluted mix crystals were obtained, the two structures are identical.

AI.5 X-ray powder diffractograms of a crude powder sample of **3** and the calculated powder pattern derived from the crystal structure of **4**.

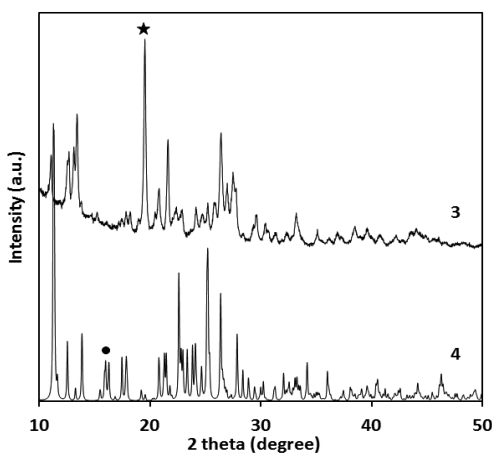


Figure AI.4. Comparison of the X-ray powder diffractogram at room temperature of a crude powder sample of **3** (top) to the calculated powder pattern derived from the crystal structure of **4** at 110 K.

AI.6 References

1. S. Bonnet, M. A. Siegler, J. S. Costa, G. Molnar, A. Bousseksou, A. L. Spek, P. Gamez and J. Reedijk, *Chem. Commun.*, 2008, 5619-5621.

Appendix II

Supplementary information on Chapter 4

- Hydrogen bonding interactions along the crystallographic c axis in compound **11c**'
- $\chi_M T$ vs. T for compounds **10a**, **12a**, and **14a**, in both heating and cooling modes
- Powder X-ray diffractograms for compounds **11**, **13** and **15**.
- A MOLDEN-generated superposition of the crystal structures of compounds **11**, **13** and **16**, with their corresponding thiocyanate analogues.

AII.1 Hydrogen bonding interactions in compound 11c'

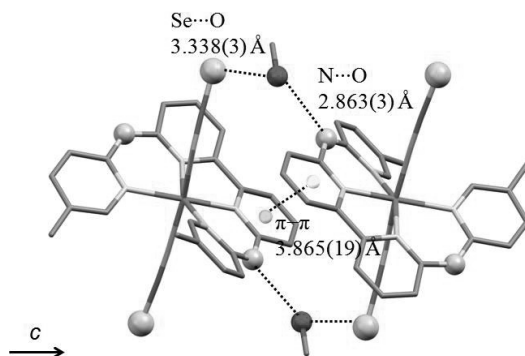


Figure AII.1. Hydrogen bonding interactions in compound 11c' along the crystallographic *c* axis at 110(2) K (HS).

AII.2 $\chi_M T$ vs. T plots for compounds 10a, 12a, and 14a

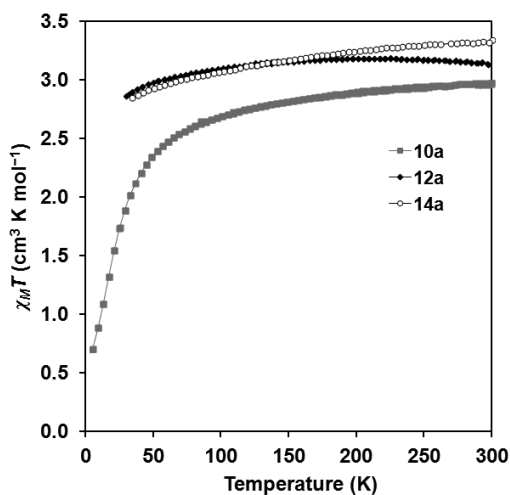


Figure AII.2. Plot of $\chi_M T$ vs. T for compounds 10a, 12a, and 14a, in both heating and cooling modes with a rate of ± 0.3 – 1.1 K min^{-1} .

AII.3 Powder X-ray diffractograms for compounds 11, 13 and 15

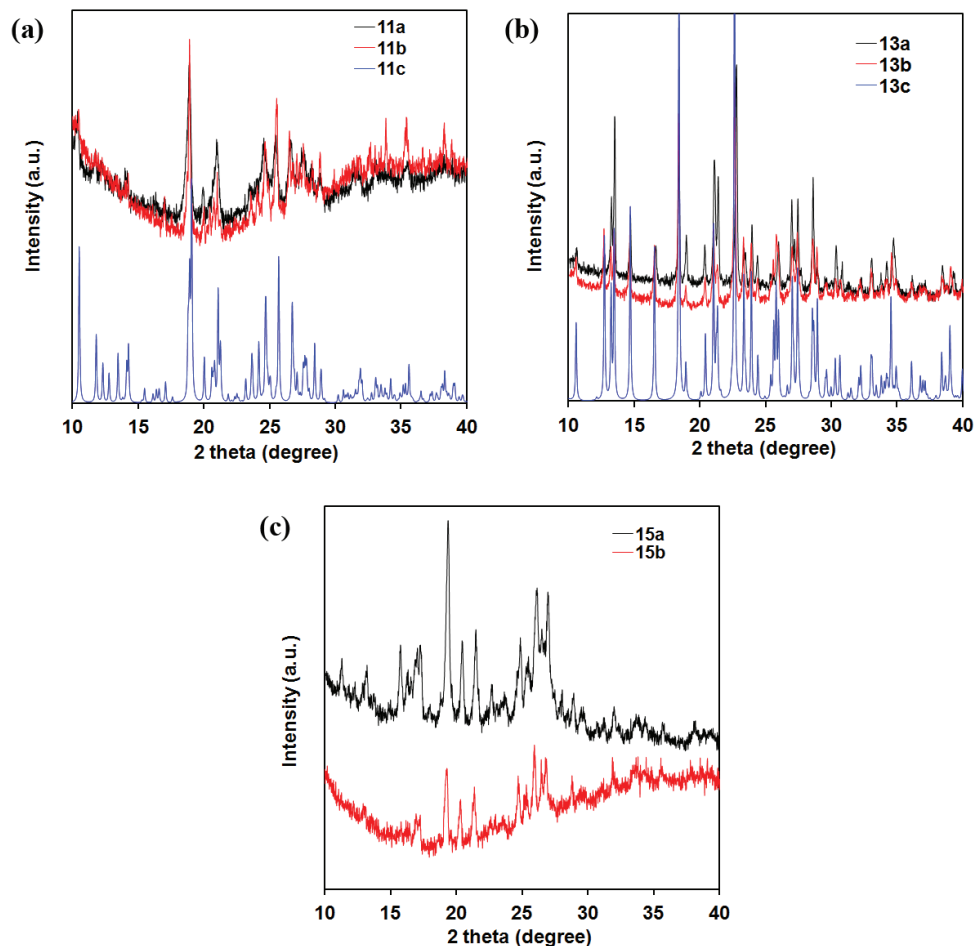


Figure AII.3. Powder X-ray diffractograms for compounds (a) **11a** and **11b** at room temperature, and the bottom curve (blue) shows the theoretical diffractogram calculated for **11c** from its single crystal X-ray structure at 200 K; (b) **13a** and **13b** at room temperature, and the bottom curve (blue) shows the theoretical diffractogram calculated for **13c** from its single crystal X-ray structure at 300 K; and (c) **15a** and **15b** at room temperature.

AII.4 A MOLDEN-generated superposition of the crystal structures of compounds 11, 13 and 16 with their NCS⁻ analogues

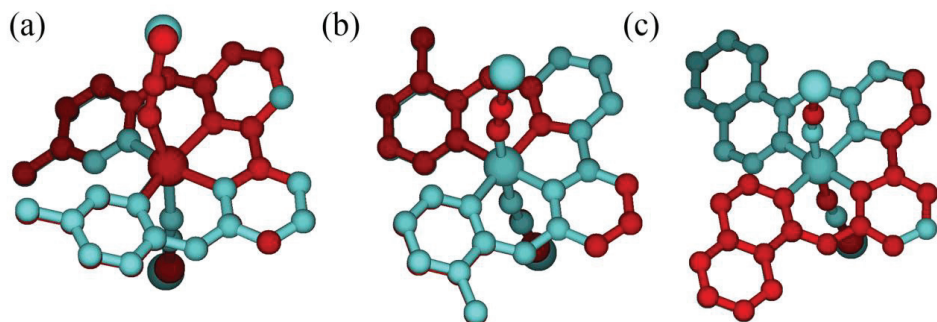


Figure AII.4. A MOLDEN-generated superposition of the crystal structures of compounds (a) [Fe(3)(NCSe)₂] (**11c**) (blue) and [Fe(3)(NCS)₂] (red) in the HS state (b) [Fe(5)(NCSe)₂] (**13c**) (blue) and [Fe(5)(NCS)₂]¹ (red) in the LS state, and (c) [Fe(8)(NCSe)₂] (**16c**) (blue) and [Fe(8)(NCS)₂]¹ (red) in the LS state.

AII.5 References

1. Z. Arcis-Castillo, S. Zheng, M. A. Siegler, O. Roubeau, S. Bedoui and S. Bonnet, *Chem. Eur. J.*, 2011, 17, 14826-14836.

Appendix III

Supplementary information on Chapter 5

- Elemental analysis results for compounds **1** and **2**
- Experimental (**1c**) and calculated (**1d**) powder X-ray diffractograms for compound [Fe(bapphen)(NCS)₂]
- $d\chi_M T/dT$ vs. T plots for compounds **1a**, **1b**, **2a** and **2b**.
- MOLDEN-generated superposition of the crystal structures for compounds [Fe(bapphen)(NCS)₂] (**1c**) and [Fe(bapbpy)(NCS)₂].

AIII.1 Elemental analysis results for compounds 1 and 2.

Table AIII.1. Elemental analysis results for compounds 1 and 2, compared with calculated values.

Compound	Calculated (%)			Found (%)			
	n = 0	n = 1	n = 2	method b	method c	method d	
[Fe(bapphen)(NCS) ₂] \cdot nDMF	C	53.74	53.21	52.79	52.57	52.87	53.36
	H	3.01	3.80	4.43	1.97	3.59	2.74
	N	20.89	20.68	20.52	20.49	20.01	20.11
	S	11.95	10.52	9.93	11.05	10.24	11.15
[Fe(bapphen)(NCSe) ₂] \cdot nDMF	C	45.74	46.11	46.41	45.15	45.73	–
	H	2.56	3.30	3.89	1.76	2.63	–
	N	17.78	17.92	18.04	17.45	17.64	–

AIII.2 Powder X-ray diffractograms for compounds 1c and 1d.

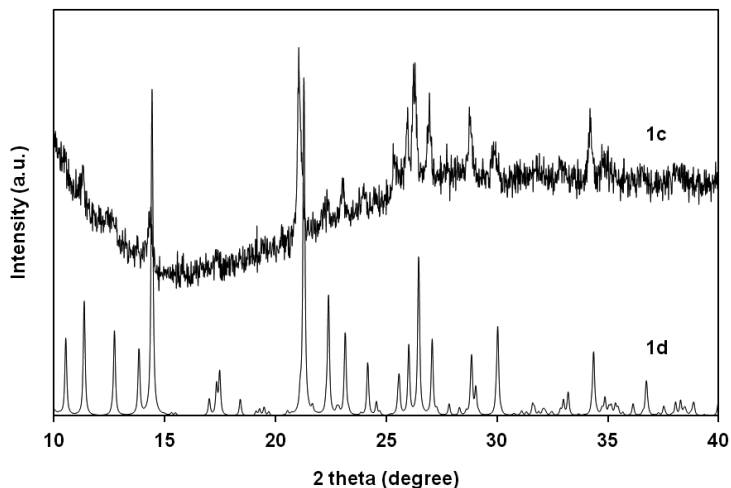


Figure AIII.1. X-ray powder diffractograms for compound 1. Experimental spectrum of sample 1c (top) at 300 K, and the calculated diffractogram (bottom) from the single crystal X-ray structure of 1d at 240 K using the program Mercury.¹

AIII.3 $d\chi_M T/dT$ vs. T plots for compounds 1a, 1b, 2a and 2b.

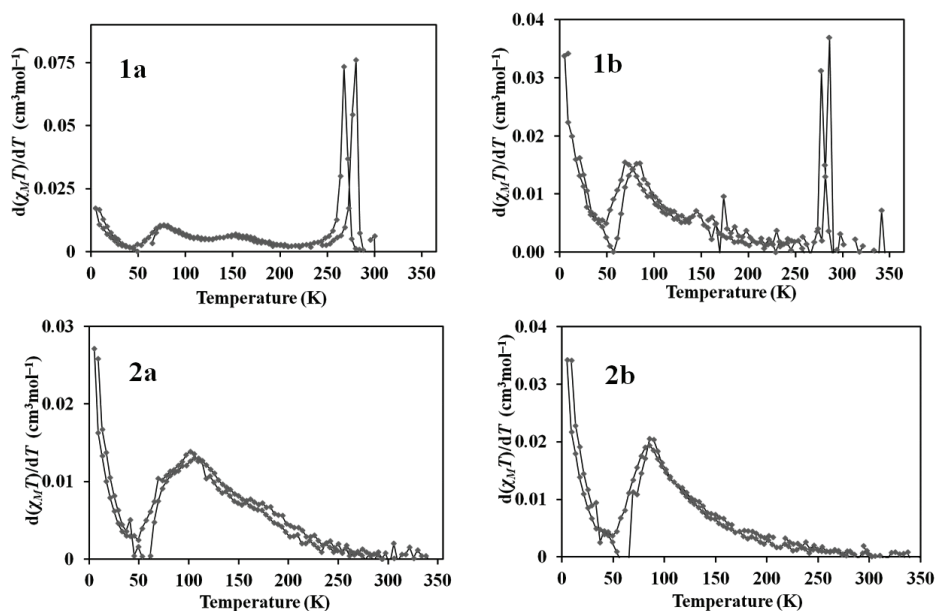


Figure AIII.2. $d\chi_M T/dT$ vs. T plots for compounds 1a, 1b, 2a, and 2b.

AIII.4 MOLDEN-generated superposition of the crystal structures for compounds 1c and $[\text{Fe}(\text{bapbpy})(\text{NCS})_2]$.

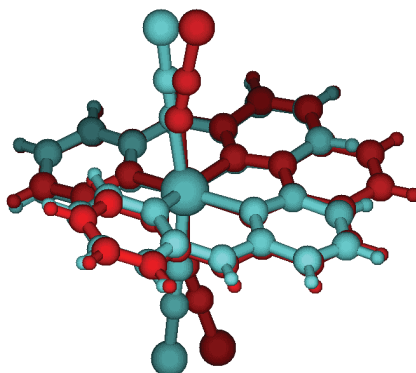


Figure AIII.3. A MOLDEN-generated superposition of the geometries of compounds $[\text{Fe}(\text{bapphen})(\text{NCS})_2]$ (1c) (dark) and $[\text{Fe}(\text{bapbpy})(\text{NCS})_2]^2$ (light grey) in the HS phase (according to crystal structures).

AIII.5 References

1. C. F. Macrae, I. J. Bruno, J. A. Chisholm, P. R. Edgington, P. McCabe, E. Pidcock, L. Rodriguez-Monge, R. Taylor, J. van de Streek and P. A. Wood, *J. Appl. Crystallogr.*, 2008, 41, 466-470.
2. S. Bonnet, M. A. Siegler, J. S. Costa, G. Molnar, A. Bousseksou, A. L. Spek, P. Gamez and J. Reedijk, *Chem. Commun.*, 2008, 5619-5621.

Appendix IV

Supplementary information on Chapter 6

- Experimental and calculated powder X-ray diffractograms for compound [Fe(bbpya)(NCS)₂] (**1**)
- Infrared spectrum of compound **1**, powder vs. single crystals
- Details of single crystal X-ray structure determination for **1**
- Details for magnetic susceptibility measurements and Differential Scanning Calorimetry (DSC)
- Details of modelization with Sorai's domain model and the Slichter-Drickamer model

AIV.1 Powder X-ray diffractograms for compound 1

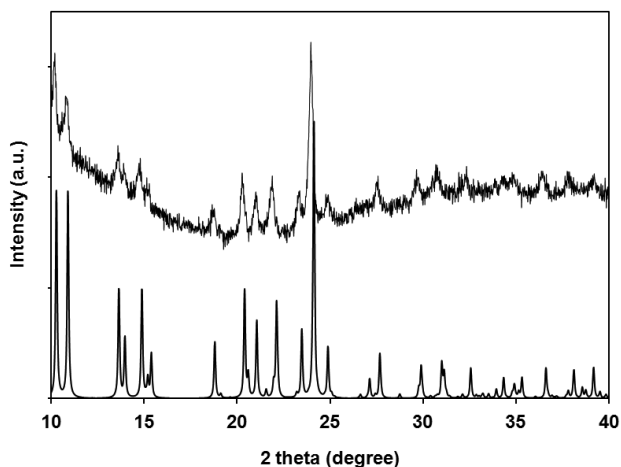


Figure AIV.1. Powder X-ray diffractograms for complex **1**. Experimental spectrum of a powder sample (top) at 300 K, and the diffractogram (bottom) calculated from the single crystal X-ray structure of **1** at 110 K.

AIV.2 Infrared spectra of compound 1, powder vs. single crystals

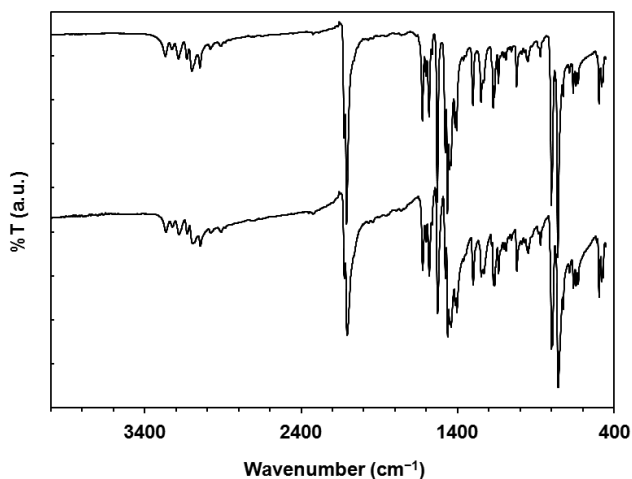


Figure AIV.2. Infrared spectra of compound **1** as the crude powder obtained at the end of the synthesis (top), and as crushed single crystals (bottom).

AIV.3 Details of single crystal X-ray structure determination for 1

All reflection intensities were measured at 110(2) K using a SuperNova diffractometer (equipped with Atlas detector) with Cu $K\alpha$ radiation ($\lambda = 1.54178 \text{ \AA}$) under the program CrysAlisPro (Version 1.171.36.28 Agilent Technologies, 2013). The program CrysAlisPro was used to refine the cell dimensions. Data reduction was done using the program CrysAlisPro. The structure was solved with the program SHELXS-2013¹ and was refined on F^2 with SHELXL-2013.¹ Analytical numeric absorption corrections based on a multifaceted crystal model were applied using CrysAlisPro. The temperature of the data collection was controlled using the system Cryojet (manufactured by Oxford Instruments). The H atoms were placed at calculated positions using the instructions AFIX 43 with isotropic displacement parameters having values 1.2 times U_{eq} of the attached C or N atoms.

AIV.4 Details for magnetic susceptibility measurements and Differential Scanning Calorimetry (DSC)

Magnetic measurements were performed on a powder sample **1** using the VSM-oven option of a Quantum Design PPMS set-up. The powder was pressed into 3 mm diameter pellets of 3.1 and 2.8 mg for the two sets of measurements performed to verify the reproducibility. The DC magnetization was determined in an applied field of 5 T, and the scan rate was 10 K/min, the smallest allowed by the set-up. Several warming-cooling scans were performed, showing only little variation between the first and second scan. The data reported here correspond to the third stable and reproducible cycle of measurement. Corrections for the diamagnetism of the sample were calculated using Pascal's constant.²

DSC measurements were performed with a Q1000 calorimeter from TA Instruments equipped with the LNCS accessory. The temperature and enthalpy scales were calibrated with a standard sample of indium, using its melting transition (156.6 °C, 3296 J mol⁻¹). The measurements were carried out using aluminium pans with a mechanical crimp, with an empty pan as reference. The zero-heat flow procedure described by TA Instruments was followed to derive heat capacities, using a synthetic sapphire as reference compound. An overall accuracy of ca. 0.2 K for the temperature and up to 5 to 10% for the heat capacity was estimated over the whole temperature range, by comparison with the synthetic sapphire. A lattice heat capacity was estimated

from data below and above the anomaly associated with the SCO process (dashed line in Figure 6.2b). Excess enthalpy and entropy were derived by integration of the excess heat capacity with respect to T and $\ln T$, respectively.

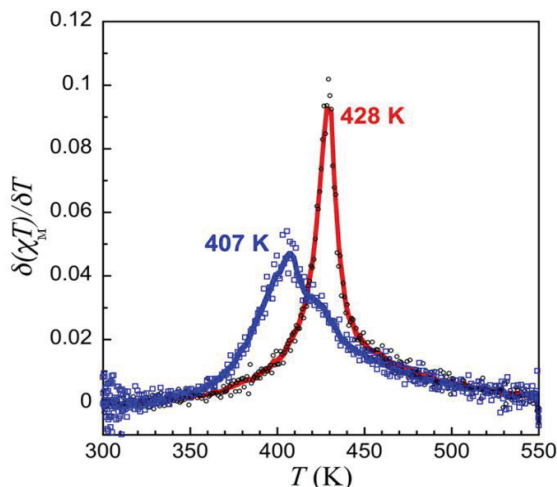


Figure AIV.3. Derivative of $\chi_M T$ versus T plot for complex **1**, in both heating (red) and cooling (blue) modes. The full lines are a weighted smoothing of the data.

AIV.5 Details of modelization with the domain model and the Slichter-Drickamer model

The phenomenological domain model developed by Sorai^{3,4} was applied here, as it is widely used to analyse the SCO behaviour in cases where calorimetric data are available. It is based on heterophase fluctuations and gives a measure of cooperativity through the number of like-spin molecules (or here the SCO centres) n per interacting domain, the larger the domain the more cooperative the transition. According to this model, the heat capacity variation can be written as:

$$\Delta C_p = \frac{n(\Delta_{SCO}H)^2}{RT^2} \frac{\exp\left[\frac{n\Delta_{SCO}H}{R}\left(\frac{1}{T} - \frac{1}{T_{1/2}}\right)\right]}{\left\{1 + \exp\left[\frac{n\Delta_{SCO}H}{R}\left(\frac{1}{T} - \frac{1}{T_{1/2}}\right)\right]\right\}^2} \quad \text{Eq. AIV.1}$$

The experimental heat capacity data were thus fitted to Eq. AIV.1 using $\Delta_{SCO}H$ as derived from integration of ΔC_p vs. T , giving $n = 10.2 / 6.5$ and $T_{1/2} = 434 / 415$ K upon

warming and cooling, respectively. For $n = 1$ the model is equivalent to a pure solution behaviour (van't Hoff equation) with no cooperative effects.

A simple phenomenological expression (see Eq. AIV.2) derived from the free energy of a regular solid solution of HS and LS molecules with an interaction term according to the mean-field theory, first used by Slichter and Drickamer,⁵ reproduces well the different forms of SCO curves (γ_{HS} vs. T , where γ_{HS} is the fraction of HS species) and also the hysteresis effect for sufficiently large values of the interaction parameter Γ . With the goal of attaining a mean-field estimation of cooperativity in the materials under study, the experimental HS fraction calculated from magnetic measurements² were fitted to Eq. AIV.2, fixing the thermodynamic figures to the ones determined by DSC calorimetry.

$$\ln\left(\frac{1-\gamma_{\text{HS}}}{\gamma_{\text{HS}}}\right) = \frac{\Delta_{\text{SCO}}H + \Gamma(1-2\gamma_{\text{HS}})}{RT} - \frac{\Delta_{\text{SCO}}S}{R} \quad \text{Eq. AIV.2}$$

Because Eq. AIV.2 can only account for the amplitude of a hysteresis loop and not for its shape, it was considered that the vertical tangents of the calculated S-curve must correspond to $T_{1/2}\uparrow$ and $T_{1/2}\downarrow$.

The HS fraction γ_{HS} was deduced from the magnetic data using the relation $\gamma_{\text{HS}}(T) = (\chi_{\text{M}}T - \chi_{\text{M}}T_{\text{LS}}) / (\chi_{\text{M}}T_{\text{HS}} - \chi_{\text{M}}T_{\text{LS}})$, where $\chi_{\text{M}}T_{\text{LS}}$ and $\chi_{\text{M}}T_{\text{HS}}$ stand respectively for the values of $\chi_{\text{M}}T$ in the LS and HS states. Values of 0.01 and 3.25 cm³ mol⁻¹ K were considered respectively.

The HS fraction γ_{HS} was deduced from the calorimetric data using the relation $\gamma_{\text{HS}}(T) = \Delta H / \Delta_{\text{SCO}}H$ where $\Delta_{\text{SCO}}H$ is the value derived by integration of the excess heat capacity vs. T , multiplied by 1.05 to take into account the likely underestimation associated with few data above the heat capacity anomaly.

AIV.6 References

1. G. M. Sheldrick and T. R. Schneider, in *Methods Enzymol.*, Academic Press, 1997, vol. 277, pp. 319-343.
2. G. A. Bain and J. F. Berry, *J. Chem. Educ.*, 2008, 85, 532.
3. M. Sorai and S. Seki, *J. Phys. Chem. Solids*, 1974, 35, 555-570.
4. M. Sorai, *Top. Curr. Chem.*, 2004, 235, 153-170.
5. C. P. Slichter and H. Drickame, *J. Chem. Phys.*, 1972, 56, 2142-2161.

Appendix V

Supplementary information on Chapter 7

- ^1H NMR spectra of compound **8** at different temperatures
- IR spectra of ligand **1** and complex **2** synthesized under different conditions
- $d\chi_M T/dT$ vs. T plots for compound **2**
- STM images of freshly cleaved HOPG, and of **2** on HOPG (500 nm \times 500 nm)
- Portion of the IR spectra assigned to the stretching frequency of the N–H bond in the known SCO compounds based on ligand babppy and its derivatives, in comparison with **2**

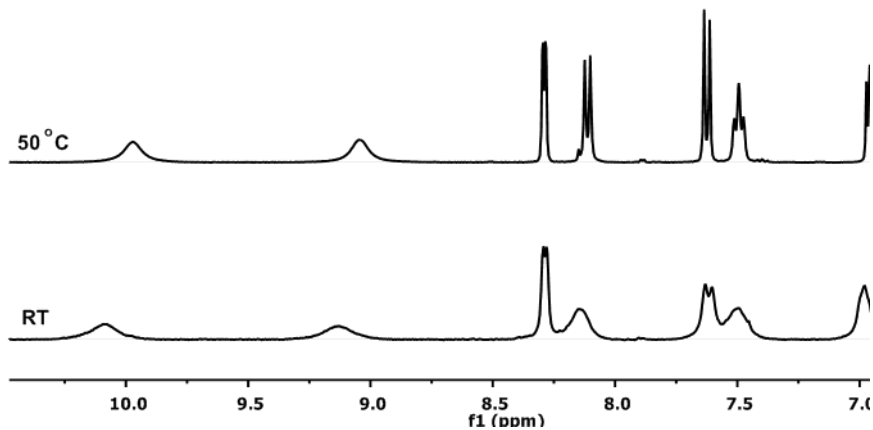
AV.1 ^1H NMR spectra of compound **8 at different temperatures**

Figure AV.1. ^1H NMR spectra of compound **8**, measured at room temperature (lower spectrum) and at 50 °C (upper spectrum) in $\text{DMSO-}d_6$.

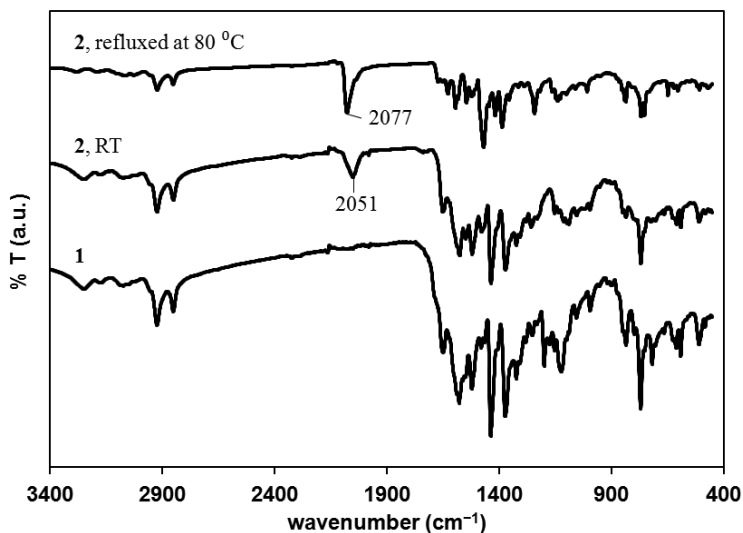
AV.2 IR spectra of ligand **1 and complex **2** synthesized under different conditions**

Figure AV.2. IR spectra of ligand **1** and complex **2** synthesized under different conditions.

AV.3 $d\chi_M T/dT$ vs. T plots for compound 2

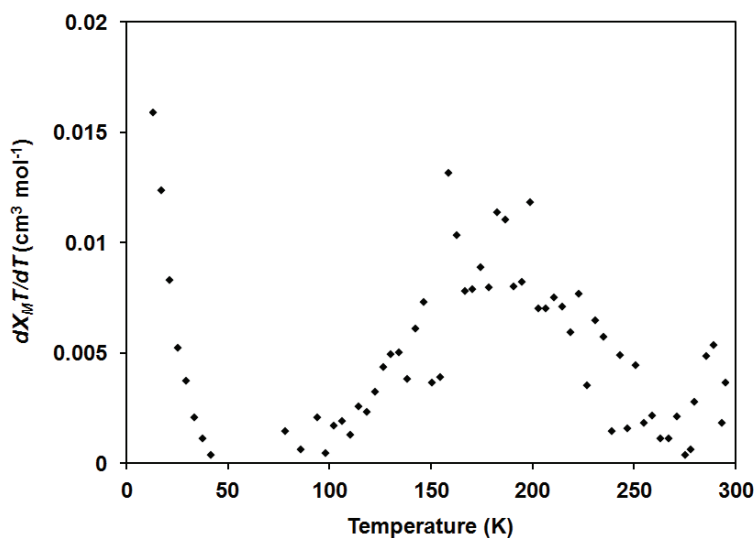


Figure AV.3. $d\chi_M T/dT$ vs. T curve for compound 2.

AV.4 STM images of freshly cleaved HOPG, and of 2 on HOPG

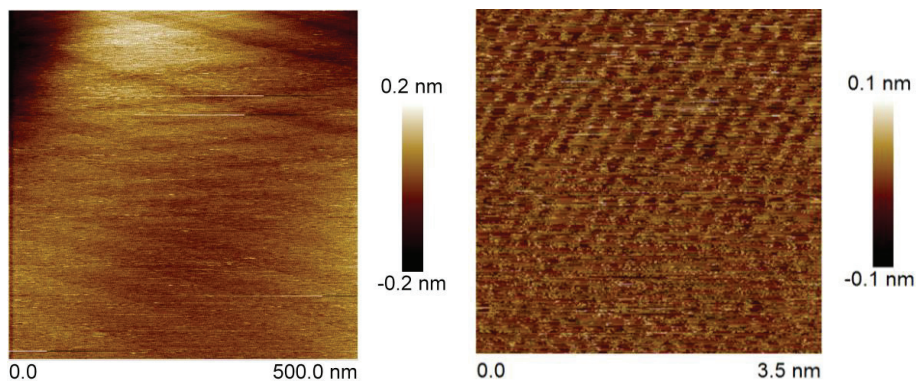


Figure AV.4. STM images of freshly cleaved HOPG, 500 nm \times 500 nm (left), and an atomic resolution image with hexagonal carbon rings are clearly visible (right). Images were taken under the following condition: $V_{\text{bias}} = +500$ mV, $I_{\text{set}} = 1$ nA, atomic resolution image was obtained with scan rate = 15.3 Hz.

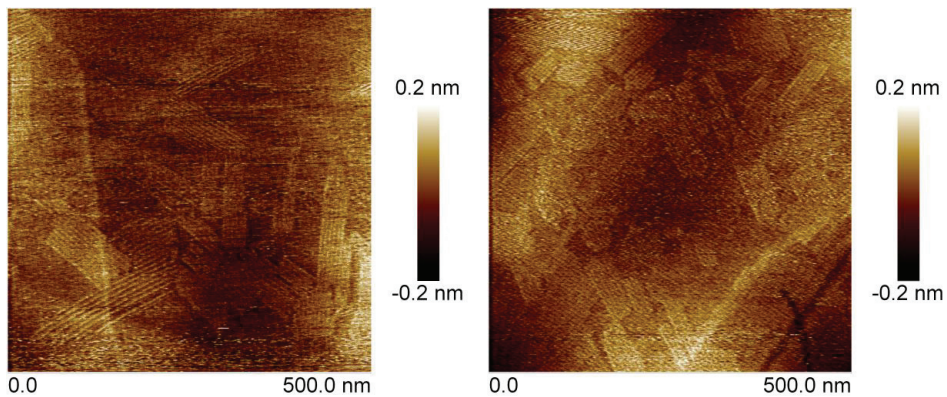


Figure AV.5. STM images of **2** on HOPG at different locations, 500 nm \times 500 nm in scan size. Images were taken under the following condition: $V_{\text{bias}} = +500$ mV, $I_{\text{set}} = 1$ nA.

AV.5 Portion of the IR spectra assigned to the stretching frequency of the N–H bond for **2** and other SCO compounds

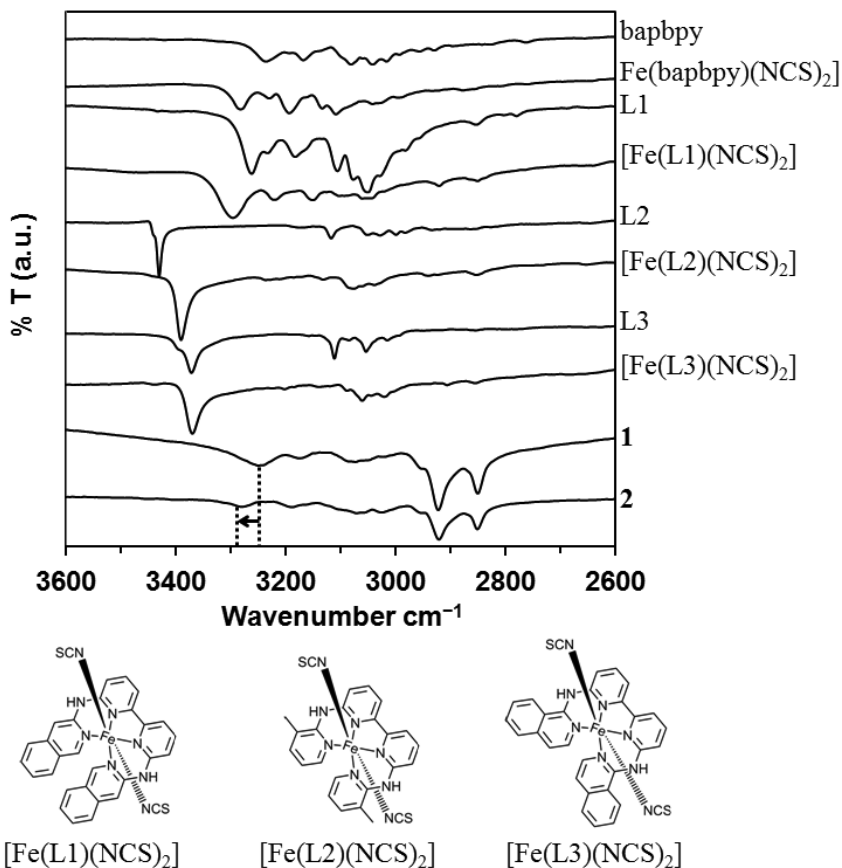


Figure AV.6. Portion of the IR spectra assigned to the stretching frequency of the N–H bond for compounds [Fe(bapbpy)(NCS)₂],¹ [Fe(L1)(NCS)₂], [Fe(L2)(NCS)₂], and [Fe(L3)(NCS)₂]² in comparison with **2**, the corresponding ligands are also shown. [Fe(bapbpy)(NCS)₂] and [Fe(L1)(NCS)₂] show cooperative SCO, while [Fe(L2)(NCS)₂] and [Fe(L3)(NCS)₂] show gradual SCO. A shift of the NH absorption band towards higher stretching frequency in **2** is visible (indicated with an arrow).

The intermolecular N⋯S distances for the above mentioned compounds were calculated based on an early recognized correlation between the N⋯S distance and the change in stretching frequency of the N–H bond reported by Bellamy and Owen (Eq. AV.1).³

$$\Delta\nu(\text{cm}^{-1}) = 50 \left[\left(\frac{d}{R} \right)^{12} - \left(\frac{d}{R} \right)^6 \right] \quad \text{Eq. AV.1}$$

Where $\Delta\nu$ is the change in stretching frequency of the N–H bond, the values of d approximately to the sum of the collision radii of the N and S atoms, and R is defined as the N \cdots S distance.

Table AV.1. Calculated N \cdots S distances based on correlation between the N \cdots S distance and the change in stretching frequency ($\Delta\nu$) of the N–H bond reported by Bellamy and Owen.³ The observed N \cdots S distances from crystal structures are also given.

Compound	d (Å)	$\Delta\nu$ (cm ⁻¹)	N \cdots S (Å, calc)	N \cdots S (Å, obs)
[Fe(bapbpy)(NCS) ₂]		45	4.187	3.424
[Fe(L2)(NCS) ₂]	4.515 ^a	52	4.160	4.160
[Fe(L3)(NCS) ₂]		2	4.486	3.932
2		35	4.235	–
[Fe(bapbpy)(NCS) ₂]		45	3.237	3.424
[Fe(L2)(NCS) ₂]	3.49 ^b	52	3.215	4.160
[Fe(L3)(NCS) ₂]		2	3.468	3.932
2		35	3.274	–
[Fe(bapbpy)(NCS) ₂]		45	3.670	3.424
[Fe(L2)(NCS) ₂]		52	3.645	4.160
[Fe(L3)(NCS) ₂]	3.957 ^c	2	3.932	3.932
2		35	3.709	–

^{a,c} Calculated from the observed N \cdots S distances in compound [Fe(L2)(NCS)₂] and [Fe(L3)(NCS)₂] respectively using Eq.AV.1. ^b obtained from reference 4, page 1200.

AV.6 References

1. S. Bonnet, M. A. Siegler, J. S. Costa, G. Molnar, A. Bousseksou, A. L. Spek, P. Gamez and J. Reedijk, *Chem. Commun.*, 2008, 5619-5621.
2. Z. Arcis-Castillo, S. Zheng, M. A. Siegler, O. Roubeau, S. Bedoui and S. Bonnet, *Chem. Eur. J.*, 2011, 17, 14826-14836.
3. L. J. Bellamy and A. J. Owen, *Spectrochim. Acta, Part A*, 1969, A 25, 329-333.
4. J. O. Hirschfelder, C. F. Curtiss and R. B. Bird, *Molecular theory of gases and liquids*, Wiley, 1964.

Samenvatting (Summary in Dutch)

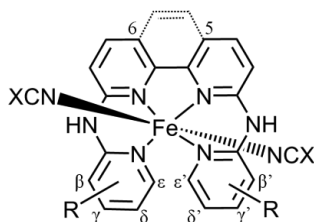
Hoofdstuk 1 geeft een algemene inleiding en formuleert de doelstellingen van het onderzoek beschreven in de latere hoofdstukken.

Ligandmodificaties en nieuwe spinovergangsmaterialen (Hfdst 2, 4, 5 en 6)

Coöperatieve ijzer(II)-spinovergangsverbindingen (SCO-verbindingen), die een thermische hysteresecyclus hebben, vertonen bistabiliteit op het gebied van magnetisme en kleur. Dit is interessant voor een aantal toepassingen zoals informatieopslag en optische displays.¹ Mononucleaire ijzer(II)-complexen hebben een aanzienlijke potentie op dit gebied en vanwege hun eigenschappen kunnen ze minder last hebben van effecten van schaalverkleining in vergelijking met SCO-polymeren, omdat de coördinatieomgeving voor elk ijzerion in het hele materiaal goed gedefinieerd blijft. Echter, het ideale mononucleaire SCO-complex is nog niet gevonden, omdat voor een hoge overgangstemperatuur en hoge coöperativiteit zowel sterkveld-liganden voor ijzer(II)-complexen *als* sterke intermoleculaire interacties vereist zijn. Een van de doelen van het onderzoek dat is beschreven in dit proefschrift was het ontwerpen en synthetiseren van nieuwe mononucleaire ijzer(II)-verbindingen gebaseerd op het ligand bapbpy, d.w.z. derivaten van de sterk coöperatieve SCO-verbinding $[\text{Fe}(\text{bapbpy})(\text{NCS})_2]$ (**1**),² maar dan met hogere overgangstemperaturen. Vier hoofdstukken van dit proefschrift zijn gericht op het onderzoek naar het verhogen van de overgangstemperatuur van **1** met behoud van een hysteresecyclus (Hoofdstukken 2, 4, 5 en 6, en Tabel 8.1).

Het ligand bapbpy is een rigide N_4 -donor en vrijwel vlak-omarmend ligand dat twee *trans* posities in een octaëderomgeving vrijlaat voor de coördinatie van axiale liganden.² Door toevoeging van elektrondonerende methylgroepen op de vier verschillende posities van de pyridinering werd slechts één verbinding $[\text{Fe}(\text{Me}_2\text{bapbpy})(\text{NCS})_2]$ met SCO-eigenschappen verkregen (Hoofdstuk 2, **2**, zie Tabel 8.1). Echter, de overgangstemperatuur van deze verbinding is laag (170 K) en vertoont ook geen hysteresecyclus. Door gebruik van meer geconjugeerde quinoline- of isoquinoline-substituenten in plaats van de pyridineringen werden twee nieuwe SCO-verbindingen verkregen. Een van deze complexen heeft vrijwel dezelfde coöperativiteit als verbinding **1** (met een hysteresecyclus), maar heeft een lage overgangstemperatuur (**3**, Tabel 8.1); de andere verbinding heeft een veelbelovende overgangstemperatuur in de buurt van kamertemperatuur (288 K, **4** in Tabel 8.1), maar heeft geen hysteresecyclus. De röntgenkristallografie-gegevens van de SCO-verbindingen **2** en **4**

laten een soortgelijke kristalpakking zien, met N–H···S waterstofbrugnetwerken. Deze intermoleculaire N–H···S-interacties zijn zwakker dan die in verbinding **1**, wat veroorzaakt wordt door de substituenten op de β, β' -posities van de pyridinering (Figuur 8.1). Voor op babppy gebaseerde SCO-verbindingen correleert de sterkte van deze N–H···S-waterstofbruggen goed met de coöperativiteit van de spinovergang, en het lijkt belangrijk te zijn om de β -posities vrij te houden om de coöperativiteit te behouden. Opvallend is dat verschillende isomeren van dezelfde mononucleaire ijzer(II)-verbinding zeer verschillende SCO-eigenschappen hebben. Kortom, door het aanpassen van de chemische structuur van het babppy-ligand is de overgangstemperatuur van een van de SCO-verbindingen verhoogd tot bijna kamertemperatuur, maar dit is wel ten koste gegaan van de coöperativiteit.



Figuur 8.1. Schematische tekening van de ijzer(II)-SCO-verbindingen bestudeerd in dit proefschrift, gebaseerd op het ligand babppy; X=S of Se.

Omdat kleine chemische veranderingen op het babppy-ligand tot significante veranderingen in de SCO-eigenschappen van de ijzer(II)-verbindingen leiden, is een andere aanpak geprobeerd, bestaande uit het vervangen van de axiale NCS^- anionen met de meer elektronendonerende NCSe^- liganden (Hoofdstuk 4). Vijf nieuwe ijzer(II)-SCO-verbindingen **5-9** (Tabel 8.1) zijn verkregen met R_2babppy -derivaten beschreven in Hoofdstuk 2. Twee verbindingen bleken coöperatieve SCO-materialen te zijn (**6** en **8**), terwijl de anderen een niet-coöperatief SCO-gedrag vertonen. Hoewel de overgangstemperaturen van **6** en **8** veel lager zijn dan kamertemperatuur, is er een trend voor deze verbindingen zichtbaar: hun overgangstemperatuur is hoger in vergelijking met de NCS^- -analogen. Bijzonder is dat verbinding **6** wel SCO vertoont, terwijl de thiocyaanaanalog dit niet doet. In overeenstemming hiermee is voor de niet-coöperatieve SCO-verbindingen **7** en **9** dezelfde trend waargenomen, waarbij de overgangstemperatuur van **9** (357 K) de hoogste gerapporteerde van alle babppy-gebaseerde verbindingen tot nu toe is. In een vergelijking van de röntgenstructuren van verbindingen **7** en **9** met die van **2** en **4** is een opvallende structurele overeenkomst gevonden tussen de thiocyaanaat- en de selenocyaanaatverbindingen, wat erop wijst dat het verhogen van de overgangstemperatuur een puur elektronische oorsprong heeft. Verbinding **5** wordt beschouwd als een uitzondering, aangezien de veel lagere

coöperativiteit vergeleken met verbinding **1**, het resultaat lijkt te zijn van een structurele verandering in de ijzer(II)-verbindingen wanneer NCS^- wordt vervangen door NCSe^- als axiaal ligand.

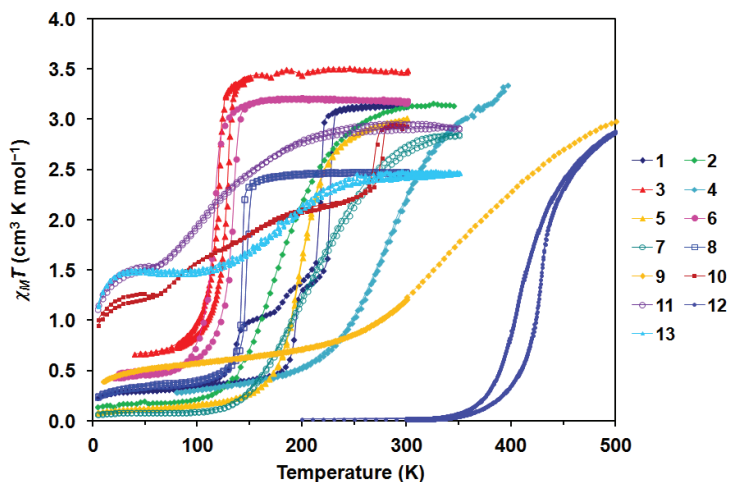
Door het gebruik van een fenantroline-basis in plaats van een bipyridine-basis, is niet alleen de starheid van het ligand verhoogd, maar ook de ligandveldsterkte, omdat fenantroline een sterkere ligandveldsplitsing geeft dan bipyridine in de spectrochemische reeks (Hoofdstuk 5). Twee nieuwe ijzer(II)-SCO-verbindingen zijn verkregen met nieuwe bapphen liganden (**10** en **11**, Tabel 8.1). Interessant is dat er verschillende vormen bestaan voor verbinding **10**, die worden verkregen door verschillende bereidingswijzen. De eerste vorm kon niet gekristalliseerd worden, maar heeft een onvolledige SCO-overgang met drie stappen, en met een hysteresecyclus net onder kamertemperatuur (298 K). De tweede vorm heeft geen SCO-eigenschappen, maar kristalliseert gemakkelijker. In verbinding **11**, waarin de NCS^- liganden vervangen zijn voor NCSe^- liganden, is er geen coöperativiteit, hetgeen vergelijkbaar is met de resultaten van de bapbpy-verbindingen (d.w.z. **5** versus **1**).

De meest veelbelovende SCO-verbinding beschreven in dit proefschrift, $[\text{Fe}(\text{bbpya})(\text{NCS})_2]$ (**12**, Tabel 8.1), is ontworpen door een heel andere aanpak waarbij een van de 6-chelaatringen van een bapbpy-gebaseerd metaalcomplex vervangen is door een 5-chelaatring (Hoofdstuk 6). Het nieuwe ligand bbpya is een rigide en een bijna vlak ligand waarin twee bipyridine-moleculen met elkaar verbonden zijn via een enkele NH-brug. Het ijzer(II)-bbpya-complex **12** heeft inderdaad een kleinere vervorming van de octaëdrische coördinatieomgeving vergeleken met **1**. Daardoor is **12** inderdaad laagspin (LS) bij kamertemperatuur in de vaste toestand en heeft het een van de hoogste overgangstemperaturen die er bekend zijn voor mononucleaire SCO-complexen. Het meest interessante is dat het een grote hysteresis-cyclus heeft van 21 K, hoewel elk bbpya ligand maar één NH-groep heeft om een waterstofbrugnetwerk te vormen. De kristalstructuur laat zien dat de coöperativiteit wordt behouden door de wanorde in de structuur, wat resulteert in oneindig lange supramoleculaire kettingen *via* waterstofbruggen en π - π -stackinginteracties. Kortom, de ongewone eigenschappen van **12** laten zien dat de strategie om 6-chelaatringen te vervangen voor 5-chelaatringen succesvol is gebleken.

Tabel 8.1. Samenvatting van de overgangstemperaturen ($T_{1/2}$) en de breedte van de hysteresecyclus (ΔT_{hyst}) van alle nieuwe SCO-verbindingen $[\text{Fe}(\text{L})(\text{NCX})_2]$ die beschreven zijn in dit proefschrift (2-13), en ter vergelijking die van verbinding $[\text{Fe}(\text{bapbpy})(\text{NCS})_2]$ (1).

	Hoofdstuk	Ligand L	NCX	$T_{1/2}$ (K) ^a	ΔT_{hyst} (K)	Speciale waarneming
1	–	bapbpy	NCS	235↓ / 239↑(1 st) 172↓ / 194↑(2 nd)	4 / 22	2-stap SCO, met duidelijke IP
2	2	β,β' -Me ₂ bapbpy	NCS	170(2)	–	
3	2	R ₂ bapbpy ^b	NCS	113(2)↓ / 125(2)↑	11(3)	
4	2	R' ₂ bapbpy ^c	NCS	288(5)	–	
5	4	bapbpy	NCSe	195(4)	–	Geleidelijke overgang
6	4	δ,δ' -Me ₂ bapbpy	NCSe	113(4)↓ / 137(4)↑	24(6)	Vervanging van NCS door NCSe geeft SCO
7	4	β,β' -Me ₂ bapbpy	NCSe	214(20)	–	
8	4	R ₂ bapbpy ^b	NCSe	141(4)↓ / 149(4)↑	8(6)	
9	4	R' ₂ bapbpy ^c	NCSe	357(19)	–	
10	5	bapphen ^d	NCS	268(4)↓ / 280(4)↑ ^e	12(6)	2 vormen, ϵ n heeft een meerstapovergang
11	5	bapphen	NCSe	101(4)	–	Geleidelijke overgang
12	6	bbpya	NCS	407(3)↓ / 428(1)↑	21(3)	LS op KT
13	7	bapphen-C ₁₂	NCS	182(25)	–	Geleidelijke overgang, ordening op HOPG

^a De verkregen $T_{1/2}$ waarden zijn gebaseerd op de magnetische susceptibiliteitsmetingen aan monsters die bereid zijn volgens methode a. ↓ en ↑ geeft $T_{1/2}$ aan bij respectievelijk afkoelen en opwarmen, de meetonzekerheid is tussen haakjes gegeven. ^b R₂bapbpy bevat isoquin-2-oline-substituenten. ^c R'₂bapbpy bevat isoquin-1-oline-substituenten. ^d De gegeven overgangstemperaturen zijn gebaseerd op het SCO-vorm van $[\text{Fe}(\text{bapphen})(\text{NCS})_2]$. ^e Alleen de overgangstemperatuur voor de hysteresis (eerste-stap-overgang) zijn gegeven.



Figuur 8.2. Overzicht van $\chi_M T$ versus T curven voor alle SCO-verbindingen 1-13 die beschreven zijn in dit proefschrift. De nummering verwijst naar Tabel 8.1.

Het begrijpen van de coöperativiteit in $[\text{Fe}(\text{bapbpy})(\text{NCS})_2]$ (Hfdst 3)

De coöperativiteit van de SCO van $[\text{Fe}(\text{bapbpy})(\text{NCS})_2]$ (**1**) is bestudeerd door het ‘verdunnen’ van het ijzercomplex met toenemende hoeveelheden van de analoge magnetisch inerte zink(II)-verbinding (Hoofdstuk 3). Het oorspronkelijke idee was om te onderzoeken in welke mate de twee-staps-SCO en de hysteresecyclus intact blijven wanneer de gemiddelde Fe–Fe-afstand groter wordt. De zinkanalogue van **1** heeft echter een andere structuur dan **1** door de verschillende geometrische voorkeur van het zink(II)-ion. Eénkristallen van gecookristalliseerde $[\text{Fe}_x\text{Zn}_{1-x}(\text{bapbpy})(\text{NCS})_2]$ zijn helaas niet verkregen, het onderzoek naar de magnetische eigenschappen van de verdunde verbindingen is uitgevoerd met poeders. Op basis van röntgendiffractie, magnetische susceptibiliteitmetingen en infraroodspectroscopie van deze poeders bleek dat in de met zink-verdunde monsters die voor het grootste deel ijzerionen bevatten ($x > 0.53$) de structuur van de ijzerverbinding bleef behouden. Bij hogere verdunningen neemt de structuur van de zinkverbinding geleidelijk de overhand, maar de SCO-overgang van de ijzerverbinding blijft waarneembaar tot een ijzergehalte van $x = 0.24$. Bij het verlagen van het ijzergehalte x werden de twee hysteresiscycli aanvankelijk smaller, en verdwenen uiteindelijk bij $x = 0.76$, wat leidde tot een één-staps SCO-materiaal met een zekere mate van coöperativiteit. Een verdere verhoging van het zinkgehalte leidde tot een geleidelijk verlies van coöperativiteit en tot een volledig niet-coöperatief SCO-materiaal op het laagste ijzergehalte dat bestudeerd is ($x = 0.24$). Dit onderzoek laat duidelijk zien dat de aanwezigheid van een twee-staps SCO en hysteresiscycli gevolgen zijn van intermoleculaire interacties tussen moleculen van

verschillende spin. Deze twee verschillende manifestaties van coöperativiteit zijn door vergroting van de Fe-Fe afstand tegelijkertijd verloren gegaan .

SCO-materiaal op een oppervlak (Hfdst 7)

Voor nanogeheugen-toepassingen is de belangrijkste uitdaging om de spinwisselingen van een enkel molecuul op een oppervlak uit te voeren. De huidige uitdaging bestaat uit het sturen van de zelfordening en de adresseerbaarheid van SCO-moleculen op oppervlaktes. Een nieuw op bapphen gebaseerd ligand is bereid dat voorzien is van een keten van 12 koolstofatomen. Hoewel de aanwezigheid van deze keten zorgt voor veranderingen in het polypyridyl-ligand, vertoont de ijzerverbinding **13** (Tabel 8.1) nog steeds SCO in het bulkmateriaal, alhoewel het een geleidelijke overgang is en geen hysteresecyclus vertoont. De lange alkylstaart helpt het complex om zichzelf te ordenen op een oppervlak van hoog georiënteerd pyrolitisch grafiet (HOPG), waarop de moleculen een stabiel en sterk geordend 2D-patroon blijken te vormen. De afstanden in de patronen zoals waargenomen met een STM (Scanning tunneling microscoop) verschillen van de afstanden in vergelijkbare patronen die gevormd worden door vrije liganden op HOPG. Een model is voorgesteld dat suggereert dat de N–H···S intermoleculaire interacties van de ijzerverbinding **13** op het HOPG oppervlak nog intact zijn. Dit suggereert dat de moleculen van **13** misschien coöperatief SCO-gedrag zullen vertonen als ze aangebracht zijn op HOPG. STM bij variabele temperatuur is echter geen eenvoudige techniek en een samenwerking op dit onderwerp met de groep van het Atomic and Molecular Conductors (AMC) van het Leids instituut voor Natuurkunde is onlangs aangegaan. Het aanbrengen van de lange alkylketens op het bapphen-ligand zonder de N–H-bridgen te blokkeren lijkt een goede strategie te zijn om SCO-moleculen op oppervlaktes te brengen en te ordenen.

Het laatste hoofdstuk geeft een samenvatting van alle resultaten en een evaluerende discussie met plannen en suggesties voor verder onderzoek.

Referenties

1. O. Kahn and C. J. Martinez, *Science*, 1998, 279, 44-48.
2. S. Bonnet, M. A. Siegler, J. Sanchez Costa, G. Molnar, A. Bousseksou, A. L. Spek, P. Gamez and J. Reedijk, *Chem. Commun.*, 2008, 5619-5621.

List of Publications

Tuning the Transition Temperature and Cooperativity of bapbpy-Based Mononuclear Spin-Crossover Compounds: Interplay between Molecular and Crystal Engineering

Z. Arcis-Castillo, **S. Zheng**, M. A. Siegler, O. Roubeau, S. Bedoui, and S. Bonnet, *Chem. Eur. J.*, 2011, 17, 14826-14836.

Triggering a Phase Transition by a Spatially Localized Laser Pulse: Role of Strain

S. Bedoui, M. Lopes, W. Nicolazzi, S. Bonnet, **S. Zheng**, G. Molnar, and A. Bousseksou, *Phys. Rev. Lett.*, 2012, 109, 135702.

Synthesis and Characterization of Iron(II) Thiocyanate Complexes with Derivatives of the Tris(pyridine-2-ylmethyl)amine (tpma) Ligand

S. Kisslinger, H. Kelm, **S. Zheng**, A. Beitat, C. Wurtele, R. Wortmann, S. Bonnet, S. Herres-Pawlis, H. J. Kruger, and S. Schindler, *Z. Anorg. Allg. Chem.*, 2012, 638, 2069-2077.

Laser-Induced Artificial Defects (LIADs): Towards the Control of the Spatiotemporal Dynamics in Spin Transition Materials

S. Bedoui, M. Lopes, **S. Zheng**, S. Bonnet, G. Molnar, A. Bousseksou, *Adv. Mater.*, 2012, 24, 2475-2478.

Effect of Metal Dilution on the Thermal Spin Transition of $[\text{Fe}_x\text{Zn}_{1-x}(\text{bapbpy})(\text{NCS})_2]$

S. Zheng, M. A. Siegler, J. Sánchez Costa, W. T. Fu, and Bonnet, S., *Eur. J. Inorg. Chem.*, 2013, 1033-1042.

Curriculum Vitae

Sipeng Zheng was born on the 21st of December 1982 in Beijing, China. After high school he moved to South Africa where he studied science at the University of Port Elizabeth (now: Nelson Mandela Metropolitan University). He obtained his Bachelor's degree (2006), Bachelor Honours degree (2007), and Master's degree in Chemistry (2010) at the same institute.

From May 2010 to June 2014 he was a PhD student in the group of Metals in Catalysis, Biomimetics & Inorganic Materials (MCBIM) at Leiden University. The research presented in this thesis was performed during this period under the supervision of Dr. S. Bonnet and Prof. Dr. E. Bouwman. During his PhD he collaborated closely with several research groups such as the Laboratoire de Chimie de Coordination in Toulouse, and the group of Atomic and Molecular Conductors (AMC) at the Leiden Institute of Physics (LION).

The author participated in several schools and workshops, namely the HRSMC Autumn School in Metal-Organic Chemistry in September 2010 in Doorn, Netherlands, the IVth European School on Molecular Nanoscience in October 2011 in Peníscola, Spain, and in May 2012 the 4th International Workshop on Phase transition and Dynamical properties of Spin Transition Materials in Versailles, France. In addition, he attended a series of training courses such as Effective communication, Time management, and Scientific Integrity organized by the Leiden University graduate school.

As a part of the PhD program, he assisted in practical courses for *Life Science and Technology* (LST) and *Molecular Science and Technology* (MST). He supervised 5 MSc students (Gabriel Theurkauff, Niels Reintjens, Silvia Spa, Pauline van Deursen, Gemma Riera), and 3 BSc students (Corné Muilwijk, Putro Vink, Natalia Loewen).

Parts of the research described in this thesis have been presented orally or with posters at various meetings: the annual Jan Reedijk symposium in Leiden in October 2010, the Royal Netherlands Chemical Society KNCV meeting in Wageningen in April 2011, the HRSMC annual symposium in Amsterdam in November 2011, the NWO CW Study group meeting 'Chemistry in relation to physics and materials science' in Veldhoven in March 2013, and the International Conference on Advanced Complex Inorganic Nanomaterials in Namur, Belgium, July 2013.